Some Problems in Thin-Film Flow

Andrew James Mitchell
Department of Mathematics and Statistics
University of Strathclyde
Glasgow, UK

March 2024

This thesis is submitted to the University of Strathclyde for the degree of Doctor of Philosophy in the Faculty of Science.

This thesis is the result of the author's original research. It has been composed by the author and has not been previously submitted for examination which has led to the award of a degree.

Acknowledgements

First and foremost, I would like to thank my primary supervisor Professor Stephen Wilson. Thank you for always taking the time to read anything I wrote, listen to any questions I had, and always respond with insightful and detailed comments. Without your guidance, this work would not have been possible.

I would also like to thank my secondary supervisor Doctor Brian Duffy. In particular, thank you for our many meetings and discussions either in your office or in recent times via video call. Your advice and expertise in mathematics and fluid mechanics helped me to get to the heart of the problems in this thesis. Furthermore, I will always be grateful for your kindness and support during difficult times.

I am grateful for the endless support from all of my family. To my Mum, my Dad, Emma, Ann, Graham, Irene, Madeline and all of "the Barretts", thank you for everything.

To all of my friends, thank you for always being there with humour and kindness throughout the time spent writing this thesis. During the Covid-19 pandemic, all of your efforts to stay in touch virtually helped me to carry on despite the difficulties we were all facing. I would particularly like to thank my fellow postgraduate friends James, Michael, Alistair and Ioana, and my life-long friend Donald for their support.

Finally, to Laura, for your constant and endless support, thank you.

Abstract

Thin-film flows are ubiquitous in nature and industry, and this thesis considers three different thin-film flow problems that are inspired by and relevant to a number of real-world situations.

Firstly, we consider the steady and unsteady coating flow of a thin film of viscous fluid on the outside of a uniformly rotating horizontal circular cylinder in the presence of an irrotational airflow with circulation. In particular, it is shown that steady full-film solutions corresponding to a thin film of fluid that covers the entire cylinder are possible only when the flux and mass of the fluid do not exceed critical values, which are determined in terms of the speed of the far-field airflow and the circulation of the airflow. Furthermore, a long-time analysis shows that unsteady full-film solutions are unconditionally stable.

Secondly, we consider the squeeze-film flow of a thin film of fluid in the gap between an impermeable disk and an open-base porous bed, subject to a constant load. In particular, we determine the finite time required for the impermeable disk and the porous bed to contact, and the behaviour of the particle paths and penetration depths of the fluid within the porous bed. These are described in terms of the permeability and porosity of the porous bed and the slip length at the interface between the fluid and porous bed. In particular, in the asymptotic limits of small and large permeability, the contact time, particle paths, and penetration depths exhibit qualitatively different behaviour.

Finally, we consider the steady flow of a thin rivulet of evaporating fluid down an inclined substrate. In particular, for three different models of evaporation, we analyse the variation of the length, width and contact angle of the rivulet as the parameters appearing in the problem vary, such as the input flux of the rivulet, the angle of inclination of the substrate, and the parameters of the relevant model of evaporation. In particular, it is shown that, rather surprisingly, the length of the rivulet only depends weakly on the mode of evaporation.

Contents

Chapter 1

Introduction

1.1 Thin-film flow

A film of fluid is said to be thin when the characteristic length L^* and thickness H^* of the film are such that the aspect ratio

$$\epsilon = H^*/L^* \ll 1 \tag{1.1}$$

is small, where a star denotes a dimensional quantity. The mathematical analysis involved in modelling fluid flows can be greatly simplified when the film of fluid is thin. In particular, in the limit of small aspect ratio, one may neglect terms that are asymptotically smaller than others, often allowing for significant analytical progress to be made. This approximation is often referred to as the thin-film approximation, and it will be used throughout this thesis.

Since it is the ratio (rather than the absolute values) of the thickness and the length that determines whether a film is thin, the actual size of a thin-film flow can be large or small and include, for example, large-scale flows of continental ice sheets and small-scale flows of ink in inkjet printers. Indeed, thin-film flows are ubiquitous in both nature and industry (see, for example, the reviews by Oron et al. [124] and Craster and Matar [30]), and so are the subject of a large scientific literature.

In human biology, thin films of fluid arise in many places inside the body, for example, in the drainage of precorneal fluid in the eye [20], in the transport of mucus within the lungs [56], and in the lubrication of the gap in the knee joint with synovial fluid between the femoral condyle and the tibial plateau [86]. Figure

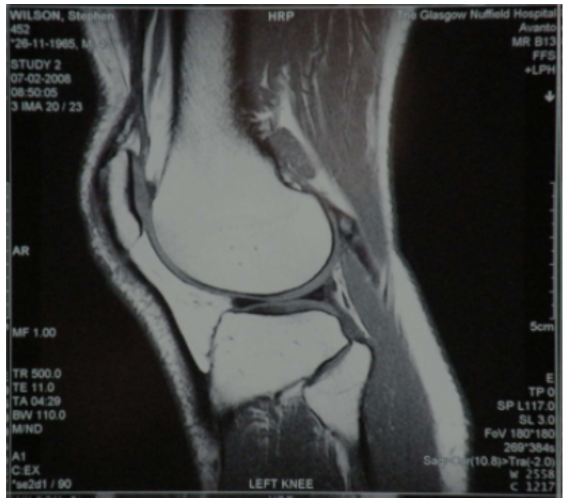

Figure 1.1: An MRI scan of a human knee (Image courtesy of Prof. Stephen K. Wilson).

1.1 shows an MRI scan of a human knee which shows the thin gap in the knee joint that is filled with a thin layer of synovial fluid, between the femoral condyle (above the gap) and the tibial plateau (below the gap).

Thin films of fluid also occur in geophysics. For example, the tidally modulated flow of brackish water from sea lochs into the sea form thin gravity currents that carry nutrients, sediments, fresh water and heat [165], the thermomechanical behaviour of large, but thin, ice sheets in the ocean subject to variations in the atmosphere over large time scales, which is an important area of study due to the ongoing problem of climate change [12], and, as shown in Figure 1.2, after volcanoes erupt, lava will begin to flow down the side of the volcano to its base, spreading out into a large but thin layer of lava [52].

Many industrial contexts involve thin film flow, for example, in the aviation industry, supercooled water droplets within clouds impact upon subzero aircraft wings and form thin layers of ice, as shown in Figure 1.3. These layers of ice can alter the aerodynamic properties of the wing and reduce lift, making ice accretion a major factor in many aircraft crashes, and so understanding how to reduce this phenomena is of great importance [114, 113, 151, 164]. Spray coating or painting, in which fluid is sprayed onto a solid surface forming a thin film of fluid upon it, is a process with many applications. Examples of the applications of spray coating include, for example, the spray painting of vehicles and their parts in the automobile industry [44], the spraying of thin layers (one atom thick) of graphine

Figure 1.2: Volcano in Iceland expelling a large lava flow. Image courtesy of Tetiana Grypachevska, sourced from [57].

onto electronic devices and machine parts [134], and, as shown in Figure 1.4, the application of protective chemicals to the inner surfaces of metal cans in order to protect them from the potentially corrosive and damaging fluids that they are used to contain [29].

The heating and cooling of thin films of fluid is a well studied topic due to its many applications such as in heat exchangers used, for example, in the food and drink industry [36], in oil and gas production [146], in microheat pipes which are used to dissipate heat in microelectronic devices [73, 88], and in the kitchen, where thin layers of fluid are subjected to heating or cooling when either cooking or refrigerating, respectively [97]. Figure 1.5 shows thin rivulets and droplets of oil forming on a frying pan, whose surface can be heated to temperatures of approximately 150°–200°.

It is clear that understanding the behaviour of thin-film flows is important for many practical contexts. Figures 1.1–1.5 show a few examples of these; however, there are, of course, many more. The research described in this thesis applies analytical and asymptotic methods to investigate a variety of thin-film flows, specifically steady and unsteady coating flow on a rotating cylinder in the presence of an external airflow, porous squeeze-film flow, and the flow of an evaporating rivulet. The remainder of this chapter will discuss the literature related to these problems, in particular, the effect of an external airflow on a thin film of fluid on a solid substrate, the flow of a thin film of fluid on the outside or inside of stationary and rotating cylinders, fluid being squeezed through a porous medium, and finally the

Figure 1.3: The accretion of ice on the wing of an aeroplane. Image courtesy of Cory W. Watts, sourced from [174].

Figure 1.4: Spray coating of a thin protective coating onto the inside of a metal can. Sourced from Cornwall [29], reprinted with permission from The American Association for the Advancement of Science (AAAS).

Figure 1.5: Rivulets of oil forming on a heated frying pan. Image courtesy of Matthew Sparks, sourced from [153].

flow and evaporation of a thin rivulet of fluid.

1.1.1 Thin-film approximation

As mentioned previously, throughout this thesis the thin-film approximation will be used to simplify the governing equations that describe the behaviour of the fluid flow and hence to allow significant analytical progress to be made. In this subsection, we shall describe, by means of the simple example of a thin-film flow down an inclined substrate, the typical mathematical analysis involved when applying the thin-film approximation.

Consider the unsteady gravity-driven flow of a thin film of an incompressible Newtonian fluid with constant density ρ^*, constant viscosity μ^*, and constant surface tension σ^* over a solid planar substrate inclined at an angle α to the horizontal. We use two-dimensional Cartesian coordinates (x^*, y^*), with the x^*-axis in the longitudinal direction, parallel to the substrate, and the y^*-axis normal to the substrate which is at $y^* = 0$. The free surface of the rivulet is at $y^* = h^*(x^*, t^*)$, where t^* denotes time.

The flow is governed by the well-known continuity equation

$$\nabla^* \cdot \mathbf{u}^* = 0, \tag{1.2}$$

and Navier–Stokes equation given by

$$\rho^* \frac{\partial \mathbf{u}^*}{\partial t^*} + \rho^* \left(\mathbf{u}^* \cdot \nabla^*\right) \mathbf{u}^* = -\nabla^* p^* + \mu^* \nabla^{*2} \mathbf{u}^* + \rho^* \mathbf{g}^*, \tag{1.3}$$

where $\mathbf{u}^* = (u^*(x^*, y^*, t^*), v^*(x^*, y^*, t^*))$ is the velocity of the fluid, $p^* = p(x^*, y^*, t^*)$ is the pressure in the fluid, and $\mathbf{g}^*$ is the acceleration due to gravity (see, for example, [15, 2]). At the substrate, the fluid satisfies the no-slip condition given by

$$\mathbf{u}^* \cdot \mathbf{t}^* - \boldsymbol{\Omega}^* \cdot \mathbf{t}^* = 0 \tag{1.4}$$

on $y^* = 0$, where $\boldsymbol{\Omega}^*$ is the velocity of the substrate, and $\mathbf{t}^*$ is a unit tangent vector to the substrate, and the no-penetration condition given by

$$\mathbf{u}^* \cdot \mathbf{n}^* - \boldsymbol{\Omega}^* \cdot \mathbf{n}^* = 0 \tag{1.5}$$

on $y^* = 0$, where $\mathbf{n}^*$ is a unit normal vector to the substrate. Note that from (1.4) and (1.5) the no-slip and no-penetration conditions can be written

$$\mathbf{u}^* = \boldsymbol{\Omega}^* \tag{1.6}$$

on $y^* = 0$. At the free surface the condition of continuity of normal stress is given by

$$\mathbf{n}^* \cdot \mathbf{T}^* \cdot \mathbf{n}^* - \mathbf{n}^* \cdot \mathbf{T}^*_{\mathrm{a}} \cdot \mathbf{n}^* = \sigma^* \Gamma^* \tag{1.7}$$

on $y^* = h^*$, where $\Gamma^* = \nabla^* \cdot \mathbf{n}^*$ is the mean curvature of the free surface, and the condition of continuity of tangential stress is given by

$$\mathbf{n}^* \cdot \mathbf{T}^* \cdot \mathbf{t}^* - \mathbf{n}^* \cdot \mathbf{T}^*_{\mathrm{a}} \cdot \mathbf{t}^* = 0 \tag{1.8}$$

on $y^* = h^*$, where $\mathbf{n}^*$ and $\mathbf{t}^*$ are now the outward unit normal and unit tangent vectors to the free surface, $\mathbf{T}^* = -p^*\mathbf{I} + 2\mu^*\boldsymbol{\tau}^*$ and $\mathbf{T}^*_{\mathrm{a}} = -p^*_{\mathrm{a}}\mathbf{I} + 2\mu^*_{\mathrm{a}}\boldsymbol{\tau}^*_{\mathrm{a}}$ are the stress tensors, with rate-of-strain tensors $\boldsymbol{\tau}^*$ and $\boldsymbol{\tau}^*_{\mathrm{a}}$ of the fluid and air, respectively, constant air pressure p^*_{a}, and constant viscosity of the air μ^*_{a} (see, for example, [15, 2]). The rate-of-strain tensor is given by

$$\boldsymbol{\tau}^* = \frac{1}{2} \left(\nabla^* \mathbf{u}^* + (\nabla^* \mathbf{u}^*)^T\right). \tag{1.9}$$

For future reference, the volume flux per unit width in the direction of increasing x^*, across a station $x^* =$ constant, is given by

$$Q^* = \int_0^{h^*} u^* \, \mathrm{d}y^*, \tag{1.10}$$

and the well-known kinematic condition $D(h^* - y^*)/Dt^* = 0$, where $D/Dt^* = \partial/\partial t^* + \boldsymbol{u^*} \cdot \nabla^*$ is the material derivative is given by

$$\frac{\partial h^*}{\partial t^*} + u^* \frac{\partial h^*}{\partial x^*} - v^* = 0, \tag{1.11}$$

which using (1.2) and (1.10) can be written

$$\frac{\partial h^*}{\partial t^*} + \frac{\partial Q^*}{\partial x^*} = 0. \tag{1.12}$$

In general, (1.2) and (1.3) may only be solved for the velocity $\mathbf{u}^*$ and pressure p^* numerically. However, by applying the thin-film approximation, i.e. using (1.1), analytical progress can be made, as will now be demonstrated. By writing (1.1) as $H^* = \epsilon L^*$, we introduce the thin film scalings

$$x^* = L^* x, \; y^* = \epsilon L^* y, \; h^* = \epsilon L^* h, \; t^* = \frac{L^*}{U^*} t, \tag{1.13}$$
$$u^* = U^* u, \; v^* = \epsilon U^* v, \; p^* - p^*_{\mathrm{a}} = \frac{\mu^* U^*}{\epsilon^2 L^*} p, \; Q^* = \epsilon L^* U^* Q,$$

where U^* is a characteristic velocity scale. Equation (1.2) and the x and y components of (1.3) become

$$\frac{\partial u}{\partial x} + \frac{\partial v}{\partial y} = 0, \tag{1.14}$$

$$\epsilon \mathrm{Re} \left(\frac{\partial u}{\partial t} + u \frac{\partial u}{\partial x} + v \frac{\partial u}{\partial y} \right) = -\frac{\partial p}{\partial x} + \sin\alpha + \frac{\partial^2 u}{\partial y^2} + \epsilon^2 \frac{\partial^2 u}{\partial x^2}, \tag{1.15}$$

$$\epsilon^3 \mathrm{Re} \left(\frac{\partial v}{\partial t} + u \frac{\partial v}{\partial x} + v \frac{\partial v}{\partial y} \right) = -\frac{\partial p}{\partial y} - \epsilon \cos\alpha + \epsilon^2 \left(\frac{\partial^2 v}{\partial y^2} + \epsilon^2 \frac{\partial^2 v}{\partial x^2} \right), \tag{1.16}$$

respectively, where

$$\mathrm{Re} = \frac{\rho^* U^* H^*}{\mu^*} \tag{1.17}$$

is the Reynolds number, which is a non-dimensional measure of the relative effect of inertia and viscosity, and

$$H^* = \left(\frac{\mu^* U^*}{\rho^* g^*}\right)^{\frac{1}{2}} \ll L^* \tag{1.18}$$

is the characteristic film thickness. We assume that the reduced Reynolds number given by $\hat{\mathrm{Re}} = \epsilon \mathrm{Re} \ll 1$ is small. The scaling choice of p in (1.13) acts to promote the pressure gradient in the y-direction to leading order in the thin-film limit. This choice is made in order to be consistent with the work of Chapter 2 and Chapter 3 in which a free surface flow experiences a normal pressure. Note that by promoting the pressure gradient to leading order in the y-direction, the effect of gravity in the y-direction (represented by the $\cos\alpha$ term in (1.15)) is reduced to first order in ϵ.

At the free surface, the unit normal and tangent vectors are given by

$$\mathbf{n} = \left(1 + \left(\epsilon\frac{\partial h}{\partial x}\right)^2\right)^{-\frac{1}{2}} \left(-\epsilon\frac{\partial h}{\partial x}, 1\right) \text{ and } \mathbf{t} = \left(1 + \left(\epsilon\frac{\partial h}{\partial x}\right)^2\right)^{-\frac{1}{2}} \left(1, \epsilon\frac{\partial h}{\partial x}\right), \tag{1.19}$$

respectively. Assuming that $\mu_{\mathrm{a}}^* \ll \mu^*$, the conditions of continuity of normal and tangential stress at the free surface then become

$$-p - \epsilon^2 \left(\left(\frac{\partial h}{\partial x}\right)^2 p + 2\frac{\partial h}{\partial x}\frac{\partial u}{\partial y} - 2\frac{\partial v}{\partial y}\right) - \epsilon^4 \left(2\frac{\partial h}{\partial x}\frac{\partial v}{\partial x} - 2\left(\frac{\partial h}{\partial x}\right)^2 \frac{\partial u}{\partial x}\right)$$
$$= -\mathrm{Ca}^{-1}\frac{\partial^2 h}{\partial x^2}\left(1 + \left(\epsilon\frac{\partial h}{\partial x}\right)^2\right)^{-\frac{1}{2}}, \tag{1.20}$$

where

$$\mathrm{Ca} = \frac{\mu^* U^*}{\epsilon^3 \sigma^*} \tag{1.21}$$

is the capillary number, which is a non-dimensional measure of the relative effect of viscosity and surface tension, and

$$\frac{\partial u}{\partial y} + \epsilon^2 \left(\frac{\partial v}{\partial x} - 2\frac{\partial h}{\partial x}\frac{\partial u}{\partial x} + 2\frac{\partial h}{\partial x}\frac{\partial v}{\partial x} - \left(\frac{\partial h}{\partial x}\right)^2 \frac{\partial u}{\partial y}\right) - \epsilon^4 \left(\frac{\partial h}{\partial x}\right)^2 \frac{\partial v}{\partial x} = 0. \tag{1.22}$$

Hence, at leading order in the limit $\epsilon \to 0$ (1.14) remains unchanged while (1.15) and (1.16) become

$$0 = -\frac{\partial p}{\partial x} + \sin\alpha + \frac{\partial^2 u}{\partial y^2} \tag{1.23}$$

and

$$0 = -\frac{\partial p}{\partial y}, \tag{1.24}$$

respectively. In the case of a stationary substrate, the no-slip and no-penetration conditions become

$$u = v = 0 \tag{1.25}$$

on $y = 0$. The conditions of continuity of normal and tangential stress at the free surface (1.20) and (1.22) become

$$p = \mathrm{Ca}^{-1}\frac{\partial^2 h}{\partial x^2} \tag{1.26}$$

and

$$\frac{\partial u}{\partial y} = 0 \tag{1.27}$$

on $y = h$, respectively. Unlike the system of equations (1.3)–(1.8), the equations (1.23) and (1.24) are easily solved subject to (1.25)–(1.27). Herein lies the usefulness of the thin-film approximation, which as we have shown, allows for analytical progress to be made whilst retaining the leading order behaviour of the thin film.

1.2 Effect of an external airflow on a thin film of fluid on a solid substrate

The interaction between an airflow and a thin film of fluid on a solid substrate is a fundamental problem in fluid mechanics, not only because of its intrinsic scientific interest, but also because of its relevance to a wide range of practical situations, such as ice accretion on aircraft wings, the jet wiping (or air knife) galvanisation process, and trickles of water on the windows of moving vehicles on rainy days.

The standard boundary conditions at the free surface of a fluid are those of continuity of normal and tangential stress, and thus models of thin-film flows in a passive atmosphere of a low-viscosity fluid (such as air) typically assume that the pressure at the free surface is equal to the constant ambient pressure in the atmosphere, and that the shear stress at the free surface is zero. However, for thin-film flow in the presence of an external airflow one or both of these conditions needs to be generalised to model the effect(s) of the airflow on the film and/or vice versa.

In Chapters 2 and 3 we will consider a thin film of fluid on a rotating horizontal cylinder in the presence of an external airflow, and so in this section we give an overview of previous work in which the pressure and/or the shear stress boundary conditions have been generalised to model the effect of an airflow.

(a) Non-zero shear stress

A simple approach to model the effect of an airflow on a thin film of fluid is to assume a condition of non-zero uniform shear stress and uniform ambient air pressure at the free surface.

Black [19] and Villegas-Díaz et al. [171] both independently investigated, using analytical and asymptotic methods, the flow of a thin film of fluid on the outside of a rotating cylinder subject to the effects of gravity and a uniform shear stress at the free surface due to the presence of an external airflow. As will be discussed in more detail in Section 1.3, both Black [19] and Villegas-Díaz et al. [171] showed that when the shear stress acts in the same direction as the rotation of the cylinder (i.e. positive shear) then the film of fluid behaves qualitatively similarly to that of the classical solution with no airflow effects obtained by Moffatt [108], however, if the shear stress acts in opposition to the rotation of the cylinder (i.e. negative shear), then the film of fluid behaves qualitatively differently to that of the classical solution with no airflow effects obtained by Moffatt [108]. In a follow-up paper motivated by the interaction between the airflow within and the film of oil on the inside of the outer shaft of the bearing chamber in a rapidly rotating aeroengine, Villegas-Díaz et al. [172] revisited this problem, with surface tension effects included, and investigated the stability of their solutions. Kay et al. [76], also motivated by the interaction between the airflow and a thin film of fluid within aeroengines, extended the analysis of Villegas-Díaz et al. [171] to include inertial effects at leading order. They showed, among other results, that the inclusion of inertial effects at leading order allowed for a greater range of thin-film solutions than had previously been obtained in the literature

Sullivan et al. [157] investigated, using analytical and asymptotic methods, the steady unidirectional flow of a thin rivulet of perfectly wetting fluid (that is, the

Figure 1.6: Rivulets of rainwater on the side window of a moving car. Image courtesy of Prof. Stephen K. Wilson.

contact angle, i.e. the angle that the free surface of the rivulet makes with the substrate at their point of contact, is zero) down an inclined substrate, subject to the effects of gravity and a longitudinal uniform shear stress due to the presence of an external airflow. Interactions such as this can be found, for example, as shown in Figure 1.6, on the windows of moving vehicles on rainy days. Sullivan et al. [157] found, in accordance with physical intuition, that for weak negative shear stress only fluid near the free surface is forced to flow back up the substrate against gravity while the bulk of the rivulet still flows in the direction of gravity. As the magnitude of the shear stress is increased more of the fluid within the rivulet is forced back up the substrate against gravity, until eventually when the shear stress dominates the effect of gravity the entire rivulet moves in the opposite direction to gravity.

A non-uniform shear stress may also be used in order to model the effect of an airflow on a thin film of fluid. For example, in the context of the spin coating process, in which a small amount of fluid is applied to the centre of a disk which is then rotated in its plane at high speed, which forces the fluid radially outwards forming a thin layer over the entire disk, can induce a large outward radial airflow, with shear stress proportional to the distance from the centre of the disk (see, for example, [103, 125, 187, 93]). This process is used extensively in the manufacturing of semiconductors, where very thin, uniform layers of photoresist are required.

Middleman [103] investigated, using analytical and asymptotic methods, the unsteady spin coating of a thin film of fluid on a rotating disk subject to the effects of gravity and a non-uniform shear stress at the free surface due to the presence of an external airflow of the form

$$\mu^* \frac{\partial v_r^*}{\partial z^*} = A^* r^*, \tag{1.28}$$

where $A^* = (\omega^{*3}\mu_{\rm a}^*\rho_{\rm a}^*)^{1/2}/2$, ω^* is the constant angular velocity of the disk, $\rho_{\rm a}^*$ is the constant density of the air, r^* is the radial distance from the centre of the disk, and v_r^* is the radial fluid velocity. Middleman [103] found that the film evolves according to the evolution equation

$$t = \beta\left(\frac{1}{H} - 1\right) - \beta^2 \ln\left(\frac{\beta H + 1}{H(1+\beta)}\right) \to \frac{1-H^2}{2H} \quad \text{as} \quad \beta \to \infty, \tag{1.29}$$

where t (non-dimensionalised with $2\rho^*\omega^{*2}h_0^{*2}/(3\mu^*)$) and H (non-dimensionalised with h_0^*) are non-dimensional measures of time and the film thickness, respectively, and the non-dimensional parameter β is defined as

$$\beta = \frac{2}{3}\frac{h_0^*\omega^{*\frac{3}{4}}\rho^*}{A^*}, \tag{1.30}$$

where h_0^* is the average film thickness. The parameter β is a non-dimensional measure of the relative effect of the angular velocity and the shear stress of the airflow. In particular, $\beta \to 0$ corresponds to infinite shear stress and $\beta \to \infty$ corresponds to zero shear stress. Figure 1.7, based on Figure 1 of Middleman [103], shows the solution of (1.29) H as a function of t for various values of β. In particular, Figure 1.7 shows that as the strength of the shear stress increases (i.e. as β decreases), the film thickness decreases. Furthermore, Figure 1.7 shows that the solution departs from the solution in the limit $\beta \to \infty$ (shown with a dashed line) at $H \sim 1/\beta$. This shows that initially the film thickness reduces due to the effect of rotation until the film reaches $H \sim 1/\beta$, after which the film thickness reduces due to the effect of the shear stress.

Wu [187] investigated, using numerical methods, the unsteady spin coating of a thin film of fluid on a rotating disk subject to the effects of gravity, thermocapillarity, thermoviscosity, van der Waals attractions, and a non-uniform shear stress due to the presence of an external airflow. In particular, Wu [187] derived an evolution equation for the thin film and solved it numerically subject to a non-uniform

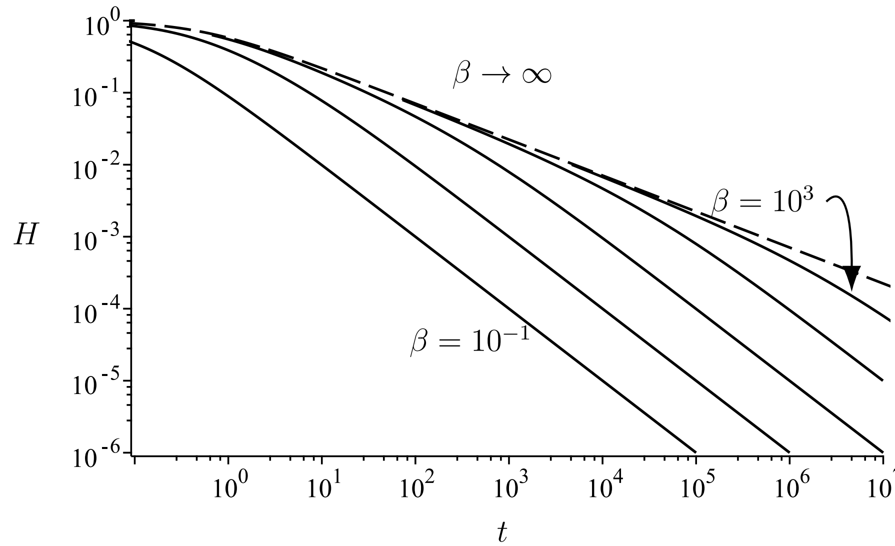

Figure 1.7: Plot of the solution of (1.29) showing a plot of the film thickness H on a spinning disk in the presence of an airflow as a function of non-dimensional time t for $\beta = 10^{-1}, 1, 10, 10^1, 10^2, 10^3$, and $\beta \to \infty$ shown with a dashed line. Based on Figure 1 of Middleman [103].

shear-stress condition at the free surface. Wu [187] analysed how the film behaves subject to all of the physical effects they included and found, among other results, that while the shear stress due to the airflow played a part in the thinning of the film, the effects of thermocapillarity and thermoviscosity had a larger influence in the thinning of the film.

(b) Non-uniform pressure distribution

Another approach used to model the effect of an airflow on a thin film of fluid is to assume a condition of non-uniform pressure but zero shear stress at the free surface.

King and Tuck [81] and Paterson et al. [130], for example, investigated the effect of an external airflow on a thin ridge of fluid on a planar substrate inclined at an angle α to the horizontal, for which the pressure at the free surface of the ridge is strongly coupled with the non-uniform pressure of the airflow. In particular, [81, 130] considered an airflow that consists of a uniform stream with constant speed far from the ridge U^*_∞ (i.e. the far-field speed), plus a non-uniform perturbation due to the presence of the ridge that was derived from classical thin-aerofoil theory (see, for example, Van Dyke [168]). In particular, this non-uniform perturbation has a velocity potential given by

$$\phi(x, y) = x + \frac{\epsilon}{2\pi} \int_0^L h'(\xi) \log[(x-\xi)^2 + y^2] \, \mathrm{d}\xi, \tag{1.31}$$

where x (non-dimensionalised by the characteristic transverse length scale L_0^*) is the transverse axis parallel to the substrate, y (non-dimensionalised with L_0^*) is the axis normal to the substrate, ϕ (non-dimensionalised with $U_\infty^* L_0^*$) is the velocity potential, L (non-dimensionalised with L_0^*) is the transverse width of the ridge, $\epsilon \ll 1$ is the small transverse non-dimensional aspect ratio of the film, and $h(x)$ (non-dimensionalised with $\epsilon L_0^* \ll L_0^*$) is the characteristic thickness of the ridge. Combining (1.31) with Bernoulli's equation, yields the pressure at the free surface given by

$$p_\mathrm{a} = -\Lambda \int_0^L \frac{(x-\xi)h'(x)}{(x-\xi)^2 + y^2} \, \mathrm{d}\xi, \tag{1.32}$$

where the non-dimensional Weber number is given by

$$\Lambda = \frac{\rho_\mathrm{a}^* L_0^* U_\infty^{*2}}{\pi \sigma^*} \geq 0, \tag{1.33}$$

which is a measure of the relative effect of the pressure forces and the surface tension.

King and Tuck [81] investigated, using analytical and numerical methods, the the flow of a thin ridge of fluid on a planar substrate inclined at an angle α to the horizontal, subject to the effects of gravity and the non-uniform pressure (1.32) due to the presence of an external airflow, but in the absence of surface tension effects (so that Λ is given instead by $\bar{\Lambda} = \rho_\mathrm{a}^* U_\infty^{*2} / \pi \rho^* g^* L_0^*$ in (1.32)). Note that King and Tuck [81] considered variation over the characteristic thickness scale of the thin ridge ($\epsilon L_0^* \ll L_0^*$), and so neglected the y in (1.32). Using this non-uniform expression for the air pressure, King and Tuck [81] derived a non-linear integro-differential equation for the thickness $h(x)$, which they solved numerically. Their analysis showed that, for each value of α, there are zero, one or two values of the strength of the external airflow for which a steady solution for the thickness $h(x)$ exists.

Paterson et al. [130] investigated, using analytical, asymptotic and numerical methods, the flow of a thin ridge of fluid on a planar substrate inclined at an angle α to the horizontal, subject to the effects of gravity, surface tension and the non-uniform pressure (1.32) due to the presence of an external airflow. In particular, Paterson et al. [130] showed, among other results, that when the substrate is nearly horizontal, i.e. near $\alpha = 0$ or $\alpha = \pi$, a very wide ridge can be supported against gravity by capillarity and/or the non-uniform air pressure, however, when the substrate is not nearly horizontal, i.e. $\alpha = \mathcal{O}(1)$, only a narrower (but still wide) rivulet can be supported.

Particularly relevant to the analysis of Chapter 2 and 3 is the investigation of Newell and Viljoen [118], who considered the evolution of an initially uniform thin film of fluid supported on the outside of a rotating horizontal cylinder against gravity by a combination of the shear that is induced by the rotation of the cylinder and the non-uniform pressure on the free surface of the film due to the presence of an external irrotational airflow. The conditions for the external airflow to be irrotational will be discussed in Chapter 2. Newell and Viljoen [118] assumed that since the film is thin, the airflow (which is assumed to be inviscid) is unaffected by the presence of the film on the cylinder. Therefore, unlike [81, 130], the airflow does not depend on the shape of the film, and the pressure at the free surface due to the external airflow is prescribed. In particular, the non-uniform pressure at the free surface of the fluid due to the external airflow, derived from classical inviscid flow theory (see, for example, Batchelor [15]), used by Newell and Viljoen [118] is the same as that used in Chapters 2 and 3. Hence, we shall briefly discuss the derivation and properties of this non-uniform pressure. The airflow considered by Newell and Viljoen [118] is assumed to be incompressible, and so, the velocity potential of the airflow ϕ^* satisfies Laplace's equation

$$\nabla^{*2}\phi^* = 0. \tag{1.34}$$

Since (1.34) is linear, different solutions for the velocity potential ϕ^* can be superposed to form a new solution. In particular, it is well known [15] that the velocity potential for the flow of an irrotational airflow with circulation around a rotating cylinder is formed by the superposition of elementary irrotational flows. In particular, considering polar coordinates (r^*, θ), with the azimuthal coordinate θ measured from the horizontal, and a cylinder of radius a^*, by superposing the velocity potentials of a uniform horizontal flow of the form

$$\phi^* = U^*_\infty r^* \cos\theta, \tag{1.35}$$

a doublet (formed by bringing together a source and a sink flow) of the form

$$\phi^* = \frac{U_\infty^* a^{*2} \cos\theta}{r^*}, \tag{1.36}$$

and a free vortex with circulation κ^* of the form

$$\phi^* = \frac{\kappa^* \theta}{2\pi}, \tag{1.37}$$

we find that the velocity potential for the flow of an irrotational airflow with circulation around a rotating cylinder is given by

$$\phi^* = U_\infty^* r^* \cos\theta \left(1 + \frac{a^{*2}}{r^{*2}}\right) + \frac{\kappa^*}{2\pi}\theta, \tag{1.38}$$

and hence the streamfunction is given by

$$\psi^* = U_\infty^* r^* \sin\theta \left(1 - \frac{a^{*2}}{r^{*2}}\right) - \frac{\kappa^*}{2\pi} \ln r^*. \tag{1.39}$$

Figure 1.8 shows the streamlines given by (1.39) for various values of the parameter $\lambda = \kappa^*/(4\pi a^* U_\infty^*)$, and, in particular, the positions of the stagnation points around the cylinder. The positions of the stagnation points are found when the radial and azimuthal components of the air velocity v_r^* and v_θ^*, given by

$$v_r^* = U_\infty^* \left(1 - \frac{a^{*2}}{r^{*2}}\right) \cos\theta \tag{1.40}$$

and

$$v_\theta^* = -U_\infty^* \left(1 + \frac{a^{*2}}{r^{*2}}\right) \sin\theta + \frac{\kappa^*}{2\pi r^*}, \tag{1.41}$$

respectively, are zero. Hence, as can be seen from Figure 1.8, the airflow has two stagnation points which lie on the cylinder at $r^* = a^*$ and $\theta = \sin^{-1}\lambda$ and $\theta = \pi - \sin^{-1}\lambda$ when $0 \leq |\lambda| < 1$, that coalesce into a single stagnation point at either the top or the bottom of the cylinder at $r^* = a^*$ and $\theta = \mathrm{sgn}(\lambda)\pi/2$ when $|\lambda| = 1$, and lie within the airflow either directly above or directly below the cylinder at $r^* = a^* \left[|\lambda| + (\lambda^2 - 1)^{1/2}\right]$ $(> a^*)$ and $\theta = \mathrm{sgn}(\lambda)\pi/2$ when $|\lambda| > 1$. Combining (1.41) with Bernoulli's equation (in the absence of gravitational effects) given by

$$p_{\mathrm{a}}^* - p_\infty^* = \frac{1}{2}\rho_{\mathrm{a}}^* \left(U_\infty^{*2} - v_\theta^{*2}\right), \tag{1.42}$$

where p_∞^* is the constant air pressure far from the cylinder (i.e. the far-field pressure), the non-uniform pressure $p_{\mathrm{a}}^*(\theta)$ at the free surface is given by

$$p_{\mathrm{a}}^* = p_\infty^* + \frac{\rho_{\mathrm{a}}^*}{2}\left[U_\infty^{*2} - \left(2U_\infty^* \sin\theta - \frac{\kappa^*}{2\pi a^*}\right)^2\right]. \tag{1.43}$$

It is clear from (1.43) that, without loss of generality, the velocity of the far field airflow can be assumed to be non-negative, i.e. that $U_\infty^* \geq 0$, while the circulation κ^* may be positive (i.e. anticlockwise), negative (i.e. clockwise) or zero (i.e. no circulation). The results of Newell and Viljoen [118] will be described in further detail in Section 1.3.

(c) A combination of non-zero shear stress and non-uniform pressure

Another approach used to model the effect of an airflow on a thin film of fluid is to combine the approaches described in sections (a) and (b) above and assume both a non-uniform pressure and a non-zero shear stress at the free surface.

King et al. [82], for example, investigated, using analytical and numerical methods, steady waves on a thin film of fluid on an inclined substrate subject to the effects of gravity, surface tension, and a constant shear stress and non-uniform pressure of the form (1.32) (again, with y neglected) due to the presence of an external airflow. In particular, King et al. [82] showed, among other results, that in the limit of weak gravitational effects, the waves approach a series of periodic single solitary sharp spikes on a thin fluid layer of otherwise constant thickness. As the shear stress becomes large, the spikes become widely separated and the substrate between these spikes becomes asymptotically dry.

Shear stress and pressure distributions due to the airflow may also be obtained from experimental studies or numerical simulations. For example, such techniques have been employed to investigate the cause of potentially damaging vibrations of the cables of cable-stayed bridges that occur on wet and windy days, known as rain–wind-induced vibrations (RWIVs). Early research on this problem was carried out by Hikami and Shiraishi [60] who reported upon the observation of RWIV of Meikonishi bridge over Nagoya Harbour in Japan, and carried out an experimental study to investigate their cause. By simulating conditions on rainy

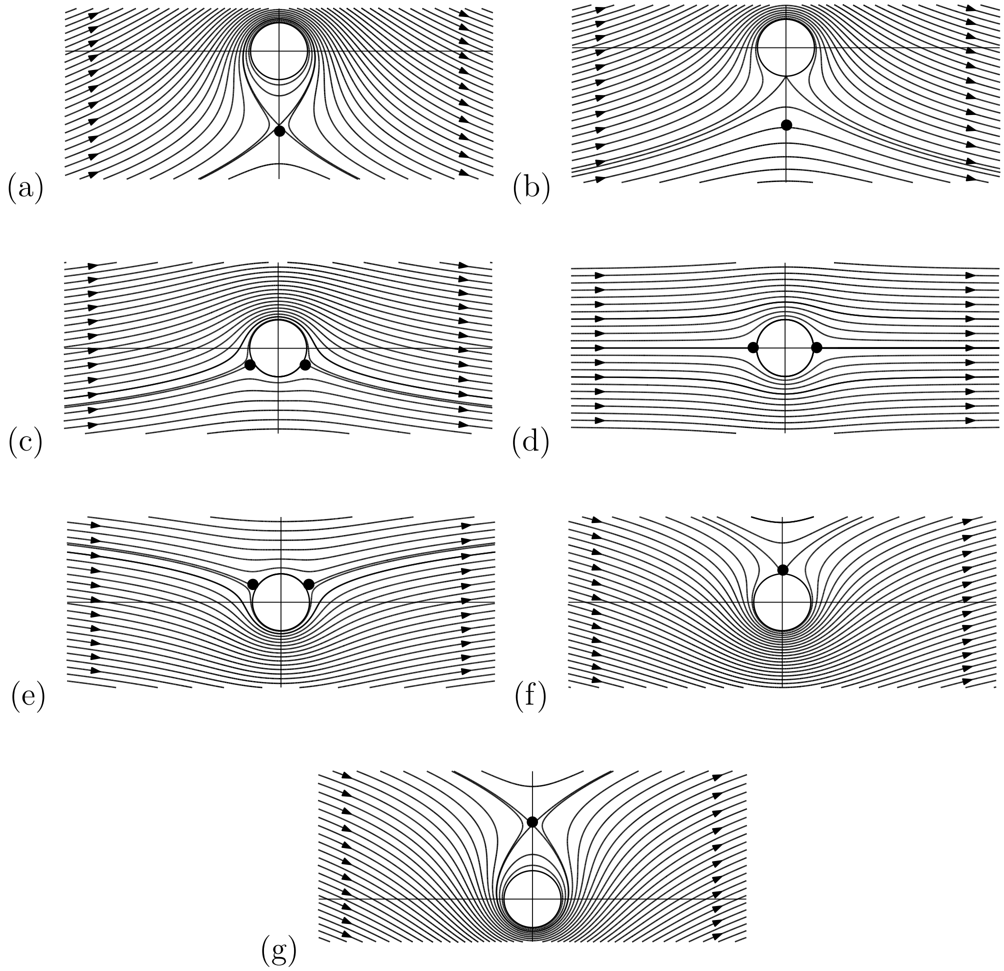

Figure 1.8: Plots of typical streamlines $\psi^* = \text{constant}$ where ψ^* is given by (1.39) with, $U^*_\infty = 1$, $a^* = 2$ (a) $\lambda = -3/2$, (b) $\lambda = -1$, (c) $\lambda = -1/2$, (d) $\lambda = 0$, (e) $\lambda = 1/2$ (f) $\lambda = 1$ (g) $\lambda = 3/2$. The locations of the stagnation points of the airflow are indicated with dots (•)

and windy days in a wind tunnel, they discovered that thin rivulets of rain water formed on the upper half of the cylindrical cables causing aerodynamic instabilities and leading to the observed potentially damaging vibrations.

Lemaitre et al. [90] modelled the flow of thin rivulets on a cable subject to the effects of gravity, surface tension, airflow due to the wind and the motion of the cable. They modelled the airflow using a pressure and shear stress (or friction) coefficients $C_{\mathrm{p}}(\theta)$ and $C_{\mathrm{f}}(\theta)$, where again θ is the azimuthal coordinate around the cylinder. Figure 1.9 shows the distributions Lemaitre et al. [90] used for the two airflow coefficients $C_{\mathrm{p}}(\theta)$ and $C_{\mathrm{f}}(\theta)$, taken originally from the experiments of Achenbach [1], who measured the air pressure and shear stress distributions around a dry cylinder placed within and orientated normal to a uniform airflow. Lemaitre et al. [90] solved numerically an evolution equation they derived for the film thickness $H(\theta, t)$ (non-dimensionalised with characteristic film thickness h_0^*) at time t (non-dimensionalised with $\mu^*/(R^* h_0^* \rho^*)$, where R^* is the radius of the cylinder). They found that for high wind speeds, two bulges in the film appear in the neighbourhood of the points in which the airflow would separate from the surface of a dry cylinder. This can be seen in Figure 1.10, which shows that the film thickness $H(\theta, t)$ is a uniform film at $t = 0$ and a non-uniform film with two bulges in the neighbourhood of the points at which the airflow separates from the cylinder (i.e. cable) on the upper and lower halves of the cylinder (i.e. cable) at $t = 1.7 \times 10^{-5}$, in agreement with the observations of Hikami and Shiraishi [60].

A series of numerical studies on RWIVs by Robertson et al. [144], Taylor and Robertson [162, 163] sought to further understand the interaction between the airflow and the rivulets that form on the cables and cause RWIVs. Robertson et al. [144] revisited the work of Lemaitre et al. [90], again using the pressure and shear stress distributions of Achenbach [1] shown in Figure 1.9, and instead they modelled rivulet formation and evolution on the cylinder using a self developed numerical model, which utilises a pseudo-spectral method, which they used to confirm the results of Lemaitre et al. [90] and further analyse the effect of the pressure and shear stress distributions on the evolution of the rivulets. The investigations by Taylor and Robertson [162] and [163] both use more advanced numerical models to analyse the effect of the airflow. The former, Taylor and Robertson [162] applied an unsteady aerodynamic solver and the latter, Taylor and Robertson [163] applied the Discrete Vortex method, whilst both employed the pseudo-spectral method of [144] to model the rivulets. In particular, Taylor and Robertson [163] investigated the effect of varying the film thickness on the formation and evolution of the rivulets as well as the effect of varying the angle of attack in the plane of the airflow, on the fluid, and hence obtained a highly detailed description of the mechanisms that lead to RWIVs. One of the potential causes of RWIVs, as described by Taylor and Robertson [163], is the formation of vortices in the wake that forms in the downstream side of the cylinder when the boundary layers in the airflow separate from the cylinder surface. Furthermore, Taylor and Robertson [163] found that it is possible for the rivulet on the upper half of the cylinder to deflect the corresponding separated boundary layer further from the

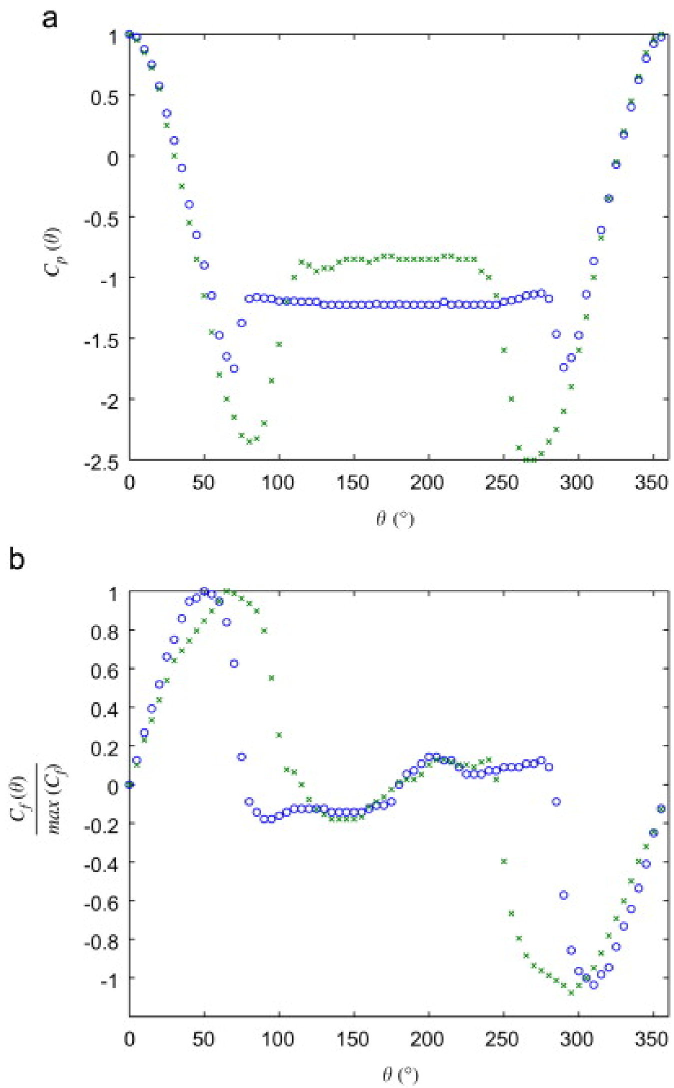

Figure 1.9: The distributions of (a) the pressure coefficient $C_{\mathrm{p}}(\theta)$ and (b) the normalised shear stress (friction) coefficient $C_{\mathrm{f}}(\theta)/\max(C_{\mathrm{f}})$ as functions of the azimuthal coordinate around the cylinder θ, where ($\circ$) represents Re $= 10^5$ and ($\times$) represents Re $= 3.6 \times 10^6$ used by Lemaitre et al. [90], obtained originally from the experiments of Achenbach [1]. Reprinted from Lemaitre et al. [90] with permission from Elsevier.

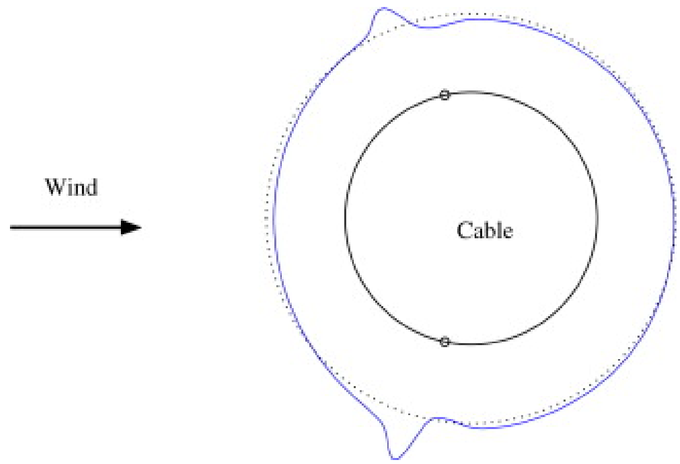

Figure 1.10: Numerical solution for the film thickness $H(\theta, t)$ on a cylinder (i.e. cable) subject to gravity, surface tension and an airflow obtained by Lemaitre et al. [90]. The solution starts as a uniform film at $t = 0$ with a dotted line and evolves to the non-uniform film with a solid line at $t = 1.7 \times 10^{-5}$. The circles ($\circ$) indicate the points at which the airflow separates from the cylinder. Reprinted from Lemaitre et al. [90] with permission from Elsevier.

horizontal centre line of the cylinder. As a result, the wake in the downstream side of the cylinder becomes wider. This wider wake reduces the interaction between the boundary layers on either side of the cylinder, which affects the characteristics of the wake, in particular, reduces the formation of vortices.

The jet-wiping (or jet-stripping) process, in which one or more impinging jets of air are used to reduce the thickness of a film of fluid on a moving substrate, is a process used, for example, in the galvanising industry to apply a thin layer of molten zinc to steel. Figure 1.11, for example, shows a schematic of the jet-wiping operation applied to the galvanisation process, in which a moving substrate, i.e. a metallic strip is submerged in a coating bath of molten zinc, so that a liquid film is carried upwards with the strip, and then passes between two jets of air supplied from high-pressure nozzles. The dynamics of the interaction between the jet of air and the thin film of fluid has been investigated extensively (see, for example, [41, 167, 117, 51, 116, 193, 71, 102, 13]), mostly with numerical simulations.

Tuck and Vanden-Broeck [167], motivated by the jet-wiping process, investigated, using analytical and numerical methods, the steady flow of a thin film of fluid on a vertical substrate moving with constant speed subject to the effects of gravity, surface tension, and a non-uniform shear stress and non-uniform pressure due to an airflow directed at the film, normal to the substrate (see, for example,

Figure 1.11). In particular, for an unknown tangential stress $T^*(y^*)$ and pressure $P^*(y^*)$, where y^* is the axis parallel to the substrate, Tuck and Vanden-Broeck [167] showed that the flux per unit axial length of the fluid Q^* is given by

$$Q^* = V^* h^* + \frac{T^*}{2\mu^*} h^{*2} - \frac{\rho^* g^* + P^{*\prime} - \sigma^* h^{*\prime\prime\prime}}{3\mu^*} h^{*3}, \tag{1.44}$$

where V^* is the constant speed of the moving substrate. If surface tension effects are negligible ($\sigma^* = 0$), and there is no shear stress ($T^* = 0$) or pressure gradient ($P^{*\prime} = 0$) due to the airflow at the free surface, then (1.44) reduces to the classical coating flow problem (see, for example, [108, 137]), which will be discussed in further detail in Section 1.3. Tuck and Vanden-Broeck [167], in the absence of shear stress at the free surface ($T^* = 0$), solved (1.44) numerically with both a quadratic and an exponential pressure gradient $P^{*\prime}$, and found that regardless the shape of the pressure distribution, as surface tension is increased, a stronger jet (i.e. a higher pressure) is required to reduce the film thickness (i.e. maintain the same jet-stripping effect). This is due to the tendency of surface tension to maintain the shape of the thin film.

More recently, Naphade et al. [117] investigated, using numerical methods, the unsteady flow of a thin film of fluid on a vertical moving substrate subject to the effects of gravity and a non-uniform shear stress and non-uniform pressure due to an airflow directed at the film, normal to the substrate (see, for example, Figure 1.11). In particular, Naphade et al. [117] derived a mathematical model which predicts the mass of fluid on the moving substrate and used Computational Fluid Dynamics (CFD) to generate the pressure and shear stress profiles due to the airflow on the free surface of the fluid. They then performed a sensitivity analysis to determine the operating window that could help improve the galvanising line operation. Naphade et al. [117] found that it is most favourable if the nozzle of the jet (as seen in Figure 1.11) is as close to the moving substrate as possible, and that the pressure of the air coming from the nozzle is as high as possible.

Mendez et al. [102] investigated, using analytical and numerical methods, the unsteady flow of a thin film of fluid on a vertical moving substrate subject to the effects of gravity and a non-uniform shear stress and non-uniform pressure due to an airflow directed at the film, normal to the substrate (see, for example, Figure 1.11). In particular, Mendez et al. [102] extended classical laminar boundary layer models for falling films with integral boundary layer models and

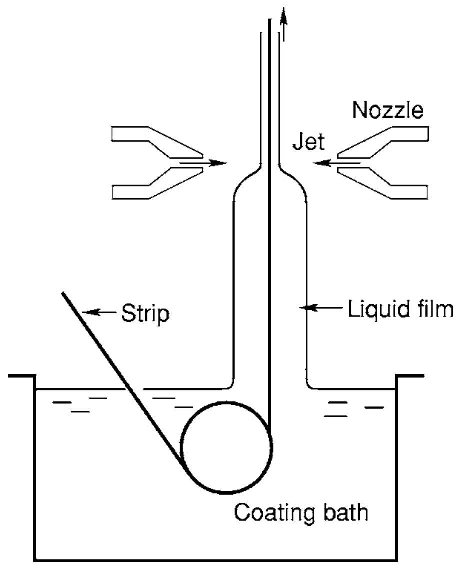

Figure 1.11: A schematic of the jet-wiping operation applied to the galvanisation process. The schematic shows the metallic strip being submerged in the coating bath of molten zinc, which then passes between two jets of air supplied from high pressure nozzles. Reprinted from Gosset and Buchlin [51] with permission from American Society of Mechanical Engineers (ASME), Copyright 2023.

used shear stress and pressure distributions due to the airflow derived from experimental studies and numerical simulations. Mendez et al. [102] compared their model and results to previous long wave and numerical studies and found good agreement. They concluded that the integral models that they derived allow for the successful simulation of the complex air-jet and fluid interaction in industrially relevant conditions.

1.3 Flow on stationary and rotating cylinders

The flow of a thin film of fluid on the outer (coating flow) or inner (rimming flow) surface of a cylinder is a well-studied problem in fluid mechanics. This problem is applicable to many practical situations, for example, the manufacturing of pipes and coating their inner surfaces [70], the coating of cylindrical fluorescent tubes [126], the flow of fluid on the outside of rollers in paper making machinery [190], and the even coating of paint from the outside of paint-coated rollers is of great importance within the printing industry [191]. This section will give an overview of the literature concerning the coating and rimming flow of fluids on stationary and rotating cylinders.

1.3.1 Flow on stationary cylinders

Coating and rimming flow on the surfaces of stationary cylinders has been an active area of research for many decades dating back to, for example, the classical work of Nusselt [120, 121], who considered the steady flow of a thin film of fluid on a stationary horizontal cylinder, subject to the effects of gravity. Nusselt [120, 121] showed that for a prescribed supply flux incident on a stationary cylinder the film thickness varies like $|\cos\theta|^{-1/3}$, where again θ is the azimuthal angle measured from the horizontal around the cylinder. This result shows that the film has left-to-right and top-to-bottom symmetry and that the film becomes infinitely large at the top ($\theta = \pi/2$) and bottom ($\theta = -\pi/2$) of the cylinder, which violates the thin-film approximation, but can be interpreted as the film falling on to and off of the cylinder at its top and bottom, respectively, as shown in Figure 1.12(a).

Duffy and Wilson [38] extended the analysis of Nusselt [120, 121] to consider the steady non-symmetric flow of a thin film of fluid on a stationary horizontal cylinder, subject to the effects of gravity, by considering a piecewise function for the azimuthal volume flux Q^* per unit axial length in the direction of increasing θ given by

$$Q^* = \begin{cases} (1-k)Q^*_{\mathrm{S}} & \text{if } \cos\theta > 0, \\ -kQ^*_{\mathrm{S}} & \text{if } \cos\theta < 0, \end{cases} \tag{1.45}$$

where $Q^*_{\mathrm{S}} > 0$ is the prescribed supply flux at the top of the cylinder and $0 \le k \le 1$ is an unknown constant which must be determined by additional information, for example, the specification of the film thickness at a prescribed point around the cylinder. Duffy and Wilson [38] obtained the solution for the film thickness $h(\theta)$ (non-dimensionalised with $(g^*/(\nu^* Q^*_{\mathrm{S}}))^{1/3}$, where ν^* denotes the kinematic viscosity) given by

$$h(\theta) = \left(\frac{3[k - H(-\cos\theta)]}{\cos\theta} \right)^{\frac{1}{3}}, \tag{1.46}$$

where $H(\cdot)$ is the Heaviside function. Figure 1.12(b), which shows the solution for the film thickness given by (1.46) in the case $k = 1/9$, shows that by considering a flux of the form (1.45), unlike the classical solution of Nusselt [120, 121], the film no longer in general exhibits left-to-right symmetry, except in the special case $k = 1/2$, in which (1.46) returns the classical symmetric solution for the film

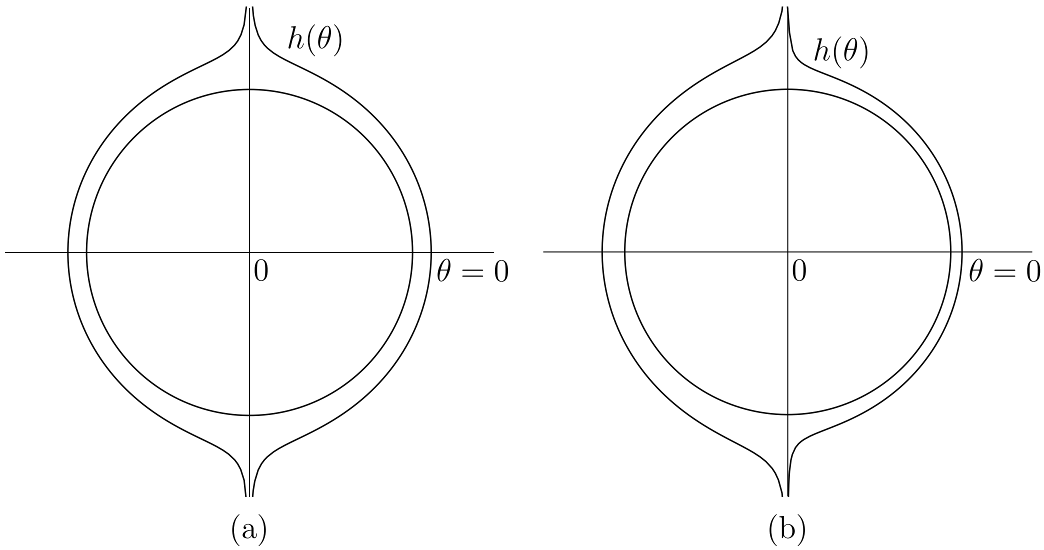

Figure 1.12: The solution for the flow of a thin film of fluid, $h(\theta)$ given by (1.46), with θ increasing anti-clockwise from $\theta = 0$, on the outside of a stationary cylinder drawn for the cases (a) $k = 1/2$ and (b) $k = 1/9$. Based on Figure 2 of Duffy and Wilson [38].

thickness given by Nusselt [120, 121], as shown in Figure 1.12(a).

The unsteady flow of thin films of fluid on stationary cylinders has also been well-studied. For example, Reisfeld and Bankoff [143] investigated, using analytical and numerical methods, the unsteady isothermal and non-isothermal flow of a fluid film on a horizontal stationary cylinder subject to the effects of gravity, surface tension, thermocapillarity and van der Waals forces. In the isothermal case, Reisfeld and Bankoff [143] found that when the Bond number, which is a non-dimensional measure of the relative effect of gravity and surface tension, given by

$$Bo = \frac{\rho^* g^* a^{*3}}{d_0^* \sigma_0^*}, \tag{1.47}$$

where d_0^* denotes the mean film thickness and σ_0^* denotes the mean surface tension, is zero ($Bo = 0$), a steady solution for the film thickness is possible, however when the Bond number is positive ($Bo > 0$) only an unsteady solution for the film thickness is possible. In the absence of van der Waals effects, the unsteady isothermal solution for the film thickness, forms a pendent-drop-like shape at the base of the cylinder with two symmetric regions of local thinning. Reisfeld and Bankoff [143] showed that as the Bond number increases, the two symmetric regions of local thinning move up the cylinder until they eventually coalesce at the top. In the non-isothermal case, Reisfeld and Bankoff [143] found that the behaviour of the film to be more complicated. They found, among other results, that for a heated cylinder, thermocapillary effects augment the effects of gravity and increase the rate of drainage from the bottom of the cylinder, whilst for a cooled cylinder they found that thermocapillary effects oppose the effects of gravity and decrease the rate of drainage from the bottom of the cylinder.

Takagi and Huppert [160] investigated, using analytical and experimental methods, the unsteady flow of a thin film of fluid on the outer surface of a stationary cylinder and sphere subject to the effects of gravity, surface tension and viscosity. In particular, they considered the problem of an instantaneous release of a constant volume of fluid at the top of the cylinder/sphere, and hence the film has an advancing front as it flows down the surface of the cylinder/sphere. Their analysis showed that for large time t (non-dimensionalised with $\nu^* a^*/g^* A^*$, where A^* is the total cross-sectional area of the fluid), near the top of the cylinder/sphere the fluid front advances as $t^{1/2}$ in the case of a cylinder and as $t^{1/4}$ in the case of a sphere and that the film thins according to $t^{-1/2}$ for both a cylinder and sphere. Takagi and Huppert [160] conducted experiments by pouring various fluids onto a perspex cylinder and a vinyl beach ball and found good agreement with their theory near the top of the cylinder/sphere. However, as the fluid front advanced further down the cylinder/sphere, eventually the fluid front would split into individual rivulets, which would then, once they reached the underside of the cylinder/sphere, detach from the surface as viscous threads.

Cachile et al. [23] investigated, using analytical, numerical and experimental methods the unsteady flow of a thin film of fluid on the outer surface of a stationary cylinder subject to the effects of gravity, surface tension and viscosity. Cachile et al. [23] derived an evolution equation for the film thickness and then used numerical methods to analyse its solutions. Their analysis found, among other results, that as the film flows from the top of the cylinder to the bottom, the film becomes thinner monotonically in time until the flow reaches the bottom of the cylinder, at which a linear stability analysis showed that Rayleigh–Taylor-like instability develops. Cachile et al. [23] conducted experiments by fully coating a steel cylinder with silicon oil and found good agreement with their theoretical predictions. They observed that the film thickness first reaches a maximum on the upper half of the cylinder, after which it decreases monotonically in time, except from near to the bottom of the cylinder, where the film destabilises and forms drops along the axis of the cylinder, which eventually coalesce and detach from the surface.

McKinlay et al. [100] investigated, using analytical and numerical methods, the unsteady flow of a thin film of fluid on the outer surface of a stationary cylinder subject to the effects of gravity and surface tension. McKinlay et al. [100] derived an evolution equation for the film thickness and described three regions that emerge at large times within which the film exhibits qualitatively different behaviour. In particular, McKinlay et al. [100] showed that near the top of the cylinder, the effects of gravity dominate the effects of surface tension, resulting in the fluid draining in the direction of gravity, which causes the film to thin. Near the bottom of the cylinder, however, the effects of gravity balance with the effects of surface tension, resulting in the formation of a quasistatic pendant drop. Connecting these two regions, there exists a narrow intermediate region, in which the film exhibits an infinite series of alternating maxima and minima.

Kay et al. [76] investigated, using analytical and numerical methods, the unsteady flow of a thin film of fluid on the inner surface of a stationary cylinder subject to the effects of gravity, surface tension, fluid inertia and a uniform shear stress at the free surface due to an airflow (as discussed in Section 1.2). Kay et al. [76] used a depth-averaging method to derive an evolution equation for the film thickness and then used asymptotic and numerical methods to analyse its solutions. They found, among other results, that the effect of fluid inertia and surface tension act to smooth out the transition between a pool of fluid that forms in the lower half of the cylinder and the thin film of fluid that coats the remainder of the cylinder surface, and that the inclusion of fluid inertia allows for solutions with a larger mass of fluid to be supported on the cylinder surface than had been predicted by previous works in the absence of inertial effects. In a follow-up paper Kay et al. [77] extended the work of Kay et al. [76] to also include thermal effects due to a heated substrate. Kay et al. [77] derived a depth-averaged energy equation for the temperature in the fluid and a depth-averaged evolution equation for the film thickness and then used numerical methods to analyse the solutions for the temperature in the fluid and film thickness, respectively. Their model predicted, among other results, the heating of recirculation regions within the pool of fluid that forms in the lower half of the cylinder, however as the effect of inertia is increased, the pools of fluid at the bottom of the cylinder give way to smooth uniform flow and the regions of backflow would begin to cool. Kay et al. [78] in a second follow-up paper, extended the work of the two previous investigations [76, 77] to

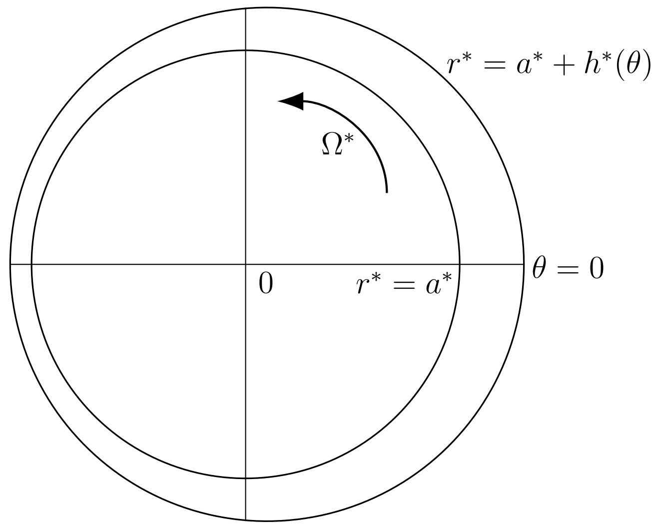

Figure 1.13: A full-film solution with film thickness at $r^* = a^* + h^*(\theta)$ on a cylinder with radius $r^* = a^*$ rotating anti-clockwise with uniform velocity Ω^* in the direction of increasing θ measured from the horizontal.

investigate the effect of an additional flux due to droplets of fluid impacting upon the free surface and a slump outlet (hole) at the bottom of the cylinder which allows for fluid to escape. They found that the additional flux due to the droplets impacting upon the free surface of the rimming flow provides either a heating or cooling effect depending on the relative temperatures of the droplets and film.

1.3.2 Flow on rotating cylinders

Coating and rimming flow on the surfaces of rotating cylinders has been studied extensively due to its intrinsic theoretical interest and also its many practical applications as previously mentioned. Early pioneering work on this problem was carried out by Moffatt [108] and Pukhnachev [137]. Moffatt [108] investigated, using analytical and experimental methods, the steady flow of a thin film of fluid on the outside of a rotating cylinder, subject to the effects of gravity. In particular, Moffatt [108] sought solutions for the film thickness which coat the entire surface of the cylinder, known as full-film solutions. Figure 1.13, shows an example of a full-film solution for coating flow on a cylinder with radius $r^* = a^*$, where again r^* is the radial polar coordinate, rotating with uniform angular speed Ω^*, with free surface $r^* = a^* + h^*(\theta)$. Note that for the corresponding rimming flow problem we simply take $r^* = a^* - h^*(\theta)$, and at leading order in the thin-film limit (but not at higher orders) the two problems are mathematically identical. On the cylinder surface, Moffatt [108] used the local Cartesian coordinates (x^*, y^*), with x^* in the direction of increasing θ (so that $x^* = a^*\theta$ locally), y^* normal to the cylinder, so that $r^* = a^* + y^*$ (for rimming flow $r^* = a^* - y^*$). Locally, on the cylinder surface, the problem then reduces to the problem of a thin film of fluid flowing down an inclined plane, described in Section 1.1, with the angle of inclination of the substrate $\alpha = \theta - \pi/2$. Using the thin-film approximation, Moffatt [108] derived an equation for the azimuthal volume flux Q per unit axial length of the fluid film in the direction of increasing θ given by

$$Q = h - \frac{h^3}{3}\cos\theta, \tag{1.48}$$

where the film thickness and flux are non-dimensionalised by $(\mu^* a^* \Omega^*/(\rho^* g^*))^{1/2}$ and $(\mu^* a^{*3} \Omega^{*3}/(\rho^* g^*))^{1/2}$, respectively. Moffatt [108] showed, among other results, that the full-film solution has a maximum at $\theta = 0$ and a minimum at $\theta = \pi$, has top-to-bottom symmetry and that the full-film solution is possible if and only if the fluid flux Q (or equivalently mass M) does not exceed a critical value, i.e. $0 \leq Q \leq Q_c$ (or equivalently $0 \leq M \leq M_c$), where the critical flux and mass are given by $Q_c = 2/3$ and $M_c \simeq 4.4427$ (the latter of which was incorrectly given by Moffatt [108] as $M_c \simeq 4.428$), respectively. They also showed that when the critical maximum flux (or mass) is achieved, a sharp corner is present in the maximum of the critical film thickness $h = h_c(\theta)$ at $\theta = 0$. Figure 1.14 shows a plot of the film thickness in the $\theta - h$ plane for varying contours of the flux Q given by (1.48) (which is by definition a curve in which Q is constant) for $0 \leq Q \leq Q_c$. As shown in Figure 1.15, Moffatt [108] also conducted simple experiments in which a rotating cylinder of perspex was lowered into and out of a trough of golden syrup, and the behaviour was observed for a variety of rotation speeds. In these experiments Moffatt [108] observed that as the rotation speed increased from zero, the film evolved from uniform to containing small periodic rings of fluid, as the rotation speed increased to larger rotation speeds, a non-axisymmetric lobe of fluid would arise and rotate around the axis of rotation at a slightly lower angular speed than that of the cylinder. The work of Pukhnachev [137], which inspired Moffatt [108], considered the coating flow problem with the additional effect of surface tension and proved the existence and uniqueness of the steady full-film solution for the film thickness.

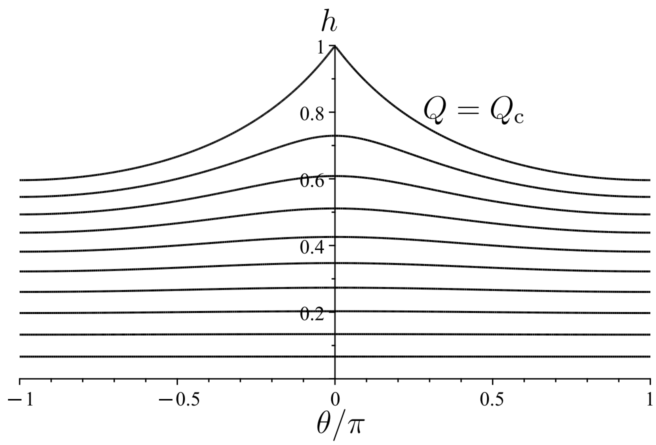

Figure 1.14: Plot of the contours of Q given by (1.48) for $0 \leq Q \leq Q_{\mathrm{c}} = 2/3$, with each contour therefore representing the film thickness $h(\theta)$ for the corresponding value of Q. The contour interval is $Q_{\mathrm{c}}/10$.

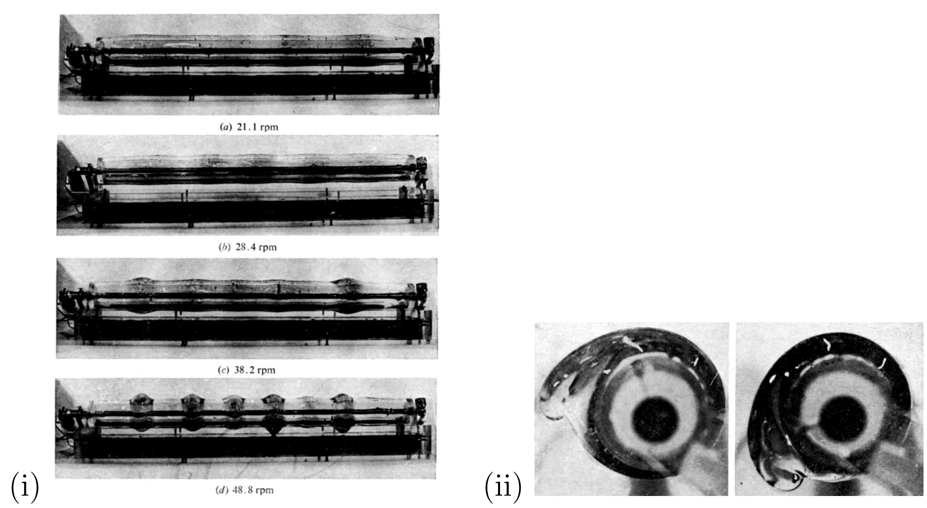

Figure 1.15: Coating flow experiments consisting of a film of golden syrup that coats a perspex rotating cylinder conducted by Moffatt [108] showing (i) the evolution from a uniform film of fluid at low rotation speeds, to a film of fluid with periodic rings of fluid at higher rotation speeds and (ii) a side view showing the lobe of fluid that forms in the film for higher rotation speeds which rotates around with the cylinder at a slightly lower speed than the cylinder itself. Reprinted from [108], with permission from Prof. H. K. Moffatt.

The problem of rimming flow was investigated further by Johnson [70] who, using analytical methods, considered steady solutions for thin films of both Newtonian and power-law fluids which either partially or entirely coat the inner surface of a rotating cylinder, subject to the effects of gravity. In the case of a Newtonian fluid which entirely coats the inner surface of the cylinder, Johnson [70] showed that, in addition to the smooth full-film solutions predicted by Moffatt [108], there also exist infinitely many jump solutions with single or multiple shocks. The experiments of Melo [101] further investigated the problem considered by Johnson [70], and determined the number and location of shocks in the film thickness that can occur in reality. The experimental results of Melo [101] are shown in Figure 1.16, which shows the shape of the film thickness $h^*(\theta)$ for various cross-sectional free surface areas A^* and rotation speeds ω^*, compared to the critical leading-order analytical solution obtained by Moffatt [108]. As shown by Figure 1.16, Melo [101] found that when the flux (or equivalently mass) exceeds its maximum value, only one shock occurs in the region $-\pi/2 \le \theta \le 0$. This corresponds physically to a pool of fluid gathering in the bottom right (the rising side) of the inside of the rotating cylinder, when the maximum flux (or equivalently mass) is exceeded. This result was confirmed in the numerical analysis of Wilson and Williams [176], who found the location of the shock to be approximately $\theta_{\mathrm{s}} = -0.4\pi$. In the corresponding problem of coating flow, when the maximum flux (or equivalently mass) is exceeded, as discussed by, for example, Wilson and Williams [176], the excess fluid will most likely simply fall off the cylinder. Figure 1.17 shows an example of such a jump solution with a shock at $\theta = \theta_{\mathrm{s}}$. Figure 1.17 shows that, as described by Johnson [70], in the case of a jump solution, the film thickness gradually increases as it approaches $\theta = \theta_{\mathrm{s}}$, and then at $\theta = \theta_{\mathrm{s}}$ the film thickness increases rapidly, and after $\theta = \theta_{\mathrm{s}}$ the film begins to gradually thin. This region of rapid variation in the film thickness near $\theta = \theta_{\mathrm{s}}$ allows for more mass to be supported on the cylinder than the critical maximum mass predicted by Moffatt [108].

The pioneering numerical investigation by Hansen and Kelmanson [58] investigated steady coating flow of a film of fluid on a rotating cylinder, subject to the effects of gravity and surface tension. Without any restriction on the thickness of the fluid film, Hansen and Kelmanson [58] employed numerical methods to solve an integral equation formulation of the streamfunction for the film thickness of the fluid on the cylinder surface, and then compared their numerical results with the thin-film results of Moffatt [108]. Specifically, they found that, regardless of the

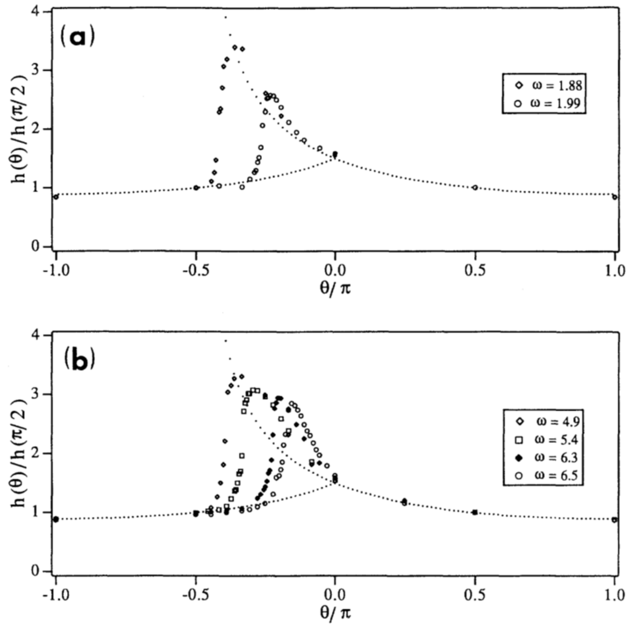

Figure 1.16: Experimental results for the the film thickness $h(\theta)^*/h^*(\pi/2)$ as a function of θ for (a) cross-sectional area of the film $A^* = 6.25$ cm^2 and rotation speed $\omega^* = 1.88$ and 1.99 rad/s, and (b) cross-sectional area of the film $A^* = 10.2$ cm^2, and rotation speed $\omega^* = 4.9, 5.4, 6.3,$ and 6.5 rad/s compared to the critical analytical solution obtained by Moffatt [108] shown with a dotted line. Reprinted from Melo [101] with permission from The American Physical Society (APS), Copyright 2023.

thickness of the film, the free surface always has its maximum and minimum at the same locations as predicted by the thin-film results and the critical maximum mass is always close to, though slightly above, that predicted by Moffatt [108]. Hansen and Kelmanson also showed that the film thickness is only weakly dependent on surface tension. In particular, considering the non-dimensional surface tension parameter $\alpha_0 = \sigma^*/(\Omega^* \mu^* a^*)$, they showed that when $\alpha_0 = 100$, there is only a very small break from the top-to-bottom symmetry of the solution obtained by Moffatt [108], for which $\alpha_0 = 0$.

Duffy and Wilson [38] investigated, using analytical and asymptotic methods, the steady flow of a thin film of fluid on a rotating cylinder, subject to the effects of gravity, and showed the existence of unbounded steady curtain solutions. Duffy and Wilson [38] showed that in addition to the full-film solution branch of (1.48) described by Moffatt [108], there are four more possible solution branches, each of which are unbounded at $\theta = \pm\pi/2$, corresponding to fluid flowing on to and off

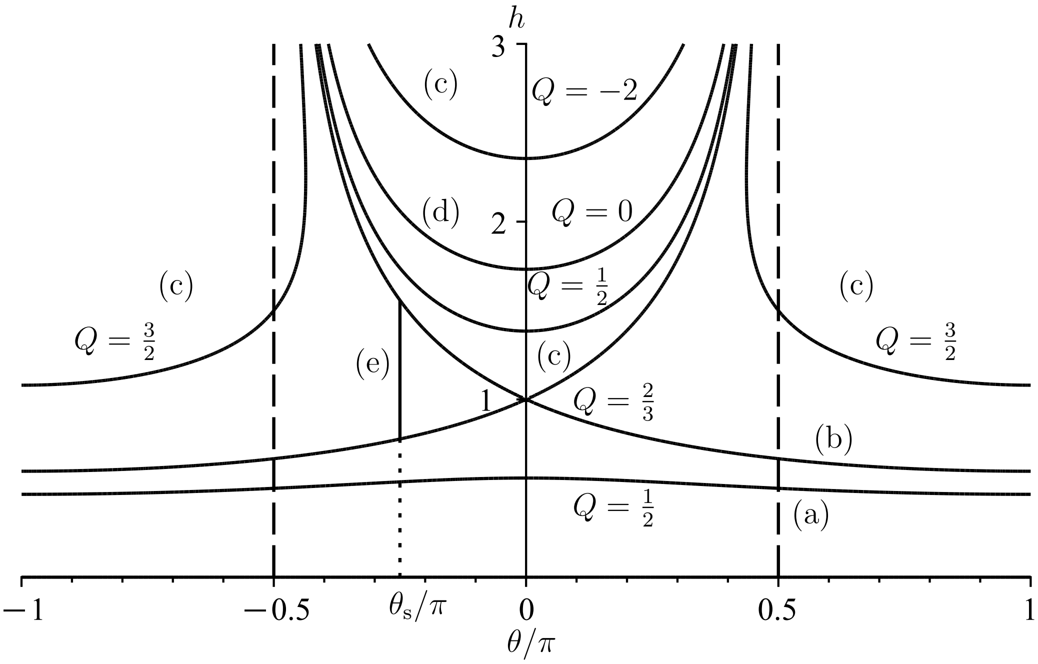

Figure 1.17: Plot showing solutions of (1.48) for the film thickness $h(\theta)$ showing an example of (a) a subcritical full-film solution with $Q = 1/2$, (b) the critical full-film solution for $Q = 2/3$, (c) unbounded curtain solutions for $Q = -2$, $Q = 1/2$, $Q = 2/3$ and $Q = 3/2$, (d) the partial-film curtain solution for $Q = 0$, and (e) a jump solution with a shock at $\theta_{\mathrm{s}}/\pi = -1/4$ composed of a full-film solution and curtain solution for $Q = 2/3$. The vertical dashed lines at $\theta/\pi = \pm 1/2$ represent the asymptotes of the curtain solutions.

of the cylinder at the top and bottom of the cylinder, respectively. In addition to describing and classifying curtain solutions, Duffy and Wilson [38] also described the possibility of partial-film curtain solutions with $Q = 0$, which do not coat the entire surface of the cylinder and are also unbounded at $\theta = \pm\pi/2$. Jump solutions, which as described previously were originally obtained by Johnson [70], were also shown to exist by Duffy and Wilson [38], which are possible when there is a shock which jumps from a full-film solution branch to a curtain solution branch. Figure 1.17 shows an example of a sub-critical full-film solution, the critical full-film solution, unbounded curtain solutions, a partial-film curtain solution, and a jump solution with a shock at $\theta = \theta_{\mathrm{s}}$.

Peterson et al. [133], using a finite element numerical scheme developed by the authors, investigated the stability and long-time dynamics of unsteady coating flow of a film of fluid on a rotating cylinder, subject to the effects of gravity, surface tension and varying initial film thickness. They found agreement with the results of Hansen and Kelmanson [58] in regard to the maximum mass that can be supported on the cylinder, in addition they showed that the rate of convergence of the solution for the film thickness to a stable steady state decreases as the parameters representing the initial film thickness, surface tension and gravity increase. They also presented simulations of load shedding that can occur once the maximum mass of fluid that can be supported on the cylinder is exceeded, as shown in Figure 1.18, which shows the development of a lobe of fluid which as time t (non-dimensionalised with the cylinder rotation rate ω^{*-1}) increases, develops into a curtain which will eventually break off from the cylinder. O'Brien [122] investigated, using analytical methods, the rimming flow of a thin film of fluid on a rotating cylinder and investigated the stability of both smooth sub-critical ($Q < 2/3$) and critical ($Q = 2/3$) with a shock (at $\theta = \theta_{\mathrm{s}}$ for $-\pi/2 < \theta_{\mathrm{s}} \leq 0$) solutions for the film thickness (as shown, for example, in Figure 1.17), subject to the effects of gravity. O'Brien [122] carried out a linear stability analysis subject to two-dimensional disturbances and showed that both the sub-critical and critical-shock solutions are neutrally stable, and concluded that retaining higher order terms in the thin-film approximation determine the stability of the rimming flow solutions. In a follow-up paper, O'Brien [127] revisited the stability of sub-critical rimming flow solutions subject to the effects of gravity and surface tension, using a linear stability analysis whilst retaining higher order terms in the thin-film approximation. They concluded that, a high cylinder rotation rate or sufficiently strong surface tension both have a stabilising effect and the absence of either (without any opposing stabilising effects) leads to unstable solutions.

Wilson et al. [180] investigated, using analytical and numerical methods, the coating flow of a thin film of fluid on a rotating cylinder, subject to the effects of gravity. In particular, Wilson et al. [180] investigated the critical solution at which the maximum mass is supported on the outside of the cylinder. They showed by considering higher-order corrections to the leading-order thin-film solution for the film thickness, that the true critical mass is slightly higher than that predicted by Moffatt [108], and that the corner in the full-film leading-order critical solution predicted by Moffatt [108] is smoothed by higher-order effects, both of which agreed with the results of their highly-accurate numerical calculations.

As described in Section 1.2, Black [19] and Villegas-Díaz et al. [171] investigated, using analytical methods, the steady coating and rimming flow of a thin

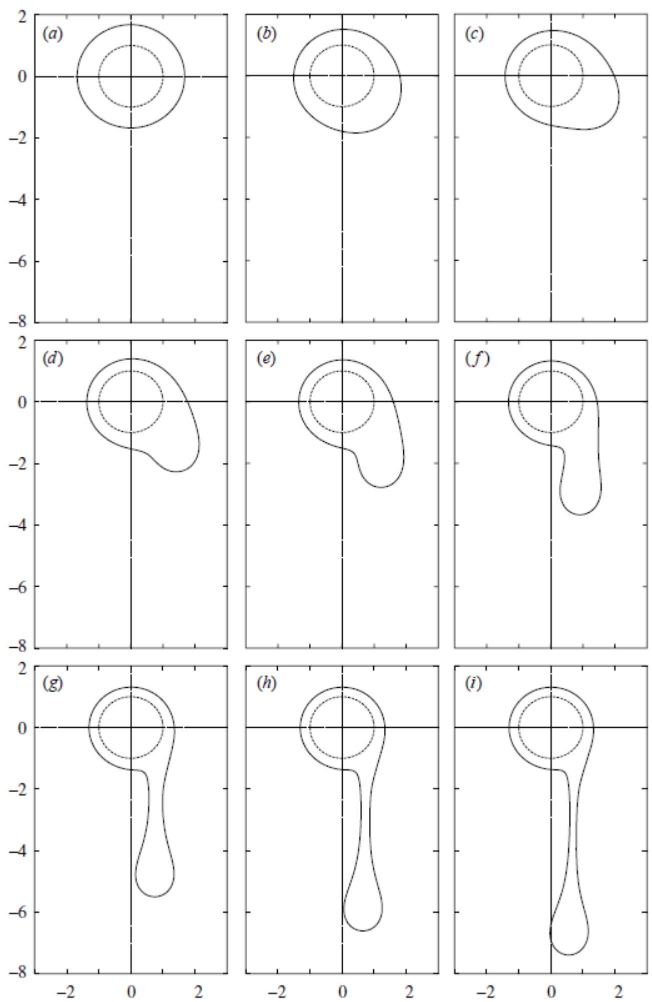

Figure 1.18: The evolution of the film thickness of a layer of fluid covering the entire surface of a cylinder, showing the development of a lobe of fluid that will eventually lead to load shedding at non-dimensional time t intervals (a) 0, (b) 1.95, (c) 3.95, (d) 7.94, (e) 10, (f) 12.8, (g) 14.46, (h) 14.74, (i) 14.85. Reprinted from Peterson et al. [133] with permission from The Royal Society (United Kingdom), Copyright 2023.

film of fluid on a rotating cylinder, respectively, subject to the effects of gravity and a uniform shear stress induced by the presence of an airflow. Both authors independently derived the governing equation for the flow given by

$$Q = h + \tau\frac{h^2}{2} - \frac{h^3}{3}\cos\theta, \tag{1.49}$$

where τ (non-dimensionalised with $(\rho^* g^* \mu^* \Omega^*)^{1/2}$) represents the strength of the uniform shear stress and described the possible solutions for the film thickness. Note that when $\tau = 0$ equation (1.49) reduces to equation (1.48), i.e. classical coating and/or rimming flow in the absence of an airflow, when $\tau > 0$ the uniform shear stress acts to aid the effect of the rotation of the cylinder and when $\tau < 0$ the uniform shear stress acts against the effect of the rotation of the cylinder. As shown in Figure 1.19, Black [19] and Villegas-Díaz et al. [171] showed that full film solutions can only exist within three regions of the $\tau - Q$ parameter plane, namely region A given by

$$0 < Q < Q_- \quad \text{for} \quad -\frac{4}{\sqrt{3}} < \tau \leq \tau_0 \tag{1.50}$$

and

$$0 < Q \leq Q_+ \quad \text{for} \quad \tau_0 < \tau \leq \infty, \tag{1.51}$$

region B given by

$$Q_- \leq Q < 0 \quad \text{for} \quad -\infty < \tau \leq -\frac{4}{\sqrt{3}}, \tag{1.52}$$

and region C given by

$$0 < Q \leq Q_+ \quad \text{for} \quad -\infty < \tau \leq -\frac{4}{\sqrt{3}} \tag{1.53}$$

and

$$Q_- \leq Q \leq Q_+ \quad \text{for} \quad -\frac{4}{\sqrt{3}} \leq \tau \leq \tau_0, \tag{1.54}$$

where

$$Q_+ = \frac{\tau^3}{12} + \frac{\tau}{2} + \frac{(\tau^2+4)^{\frac{3}{2}}}{12}, \tag{1.55}$$

$$Q_- = \frac{\tau^3}{12} - \frac{\tau}{2} - \frac{(\tau^2-4)^{\frac{3}{2}}}{12} \tag{1.56}$$

and the point (τ_0, Q_0) at which $Q_+ = Q_-$ is given by

$$(\tau_0, Q_0) = \left(-\frac{2^{\frac{3}{2}}}{3^{\frac{1}{4}}}, \frac{2^{\frac{1}{2}}}{3^{\frac{7}{4}}} \right) \simeq (-2.1491, 0.2068). \tag{1.57}$$

Black [19] and Villegas-Díaz et al. [171] both found that in region A the film of fluid has a maximum at $\theta = 0$, a minimum at $\theta = \pi$ and displays top-to-bottom symmetry, which is qualitatively similar to the behaviour of the full-film solution obtained by Moffatt [108], and hence Black [19] describes these solutions as "Moffatt modes". In region B, they found that the film of fluid has a maximum at $\theta = \pi$, a minimum at $\theta = 0$ and displays top-to-bottom symmetry, which is qualitatively different behaviour to the behaviour of the full-film solution obtained by Moffatt [108], and hence Black [19] describes these solutions as "shear modes". Finally, they both found that region C contain both Moffatt and shear modes, i.e. at any point in region C there are two distinct possible modes of behaviour, a Moffatt mode or a shear mode. Therefore, Villegas-Díaz et al. [171] and Black [19] both showed that for a sufficiently strong shear stress in opposition to the effect of the rotation of the cylinder, qualitatively different behaviour to that in the absence of a shear stress is possible. Figure 1.20 shows an example of a Moffatt mode and a shear mode for $\tau = 1$ and $\tau = -3$, respectively. Villegas-Díaz et al. [171] also showed the existence and stability of jump solutions with a shock at $\theta = 0$ and $\theta = \pi$. Villegas-Díaz et al. [172] in a follow-up paper included higher-order effects of surface tension and gravity in order to further investigate the mathematical and physical relevance of the jump solutions described in Villegas-Díaz et al. [171]. They found that such jump solutions with shocks at $\theta = 0$ and/or $\theta = \pi$ are still possible with the higher order physical effects included, and that the inclusion of the uniform shear stress due to an airflow allows for a jump solution with a single shock anywhere on the surface of the cylinder and a jump solution with a double shock-structure located in the lower half of the cylinder on the descending side of the flow $(-\pi \leq \theta \leq -\pi/2)$.

Ashmore et al. [11] investigated, using analytical and numerical methods, the rimming flow of a thin film of fluid on a rotating cylinder, subject to the effects of gravity, surface tension and viscosity. In particular, Ashmore et al. [11] investigated how surface tension affects the behaviour and location of the pool of fluid that gathers at the bottom of the cylinder in the rimming flow problem. They found,

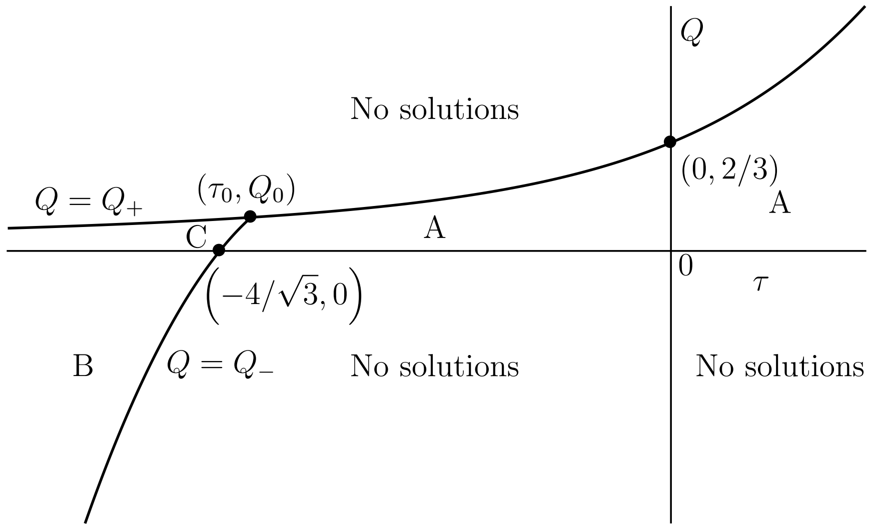

Figure 1.19: The $\tau - Q$ parameter plane obtained by Black [19] and Villegas-Díaz et al. [171] in which the curves $Q = Q_+$ given by (1.55) and $Q = Q_-$ given by (1.56) divide the plane into three distinct regions A, B and C. Region A contains Moffatt mode full-film solutions, region B contains shear mode full film solutions, and region C contains both Moffatt mode and shear mode full-film solutions and out with these regions no full-film solutions exist. The point (τ_0, Q_0) is given by (1.57).

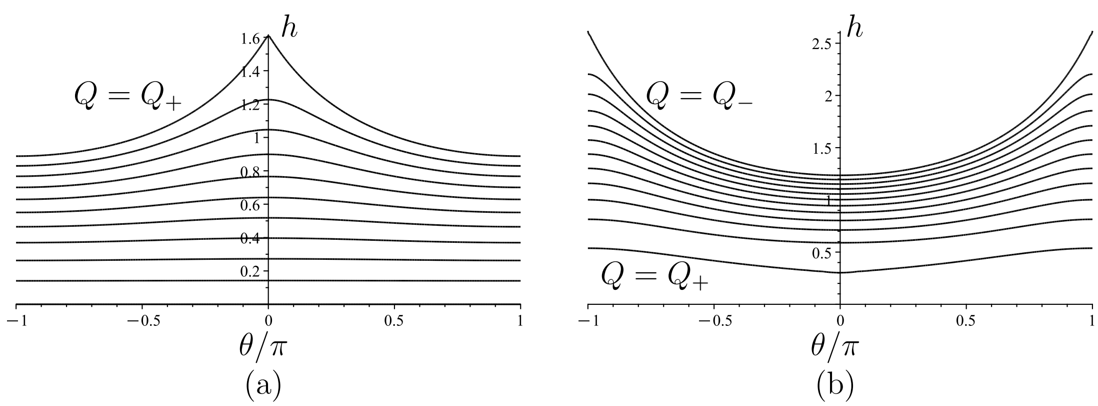

Figure 1.20: Plot of the contours of Q given by (1.49) for (a) $\tau = 1$ and $0 \leq Q \leq Q_+ \simeq 1.618$ and contour interval $Q_+/10$ and for (b) $\tau = -3$ and $0.303 \simeq Q_+ \leq Q \leq Q_- \simeq 2.618$ with contour interval $Q_-/10$.

among other results, that surface tension effects cause a dimple to appear in the film of fluid as it re-enters the pool at the bottom of the cylinder, and that when the effects of gravity and viscosity are of the same magnitude, discontinuities occur in the solution for the film thickness. However, these discontinuities can be smoothed out by including either surface tension or higher-order gravity effects.

Particularly relevant to the work of Chapter 3 is the investigation by Hinch and Kelmanson [61]. In particular, Hinch and Kelmanson [61] investigated, using analytical methods, the long-time dynamics of unsteady coating flow of a thin film of fluid on a rotating cylinder, subject to the effects of gravity and surface tension. In particular, Hinch and Kelmanson [61] used a two-timescale approach to derive an evolution equation for a thin film of fluid on the outside of a rotating cylinder and found an initially uniform asymptotic solution for the film thickness in the limit of weak gravitational effects. Their analysis of their solution showed that the initially uniform film thickness remains finite for all time and slowly decays to a stable steady state and that the film experiences a gravity-induced phase lag relative to the cylinder. In particular, Hinch and Kelmanson [61] showed that, at very long times, the free surface is a cylinder whose radius is $r = 1 + h$ and whose centre is offset from the axis of the rotating cylinder by the Cartesian displacement

$$d = \gamma(1 + \hat{A}(t_1)\cos t_0 - \hat{B}(t_1)\sin t_0, \hat{A}(t_1)\sin t_1 + \hat{B}(t_1)\cos t_0), \tag{1.58}$$

where d (non-dimensionalised with h_0^*) is the displacement,

$$\gamma = \epsilon^2 \frac{\rho^* g^* a^*}{\Omega^* \mu^*} \geq 0 \tag{1.59}$$

is a non-dimensional measure of the relative effect of gravity and viscosity, $t_0 = t$ is an $\mathcal{O}(1)$ time scale and $t_1 = \gamma^2 t$ is a long time scale, and the functions $\hat{A}$ and $\hat{B}$ are given by

$$\hat{A}(t_1) = -\exp(s_1 t_1)\cos(s_2 t_1) \quad \text{and} \quad \hat{B}(t_1) = \exp(s_1 t_1)\sin(s_2 t_1), \tag{1.60}$$

where

$$s_1 = -\frac{81\hat{\alpha}}{144\hat{\alpha}^2 + 1} \quad \text{and} \quad s_2 = \frac{3(72\hat{\alpha}^2 + 5)}{2(144\hat{\alpha}^2 + 1)}, \tag{1.61}$$

and

$$\hat{\alpha} = \epsilon^3 \frac{\sigma^*}{\mu^* \Omega^* a^*} \geq 0 \tag{1.62}$$

is a non-dimensional measure of the relative effect of surface tension and viscosity, such that

$$\gamma^2 \ll \hat{\alpha} \ll \gamma \ll 1. \tag{1.63}$$

Note that the growth rate s_1 given by (1.61), for $\hat{\alpha} > 0$, is clearly negative, showing that the functions $\hat{A}$ and $\hat{B}$ in (1.60) always decay. Hence the asymptotic solution derived by Hinch and Kelmanson given by

$$h(\theta, t) = 1 + \gamma[\cos(\theta) + \hat{A}(t_1)\cos(\theta - t_0) + \hat{B}(t_1)\sin(\theta - t_0)] + \mathcal{O}(\gamma^2), \tag{1.64}$$

is stable in the sense that it decays to a steady state at very large times, and for $\hat{\alpha} = 0$ is clearly zero, showing that the solution is neutrally stable in the absence of capillarity. As Hinch and Kelmanson [61] show, the asymptotic solution for the film thickness (1.64) is only weakly dependent on $\hat{\alpha}$, in agreement with the results of Hansen and Kelmanson [58], who as mentioned previously showed that the film thickness varies only slightly as their surface tension parameter α_0 is increased from 0 to 100. Hence whilst the results of Hinch and Kelmanson [61] are formally valid for the regime (1.63), they are in practice valid up to $\hat{\alpha} = \mathcal{O}(1)$. Chapter 3 will describe in further detail the analysis of Hinch and Kelmanson [61]. In a follow-up paper, Hinch, Kelmanson and Metcalfe [62] extended the work of Hinch and Kelmanson [61] to investigate and describe shock-like solutions that are possible when the surface tension becomes small.

Kelmanson [79] revisited the problem considered by Hinch and Kelmanson [61] and investigated unsteady coating flow of a thin film of fluid on a rotating cylinder subject to the effects of gravity, surface tension and fluid inertia. In particular, Kelmanson [79] found a two-timescale asymptotic initially uniform solution for the evolution of the film thickness in the regime of small surface tension effects, in which the asymptotic solution found by Hinch and Kelmanson [61] breaks down and is no longer valid. Then, using their asymptotic analysis and numerical simulations investigated the effect of fluid inertia on the film. Kelmanson [79] found, among other results, that the inclusion of the effects of surface tension and fluid inertia on the film act to move the position of the maximum film thickness down the cylinder, in the direction of gravity from its original location at the right-hand side of the cylinder at $\theta = 0$ as predicted by Moffatt [108] in the absence of these effects. Following the work of Kelmanson [79], a series of works then followed by Groh and Kelmanson [53, 54, 55] which further investigated the long-time evolution of the coating flow problem. Specifically, Groh and Kelmanson [53] proposed an m-timescale thin-film asymptotic expansion (where $m > 1$ is an integer) of the film thickness in order to find closer agreement to their numerically obtained solutions for the evolution of the film thickness. Groh and Kelmanson [54] further generalised the m-timescale thin-film asymptotic expansion described by Groh and Kelmanson [53] to allow for general initial conditions, and hence showed that their multiple timescale asymptotic method can be used to find highly accurate solutions for the film thickness in the coating flow problem, but also be applied to more general free-surface thin-film problems as well. Groh and Kelmanson [55] then used the multiple timescale thin-film asymptotic method described in Groh and Kelmanson [53, 54] to describe the transition from stable to unstable solutions for the film thickness in the coating flow problem with the additional effect of fluid inertia. They found excellent agreement between their multiple timescale thin-film asymptotic solution and their spectrally accurate numerical results.

As mentioned in Section 1.2, Newell and Viljoen [118], motivated by a proposed method for applying pesticides to crops with minimal amounts of chemical and with minimal drift, investigated unsteady coating flow of a thin film of fluid on a rotating cylinder, subject to the effects of gravity, surface tension and a non-uniform pressure on the free surface due to the presence of an external airflow. Newell and Viljoen [118] followed closely the analysis of Hinch and Kelmanson [61] and derived a two-timescale, initially uniform asymptotic expansion for the film thickness in the limit of weak gravitational effects (i.e. in the regime (1.63)), with the additional parameters included due to the effect of the airflow. Note that, following Hinch and Kelmanson [61], Newell and Viljoen [118] assumed that the film thickness is only weakly dependent on surface tension and hence allowed $\hat{\alpha}$ to be as large as $\mathcal{O}(1)$. They found that for certain values of the airspeed the asymptotic solution for the film thickness would grow without bound, and hence concluded that it would be conditionally unstable. In Chapter 3 we shall revisit the unsteady coating flow problem subject to a non-uniform air pressure considered by Newell and Viljoen [118] and show that in fact the asymptotic solution for the film thickness is in reality always finite for all parameter values and is therefore unconditionally stable.

Evans et al. [42, 43] investigated, using analytical and numerical methods, two- and three-dimensional coating flow of a thin film of fluid on a rotating cylinder, respectively, subject to the effects of gravity, surface tension, viscosity, and centrifugation. In particular, in the two-dimensional case, Evans et al. [42] solved numerically the thin-film governing equations for the film thickness with first-order terms retained and then investigated the effect that the rotation rate has upon the film of fluid on the cylinder. They found that, in the parametric region of low rotation speed, as the rotation speed is increased from zero, a lobe forms near the bottom of the cylinder and begins to rise up the right-hand side of the cylinder. Once the rotation speed reaches a critical value, Evans et al. [42] found that the solution for the film thickness reaches a steady state in which the bulge of fluid remains at the right-hand side of the cylinder and the film thickness has top-to-bottom symmetry. If the rotation speed is increased above this critical value, the bulge of fluid begins to rotate around the cylinder. In the three-dimensional case, Evans et al. [43] found that for small cylinders, when the rotation speed is low, droplets of fluid form on the underside of the cylinder, then these droplets become elongated and eventually become rings around the cylinder as the rotation speed increases. For larger cylinders droplets form on the underside of the cylinder at low speeds and then develop into "fingers" of fluid as the rotation speed increases.

Leslie et al. [91] investigated, using analytical and asymptotic methods, the steady coating and rimming flow of a thin film of fluid on a rotating cylinder, subject to the effects of gravity and thermoviscosity due to the fluid flowing over a cylinder which is uniformly hotter or colder than the fluid. In particular, Leslie et al. [91], investigated the effect of two non-dimensional parameters, the Biot number, B and, the less standard parameter, V, representing heat transfer and thermoviscosity, respectively. Leslie et al. [91] identified the region of the $B-V$ parameter space corresponding to full film solutions. They also showed that for a small region of the $B-V$ parameter plane, for small values of the mass of fluid, a region of backflow within the film exists on the right-hand side of the cylinder, i.e. in the region of $\theta = 0$.

Leslie et al. [92] investigated, using analytcial and asymptotic methods, the three-dimensional coating and rimming flow of a thin film of fluid on a rotating cylinder, subject to the effects of gravity. In particular, Leslie et al. [92] found "full-ring" solutions, corresponding to a ring of fluid which extends all the way around the surface of the cylinder (analogous to the full-film solutions in the two-dimensional case). They found that full-ring solutions can only exist below a critical mass (if the rotation speed is prescribed) or above a critical speed (if the mass is prescribed). Leslie et al. [92] described the behaviour of the critical and subcritical full-ring solutions in the limits of small and large rotation speed and found that, while for most values of the rotation speed and mass, the azimuthal velocity is in the same direction as the rotation of the cylinder, there does exist a region of the parameter space close to the critical solution, in a small region on the upwards-moving side of the cylinder, in which backflow occurs.

Lopes et al. [94] investigated, using analytical and numerical methods, both coating and rimming flow of a thin film of fluid on a rotating cylinder, subject to the effects of gravity and surface tension. Lopes et al. [94] compared their numerically obtained full Stokes flow solution with three analytical lubrication (thin-film) approximation models. The lubrication models considered were, the "Standard Lubrication Model'" (SLM) (used by, for example, [137, 143, 61]) which is the most commonly used model to describe the evolution of the coating or rimming flow problem, the "Extended Lubrication Model" (ELM) (used by, for example, [42, 43, 18]) which assumes that the Bond number is small, unlike the SLM which assumes that it is of order one, and the "Variational Lubrication Model" (VLM), derived by Lopes et al. [94] which retains the full expression for the curvature, instead of neglecting small terms in the thin-film limit, unlike the SLM and ELM which neglect these terms. In the case of coating flow, Lopes et al. [94] found that generally the SLM and ELM lubrication models underpredict the film thickness due to their leading-order approximations of the curvature, and that their VLM model gave much better agreement with their numerically obtained full Stokes solution for the film thickness. In the case of rimming flow they generally found much better agreement with their numerically obtained full Stokes solution for the film thickness for all three of the lubrication models considered.

Wray et al. [184] developed a novel reduced-order model in order to obtain better agreement with the direct numerical simulation (DNS) of the behaviour of thick films of fluid flowing over curved substrates than had previously been achieved with thin-film models in the literature. A key distinction Wray et al. [184] made was the difference between the long-wave and thin-film approximation, which for a planar substrate are equivalent, but for a curved substrate are different. They then used the long-wave approximation (while maintaining a film with order one thickness) to obtain approximate solutions to a variety of examples of fluid flow problems on curved substrates, in particular, the flow of a film of fluid on the outside of a rotating cylinder, subject to the effects of gravity, surface tension and viscosity. For this particular problem, Wray et al. [184] found very close agreement between their long-wave approximate solution and the DNS of the full Stokes equations, finding a maximum error of 5%, whereas they found that the thin-film approximate solution does not give such close agreement, with a maximum error of 18%. Wray et al. [183] further investigated the coating flow of a film of fluid on a rotating cylinder, subject to the effects of gravity, surface tension, viscosity and fluid inertia, again comparing the long-wave theory, introduced in [184], to the DNS of the full Stokes equations. They again found excellent agreement between the long-wave approximate solutions and the DNS of the Stokes equations and were also able to investigate regimes that were previously inaccessible to other thin-film models, for example, solution branches for the film thickness that contain multiple solutions, discussed in Lopes et al. [94].

1.4 Porous squeeze-film flow

The study of flow within porous media continues to be a very active area of research, as it has been for many decades. This is exemplified by the review by Gambaryan-Roisman in 2014 [45] which summarised the understanding at the time of the problem of droplet imbibition into a partially-wetted porous substrates.

As will be discussed subsequently, many investigations employ the well-known Darcy equation to model the fluid flow within porous media. Within this section we shall describe the Darcy equation, followed by a discussion of appropriate choices of boundary condition between a fluid and a porous medium (i.e. the fluid–porous boundary) and finally a discussion of porous-squeeze film flow, which will be the focus of the research in Chapter 4.

1.4.1 Darcy equation

The famous pioneering experimental work on modelling the flow of a fluid within a porous medium (specifically, the flow of water through sand) was carried out by Darcy [32], who derived empirically the now well-known and widely-used Darcy equation, given by

$$\mathbf{U}^* = -\frac{k^*}{\mu^*}\left(\nabla^* P^* - \rho^* \mathbf{g}^*\right), \tag{1.65}$$

where $\mathbf{U}^*$ is the volume flux per unit area of the fluid in the porous medium, which represents the velocity of the fluid through the porous medium and henceforth

Porous medium	Porosity $0 \leq \phi \leq 1$
Limestone	$0.01 - 0.1$
Gravel	$0.3 - 0.4$
Sand and gravel mix	$0.3 - 0.35$
Fine sand	$0.3 - 0.5$
Clay	$0.45 - 0.55$

Table 1.1: Approximate ranges of values of the porosity of various common porous media taken from Bear [16].

Porous medium	Permeability k^* cm^2
Clay	$10^{-12} - 10^{-15}$
Limestone	$10^{-12} - 10^{-13}$
Fine sand	$10^{-8} - 10^{-11}$
Sand and gravel mix	$10^{-5} - 10^{-7}$
Gravel	$10^{-3} - 10^{-4}$

Table 1.2: Approximate ranges of values of the permeability of various common porous media taken from Bear [16].

referred to as the Darcy velocity, k^* is the permeability of the porous medium, μ^* is the viscosity of the fluid, P^* is the pressure in the porous medium and henceforth referred to as the Darcy pressure, ρ^* is the density of the fluid, and $\mathbf{g}^*$ is the acceleration due to gravity. Note that the true fluid velocity through the pores within the porous medium is given by $\mathbf{U}^*/\phi$, where ϕ is the porosity of the porous medium. The porosity ϕ is a dimensionless measure of the empty space within the porous medium found by dividing the volume of the empty space within a porous medium by the total volume of the porous medium, and hence $0 \leq \phi \leq 1$. Table 1.1 shows approximate ranges of the porosity for various common porous media. The permeability k^* is a measure of how well connected the pores in a material are, and hence, the ability of a fluid to pass through it. The permeability, for most real-world materials is small, $k^* \ll 1$, however it can span many orders of magnitude, as shown in Table 1.2, which shows approximate ranges of the permeability for various common porous media. Later, Whittaker [175] derived the Darcy equation theoretically, directly from the Navier–Stokes equations.

Brinkman [21] derived a modification to the Darcy equation (1.65) in the absence of gravitational effects which accounts for the viscous shear stress that becomes significant when the permeability k^* of the porous medium is large, now known as the Brinkman equation and given by

$$\nabla^* P^* = -\frac{\mu^*}{k^*}\mathbf{U}^* + \mu^{*\prime}\nabla^{*2}\mathbf{U}^*, \qquad (1.66)$$

where $\mu^{*\prime}(\neq \mu^*)$ is an effective viscosity. An advantage of using the Brinkman equation (1.66) rather than the Darcy equation (1.65) is that (1.66) is of a higher order than (1.65) and so can satisfy all four of the standard boundary conditions at the fluid–porous boundary, namely continuity of tangential and normal stress and continuity of tangential and normal velocity, unlike (1.65) which can only satisfy three of them. In a short note Nield [119] concludes that although this advantage is useful mathematically, the Brinkman equation (1.66) remains semi-empirical (due to the ad-hoc introduction of the effective viscosity parameter $\mu^{*\prime}$), and states that when modelling a multiphase fluid layer and porous medium problem, it is preferable to employ the Darcy equation along with the Beavers–Joseph condition at the fluid–porous boundary, which explicitly involves another empirical parameter α, both of which will be described subsequently.

For an incompressible fluid, combining the Darcy equation (1.65) with the continuity equation

$$\nabla^* \cdot \mathbf{U}^* = 0, \qquad (1.67)$$

shows that the pressure in the porous medium satisfies Laplace's equation, given by

$$\nabla^{*2} P^* = 0. \qquad (1.68)$$

1.4.2 Fluid–porous boundary condition

When considering a problem with a fluid–porous boundary, the continuity of normal velocity boundary condition may be imposed, however, the boundary condition for the velocity in the tangential direction is not as simple as there are multiple valid choices, depending on the properties of the porous medium under consideration. In this subsection, we will describe four possible choices, no-slip relative to the solid which makes up the porous medium, no-slip relative to the fluid in the porous medium, the Beavers–Joseph condition and the Saffman–condition.

A simple choice of a tangential velocity boundary condition between the fluid layer and the porous medium is the choice of no-slip relative to the solid which makes up the porous medium, i.e. at the boundary, the velocity of the fluid in the fluid layer is equal to the velocity of the solid which makes up the porous medium. This choice of boundary condition is appropriate when the permeability of the porous medium is small (compared to, for example, the macroscopic length scales of the porous medium). Another simple choice of a tangential velocity boundary condition between the fluid layer and the porous medium is no-slip relative to the fluid in the porous medium, i.e. at the boundary the velocity of the fluid in the fluid layer is equal to the velocity of the fluid in the porous medium. This choice of boundary condition is appropriate when the permeability of the porous medium is large (compared to, for example, the size of the porous medium).

Beavers and Joseph [17] investigated, using analytical and experimental methods, the rectilinear flow of a viscous fluid through a two-dimensional parallel channel formed by an impermeable layer above and a porous medium below. Beavers and Joseph [17] postulated that there exists a thin boundary layer over which the tangential velocity and shear stress in the fluid layer transition rapidly to the tangential Darcy velocity and shear stress in the porous medium. Mikelić and Jäger [104] later showed that the size of the boundary layer is of the same order as the characteristic pore size, which is small compared to the characteristic length scale of the porous medium. Figure 1.21 shows a sketch, using Cartesian coordinates (x^*, z^*), of the two-dimensional flow of a viscous fluid between an impermeable layer and a porous medium in which a parabolic velocity profile in the fluid layer $u^*(x^*)$ transitions rapidly in the boundary layer to a uniform velocity profile $U^*(x^*)$ in the porous medium. Beavers and Joseph [17] proposed that the rapid transition in tangential velocity and shear stress in the boundary layer can be approximated by a slip boundary condition at the fluid–porous boundary, and assumed that the slip velocity is proportional to the shear stress at the boundary, leading to the now well-known Beavers–Joseph condition given by

$$u^* - U^* = \frac{k^{*\frac{1}{2}}}{\alpha} \frac{\partial u^*}{\partial z^*} \tag{1.69}$$

on $z^* = 0^+$, where $l_s^* = k^{*1/2}/\alpha$ is the slip length, and α is the dimensionless Beavers–Joseph constant which, as described by Beavers and Joseph [17], depends on the material properties of the porous medium at the fluid–porous boundary. For example, the results of one of the experiments of Beavers and Joseph [17] showed that the value of α increased as the average pore size increased.

Saffman [145] proposed that since the Darcy velocity is generally much smaller than the fluid layer velocity (as for most porous media $k^* \ll 1$), the second term on the right-hand side of (1.69) could be dropped, and hence the Beavers–Joseph condition reduces to the Saffman condition given by

$$u^* = \frac{k^{*\frac{1}{2}}}{\alpha} \frac{\partial u^*}{\partial z^*} \tag{1.70}$$

on $z^* = 0^+$. In the limit of small slip length $l_s^* \to 0$, i.e. in the limit of no slip, the Beavers–Joseph condition (1.69) reduces to the condition of no-slip relative to the fluid in the porous medium given by

$$u^* = U^* \tag{1.71}$$

on $z^* = 0$, whilst the Saffman condition (1.70) reduces to the condition of no-slip relative to the solid which makes up the porous medium given by

$$u^* = 0 \tag{1.72}$$

on $z^* = 0$. In the limit of large slip length $l_s^* \to \infty$, i.e. in the limit of infinite slip, the Beavers–Joseph condition (1.69) and Saffman condition (1.70) both reduce to the condition of zero shear in the fluid layer given by

$$\frac{\partial u^*}{\partial z^*} = 0 \tag{1.73}$$

on $z^* = 0$.

1.4.3 Porous squeeze-film flow literature

Newtonian squeeze-film flow, in which a thin film of Newtonian fluid is squeezed between two impermeable layers of material (for example, metal, glass or plastic), is a classical problem in fluid mechanics (see, for example, Acheson [2], Szeri [159]). It is well known that, subject to a prescribed constant load, theoretically, it takes infinite time to squeeze all the fluid out of the gap and achieve contact between the layers (see, for example, Stone [156]). However, if instead we consider porous squeeze-film flow, in which one or both of the layers is porous (for example, a porous sponge, wood or rock) it has been shown theoretically that it instead takes a finite time for the two plates to contact (see, for example, Goren [50]).

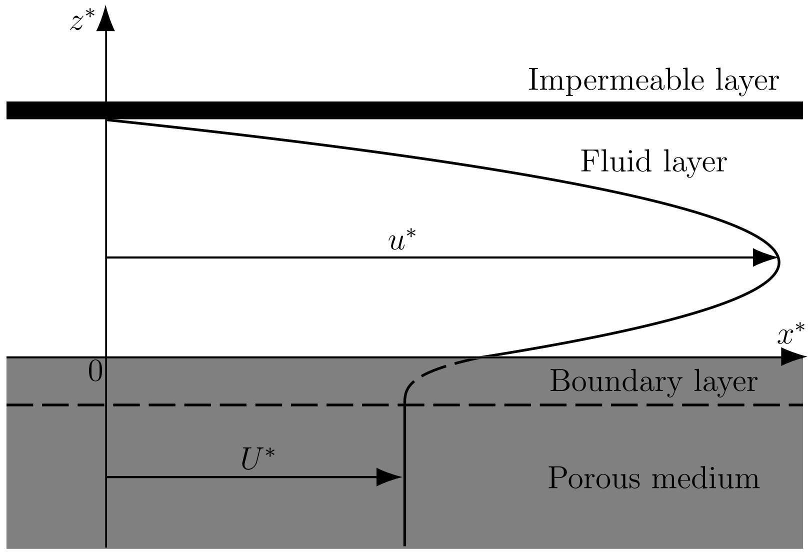

Figure 1.21: Sketch of the two-dimensional flow of a viscous fluid between an impermeable layer and a porous medium in which Beavers and Joseph [17] proposed that the parabolic velocity profile in the fluid layer $u^*(x^*)$ transitions rapidly in a boundary layer to the uniform velocity profile $U^*(x^*)$ in the porous medium.

Porous squeeze-film flow is applicable in a variety of different practical applications. Early work on porous squeeze-film flow was concerned with modelling the engagement of friction clutches used in automatic transmissions. Friction clutches, often used in automobiles, squeeze a thin film of oil between a metal plate and a sintered (porous) metal plate. In order to better understand the characteristics of friction clutches, a number of investigations have been undertaken to model the porous squeeze-film flow that takes place within these clutches and to describe important aspects that affect their performance and wear such as the pressure distribution, load capacity and time of approach of the plates. Porous-fluid bearings are also well studied within the porous squeeze-film literature due to their widespread use within industry. Typical porous-fluid bearings consist of a solid metallic disk and an externally pressurised (with either gas or liquid) disk-shaped porous pad and fluid layer in between. Porous-fluid bearings are used in heavy machinery to support very large loads. Typical characteristics that are used to measure the performance of a porous-fluid bearing are the load capacity and the static stiffness, which is the rate of change of the load capacity with respect to the height of the fluid layer. The static stiffness is often used to set the limits of the useful range of operation for the bearing, and so is of particular importance. In human biology, the squeezing of synovial fluid between layers of cartilage knee and hip joints has been modelled by considering porous squeeze-film flow, as shown, for example, in Figure 1.1. Of particular relevance to the application of squeezing synovial fluid between cartilage in the knee and hip joints is the length of time that the layers remain lubricated for, i.e. the amount of time before all of the synovial fluid is squeezed out of the fluid layer and the cartilage layers make contact. Also of particular interest is understanding how nutrients within the synovial fluid are carried to the cartilage layer, which are avascular (i.e. they do not have a blood supply), and so synovial fluid squeezed into the porous cartilage is the only mechanism by which the cartilage receives nutrients. The squeezing of contaminated fluid through porous filters is encountered in many practical situations, for example, water purification, fuel filters and in the food industry in which they are used to remove impurities from fluids like bacteria, debris, or other particulates. Of particular relevance to the porous squeeze film problem are filters in which fluid is squeezed through by a solid flat bearing, for example, syringe filters [47] and hydraulic press filters [131]. Figure 1.22 shows an idealised version of a common filtration process as described in Sparks and Chase [154], which describes a slurry being forced through a "filter cloth" and saturated porous "filter cake".

In what follows in this section, we will describe the literature associated with each of the aforementioned practical applications of the porous squeeze film problem. However, in Chapter 4 we will analyse the porous squeeze film problem, with no particular application in mind, with the knowledge that the general analysis can be applied to practical situations.

(a) Friction clutches

Wu [186], motivated by friction clutches, using analytical methods, analysed porous squeeze-film flow of a thin film of fluid between an impermeable annular disk and a porous annular disk. The porous annular disk is bounded below by the thin fluid layer and above by a flat impermeable annular disk, so that the face of the porous annular disk opposite to the fluid layer is sealed and the inner and outer edges of the porous annular disk are open to the atmosphere. Hence, fluid that is squeezed into the porous annular disk cannot flow vertically out of the face but it may flow radially out of the edges. In particular, Wu [186] investigated the pressure distribution, load capacity, and time of approach of the plates. They found that

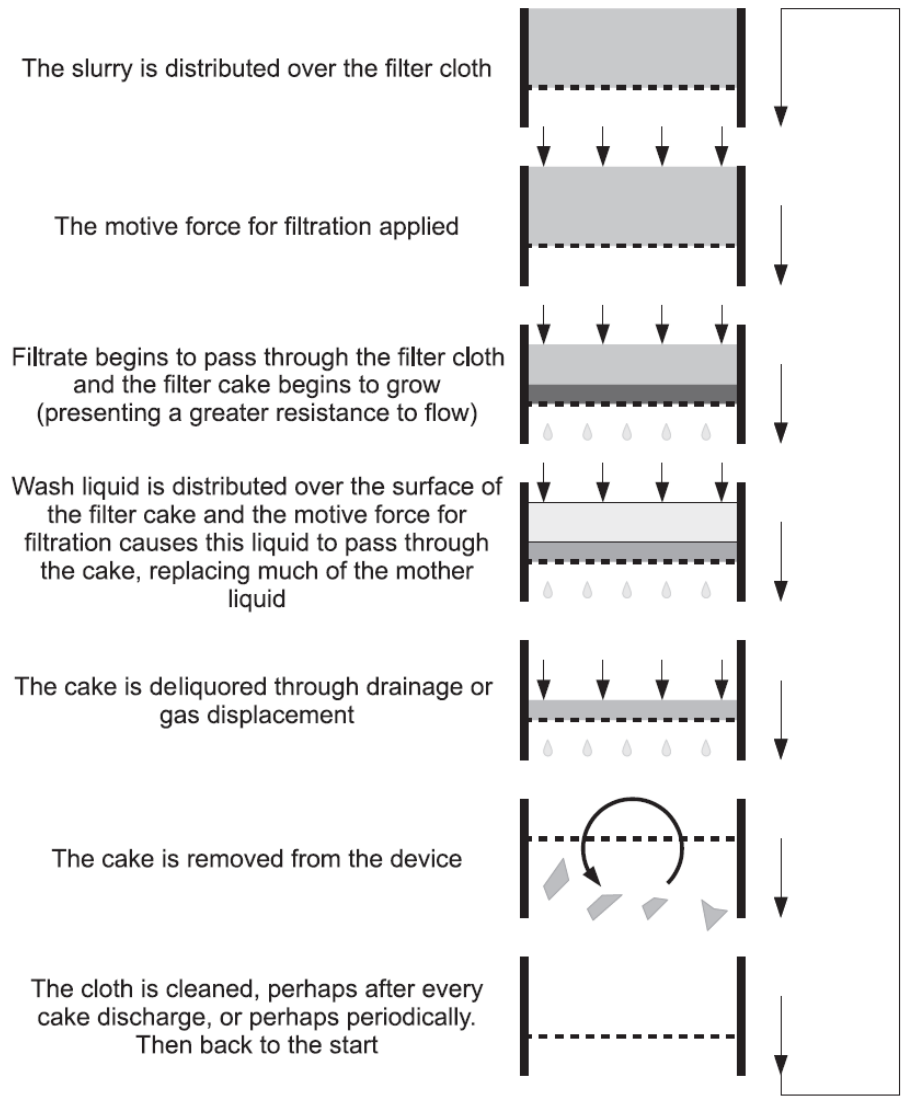

Figure 1.22: An example of the filtration process in which fluid is squeezed through a porous medium. Reprinted with permission from Sparks and Chase [154].

the load capacity and pressure within the fluid layer decrease as the permeability increases and that the time for the bearing to reach any prescribed final value also decreases as the permeability increases.

Murti [111] extended the work of Wu [186] to investigate the porous squeeze-film flow of a thin film of fluid between an impermeable circular disk and a porous circular disk (as opposed to annular disks) with a sealed face and open edge. Murti [111] noted that the solutions for the pressure in the thin fluid layer and the porous annular disk derived by Wu [186] were not valid for circular disks as the annular geometry considered by Wu [186] required a non-continuous pressure gradient at the centre of the annulus. In order to overcome this, Murti [111] prescribed a condition of zero pressure gradient at the centre of the circular disk and derived a solution for the pressure in the thin fluid layer and porous disk, and hence, using analytical and numerical methods, analysed the load capacity, pressure distribution, and time of approach of the disks. Murti [111] found, in agreement with Wu [186], that the load capacity and pressure within the fluid layer decreases as the permeability increases, and that the time for the bearing to reach any prescribed final value also decreases as the permeability increases. Murti [111] also concluded that increasing the permeability creates a more uniform pressure distribution within the fluid layer, and hence that a more permeable porous disk reduces the overall wear of the clutch plates over time.

(b) Porous-gas bearings

Murti [112], motivated by porous-gas bearings, using analytical methods, analysed porous squeeze-film flow of a thin film of fluid between an impermeable circular disk and a thin porous circular disk bounded above by the fluid layer and below by an ambient atmosphere, subject to the Saffman condition (1.70) at the fluid–porous boundary. Murti [112] identified that in the limit of a thin porous circular disk, the flow in the porous disk is predominantly axial, and hence Laplace's equation for the Darcy pressure (1.68) is satisfied by conditions at the upper and lower faces of the porous disk only, and so there is no need to specify conditions at the origin and edge of the porous disk as in, for example, Murti [111]. Murti [112], using analytical methods, derived expressions for the pressure and velocity in the fluid layer, and described the behaviour of the load capacity and static stiffness in terms of a dimensionless parameter called the bearing number defined as

$$\Lambda = \frac{12k^* r_0^{*2}}{H^* h^{*3}\left(1 + \frac{3}{1+\alpha\sigma}\right)}, \tag{1.74}$$

where r_0^* is the radius of the bearing, H^* is the thickness of the porous disk, h^* is the thickness of the fluid layer, $\alpha\sigma$ is the dimensionless slip parameter, where $\sigma = h^*/k^{*1/2}$. Murti [112] showed that the load capacity of the bearing increases with the bearing number, or equivalently, the permeability of the porous disk, and hence, as would be expected, in the limit of an impermeable layer the load capacity goes to zero, and so no gas is able to enter the bearing. In the limit of a very permeable layer, Murti [112] showed that the load capacity asymptotically approaches a maximum value. The effect of velocity slip was also investigated by Murti [112], who showed that increasing the velocity slip (i.e. decreasing $\alpha\sigma$) reduces the load capacity.

Verma [170] revisited the problem considered by Murti [112], but instead of considering the Saffman condition (1.70) at the fluid–porous boundary, considered the Beavers–Joseph condition (1.69). Verma [170] found that the form of the expressions for the pressure and load capacity are the same as those found by Murti [112] when the Beavers–Joseph condition is applied, with the main difference being the definition of the bearing number, which Verma [170] defines as

$$\bar{\Lambda}_1 = \frac{12k^* r_0^{*2}}{H^* h^{*3}\left(1 + \frac{3(2\alpha+\sigma)}{1+\alpha\sigma}\right)}, \tag{1.75}$$

so that, by comparing (1.74) and (1.75), Verma [170] found that

$$\bar{\Lambda}_1 = \frac{4 + \alpha\sigma}{4\sigma + 6\alpha + \alpha\sigma^2}\Lambda. \tag{1.76}$$

Unfortunately, there are a number of errors in the analysis of Verma [170]. The most important error, which renders their analysis incorrect, is found in the bearing number given by Verma [170], which instead of (1.75) should be

$$\bar{\Lambda}_2 = \frac{12k^* r_0^{*2}}{H^* h^{*3}\left(1 + \frac{3(2\alpha+\sigma)}{\sigma(1+\alpha\sigma)}\right)}. \tag{1.77}$$

As a result of this, (1.76) is also incorrect, and should be

$$\bar{\Lambda}_2 = \frac{(4 + \alpha\sigma)\sigma}{4\sigma + 6\alpha + \alpha\sigma^2}\Lambda. \tag{1.78}$$

There are also a number of presentational and typographical errors in Verma [170], which do not carry through in their analysis, a sign error in the Beavers–Joseph condition, and their equation for the velocity in the fluid layer (i.e. their equation (10)) is bracketed incorrectly and should read

$$u = \frac{h^2}{2\eta}\left(-\frac{\mathrm{d}p}{\mathrm{d}r}\right)\left[\frac{z}{h} - \frac{z^2}{h^2} + \frac{z(2\alpha + \sigma)}{h(1 + \alpha\sigma)}\right], \tag{1.79}$$

where, in their notation, p is the pressure in the fluid layer and η is the viscosity of the fluid. Moreover, in the text below their equation (31) the non-dimensionalisation of their load capacity W with $\bar{W}$ is incorrect, and should be

$$\bar{W} = \frac{W}{\pi r_0^2(p_s - p_a)}, \tag{1.80}$$

and finally in the text below their equation (31), the constant value p_{e} that appears should in fact be p_{s}. Hence, the work of Verma [170], which intended to extend the work of Murti [112], falls short of this intention.

Recently, Venerus [169] investigated, using analytical and asymptotic methods, the squeeze-film flow of a thin film of fluid between an impermeable circular disk and a porous circular disk that has either (a) an open face and closed edge or (b) a closed face and open edge. Venerus [169], using analytical, asymptotic and numerical methods, analysed the flow in the porous disk and thin fluid layer using the Beavers–Joseph condition (1.69) at the fluid–porous boundary. They derived expressions for the velocity and pressure in the fluid layer and porous disk and the force exerted by the fluid on the porous disk. In particular, Venerus [169] showed that in the case of no-slip at the fluid–porous boundary, their expressions for the pressure in the fluid layer and force exerted on the porous disk reduce to those of Murti [111] for configuration (b), and that in the limit of a thin porous disk and no-slip at the fluid–porous boundary their expression for the pressure in the fluid layer reduces to that found by Murti [112] and Verma [170] for configuration (a). In addition, they found that the force exerted on the porous disk decreases as the permeability increases and that it decreases as the velocity slip decreases, and also that the time to squeeze all of the fluid out of the fluid layer (i.e. the contact time) decreases as the permeability increases for both configurations (a) and (b).

(c) Human biology

Motivated by the squeezing of synovial fluid between two layers of cartilage in the hip joint of a human body, the series of papers by Hlaváček and Hlaváček and Novak [63, 64, 65] investigated, using analytical and numerical methods, the porous squeeze-film flow of both a Newtonian fluid and a non-Newtonian power-law fluid between either two porous circular disks or two porous spheres subject to the condition of no-slip relative to the fluid in the porous disks/spheres at the fluid–porous boundary. In particular, Hlaváček [63, 64, 65] considered the squeezing of the synovial fluid subject to a step-load squeezing force, i.e. a force that increases linearly up to a critical time after which the force is constant. Hlaváček [63, 64, 65] found that in the case of squeezing fluid between two porous circular disks, the axial Darcy velocity in the porous disks is uniform, and in the case of squeezing fluid between two porous spheres, the axial Darcy velocity in the porous spheres varies quadratically.

Knox et al. [86], motivated by the squeezing of synovial fluid between the femoral condyle and the tibial plateau in the human knee, investigated, using analytical and asymptotic methods, the porous squeeze-film flow of a fluid between an impermeable circular disk and a thin porous circular bed with a sealed face, subject to the Beavers–Joseph condition (1.69) at the fluid–porous boundary. In particular, Knox et al. [86] investigated the finite time t (non-dimensionalised with R^*/V^* where, R^* is the radius of the porous bed and V^* is a characteristic velocity scale) required for the disks to contact, i.e. the contact time $t = t_c$, the particle paths, and the penetration depths of the fluid within the porous bed. As will be discussed in further detail in Chapter 4, Knox et al. [86] showed that the contact time t_c in the limit of a porous bed with small permeability, i.e. $k \to 0$ (non-dimensionalised with H_p^{*2} where, H_p^* is the height of the porous bed) is $\mathcal{O}(k^{-2/3}) \to \infty$ and in the limit of large permeability, i.e. $k \to \infty$ is $\mathcal{O}(k^{-1}) \to 0$. In relation to the application to synovial fluid squeezing within the human knee, Knox et al. [86] noted that typical values of the permeability of cartilage in the human knee are typically $k^* = \mathcal{O}(10^{-18})$ m^2, and so the limit $k = k^*/H_p^{*2} \to 0$ is the most physically relevant. In this limit, Knox et al. [86] showed that for typical physical dimensional parameter values the contact time of the impermeable layer and porous bed is approximately 10 s, and so concluded that their model suggests that if a person is standing still for a short period of time their knees will remain fluid lubricated, but if do so for a long period of time contact between the cartilage coated surfaces may occur. Knox et al. [86] also found that the typical penetration depths of the fluid in the porous bed was much less than the thickness of the porous bed (based on the typical thickness of cartilage within the knee), and hence concluded that nutrients within the fluid layer penetrate only a relatively small distance into the porous cartilage layer.

Knox et al. [85] extended the work of Knox et al. [86] to consider the squeeze-film flow of a curved impermeable layer and a flat porous circular bed. In particular, Knox et al. [85] considered an impermeable layer with a surface given by $H^*(r^*) = (R^*/2n)(r^*/R^*)^{2n}$, where $n \geq 1$ is an integer and R^* is the radius of the axisymmetric layer. Knox et al. [85], using analytical, and asymptotic methods, subject to the Beavers–Joseph condition (1.69) at the fluid–porous boundary, derived equations for the pressure and load exerted on the impermeable layer by the fluid, the time t, and contact time $t_{\rm c}$ of the curved impermeable layer and the porous bed, as well as describing the particle paths and penetration depths of the fluid in the porous bed. Among other results, Knox et al. [85] showed that in the limit of small permeability ($k \to 0$) the contact time is $t_{\rm c} = \mathcal{O}(\ln(k^{-1})) \to \infty$ for $n = 1$ and $t_{\rm c} = \mathcal{O}(\ln(k^{-2(n-1)/3n})) \to \infty$ when $n \geq 2$, and that in the limit of large permeability ($k \to \infty$) the contact time is $t_{\rm c} = \mathcal{O}(k^{-1/2}\ln(k)) \to 0$ for $n = 1$ and $t_{\rm c} = \mathcal{O}(k^{-(2n-1)/2n}) \to 0$ when $n \geq 2$, hence that the contact time becomes large in the limit of small permeability and small in the limit of large permeability, consistent with Knox et al. [86].

Karmakar and Raja Sekhar [75] extended the work of Knox et al.[86] to include the effect of an anisotropic permeability in the porous bed. In particular, Karmakar and Raja Sekhar [75] considered a two-dimensional geometry and used analytical, asymptotic and numerical methods to analyse the squeeze-film flow between a flat impermeable layer and a flat porous bed with two permeabilities K_1 and K_2 along two principal axes within the porous bed, where the K_2 axis is at angle $0 \leq \Phi \leq \pi/2$ to the horizontal. In particular, Karmakar and Raja Sekhar [75] derived expressions for the pressure in the fluid layer and porous bed and the load exerted by the fluid on the impermeable layer, and the contact time of the porous bed and impermeable layer. Considering the parameter $\lambda = K_1/K_2$, Karmakar and Raja Sekhar [75] showed that the contact time decreases as λ increases and that it increases as Φ increases.

(d) Filtration

Motivated by a further understanding of particle deposition within porous filter membranes, which can lead to coagulation of unwanted material deposition within filters, Goren [50] and the series of investigations by Ramon and Hoek [138], Ramon et al. [139] and Ofner and Ramon [123] investigated the permeation-induced hydrodynamic force that pulls particles suspended in fluid towards the porous layer.

Goren [50] considered a spherical particle suspended in fluid approaching a thin, flat porous layer at constant velocity, subject to no-slip at the fluid–porous boundary. Goren [50], using analytical and numerical methods, derived an expression for the force exerted on the spherical particle. In particular, Goren [50] showed that the force exerted on the spherical particle scales as $(R^*\ell^*_{\rm m}/k^*)^{1/2}$, where $\ell^*_{\rm m}$ is the thickness of the porous layer, and presented a table of numerically-calculated values of the force exerted on the spherical particle for a large range of permeabilities.

Ramon and Hoek [138] considered a spherical particle suspended in fluid approaching a flat porous layer at constant velocity, subject to no-slip at the fluid–porous layer boundary. Ramon and Hoek [138], using analytical and asymptotic methods, derived expressions for the pressure in the thin fluid layer between the sphere and the porous layer, and force exerted on the particle upon close approach to the porous layer in the limits of small and large permeability. Ramon and Hoek [138] found excellent agreement with the numerical results of Goren [50].

Ramon et al. [139] considered a particle with general shape $r^* = \delta^* + R^* - (R^{*n} - r^{*n})^{1/n}$, where δ^* is the distance from the porous layer to the particle at $r^* = 0$ (in the centre of the particle) and $n > 1$ is an integer, suspended in fluid, approaching a flat porous layer subject to no-slip at the fluid–porous boundary. Ramon et al. [139], using analytical and asymptotic methods, derived asymptotic solutions for the pressure in the thin fluid layer and the force exerted on the sphere in the limit of small and large permeability. Ramon et al. [139] also found, among other results, that upon close approach the velocity of the particle $V^*_{\rm par}$, in the limit of small permeability, scales as $V^*_{\rm par} \propto k^{*1/2}$, $V^*_{\rm par} \propto k^{*3/4}$ and $V^*_{\rm par} \propto k^*$ for a spherical ($n = 2$ in three dimensions), cylindrical ($n = 2$ in two dimensions) and flat ($n \to \infty$) particle, respectively, and for a general particle shape that the force f^*_{par} exerted on the particle scales as $f^*_{\text{par}} \propto ((R^* \ell^*_{\text{m}}/k^*)^{(3n-4)/(3n-2)})$, and hence the force becomes more sensitive to the permeability of the porous layer as the particle becomes flatter (i.e. as n increases).

Ofner and Ramon [123] considered a spherical particle approaching a flat porous layer coated with a polymer brush, which has been shown to reduce the deposition of particles and reduce coagulation in filters. Ofner and Ramon [123], using analytical, asymptotic and numerical methods, analysed the equilibrium position of the particle at which the repulsive force of the brush is balanced by the permeation-induced force of the porous layer, and showed mathematically that the equilibrium position is higher in the limit of a brush with a high density of fibres compared to a brush with a low density of fibres, hence as would be expected, the more dense the brush the better protected the porous filter is from particle deposition.

Khabthani et al. [80] extended the work of Ramon et al. [139] in the case of a spherical particle suspended in fluid approaching a flat porous layer with constant velocity by including the Saffman condition (1.70) at the porous–fluid boundary in order to investigate the effect of velocity slip at the interface. Khabthani et al. [80] using analytical, asymptotic and numerical methods, derived equations for the pressure in the fluid layer and the force exerted on the particle by the fluid in the limits of small and large permeability. They showed that the force exerted on the particle decreases as the permeability of the porous layer increases and that it increases as the velocity slip length increases.

Recently, a series of investigations by Reboucas and Loewenberg [141, 140, 142], used analytical, asymptotic and numerical methods to investigate the motion of two porous spheres suspended in fluid approaching each other. In particular, Reboucas and Loewenberg [141] considered the near-contact approach of the two porous spheres and allowed each sphere to have its own permeability denoted by k_1 and k_2, respectively. Considering the average permeability $K = k_1 + k_2$, Reboucas and Loewenberg [141], among other results, showed that the contact time t_{c} of the two spheres in the limit $K \to 0$ is $t_{\text{c}} = C_\infty - \log(C(\alpha)K^{2/5})$, where C_∞ is constant which depends on the initial separation height of the two spheres and $C(\hat{\alpha}) = 0.7224$ in the limit of no-slip and $C(\hat{\alpha}) = 6\hat{\alpha}\text{e}^{-3/2}$ in the limit of large slip (where $\hat{\alpha} = 1/\alpha$, and both spheres have the same value for the Beavers–Joseph constant α).

1.5 Rivulet flow and evaporation

Rivulet flow, in which a long slender film of fluid flows predominantly in the direction of its longer length, is a common occurrence in many real-world situations. For example, small-scale rivulets can occur within kitchen sinks and on car windows on rainy days, and large-scale rivulets can occur in rivers and lava flows, as shown in Figure 1.2. Chapter 5 of this thesis will investigate the flow of a thin rivulet of fluid that is evaporating, and hence in this section we shall discuss the literature related to rivulet flow followed by a discussion of the literature related to modelling evaporation.

1.5.1 Rivulet Flow Literature

The early work of Towell and Rothfeld [166] investigated, using analytical, asymptotic, numerical and experimental methods, the steady flow of a rivulet of fluid down an inclined plane subject to the effects of gravity and surface tension. In particular, Towell and Rothfeld [166] derived expressions for the free surface and velocity of the fluid in the asymptotic limits of a narrow and a wide rivulet, and analysed numerically the general solution for the free surface of the rivulet, showing that the width of the rivulet increases as the flow rate increases and that their asymptotic solutions matched closely with their numerical solutions in the appropriate limits. Furthermore, Towell and Rothfeld [166] carried out experiments measuring the width and contact angle of rivulet flows down inclined planes with various flow rates and found excellent agreement with their theoretical predictions.

Allen and Biggin [8] investigated, using analytical, asymptotic and numerical methods, the steady flow of a thin rivulet of fluid down an inclined plane subject to the effects of gravity and surface tension. In particular, Allen and Biggin [8] derived leading and first order asymptotic solutions for the free surface of the rivulet and the velocity in the limit of a thin rivulet, and found good agreement with their numerical solutions.

Duffy and Moffatt [37] investigated, using analytical and asymptotic methods, the locally-unidirectional steady flow of a thin rivulet of fluid down an inclined plane subject to the effects of gravity and surface tension. As will be discussed in more detail in Chapter 5, Duffy and Moffatt [37] derived solutions for the free surface of the rivulet in the cases of rivulets which are a sessile (i.e. angle of inclination of the plane less than $\pi/2$), vertical, and pendant (i.e. angle of inclination of the plane greater than $\pi/2$), and showed that this can be interpreted as the rivulet flowing from the top to the bottom of a horizontal cylinder. Duffy and Moffatt [37] showed that the width of the rivulet tends to infinity near the top of the cylinder with finite thickness, and that the width of the rivulet becomes finite and the thickness tends to infinity near the bottom of the cylinder. Wilson and Duffy [178], using analytical and asymptotic methods, revisited the problem investigated by [37] and considered the special case of a perfectly wetting rivulet. They showed, in particular, that on the upper half of the cylinder no perfectly wetting rivulets can exist, however on the lower half of the cylinder an array of infinitely many solutions for the free surface of the rivulet can exist, each of which is a rescaled copy of the single rivulet solution.

Holland et al. [66] investigated, using analytical and asymptotic methods, the steady flow of a thin rivulet of fluid that flows from the top to the bottom of a large cylinder, where the cylinder is either uniformly hotter or cooler than the surrounding atmosphere, subject to the effects of gravity, surface tension and thermocapillarity. In particular, Holland et al. [66] showed that a linear dependence of the surface tension on temperature drives a transverse flow that causes the fluid particles to spiral down the rivulet in helical vortices. Furthermore, Holland et al. [66], showed that near the top of the cylinder the rivulet has finite depth and infinite width, in agreement with [37], near the bottom of the cylinder the rivulet has infinite depth and finite width if the substrate is heated or slightly cooled, or finite depth and infinite width if the substrate is significantly cooled. They concluded that these marked differences in the width and depth of the rivulet could potentially dramatically affect the heat transfer between the cylinder and the surrounding atmosphere.

Perazzo and Graton [132] investigated, using analytical and numerical methods, the unidirectional steady flow of a rivulet of fluid down an inclined plane subject to the effects of gravity and surface tension. In particular, Perazzo and Graton [132] derived an analytical solution for the free surface of the rivulet and analysed the velocity of the rivulet numerically and, in addition, derived an analytical solution for the velocity of the rivulet in the special case of a vertical substrate. Perazzo and Graton [132] compared their exact and numerical solutions with solutions obtained using the thin-film approximation and found that the thin-film approximation predicted global properties such as cross-sectional area, volumetric flow and average velocity reasonably well. Tanasijczuk et al. [161], using analytical and numerical methods, extended the work of Perazzo and Graton [132] to include arbitrary variation in the shape of the substrate transverse to the direction of the flow. In particular, Tanasijczuk et al. [161] derived analytical solutions for the free surface of the rivulet and analysed the velocity of the rivulet numerically. Tanasijczuk et al. [161] compared their results with various previous experimental investigations and found good agreement with their theory.

Paterson et al. [129] investigated, using analytical and asymptotic methods, the steady flow of a rivulet over a large horizontal cylinder with fixed constant contact angle (allowing the width to vary) and a rivulet with fixed width (allowing the contact angle to vary). Paterson et al. [129], among other results, showed that unlike in the case of a rivulet with fixed contact angle and varying width considered by Duffy and Moffatt [37], in which the rivulet may flow continuously from the top to the bottom of the cylinder, in the case of a rivulet with varying contact angle and fixed width, the rivulet may flow from the top to the bottom if the rivulet is sufficiently narrow, however if the rivulet is not sufficiently narrow, then the rivulet can only flow from the top of the cylinder down to a critical azimuthal angle on the lower half cylinder. In particular, considering the azimuthal angle α, measured from $\alpha = 0$ at the top of the cylinder, and the fixed semi-width of the rivulet $\bar{a}$, the critical azimuthal angle is given by

$$\alpha_{\text{crit}} = \cos^{-1}\left(-\frac{\pi^2}{\bar{a}^2}\right) \tag{1.81}$$

for $\bar{a} > \pi$. Paterson et al. [129] explained that the critical angle at which the rivulet with constant width $\bar{a} > \pi$ could no longer flow with fixed (i.e. pinned) contact lines can be considered to be the point at which the contact lines de-pin and the rivulet flows from α_{crit} to the bottom of the cylinder according to the perfectly wetting solution with varying width and zero contact angle described by Wilson and Duffy [178].

Howell et al. [68], inspired by the example of rain water flowing over a leaf, investigated, using analytical and numerical methods, the steady flow of a rivulet of fluid over an elastic beam subject to the effect of gravity. In particular, Howell et al. [68] considered two cases, one in which the beam deflection is small (small-deflection regime), and one in which the beam deflection is large (large-deflection regime). In the small-deflection regime, Howell et al. [68] showed that for both regimes, the film thickness first increases to a maximum value and then decreases as the length of the beam increases. This phenomenon is due to the greater deflection experienced by a longer beam, which in turn enhances the gravitational forcing experienced by the fluid, and therefore promotes flow away from the applied source at the beginning of the beam. Hence, the analysis of Howell et al. [68] confirmed that the deflection of a leaf in the rain facilitates the removal of water from its surface. Howell et al. [67] further investigated the problem considered by Howell et al. [68], using analytical and experimental methods. In particular, Howell et al. [67] performed experiments for the small-deflection and large-deflection regimes, as shown in Figure 1.23(a) and (b), respectively. The experiments in Figure 1.23(a) show that in the small-deflection regime, the beam is initially nearly horizontal, and over time the rivulet front advances further down the beam, which in turn increases the deflection of the beam. The experiments in Figure 1.23(b), show that in the large-deflection regime, the beam is initially deflected much further than in Figure 1.23(a), and over time the rivulet advances further down the beam, which drastically increases the deflection of the beam, until it is nearly vertical. Howell et al. [67] predicted analytically, in the small-deflection regime, that in the limit of small time, the position of the rivulet front is $\mathcal{O}(t^{4/5})$ and in the limit of large time is $\mathcal{O}(t^4)$. In the large-deflection regime, in the limit of small time, the position of the rivulet front is $\mathcal{O}(t^4)$ and in the limit of large time is $\mathcal{O}(t)$. The analytical predictions for the position of the rivulet front agreed well with the corresponding experimental results.

Ghillani et al. [48] investigated, using analytical, numerical and experimental methods, the unsteady flow of a rivulet of fluid along the inside of a corner formed by a cylinder and a flat heated solid substrate subject to the effects of surface tension, viscosity and evaporation. In particular, Ghillani et al. [48] investigated the capillary rise of the rivulet subject to evaporation with constant evaporative flux at the free surface of the fluid. Ghillani et al. [48] derived an evolution equation for the film thickness and solved it numerically. They compared their solutions with experiments that they carried out in which droplets of fluid were placed on a fibrous mat (the individual fibres acting as the cylinder in the model) laid over a flat solid substrate and the droplet spreading was observed. Ghillani et al. [48] found good agreement with their numerical and experimental results in the case of a rivulet with zero contact angle with the cylinder, however in general their numerical results did not match as closely with their experimental results. Ghillani et al. [48] concluded that this shows that capillary rise of a rivulet within

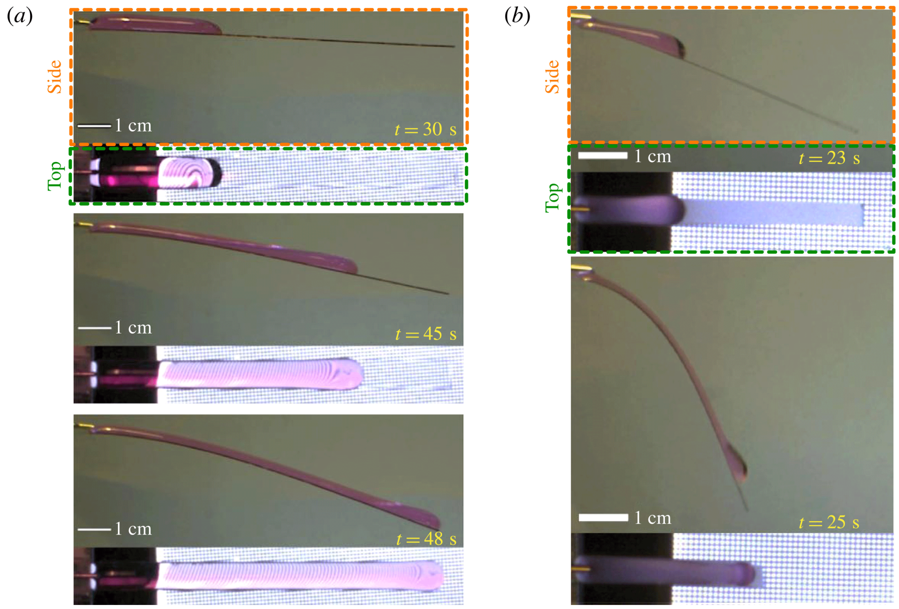

Figure 1.23: Side and top views of fluid flow over an elastic beam, where (a) shows a beam with small deflection and (b) shows a beam with large deflection. Reprinted from Howell et al. [67] with permission from Cambridge University Press.

the corner between a solid substrate and a cylinder can explain the imbibition of the fluid into the porous fibres of the fibre mat in the first layer of fibres closest to the solid substrate, however for subsequent fibre layers other physical effects not considered in their model, such as Marangoni effects, may become more significant.

Alshaikhi et al. [9] investigated, using analytical and asymptotic methods, the steady locally-unidirectional flow a thin rivulet of fluid down an inclined slippery substrate (for example, a porous substrate) subject to the effect of gravity. In particular, Alshaikhi et al. [9], instead of the commonly applied no-slip condition at the substrate, considered a Navier slip condition. Alshaikhi et al. [9] showed that while much of the qualitative behaviour of the rivulet remained the same as that of a rivulet with no slip at the substrate, described by, for example, Duffy and Moffatt [37], the shape, size and velocity within the rivulet all depend strongly on the slip length. For example, they showed that increasing the slip length decreases the viscous resistance at the substrate, and so increases the velocity within the rivulet, and hence a smaller rivulet is required than would be in the case of no slip to achieve the same prescribed flux.

1.5.2 Rivulet breakup

A commonly observed phenomenon is the breakup of the rivulet into smaller subrivulets or droplets (see, for example, Figure 1.5). The break up of rivulets may occur due to many factors [152, 87, 10], for example, the viscosity, surface tension, inertia, contact angle, width, and the evaporation of the rivulet, or the angle of inclination, roughness, and permeability of the substrate. In this subsection we shall first discuss examples of literature which include theoretical investigations, followed by examples of literature which carried out experiments and numerical simulations, of rivulet breakup.

(a) Theoretical investigations

Myers et al. [115] investigated, using analytical, asymptotic and numerical methods, the locally unidirectional steady flow of a rivulet of fluid flowing down an inclined plane subject to the effects of gravity, surface tension and a constant shear stress at the free surface due to the presence of an external airflow. In particular, Myers et al. [115] derived an analytical solution for the velocity and free surface shape in the limit of a thin rivulet and also computed numerically the velocity and free surface shape for a non-thin rivulet, and compared these results to experimental data from previous investigations, finding excellent agreement with their numerical solutions and less agreement with their analytical solution, due to the high contact angle in the experiments. Myers et al. [115] also investigated the stability of the rivulet flow, and used energy arguments to calculate if it was energetically favourable for the rivulet to split into two or more subrivulets. They found that for a rivulet driven by a shear stress at the free surface it is not energetically favourable for the rivulet to split, but for a rivulet that is driven by gravity it is energetically favourable for it to split.

Wilson and Duffy [179] investigated, using analytical, asymptotic and numerical methods, the unidirectional steady flow of a thin rivulet of fluid down a vertical plane subject to the effects of gravity and a constant shear stress at the free surface due to the presence of an external airflow. Among other results, Wilson and Duffy revisited the problem considered by Myers et al. [115] of when it is energetically favourable for the rivulet to split into two rivulets. In the case of a rivulet that is driven by gravity only they agreed with Myers et al. [115] that it is always energetically favourable for the rivulet to split into two subrivulets, however in the case of a rivulet driven by a shear stress at the free surface only they showed that Myers et al. [115] was mistaken and in fact it is always energetically favourable for the rivulet to split into two subrivulets in this case as well. Wilson and Duffy [179] then numerically calculated when it was energetically favourable for rivulets in which gravity and surface shear stress effects are both significant and presented their results in parameter planes of the semi-width of the rivulet vs the shear stress and the fluid flux vs the shear stress showing regions of the parameter space in which it is and is not energetically favourable for the rivulet to split. Wilson et al. [181] revisited the problem investigated by Wilson and Duffy [179] to describe energetics of the breakup of both a sheet and a rivulet of fluid on a vertical substrate subject to the effects of gravity and a shear stress at the free surface due to an airflow. Wilson et al. [181] identified and analysed the regions within the parameter space in which it is energetically favourable for a thin sheet of fluid with uniform thickness to break up into an array of infinitely many thin subrivulets and when it is energetically favourable for a thin rivulet to break up into one or more identical subrivulets.

Gambaryan-Roisman and Stephan [46] investigated, using analytical and asymptotic methods the unsteady flow of a rivulet of fluid flowing over a heated inclined substrate with a concave triangular groove shape subject to the effects of gravity, surface tension and thermocapillarity. In particular, Gambaryan-Roisman and Stephan [46] investigated the stability of the rivulet flow subject to the physical effects included in their model and showed that long-wave thermocapillary instabilities can lead to splitting of the rivulet into droplets or slender rivulets, and kinematic-wave instabilities can be suppressed entirely as the groove angle of the substrate decreases.

Alshaikhi et al. [10] investigated, using analytical and asymptotic methods, the steady flow of a thin rivulet of fluid over and through an inclined porous substrate subject to the effect of gravity. In particular, Alshaikhi et al. [10] derived a differential equation for the semi-width a^* and contact angle β^* by considering a statement of global conservation of mass of the form

$$Q^*(a^*, \beta^*) = \bar{Q}^* + Q^*_{\mathrm{p}}(a^*, \beta^*), \tag{1.82}$$

where Q^* is the flux along the rivulet in the longitudinal direction, $\bar{Q}^*$ is the flux of the rivulet at the start of the porous substrate, and $Q^*_{\mathrm{p}} < 0$ is the volume flux through the base of the rivulet into the porous substrate. In Chapter 5 we shall adopt a similar strategy to derive a differential equation for the semi-width and contact angle of the rivulet by considering a statement of global conservation of mass of the form (1.82), with mass lost due to evaporation rather than flow into a porous substrate. Alshaikhi et al. [10] analysed the length, area of the base, volume and shape of the rivulet in both the case of a rivulet with fixed contact angle and a rivulet with fixed semi-width for sessile, vertical and pendant rivulets. The results of Alshaikhi et al. [10] will be revisited in Chapter 5.

(a) Experiments and numerical simulations

Singh et al. [152] investigated, using numerical and experimental methods, the flow and subsequent breakup of a rivulet over an inclined plane subject to the effects of gravity and surface tension. In particular, Singh et al. [152] investigated regimes of a stable rivulet flow and an unstable rivulet flow which leads to rivulet breakup in terms of a critical value of the Weber number, which, in the notation of Singh et al. [152] is given by

$$\mathrm{We} = \frac{\rho^* U^{*2} D^*}{\sigma^*}, \tag{1.83}$$

where U^* and D^* are the velocity of the fluid at, and diameter of, the supply inlet (i.e. a small hole through which the fluid is initially introduced to the substrate), respectively. Figure 1.24 shows the numerical simulations of Singh et al. [152], which show the shape of a water rivulet, and subsequent break up of the rivulet, as the Weber number is reduced. It is also clear from Figure 1.24, that as We is decreased, at first, the rivulet width decreases (We = 2.82 to We = 0.53). As We is reduced further, the rivulet breaks up into smaller rivulets and droplets (We = 0.37 to We = 0.13). Therefore, rivulet breakup occurs between the values We = 0.53 to We = 0.37. This breakup is due to the reduction in the velocity of the rivulet, which allows surface tension effects to dominate over inertial effects, which acts to destabilise the film and cause the rivulet to break up. Singh et al. [152] also carried out experiments and found good agreement with their numerical simulations.

Kochkin et al. [87] investigated, using experimental methods, the flow and subsequent breakup of a rivulet over a vertical heated plane. In particular, Kochkin et al. [87] investigated the effect of a uniformly heated substrate on the flow of the rivulet and the heat transfer from the substrate to the rivulet. Figure 1.25

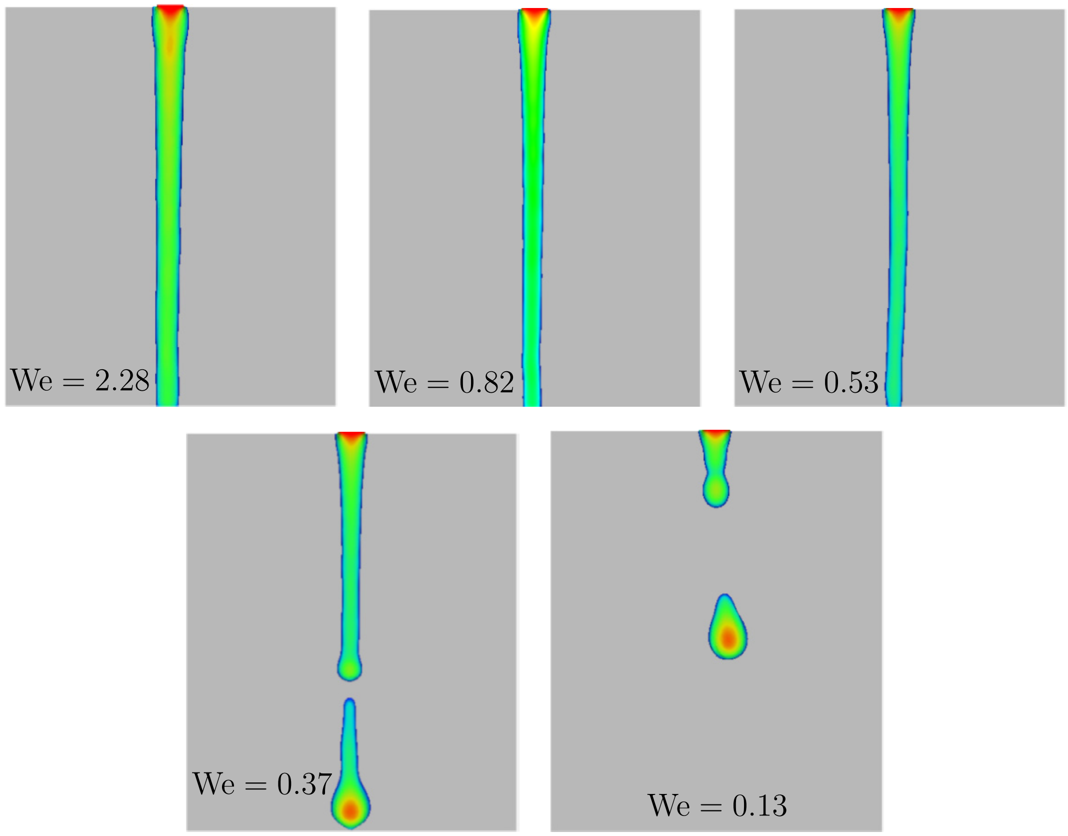

Figure 1.24: Shape of a water rivulet and subsequent rivulet breakup as the Weber number (1.83) is decreased. Reprinted from Singh et al. [152], with the permission of AIP Publishing.

shows Schlieren images of the flow of a rivulet on a vertical heated substrate for increasing uniform substrate temperatures. Kochkin et al. [87] showed, as shown in Figure 1.25, that as the substrate temperature is increased, the heat flux Q^*_{H} from the heated substrate into the rivulet, measured in watts per centimetre squared ($\mathrm{W/cm^2}$), increases, and five distinct regimes of behaviour of the rivulet are observed. The first of these regimes, which occurs when there is no heat flux ($Q^*_{\mathrm{H}} = 0$ $\mathrm{W/cm^2}$), is the stable-rivulet regime, characterised by a thin, stable rivulet, as shown in Figure 1.25(a). The second is the meandering-rivulet regime, which occurs when the substrate is slightly heated, so that $Q^*_{\mathrm{H}} = 1.77$ $\mathrm{W/cm^2}$, is characterised by the rivulet bending, as shown in Figure 1.25(b). As the substrate is further heated, so that $Q^*_{\mathrm{H}} = 2.28$ $\mathrm{W/cm^2}$, the rivulet enters the ribbed-rivulet regime, characterised by the appearance of periodic constrictions along the rivulet, as shown in Figure 1.25(c). The rivulet eventually breaks up as the heating of the

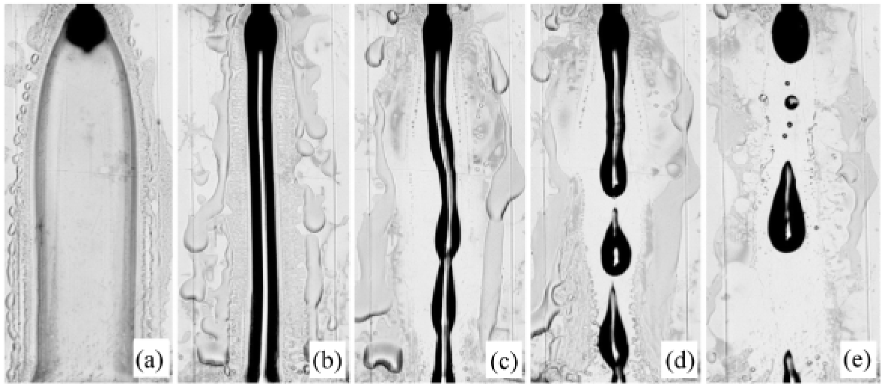

Figure 1.25: Schlieren images of the rivulet flow on a vertical heated substrate at a low fluid flow rate of 0.5 ml/min. From left to right, (a)–(e) show the characteristic regimes of behaviour of the rivulet as the temperature of the substrate is increased, where (a) shows the stable-rivulet regime ($Q_{\mathrm{H}}^{*} = 0$ W/cm^2), (b) shows the meandering-rivulet regime ($Q_{\mathrm{H}}^{*} = 1.77$ W/cm^2), (c) shows the ribbed-rivulet regime ($Q_{\mathrm{H}}^{*} = 2.28$ W/cm^2), (d) shows the rivulet-drop regime ($Q_{\mathrm{H}}^{*} = 2.44$ W/cm^2), and (e) shows the drop regime ($Q_{\mathrm{H}}^{*} = 2.61$ W/cm^2). Reproduced from Kochkin et al. [87] with permission from Springer Nature.

substrate is increased further, so that $Q_{\mathrm{H}}^{*} = 2.44$ W/cm^2 and $Q_{\mathrm{H}}^{*} = 2.61$ W/cm^2, and the rivulet enters the rivulet-drop regime and the drop regime, as shown in Figures 1.25(d) and (e), respectively. The rivulet-drop regime is characterised by the rivulet eventually breaking up into droplets further down stream, and the drop regime is characterised by the stream immediately breaking up into drops. It is also observed that as the heat flux increases, the width of the rivulet decreases, as can be seen most significantly, by comparing Figure 1.25(a) with (b).

1.5.3 Modelling evaporation

In order to theoretically model evaporation from the free surface of a fluid, it is necessary to describe the evaporative flux, i.e. the mass of fluid escaping into the atmosphere per unit area per unit time. The evaporative flux depends on both the rate of transfer of fluid molecules across the free surface and the transport of vapour molecules (by, for example, diffusion or advection) away from the free surface into the surrounding atmosphere (see, for example, Ajaev [4]).

In Chapter 5 we will consider the evaporation of a rivulet subject to three different mathematical models for the evaporative flux, namely, a uniform evaporative flux, an evaporative flux derived from the diffusion-limited evaporation model, and an evaporative flux derived from the one-sided evaporation model. In the remainder of this section, we will summarise the literature associated with two of the most popular evaporation models, namely the diffusion-limited and one-sided models.

1.5.4 Diffusion-limited model of evaporation

The mathematical model which accounts for the diffusion of the vapour away from the free surface of a fluid and neglects the rate of transfer of fluid across the free surface boundary is known as the diffusion-limited model of evaporation (see, for example, [35, 4]). Considering a fluid in a quiescent atmosphere, the transfer of molecules across the free surface boundary can be much faster than the transfer of vapour away from the free surface into the atmosphere [89]. In this scenario, the rate of diffusion of the vapour away from the free surface into the atmosphere is the rate-limiting mechanism of the evaporation, and hence the diffusion-limited model is appropriate [110]. This model is often used to model situations in which the fluid is not being heated and the atmosphere consists of both fluid vapour and passive gas [110, 4].

Many investigations of evaporating films and droplets of fluid have used the diffusion-limited model to analyse the evaporation of the fluid, for example, the pioneering work of Picknett and Bexon [135] who derived expressions for the evolution and lifetime of a droplet subject to diffusion-limited evaporation. The seminal work of Deegan et al. [34], who first described the now well-known coffee-stain effect in which the diffusion-limited evaporation of colloid-containing fluids leaves deposits of particles on the substrate as it evaporates, followed by many subsequent investigations considering various different aspects of droplet evaporation governed by the diffusion-limited model (see, for example, the review by Wilson and D'Ambrosio [177] and the investigations of Deegan [33, 35], Sultan et al. [158], Dunn et al. [39, 40], McHale et al. [99, 98], Popov [136], Larson [89], Schofield et al. [148, 149, 147], D'Ambriosio et al. [31], and Wray et al. [185]).

1.5.5 One-sided model of evaporation

A mathematical model which accounts for the rate of transfer of fluid across the free surface boundary and neglects the diffusion of the vapour is the one-sided model of evaporation [22]. Unlike the diffusion-limited model, the one-sided model assumes that the rate of transfer of molecules across the free surface boundary is the rate-limiting mechanism [110]. In particular, the one-sided model assumes that the density, viscosity and thermal conductivity of the atmosphere are small compared to that of the fluid [22, 4]. This model is most commonly used to model situations in which the fluid is being heated and the atmosphere consists entirely of fluid vapour [22, 110, 4].

Many investigations of evaporating films of fluid have applied the one-sided model to analyse the evaporation of the fluid. For example, the pioneering work of Burelbach et al. [22] derived the one-sided model for the evaporation of a film of fluid on a horizontal heated substrate and analysed the effect of the evaporation, Marangoni forces, vapour recoil and van der Waals forces on the shape and evolution of the film, followed by many subsequent investigations considering many different aspects of evaporation governed by the one-sided model (see, for example, Warner et al. [173], Ajaev [3], Ajaev et al. [5], Murisic and Kondic [110], Ajaev and Kabov [6], Charitatos et al. [26], and Charitatos and Kumar [25]).

1.6 Outline of Thesis

In this thesis we shall use a range of different analytical and asymptotic methods to investigate three different but related problems in thin-film flow.

In Chapter 2 we shall consider the steady flow of a thin film of fluid on the outside of a rotating horizontal cylinder subject to the effects of gravity and a non-uniform air pressure due to the presence of an external airflow. In particular, we shall derive the equations for the pressure, velocity and film thickness of the fluid and categorise the behaviour of the film thickness into different regions depending on the air speed and circulation of the airflow. A linear stability analysis will also show that the sub-critical full-film solution for the film thickness is neutrally stable to small two-dimensional disturbances.

In Chapter 3 we shall consider the unsteady flow of a thin film of fluid on the outside of a rotating horizontal cylinder subject to the effects of gravity, surface tension and a non-uniform air pressure due to the presence of an external airflow. In particular, we shall derive an evolution equation for the initially uniform film thickness and solve it in the limit in which the effects of gravity and surface tension are weak compared to surface shear. We shall investigate the stability of the flow and describe the evolution of the film for different values of the air speed and circulation of the airflow.

In Chapter 4 we shall consider the axisymmetric and two-dimensional squeezing of a thin film of fluid between an impermeable flat bearing and a flat porous bed with either a sealed face or open face subject to a constant load. In particular, we shall briefly summarize the results of Knox et al. [86], who solved the closed-face porous bed problem, and then go on to analyse the open-face porous bed problem. For both the closed face and open face problems we shall determine the finite time required for all of the fluid to be squeezed out of the gap between the impermeable bearing and porous bed, i.e. the finite time required for the impermeable bearing and the porous bed to contact, and then derive asymptotic solutions for the contact time in the limits of a porous bed with small and large permeability. We shall then describe the behaviour of the particle paths, and penetration depths of the fluid into the porous bed.

In Chapter 5 we shall consider the steady flow of a thin rivulet of evaporating fluid flowing down an inclined substrate subject to the effect of gravity. In particular, we shall consider three evaporation models, namely, constant evaporation, diffusion-limited evaporation and one-sided model evaporation, and in each case determine the length, area and volume of the rivulet as the contact angle varies (when the semi-width of the rivulet is fixed) and as the semi-width varies (when the contact angle is fixed).

In Chapter 6 we shall summarise the main results obtained in the thesis, and discuss possible further work for each problem.

1.7 Publications and Presentations

The work in Chapters 2 and 3 of this thesis has been published in the Journal of Fluid Mechanics (Mitchell et al. [105]) and Physics of Fluids (Mitchell et al. [106]), respectively.

The work in Chapter 2 has been presented at the British Applied Mathematics Colloquium at the University of Bath in 2019, and the Continuum Mechanics and Industrial Mathematics research group meeting in the Department of Mathematics and Statistics in the University of Strathclyde in 2019. The work in Chapters 2 and 3 has been presented together at the UK Fluids Conference virtually in 2021, the Scottish Fluid Mechanics Meeting at The Scottish Association for Marine Science in Oban in 2022, and the First Spanish Fluid Mechanics Conference at the Universidad de Cádiz in 2022.

The work in Chapter 4 has been presented at the Annual Meeting of the American Physical Society Division of Fluid Dynamics virtually in 2020, British Applied Mathematics Colloquium virtually in 2021, the International Micro and Nano Flows Conference virtually in 2021, and the UK Fluids Conference virtually in 2021.

Chapter 2

Coating flow of a thin film subject to an irrotational airflow with circulation

2.1 Introduction

As discussed in Section 1.3, since the publication of the works of Moffatt [108] and Pukhnachev [137] there have been many investigations extending the classical coating flow problem. However, there has been very little work on the problem investigated in this and the next chapter, namely the effect of an airflow with circulation external to a thin film of fluid on the outside of a rotating horizontal cylinder. In Section 1.2 we discussed investigations that use conditions of non-zero shear stress and/or non-uniform pressure due to the effect of an external airflow at the free surface of a thin film of viscous fluid. In particular, we described the non-uniform pressure $p^* = p^*_{\mathrm{a}}(\theta)$ given by (1.43) considered by Newell and Viljoen [118] to model the effects of an external irrotational airflow on the evolution of an initially uniform thin film of fluid on a rotating horizontal cylinder. In this chapter, we combine the classical work of Moffatt [108] and Pukhnachev [137] with the non-uniform air pressure considered by Newell and Viljoen [118] to undertake the first detailed analysis of steady two-dimensional coating flow of a thin film of fluid on the outside of a rotating horizontal cylinder in the absence of surface-tension effects but in the presence of a non-uniform pressure, given by (1.43), due to the presence of an external irrotational airflow with circulation. This problem is not only of interest in its own right, both as a rare example of an analytically tractable problem involving the interaction between an airflow and a fluid film and as a novel extension to the classical coating-flow problem, but also as a paradigm for the wide range of practical situations, including those mentioned in Sections 1.2 and 1.3, in which a thin film of fluid on a moving solid substrate is subject to an external airflow.

2.2 Governing equations

Figure 2.1 shows the set up of the current problem of a thin film of fluid coating the entire outer surface of a rotating cylinder in the presence of an external airflow. In particular, following Moffatt [108] (as described in Section 1.3), with respect to cylindrical polar coordinates (r^*, θ), with azimuthal angle θ measured increasing anticlockwise from the horizontal and radial distance r^* measured from the origin, consider the two-dimensional unsteady coating flow of a thin film of incompressible viscous Newtonian fluid with constant density ρ^* and viscosity μ^* on a horizontal circular cylinder of radius a^* rotating anticlockwise with uniform angular speed $\Omega^*\,(> 0)$. Furthermore, as described in Section 1.3, locally, on the surface of the cylinder, we recover the problem of flow down an inclined plane described in Section 1.1.1. Specifically, we use local Cartesian coordinates (x^*, y^*) with x^* in the direction of increasing θ (so that $x^* = a^*\theta$ locally) and y^* normal to the cylinder, so that $r^* = a^* + y^*$ (for rimming flow $r^* = a^* - y^*$). The free surface is located at $y^* = h^*(\theta, t^*)$.

As in Section 1.1.1, the flow is governed by the continuity equation (1.2) and Navier–Stokes equation (1.3) (with $\alpha = \theta - \pi/2$), which are solved subject to the no-slip and no-penetration conditions (1.6), with $\mathbf{\Omega}^* = (a^*\Omega^*, 0)$, where $a^*\Omega^*$ is the angular speed of the cylinder surface, and the continuity of normal and tangential stress conditions (1.7) and (1.8), where now $\mathbf{T}^*_{\mathrm{a}} = -p^*_{\mathrm{a}}(\theta)\mathbf{I} + 2\mu^*_{\mathrm{a}}\boldsymbol{\tau}^*_{\mathrm{a}}$. The azimuthal volume flux per unit axial length in the direction of increasing θ is given by (1.10) and the constant mass per unit axial length on the cylinder is given by

$$M^* = \rho^* \int_{-\pi}^{\pi} h^*(\theta, t^*)\ \mathrm{d}\theta. \tag{2.1}$$

In addition, the stream function for the flow of the film, $\psi^* = \psi^*(\theta, y^*, t^*)$, is defined by

$$\frac{\partial \psi^*}{\partial y^*} = u^* \quad \text{and} \quad \frac{1}{a^*}\frac{\partial \psi^*}{\partial \theta} = -v^* \tag{2.2}$$

subject to $\psi^* = 0$ at $y^* = 0$.

Following Newell and Viljoen [118] (as described in Section 1.2), the air above the film is taken to be incompressible and inviscid, so that there is a non-uniform pressure $p_{\mathrm{a}}^*(\theta)$ (but no shear stress) of the form (1.43) on the free surface of the film due to the presence of the external airflow, where the film is supported on the cylinder against gravity by a combination of the shear that is induced by the rotation of the cylinder and the air pressure on the free surface of the film. We assume that the thickness of the film is much less than the radius of the cylinder, and hence that the airflow round the cylinder is unaffected by the presence of the film.

We non-dimensionalise the problem according to

$$\begin{gathered} x^* = a^*\theta, \quad y^* = H^*y, \quad h^* = H^*h, \quad p^* = p^*_\infty + \frac{\sigma^*}{a^*} + \frac{\mu^* U^* a^*}{H^{*2}}p, \\ p^*_{\mathrm{a}} = p^*_\infty + \frac{\mu^* U^* a^*}{H^{*2}}p_{\mathrm{a}}, \quad t^* = \frac{a^*}{U^*}t, \quad u^* = U^*u, \quad v^* = \epsilon U^* v, \quad \psi^* = U^*H^*\psi, \\ Q^* = U^*H^*Q, \quad M^* = H^*\rho^*M, \end{gathered} \tag{2.3}$$

where $U^* = a^*\Omega^*$, the characteristic film thickness H^* is given again by (1.18) and $H^*/a^* = \epsilon \ll 1$. The mean curvature of the free surface, to first order in the limit $\epsilon \to 0$ is now

$$\Gamma = 1 - \epsilon\left(h(\theta) + h''(\theta)\right). \tag{2.4}$$

At leading order in the limit $\epsilon \to 0$, the governing equations become (1.14), (1.23), and (1.24) (again, with $\alpha = \theta - \pi/2$). These are solved subject to the no-slip and no-penetration conditions

$$u = 1 \quad \text{and} \quad v = 0 \tag{2.5}$$

on $y = 0$, the conditions of continuity of normal stress

$$p = p_{\mathrm{a}}(\theta) - \mathrm{Ca}^{-1}\left(\frac{\partial^2 h}{\partial \theta^2} + \frac{\partial h}{\partial \theta}\right), \tag{2.6}$$

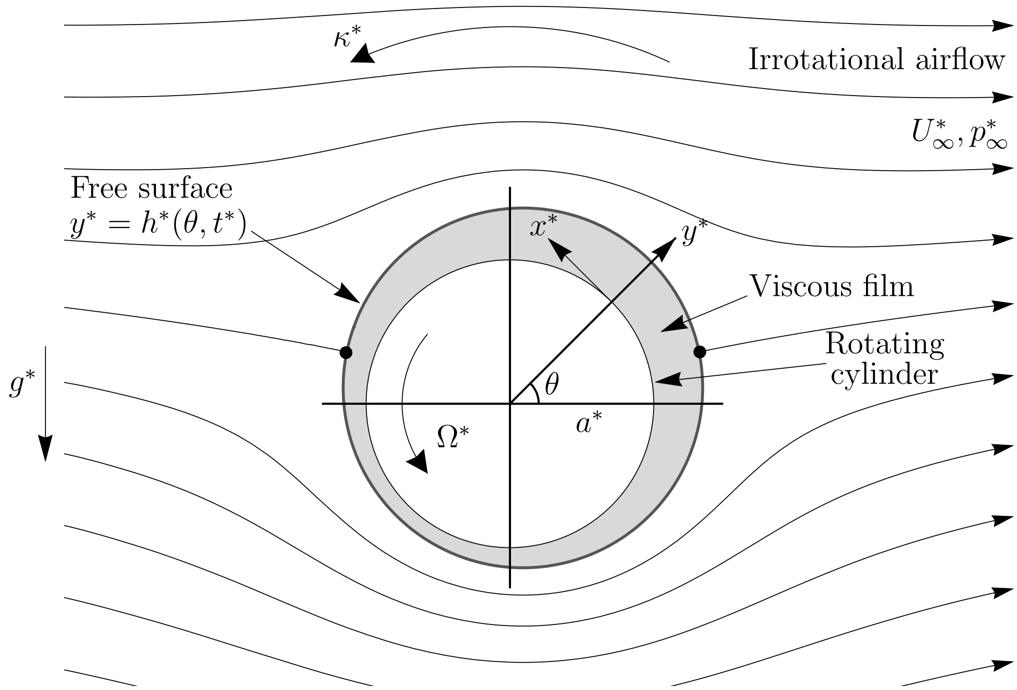

Figure 2.1: Sketch of coating flow of a thin film of viscous fluid of thickness $h^*(\theta, t^*)$ on a horizontal circular cylinder of radius a^* rotating anticlockwise with uniform angular speed Ω^* in the presence of an irrotational airflow with uniform horizontal velocity U^*_∞ (≥ 0) from left to right and pressure p^*_∞ in the far field and a circulation κ^* shown in the case when $\lambda = \kappa^*/(4\pi a^* U^*_\infty) = K/(2F)$ satisfies $0 < \lambda < 1$. The locations of the stagnation points of the airflow are indicated with dots (•).

and continuity of tangential stress (1.27) on $y = h$. The streamfunction (2.2) becomes

$$\frac{\partial \psi}{\partial y} = u \quad \text{and} \quad \frac{\partial \psi}{\partial \theta} = -v, \tag{2.7}$$

the azimuthal volume flux per unit axial length of the fluid in the film in the direction of increasing θ becomes

$$Q = \int_0^h u(\theta, y, t)\, \mathrm{d}y, \tag{2.8}$$

and the constant mass of fluid per unit axial length on the cylinder (2.1) becomes

$$M = \int_{-\pi}^{\pi} h(\theta, t)\, \mathrm{d}\theta. \tag{2.9}$$

2.3 Steady coating flow in the presence of an external airflow

In the remainder of this chapter we will consider steady two-dimensional coating flow, so that now $h = h(\theta)$, $u = u(\theta, y)$, $v = v(\theta, y)$, and $\psi = \psi(\theta, y)$, in the presence of gravity and a non-uniform air pressure $p_{\mathrm{a}}(\theta)$ due to an external horizontal irrotational airflow, but in the absence of surface tension effects, so that $\mathrm{Ca}^{-1} \ll 1$, and hence (2.6) reduces to

$$p = p_{\mathrm{a}}(\theta) \tag{2.10}$$

on $y = h$.

Solving (1.24) subject to (2.10), implies immediately that the pressure in the film is independent of y, and hence $p = p_{\mathrm{a}}(\theta)$ throughout the film. Therefore, the expression for the pressure within the film given by (1.43) subject to the scalings (2.3), becomes

$$p = p_{\mathrm{a}} = \frac{1}{2}\left[F^2 - (2F\sin\theta - K)^2\right], \tag{2.11}$$

where F (≥ 0) and K, defined by

$$F = \left(\frac{\rho_{\mathrm{a}}^* U_\infty^{*2}}{\rho^* g^* a^*}\right)^{1/2}, \qquad K = \frac{\kappa^*}{2\pi a^*}\left(\frac{\rho_{\mathrm{a}}^*}{\rho^* g^* a^*}\right)^{1/2}, \tag{2.12}$$

are nondimensional measures of the speed of the far-field airflow and the circulation of the airflow, respectively.

Solving (1.23) with respect to (2.5) and (1.27) gives the velocity

$$u = 1 - \frac{1}{2} f\left(2hy - y^2\right). \tag{2.13}$$

From (2.7) the streamfunction is given by

$$\psi = y - \frac{1}{6} f\left(3hy^2 - y^3\right), \tag{2.14}$$

and from (2.8) the flux is given by

$$Q = h - \frac{h^3}{3} f, \tag{2.15}$$

where we have introduced the function $f = f(\theta)$ defined by $f(\theta) = \cos\theta + p_{\mathrm{a}}'$, i.e.

$$f(\theta) = \bigl(1 + 2FK - 4F^2 \sin\theta\bigr)\cos\theta. \tag{2.16}$$

The mass M (2.9) is now given by

$$M = \int_{-\pi}^{\pi} h(\theta)\,\mathrm{d}\theta, \tag{2.17}$$

In the present work we restrict our attention to the full-film solutions discussed in Section 1.3 (i.e. to solutions for h that are continuous and strictly positive for all $-\pi < \theta \leq \pi$, corresponding to a film of fluid covering the entire cylinder). For such a solution, the flux Q given by (2.15) is a constant (i.e. it is independent of θ), but its value is unknown *a priori* and has to be determined as part of the solution from either the condition of prescribed mass M given by (2.17) or an appropriate criticality condition.

As discussed in Section 1.2, the external airflow is assumed to be irrotational. For this assumption to be true, the Reynolds number of the airflow must be large and the boundary layer that forms in the air at the cylinder surface must remain attached to the cylinder. The classical analysis of Glauert [49] and Moore [109], supported by numerical studies by Kang et al. [74], Stojkovic et al. [155], Mittal and Kumar [107] and Aljure et al. [7], shows that, at least for the case of a cylinder without a thin film of viscous fluid, the rotation of the cylinder acts to suppress the tendency of the boundary layer in the airflow to separate on the downstream side of the cylinder. In particular, Glauert [49] and Moore [109] showed that when the Reynolds number of the airflow based on the circumferential speed of the cylinder, $\rho_{\mathrm{a}}^* a^{*2}\Omega^*/\mu_{\mathrm{a}}^* \gg 1$, is large, and the circumferential speed of the cylinder is large compared with that of the far-field airflow, $a^*\Omega^* \gg U_\infty^*$, where Ω^* is the constant angular speed of the rotation of the cylinder, the boundary layer remains attached all the way around the cylinder, and the circulation takes the value $\kappa^* = 2\pi a^{*2}\Omega^*$. Expressed in terms of F and K this corresponds to the regime $F/K = U_\infty^*/(a^*\Omega^*) \ll 1$. Moreover, Mittal and Kumar [107] showed numerically that when the value of the Reynolds number of the airflow based on the far-field airflow and the diameter (rather than the radius) of the cylinder, $2\rho_{\mathrm{a}}^* a^* U_\infty^*/\mu_{\mathrm{a}}^*$, is 200, the pressure distribution on the cylinder is qualitatively similar to that of the inviscid airflow (1.43) in the case $\kappa^* = 2\pi a^{*2}\Omega^*$ when $F/K = 1/4$. However, what (if any) effect the presence of a non-uniform thin film of viscous fluid on a rotating cylinder has on the suppression of boundary-layer separation remains an open question, and so in Chapters 2 and 3 we describe the behaviour of the film for all values of F and K, while bearing in mind that the regime $F/|K| \lesssim 1$ is likely to be the most physically relevant. This approach is in the same spirit as that of Newell & Viljoen [118], who (in our notation) took $\kappa = 2\pi a^2\Omega$ and then considered all values of $U_\infty/(a\Omega)$ in the range $|U_\infty/(a\Omega)| \leq 1$. As well as being of interest in their own right, the results of the present analysis for all values of F and K also provide an analytical benchmark for future studies of regimes in which boundary-layer separation occurs.

Equations (2.13)–(2.15) show that the flow of the film is a combination of flows due to four different competing physical effects, namely a uniform velocity $u \equiv 1$ with flux h due to the rotation of the cylinder and semi-parabolic (in y) velocities with fluxes $-(h^3/3)\cos\theta$, $-(2FKh^3/3)\cos\theta$, and $(2F^2h^3/3)\sin 2\theta$ due to the azimuthal component of gravity, the gradient of the air pressure due to the circulation of the airflow in combination with the far-field airflow, and the gradient of the air pressure due to the far-field airflow, respectively.

In the special case of no far-field airflow, $F = 0$, the pressure $p = p_{\mathrm{a}} = -K^2/2$ is constant, $f = \cos\theta$, and hence (2.15) reduces to the familiar expression for the flux in classical coating flow given by equation (1.48) showing that the behaviour of the film is entirely unaffected by a purely circulatory airflow. On the other hand, in the special case $FK = -1/2$ the fluxes due to gravity and circulation cancel each other out exactly, and so the behaviour of the film is due only to the rotation of the cylinder and the far-field airflow. The behaviour of the film for all values of F and K will be described in detail in this chapter.

For future reference, as described in Section 1.2, and illustrated in Figure 1.8, it is useful to recall that the position of the stagnation points in the airflow depends on the value of $\lambda = \kappa^*/(4\pi a^* U_\infty^*) = K/(2F)$. Specifically, the airflow has two stagnation points on the cylinder when $0 \leq |K|/(2F) < 1$, one stagnation point on either the top or the bottom of the cylinder when $|K|/(2F) = 1$, and one stagnation point within the airflow either directly above or directly below the cylinder when $|K|/(2F) > 1$ (see Figure 1.8).

For completeness, in Appendix A we provide the corresponding equations for the more general situation in which the far-field airflow, rather than being horizontal, is inclined at some prescribed angle α to the horizontal, but in the present work we restrict our attention to the case in which the far-field airflow is horizontal, as shown in Figure 2.1.

2.4 Full-film solutions

Equation (2.15) is a cubic polynomial equation for h as a function of θ, parameterised by Q, whose full-film solution may be written in the explicit real form

$$h(\theta) = \begin{cases} \dfrac{2}{f(\theta)^{1/2}} \sin\left(\dfrac{1}{3}\sin^{-1}\dfrac{3Qf(\theta)^{1/2}}{2}\right) & \text{if } f > 0, \\ Q & \text{if } f = 0, \\ \dfrac{2}{[-f(\theta)]^{1/2}} \sinh\left(\dfrac{1}{3}\sinh^{-1}\dfrac{3Q\,[-f(\theta)]^{1/2}}{2}\right) & \text{if } f < 0. \end{cases} \tag{2.18}$$

In order to understand the qualitative features of the full-film solution (2.18) it is easiest to consider equation (2.15) graphically in the θ–h plane, regarding Q as a function of θ and h, and exploiting the fact that, since $\psi = Q$ on $y = h$, any contour of Q (which is, by definition, a curve on which Q is constant) potentially provides a solution for the free surface $y = h$. In particular, we can use this approach to show that, just as for classical coating flow, equation (2.15) has full-film solutions only when the flux Q and mass M of fluid do not exceed certain critical values, which we denote by Q_{c} and M_{c}, respectively, and will subsequently determine in terms of F and K. The critical film thickness (i.e. the solution for h with $Q = Q_{\mathrm{c}}$) is denoted by $h_{\mathrm{c}} = h_{\mathrm{c}}(\theta)$.

Figure 2.2 shows plots of contours of Q when $K = 0$ for $0 \le Q \le Q_{\mathrm{c}}$, with each contour therefore representing the film thickness h for the corresponding value of Q, for a range of values of F. In particular, Figure 2.2 shows that, as in classical coating flow, critical solutions with $Q = Q_{\mathrm{c}}$ always have a corner in their free surface $y = h_{\mathrm{c}}$ but subcritical solutions with $0 < Q < Q_{\mathrm{c}}$ always have a smooth free surface $y = h$. The position of the corner in the critical free surface is denoted by $\theta = \theta_{\mathrm{c}}$.

Despite a superficial resemblance, it should be noted that (except for the critical free surface $y = h_{\mathrm{c}}$ and the substrate $y = 0$) the contours of Q shown in Figure 2.2 do *not* correspond to streamlines of the critical solution. This is confirmed by Figure 2.3, which shows plots of typical streamlines ψ = constant, where ψ

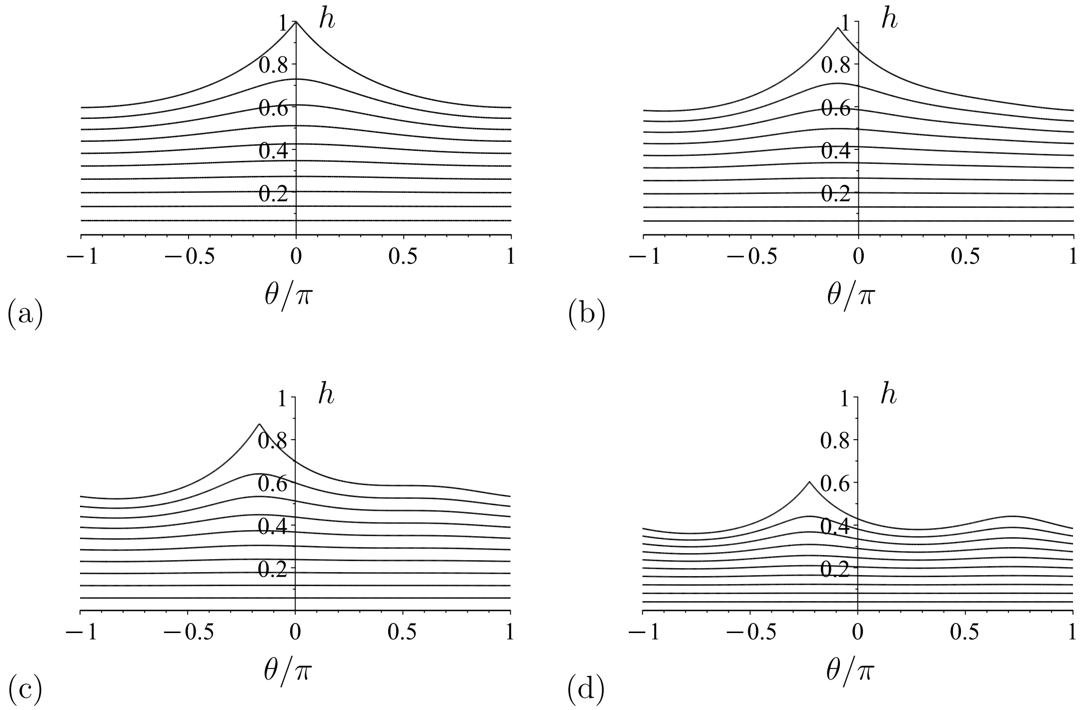

Figure 2.2: Plots of contours of Q when $K = 0$ for $0 \le Q \le Q_c$, with each contour therefore representing the film thickness h for the corresponding value of Q, for (a) $F = 0$ (i.e. classical coating flow) ($\theta_c = 0$, $Q_c = 2/3$, $M_c \simeq 4.443$), (b) $F = 3/10$ ($\theta_c = -0.096\pi$, $Q_c \simeq 0.648$, $M_c = 4.299$), (c) $F = 1/2$ ($\theta_c = -\pi/6$, $Q_c \simeq 0.585$, $M_c \simeq 3.838$), and (d) $F = 1$ ($\theta_c = -0.224\pi$, $Q_c \simeq 0.403$, $M_c \simeq 2.628$). In each case the contour interval is $Q_c/10$.

is given by (2.14), for a critical and a subcritical solution. In particular, Figure 2.3(a) shows that *all* of the streamlines of the critical solution (except, of course, for the substrate $y = 0$), and not just the critical free surface $y = h_c$, have a corner at the *same* position $\theta = \theta_c$.

2.5 Properties of the full-film solutions

In this section we describe some of the properties of the full-film solutions obtained in Section 2.4 and illustrated when $K = 0$ in Figures 2.2 and 2.3. Then in Sections 2.6 and 2.7 we describe the behaviour of the solutions in the special case when the airflow has no circulation ($K = 0$) and in the general case when the airflow has non-zero circulation ($K \neq 0$), respectively, and finally in Section 2.8 we consider the mass of fluid on the cylinder.

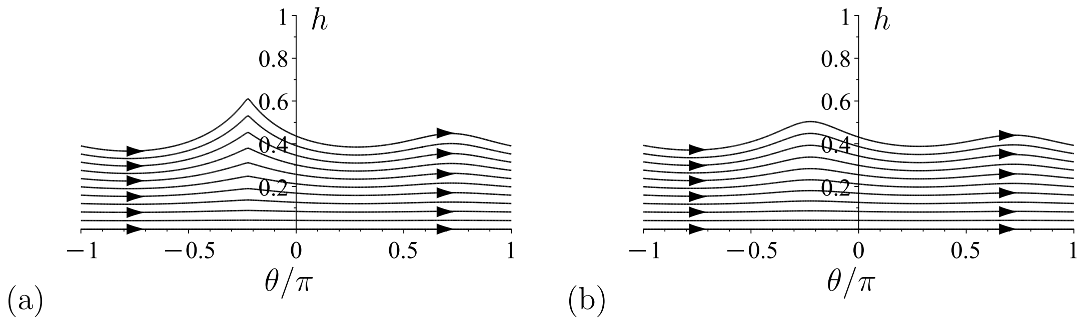

Figure 2.3: Plots of typical streamlines $\psi =$ constant, where ψ is given by (2.14), for (a) the critical solution with $Q = Q_\mathrm{c} \simeq 0.403$ and (b) the subcritical solution with $Q = 9Q_\mathrm{c}/10 \simeq 0.363\,(< Q_\mathrm{c})$, when $F = 1$ and $K = 0$.

2.5.1 General properties

In this subsection we describe some of the general properties of the full-film solutions.

At any fixed position θ, differentiating (2.15) with respect to Q gives $(1 - h^2 f)(\partial h/\partial Q) = 1$, and since, as shown in Appendix B, for full-film solutions it is necessary that $h^2 f \leq 1$, we deduce immediately that $\partial h/\partial Q > 0$, and hence that h increases monotonically with Q.

On the other hand, for any fixed value of Q, differentiating (2.15) with respect to θ gives $(1-h^2 f)h' = h^3 f'/3$, showing that h' has the same sign as f' everywhere, and hence that the positions of the stationary points of h are determined by the equation $f' = 0$, which may be written in the form

$$8F^2 \sin^2\theta - (1 + 2FK)\sin\theta - 4F^2 = 0, \tag{2.19}$$

whose solutions for θ satisfy

$$\sin\theta = \frac{1 + 2FK \pm \left[(1 + 2FK)^2 + 128F^4\right]^{1/2}}{16F^2}. \tag{2.20}$$

As these solutions are independent of Q, the stationary points of h occur at the same positions θ for all values of Q. Moreover, at all of the stationary points of h we have $3(1 - h^2 f)h'' = h^3 f''$ and also, from (2.16) and (2.20), $f'' = \pm\left[(1 + 2FK)^2 + 128F^4\right]^{1/2}\cos\theta$, which, taken together, show that the nature of each stationary point is given by the sign of $\pm\cos\theta$ there. In classical coating flow, h has two stationary points, namely a maximum at $\theta = 0$ (i.e. on the right-hand side of the cylinder) and a minimum at $\theta = \pi$ (i.e. on the left-hand side of the cylinder); however, the presence of the airflow can result in qualitatively different behaviour of the fluid film. In particular, as will be described subsequently, in the present problem h can have as many as four stationary points. Moreover, as mentioned in Section 1.3, in classical coating flow h has top-to-bottom, but not right-to-left, symmetry; however, the presence of the airflow means that, in general, in the present problem h has neither top-to-bottom nor right-to-left symmetry.

The function f given by (2.16) has zeros at $\theta = \pm\pi/2$ and at $\theta = \sin^{-1}((1 + 2FK)/(4F^2))$ when $|1 + 2FK|/(4F^2) \leq 1$. From either (2.13)–(2.15) or (2.18) it is immediately apparent that at any zero of f the film has thickness $h = Q$, and that the fluid there moves locally with uniform velocity $u \equiv 1$ (i.e. as a plug). Moreover, the fact that $Q = h > 0$ for such values of θ means that the constant flux Q is always positive, i.e. for full-film solutions the flux is always everywhere in the direction of the rotation of the cylinder (i.e. anticlockwise). In fact, as shown in Appendix C, we can obtain the stronger result that the velocity u (and not just the flux Q) is always positive, i.e. the flow of the film is always everywhere in the direction of the rotation of the cylinder.

2.5.2 Critical solutions

In this subsection we describe the behaviour of the critical full-film solutions, i.e. solutions for which the flux and mass of fluid take the critical values $Q = Q_{\mathrm{c}}$ and $M = M_{\mathrm{c}}$, respectively, above which no full-film solution exists, so that M_{c} is the maximum mass of fluid that can be supported on the cylinder for given values of F and K. As mentioned in Section 2.4, all of the streamlines of the critical solution (except for the substrate $y = 0$), and, in particular, the critical free surface $y = h_{\mathrm{c}}$, have a corner at $\theta = \theta_{\mathrm{c}}$.

As in classical coating flow, the critical solution corresponds to a saddle of the function Q given by (2.15), at which Q satisfies the criticality conditions

$$\frac{\partial Q}{\partial h} = 0, \qquad \frac{\partial Q}{\partial \theta} = 0, \tag{2.21}$$

leading to

$$h^2 f(\theta) = 1, \qquad f'(\theta) = 0, \tag{2.22}$$

and any saddle of Q corresponds to a corner in the critical free surface $y = h_{\mathrm{c}}$. As

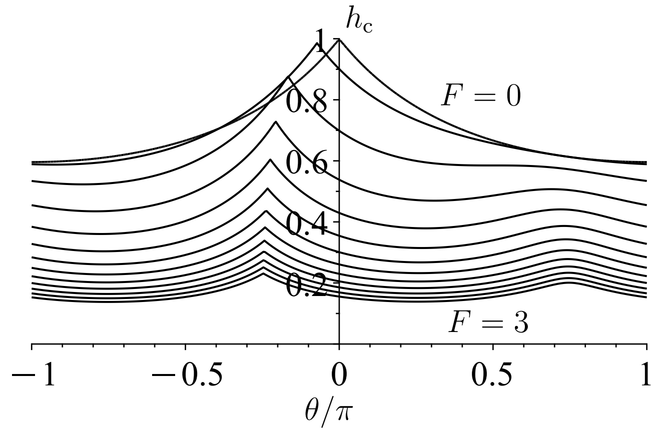

Figure 2.4: Plots of the critical film thickness h_c when $K = 0$ as a function of θ/π for $F = 0, 1/4, 1/2, \ldots, 3$.

shown in Appendix D, the function Q has no maximum or minimum stationary points, and, depending on the values of F and K, has either one or two saddle points; in the latter case it is the saddle associated with the smaller value of Q (and hence the smaller value of M) that corresponds to the critical solution.

The first of the criticality conditions (2.22) gives the thickness of the critical film at the corner, namely

$$h_c(\theta_c) = \frac{1}{f(\theta_c)^{1/2}} \tag{2.23}$$

(which, in particular, shows that a corner may occur only where $f(\theta_c) > 0$), while the second of the criticality conditions (2.22) shows that solutions for θ_c satisfy (2.20). Physically, the critical maximum height (2.23) occurs due to gravity pulling vertically down on the fluid on the right hand side of the cylinder and the shear induced by the rotation of the cylinder pulling up, similar to the critical maximum that occurs in the classical problem in the absence of airflow effects. As the airflow effects become stronger, a second maximum occurs on the upper left quadrant of the cylinder. This maximum is due to the competing effects of the pressure gradient which forces the fluid up the cylinder from $\theta = \pi$ to $\theta = \pi/2$ in competition with gravity and the shear induced by the rotation of the cylinder pulling the fluid vertically down.

Figure 2.4 shows plots of the critical film thickness h_c when $K = 0$ as a function of θ/π for a range of values of F. As Figure 2.4 illustrates, the global maximum thickness of the critical film (and hence the maximum possible thickness of *any* film for given values of F and K) always occurs at the corner, and expanding

(2.15) about $\theta = \theta_c$ shows that near the corner the critical free surface $y = h_c$ has the local form

$$h_c = h_c(\theta_c) + h_1|\theta - \theta_c| + \mathcal{O}(\theta - \theta_c)^2, \tag{2.24}$$

where

$$h_1 = -\frac{h_c^2[-f''(\theta_c)]^{1/2}}{\sqrt{6}} \ (< 0). \tag{2.25}$$

Evaluating (2.15) at $\theta = \theta_c$ gives the critical flux,

$$Q_c = \frac{2h_c(\theta_c)}{3} = \frac{2}{3f(\theta_c)^{1/2}}, \tag{2.26}$$

and (2.17) gives the critical mass,

$$M_c = \int_{-\pi}^{\pi} h_c(\theta)\,\mathrm{d}\theta. \tag{2.27}$$

Note that critical free surfaces with *two* corners may also occur, but only at leading order in the limit of a fast far-field airflow, $F \to \infty$, and in the special case $FK = -1/2$; these exceptional situations will be described in Sections 2.6 and 2.7, respectively.

2.5.3 Subcritical solutions

In this subsection we describe the behaviour of the subcritical full-film solutions, i.e. solutions for which the flux Q and mass M of fluid satisfy $0 < Q < Q_c$ and $0 < M < M_c$. As mentioned in Section 2.4, unlike for the critical solutions described in Section 2.5.2, all of the streamlines of the subcritical solutions, and, in particular, the subcritical free surface $y = h$, are smooth. However, as described in Section 2.5.1, the global maximum of the subcritical film thickness still always occurs at $\theta = \theta_c$ (i.e. at the same position as the corner in the critical free surface $y = h_c$), and expanding (2.15) about $\theta = \theta_c$ shows that near the maximum the subcritical free surface $y = h$ has the locally parabolic form

$$h = h_0 + \frac{h_0^3 f''(\theta_c)}{6[1 - h_0^2 f(\theta_c)]}(\theta - \theta_c)^2 + \mathcal{O}(\theta - \theta_c)^3, \tag{2.28}$$

where $h_0 = h(\theta_c)$ $(0 < h_0 < h_c(\theta_c))$ is the value of h at $\theta = \theta_c$ obtained from (2.15).

In the regime of small flux, $Q \ll 1$, the subcritical film thickness h is given by

$$h = Q + \frac{f}{3}Q^3 + \frac{f^2}{3}Q^5 + \mathcal{O}(Q^7), \tag{2.29}$$

and hence from (2.17) the mass M is given by

$$M = 2\pi Q + \frac{\pi}{3}\left[(1+2FK)^2 + 4F^4\right]Q^5 + \mathcal{O}(Q^9). \tag{2.30}$$

Eliminating Q between (2.29) and (2.30) we obtain the expression for h in the regime of small mass, $M \ll 1$, namely

$$h = \frac{M}{2\pi} + \frac{f}{24\pi^3}M^3 - \frac{(1+2FK)^2 + 4F^4 - 2f^2}{192\pi^5}M^5 + \mathcal{O}(M^7), \tag{2.31}$$

showing that the film is very thin with uniform thickness $M/2\pi \ll 1$ at leading order in this limit.

2.6 Solutions when the airflow has no circulation ($K = 0$)

In this section we use the results obtained thus far to describe the behaviour of the full-film solutions when the airflow has no circulation, corresponding to $K = 0$ and illustrated in Figures 2.2–2.4.

In this case the pressure gradient within the film is entirely due to the far-field airflow, and the flux it induces, namely $(2F^2h^3/3)\sin 2\theta$, drives flow away from the left-hand and right-hand sides of the cylinder and towards the top and bottom of the cylinder (i.e. away from $\theta = 0$ and $\theta = \pi$ and towards $\theta = \pi/2$ and $\theta = -\pi/2$). The behaviour of the film is therefore a consequence of the competition between this flux and those due to the rotation of the cylinder and gravity, which, as in classical coating flow, drive flow in the direction of the rotation of the cylinder (i.e. anticlockwise) and away from the top and towards the bottom of the cylinder (i.e. away from $\theta = \pi/2$ and towards $\theta = -\pi/2$), respectively.

As described in Section 2.5.1, the positions of the stationary points of h are given by (2.20), which reduces to

$$\sin\theta = \frac{1 \pm (1+128F^4)^{1/2}}{16F^2} \tag{2.32}$$

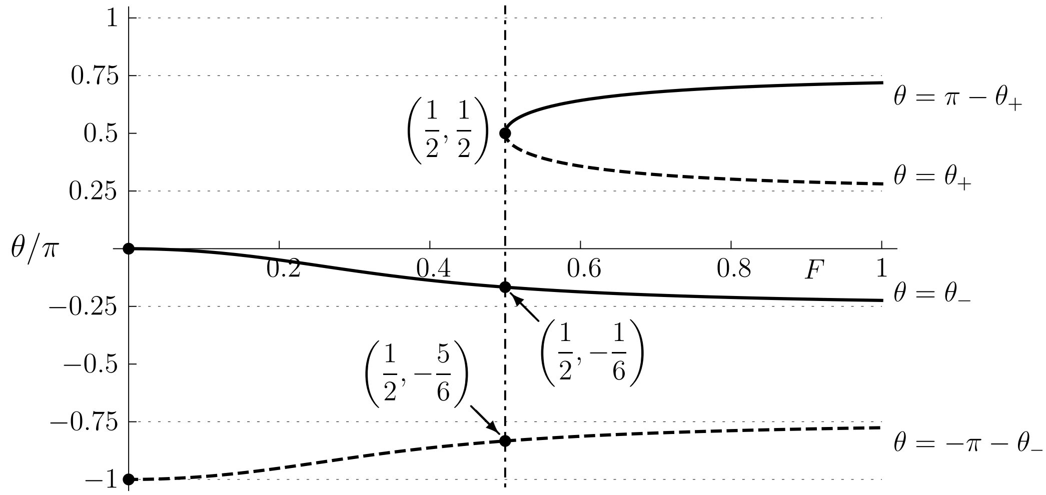

Figure 2.5: Plot of the scaled positions θ/π of the stationary points of h when $K = 0$ given by (2.32) as functions of F. The positions corresponding to a local maximum and a local minimum of h are plotted with solid lines and dashed lines, respectively.

when $K = 0$, and the nature of each stationary point is given by the sign of $\pm\cos\theta$. We denote the solutions of (2.32) in the interval $-\pi/2 \leq \theta \leq \pi/2$ by $\theta = \theta_+$ ($\pi/4 \leq \theta_+ \leq \pi/2$) and $\theta = \theta_-$ ($-\pi/4 \leq \theta_- \leq 0$), respectively, where the subscript $\pm$ corresponds to the $\pm$ in (2.32), and in terms of which the solutions of (2.32) are given by $\theta = \theta_+$ and $\theta = \pi - \theta_+$ for $F \geq 1/2$ and $\theta = \theta_-$ and $\theta = -\pi - \theta_-$ for $F \geq 0$.

Figure 2.5 shows a plot of the scaled positions θ/π of the stationary points of h when $K = 0$ given by (2.32) as functions of F. The positions corresponding to a local maximum and a local minimum of h are plotted with solid lines and dashed lines, respectively. In particular, Figure 2.5 shows that when $K = 0$ the film thickness h has two stationary points when $0 \leq F < 1/2$, three stationary points when $F = 1/2$, and four stationary points when $F > 1/2$, and that the positions of these stationary points on the cylinder are symmetrical about the vertical line $\theta = \pm\pi/2$.

The plots of the film thickness h for a range of values of Q and F shown in Figure 2.2 illustrate the qualitative changes in the behaviour of h as the speed of the far-field airflow is increased from zero (i.e. as F is increased from zero).

As mentioned in Section 2.5.1, in classical coating flow h has a maximum at $\theta = \theta_- = 0$ and a minimum at $\theta = -\pi - \theta_- = -\pi$ (i.e. at $\theta = \pi$) (see Figure 2.2(a)). As F is increased from $F = 0$ to $F = 1/2$ both the maximum at $\theta = \theta_-$

$(-\pi/6 < \theta_- < 0)$ and the minimum at $\theta = -\pi - \theta_-$ $(-\pi < -\pi - \theta_- < -5\pi/6)$ (see, for example, the case $F = 3/10$ shown in Figure 2.2(b)) move towards the bottom of the cylinder (i.e. towards $\theta = -\pi/2$), reaching $\theta = -\pi/6$ and $\theta = -5\pi/6$, respectively, when $F = 1/2$. When $F = 1/2$ a point of inflection in h appears at the top of the cylinder (i.e. at $\theta = \theta_+ = \pi - \theta_+ = \pi/2$) (see Figure 2.2(c)). As F is increased from $F = 1/2$ both the maximum at $\theta = \theta_-$ $(-\pi/4 < \theta_- < -\pi/6)$ and the minimum at $\theta = -\pi - \theta_-$ $(-5\pi/6 < -\pi - \theta_- < -3\pi/4)$ continue to move towards the bottom of the cylinder, approaching $\theta = -\pi/4$ and $\theta = -3\pi/4$, respectively, in the limit of a fast far-field airflow, $F \to \infty$. Meanwhile, the point of inflection splits into a minimum at $\theta = \theta_+$ $(\pi/4 < \theta_+ < \pi/2)$ and a maximum at $\theta = \pi - \theta_+$ $(\pi/2 < \pi - \theta_+ < 3\pi/4)$, both of which move away from the top of the cylinder (i.e. away from $\theta = \pi/2$), approaching $\theta = \pi/4$ and $\theta = 3\pi/4$, respectively, in the limit of a fast far-field airflow, $F \to \infty$ (see, for example, the case $F = 1$ shown in Figure 2.2(d)). Moreover, as Figures 2.2–2.4 illustrate, when $K = 0$ the largest maximum and the smallest minimum of h are always located on the lower half of the cylinder. In particular, except in the exceptional situation mentioned in Section 2.5.2 in which it has two corners, the corner in the critical free surface $y = h_{\rm c}$ always occurs at $\theta = \theta_{\rm c} = \theta_-$.

From (2.23) and (2.32) the thickness of the critical film at the corner, $h_{\rm c}(\theta_{\rm c})$, (i.e. the maximum possible thickness of any film for a given value of F) is given explicitly in terms of F by

$$h_{\rm c}(\theta_{\rm c}) = \left(\frac{32\left[1 + (1 + 128F^4)^{1/2}\right]}{\left[3 + (1 + 128F^4)^{1/2}\right]^3} \right)^{1/4}, \tag{2.33}$$

and hence from (2.26) the critical flux is given explicitly in terms of F by

$$Q_{\rm c} = \left(\frac{512\left[1 + (1 + 128F^4)^{1/2}\right]}{81\left[3 + (1 + 128F^4)^{1/2}\right]^3} \right)^{1/4}. \tag{2.34}$$

Figure 2.6 shows a plot of $h_{\rm c}(\theta_{\rm c})$ given by (2.33) as a function of F. In particular, Figure 2.6 shows that $h_{\rm c}(\theta_{\rm c})$ is a monotonically decreasing function of F satisfying

$$h_{\rm c}(\theta_{\rm c}) = 1 - 4F^4 + \mathcal{O}(F^8) \to 1^- \quad \text{as} \quad F \to 0^+ \tag{2.35}$$

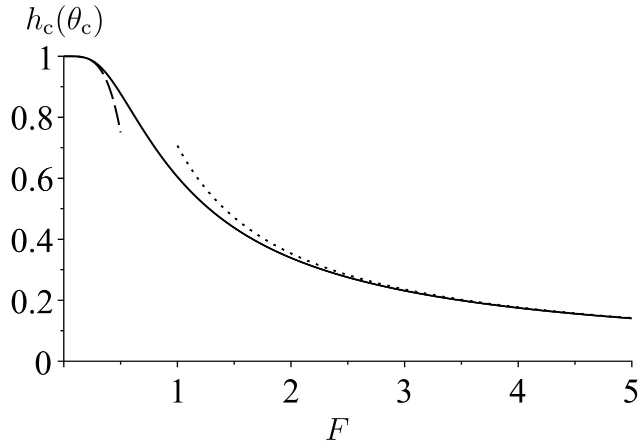

Figure 2.6: Plot of the thickness of the critical film at the corner, $h_c(\theta_c)$, when $K = 0$ given by (2.33) as a function of F. The asymptotic behaviours of $h_c(\theta_c)$ in the limits $F \to 0^+$ given by (2.35) and $F \to \infty$ given by (2.36) are plotted with dashed and dotted lines, respectively.

and

$$h_c(\theta_c) \sim \frac{1}{\sqrt{2F}} \to 0^+ \quad \text{as} \quad F \to \infty. \tag{2.36}$$

At leading order in the limit of a fast far-field airflow, $F \to \infty$, the behaviour of the film is due only to the rotation of the cylinder and the far-field airflow. In this limit the film is very thin, $h = \mathcal{O}(1/F) \ll 1$, and both the flux $Q = \mathcal{O}(1/F) \ll 1$ and the mass $M = \mathcal{O}(1/F) \ll 1$ are correspondingly very small. Thus if we write the leading-order solution as $h(\theta) = \hat{h}(\theta)/F$, $Q = \hat{Q}/F$ and $M = \hat{M}/F$, where hatted quantities are $\mathcal{O}(1)$ in the limit $F \to \infty$, then the rescaled film thickness $\hat{h}$ has the form of the solution for h given in (2.18) with $f = -2\sin 2\theta$, while from (2.15) and (2.17) the rescaled flux $\hat{Q}$ and the rescaled mass $\hat{M}$ are given by

$$\hat{Q} = \hat{h} + \frac{2\hat{h}^3}{3}\sin 2\theta \quad \text{and} \quad \hat{M} = \int_{-\pi}^{\pi} \hat{h}(\theta)\,\mathrm{d}\theta, \tag{2.37}$$

respectively. Figure 2.7 shows plots of contours of $\hat{Q}$ for $0 \le \hat{Q} \le \hat{Q}_c$, with each contour therefore representing the rescaled film thickness $\hat{h}$ for the corresponding value of $\hat{Q}$. As Figure 2.7 shows, the rescaled film thickness $\hat{h}$ has period π, with two identical maxima at $\theta = 3\pi/4$ and $\theta = -\pi/4$, and two identical minima at $\theta = \pi/4$ and $\theta = -3\pi/4$. In particular, as mentioned in Section 2.5.2, the rescaled critical free surface $y = \hat{h}_c(\theta)$ corresponding to $\hat{Q} = \hat{Q}_c = \sqrt{2}/3 \simeq 0.471$ and

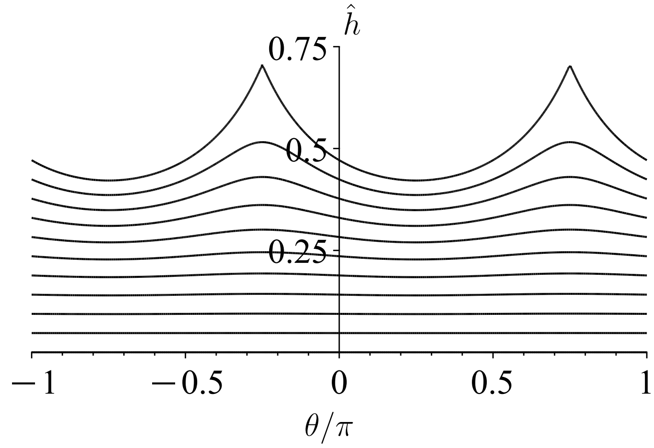

Figure 2.7: Plots of contours of $\hat{Q}$ for $0 \le \hat{Q} \le \hat{Q}_\mathrm{c} = \sqrt{2}/3 \simeq 0.471$, with each contour therefore representing the rescaled film thickness $\hat{h}$ for the corresponding value of $\hat{Q}$. The contour interval is $\hat{Q}_\mathrm{c}/10$.

$\hat{M} = \hat{M}_\mathrm{c} \simeq 3.141$ has two identical corners at $\theta = \theta_\mathrm{c} = 3\pi/4$ and $\theta = \theta_\mathrm{c} = -\pi/4$ at both of which $\hat{h}_\mathrm{c}(\theta_\mathrm{c}) = 1/\sqrt{2} \simeq 0.707$.

2.7 Solutions when the airflow has non-zero circulation ($K \neq 0$)

In this section we use the results obtained thus far to describe the behaviour of the full-film solutions when the airflow has non-zero circulation, corresponding to $K \neq 0$.

In this case, in addition to the pressure gradient due to the far-field airflow described in Section 2.6, the pressure gradient within the film has an additional contribution due to the circulation of the airflow in combination with the far-field airflow, and the additional flux it induces, namely $-(2FKh^3/3)\cos\theta$, either cooperates (when $K > 0$) or competes (when $K < 0$) with the flux due to gravity by driving flow either away from the top and towards the bottom of the cylinder (i.e. away from $\theta = \pi/2$ and towards $\theta = -\pi/2$) when $K > 0$ or *vice versa* when $K < 0$. As might have been anticipated, the presence of non-zero circulation leads to somewhat more complicated behaviour of the film than that in the absence of circulation described in Section 2.6.

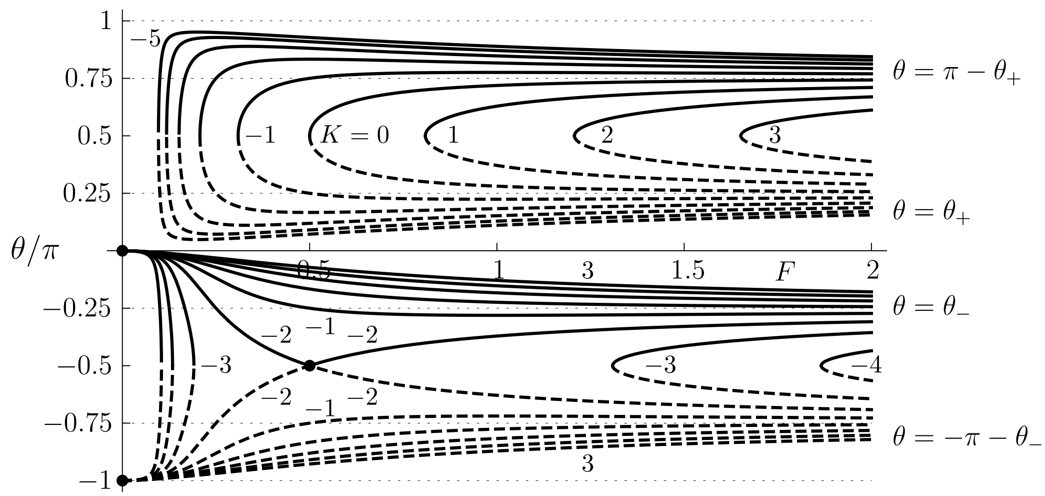

Figure 2.8: Plot of the scaled positions θ/π of the stationary points of h given by (2.39) as functions of F for $K = -5, -4, \ldots, 3$. The positions corresponding to a local maximum and a local minimum of h are plotted with solid lines and dashed lines, respectively.

When $K \neq 0$ it is convenient to introduce the parameter β defined by

$$\beta = \frac{1 + 2FK}{4F^2}, \tag{2.38}$$

which may be regarded as a reduced measure of K, in terms of which it is useful to note that the solution for h is invariant under the simultaneous changes $\theta \to \theta \pm \pi$ and $\beta \to -\beta$ (that is, $K \to -K - (1/F)$), which provides a simple check on the results in what follows.

As described in Section 2.5.1, the positions of the stationary points of h are given by (2.20), which, in terms of the parameter β defined by (2.38), takes the form

$$\sin\theta = \frac{\beta \pm (\beta^2 + 8)^{1/2}}{4}, \tag{2.39}$$

and the nature of each stationary point is again given by the sign of $\pm\cos\theta$. As for equation (2.32) in Section 2.6, we denote the solutions of (2.39) in the interval $-\pi/2 \leq \theta \leq \pi/2$ by $\theta = \theta_+$ $(0 \leq \theta_+ \leq \pi/2)$ and $\theta = \theta_-$ $(-\pi/2 \leq \theta_- \leq 0)$, respectively, where the subscript $\pm$ corresponds to the $\pm$ in (2.39), and in terms of which the solutions of (2.39) are given by $\theta = \theta_+$ and $\theta = \pi - \theta_+$ for $\beta \leq 1$ and $\theta = \theta_-$ and $\theta = -\pi - \theta_-$ for $\beta \geq -1$.

Figure 2.8 shows a plot of the scaled positions θ/π of the stationary points of

h given by (2.39) plotted as functions of F for a range of values of K (including the case $K = 0$ shown in Figure 2.5). The positions corresponding to a local maximum and a local minimum of h are again plotted with solid lines and dashed lines, respectively. In particular, Figure 2.8 shows that the film thickness h has two stationary points when $K < K_1$ and $K > K_3$, three stationary points when $K = K_1$ and $K = K_3$, and four stationary points when $K_1 < K < K_3$, where the critical values $K = K_1$, $K = K_2 = (K_1 + K_3)/2$ and $K = K_3$, corresponding to $\beta = -1$, $\beta = 0$ and $\beta = 1$, respectively, and satisfying $K_1 < K_2 < 0$ and $K_3 > K_2$, are defined by

$$K_1 = -2F - \frac{1}{2F}, \quad K_2 = -\frac{1}{2F} \quad \text{and} \quad K_3 = 2F - \frac{1}{2F}, \tag{2.40}$$

and the positions of these stationary points on the cylinder are again symmetrical about the vertical line $\theta = \pm\pi/2$.

Figure 2.9 shows plots of contours of Q for $0 \leq Q \leq Q_c$, with each contour therefore representing the film thickness h for the corresponding value of Q, for a range of values of F and K. The plots shown in Figure 2.9 illustrate the qualitative changes in the behaviour of h as the speed of the far-field airflow and the circulation are varied (i.e. as F and K are varied).

As Figures 2.9(e)–(g) illustrate, different qualitative changes in the behaviour of h occur on the upper and lower halves of the cylinder as K is increased from $K = K_2$. On the lower half of the cylinder as K is increased from $K = K_2$, the maximum at $\theta = \theta_-$ $(-\pi/4 < \theta_- < 0)$ and the minimum at $\theta = -\pi - \theta_-$ $(-\pi < -\pi - \theta_- < -3\pi/4)$ move away from the bottom of the cylinder (i.e. away from $\theta = -\pi/2$), approaching the right-hand and left-hand sides of the cylinder (i.e. approaching $\theta = 0$ and $\theta = \pi$), respectively, in the limit of a strong anticlockwise circulation $K \to \infty$. Simultaneously, on the upper half of the cylinder as K is increased from $K = K_2$ towards $K = K_3$, the minimum at $\theta = \theta_+$ $(\pi/4 < \theta_+ < \pi/2)$ and the maximum at $\theta = \pi - \theta_+$ $(\pi/2 < \pi - \theta_+ < 3\pi/4)$ move towards the top of the cylinder (i.e. towards $\theta = \pi/2$) (see, for example, the case $F = 3/2$ and $K = 5/6$ shown in Figure 2.9(e)), before merging into a point of inflection at the top of the cylinder when $K = K_3$ (see, for example, the case $F = 1$ and $K = 3/2$ shown in Figure 2.9(f)), and then disappearing (see, for example, the case $F = 1/2$ and $K = 1$ shown in Figure 2.9(g)). Moreover, as Figures 2.9(e)–(g) illustrate, when $K > K_2$ the largest maximum and the smallest minimum of h always occur

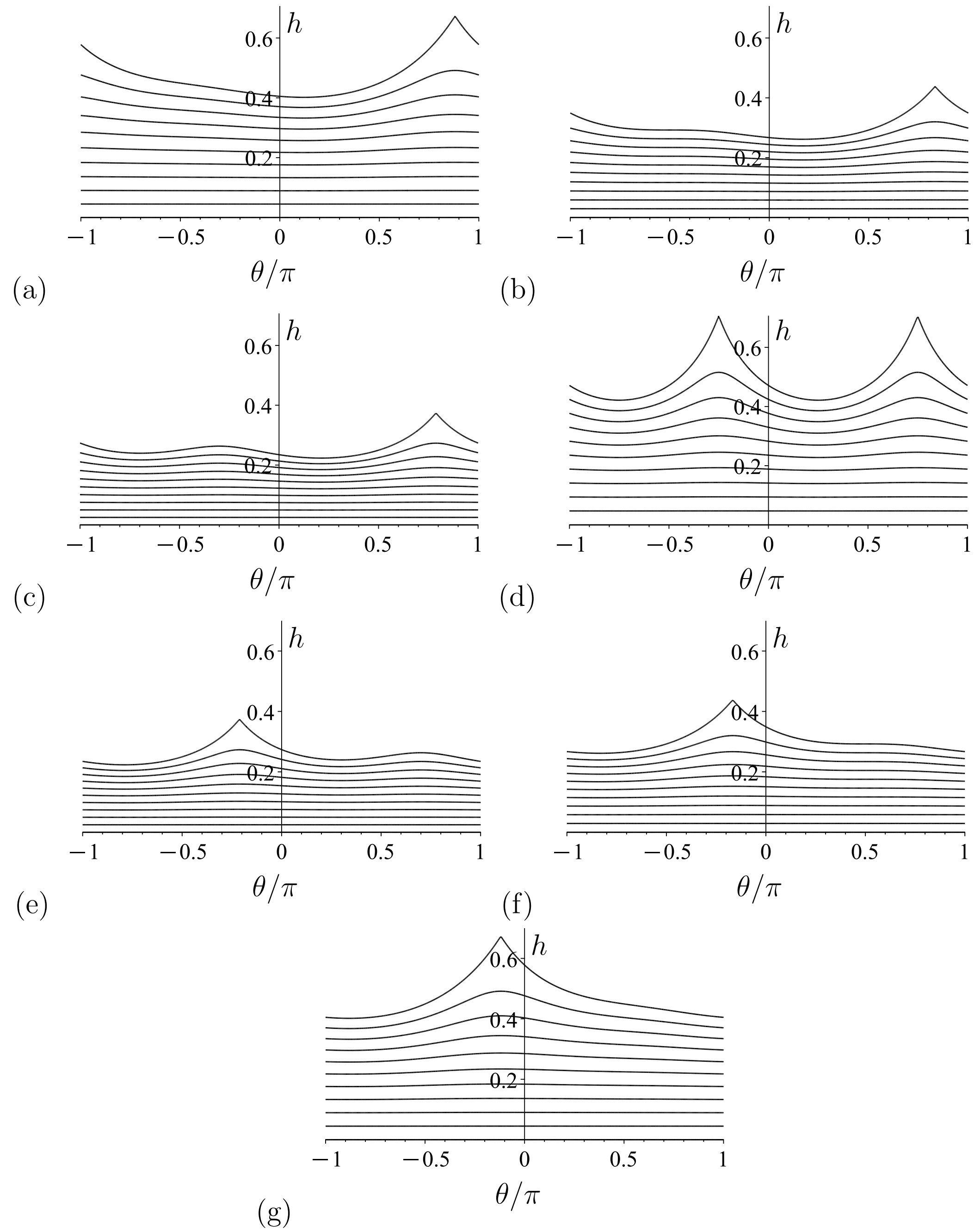

Figure 2.9: Plots of contours of Q for $0 \leq Q \leq Q_{\rm c}$, with each contour therefore representing the film thickness h for the corresponding value of Q, for (a) $F = 1/2$ and $K = -3$ ($\beta = -2$, $\theta_{\rm c} = 0.881\pi$, $Q_{\rm c} \simeq 0.449$, $M_{\rm c} \simeq 2.970$), (b) $F = 1$ and $K = -5/2$ ($\beta = -1$, $\theta_{\rm c} = 0.833\pi$, $Q_{\rm c} \simeq 0.292$, $M_{\rm c} \simeq 1.919$), (c) $F = 3/2$ and $K = -3/2$ ($\beta = -7/18$, $\theta_{\rm c} = 0.789\pi$, $Q_{\rm c} \simeq 0.250$, $M_{\rm c} \simeq 1.628$), (d) $F = 1$, and $K = -1/2$ ($\beta = 0$, $\theta_{\rm c} = 3\pi/4$ and $-\pi/4$, $Q_{\rm c} \simeq 0.471$, $M_{\rm c} \simeq 3.141$), (e) $F = 3/2$ and $K = 5/6$ ($\beta = 7/18$, $\theta_{\rm c} = -0.211\pi$, $Q_{\rm c} \simeq 0.250$, $M_{\rm c} \simeq 1.628$), (f) $F = 1$ and $K = 3/2$ ($\beta = 1$, $\theta_{\rm c} = -\pi/6$, $Q_{\rm c} \simeq 0.292$, $M_{\rm c} \simeq 1.919$), and (g) $F = 1/2$ and $K = 1$ ($\beta = 2$, $\theta_{\rm c} = -0.119\pi$, $Q_{\rm c} \simeq 0.449$, $M_{\rm c} \simeq 2.970$). In each case the contour interval is $Q_{\rm c}/10$.

on the lower half of the cylinder, and the corner in the critical free surface always occurs at $\theta = \theta_c = \theta_-$.

As Figures 2.9(a)–(c) illustrate, analogous qualitative changes in the behaviour of h occur as K is decreased from $K = K_2$. In particular, when $K < K_2$ the largest maximum and the smallest minimum of h always occur on the upper half of the cylinder, and the corner in the critical free surface always occurs at $\theta = \theta_c = \pi - \theta_+$.

The qualitative changes in the behaviour of the film thickness h as F and K are varied are summarised in Figure 2.10, which represents one of the key results of the present chapter. Specifically, Figure 2.10 is a plot of the F–K parameter plane showing how the three curves $K = K_1$, $K = K_2$ and $K = K_3$ given by (2.40) divide the plane into the four regions $K < K_1$, $K_1 < K < K_2$, $K_2 < K < K_3$ and $K > K_3$ in which the behaviour of the film thickness h (typical examples of which are sketched in the insets) is qualitatively different. In addition, the asymptotes of $K = K_1$ and $K = K_3$ as $F \to \infty$, namely $K = \mp 2F$, are plotted with dashed lines. Note that these two straight lines correspond to $\lambda = \kappa/(4\pi a U_\infty) = K/(2F) = \mp 1$ and so, as described in Section 2.3, they also separate the F–K parameter plane into the three regions $K < -2F$, $-2F < K < 2F$ and $K > 2F$ in which the stagnation points of the airflow are directly below the cylinder, on the cylinder, and directly above the cylinder, respectively.

From (2.23) and (2.39) the thickness of the critical film at the corner, $h_c(\theta_c)$, (i.e. the maximum possible thickness of any film for given values of F and K) is given explicitly in terms of F and β by

$$h_c(\theta_c) = \frac{1}{F}\left(\frac{2}{8 + 20\beta^2 - \beta^4 + |\beta|(\beta^2+8)^{3/2}}\right)^{1/4}, \tag{2.41}$$

and hence from (2.26) the critical flux is given explicitly in terms of F and β by

$$Q_c = \frac{2}{3F}\left(\frac{2}{8 + 20\beta^2 - \beta^4 + |\beta|(\beta^2+8)^{3/2}}\right)^{1/4}. \tag{2.42}$$

Note that $\theta_\pm$, θ_c, $Fh_c(\theta_c)$ and FQ_c depend on F and K only via β, and that, in particular, $Fh_c(\theta_c)$ and FQ_c are even functions of β. Figure 2.11 shows a plot of $Fh_c(\theta_c)$ given by (2.41) as a function of β. In particular, Figure 2.11 shows that

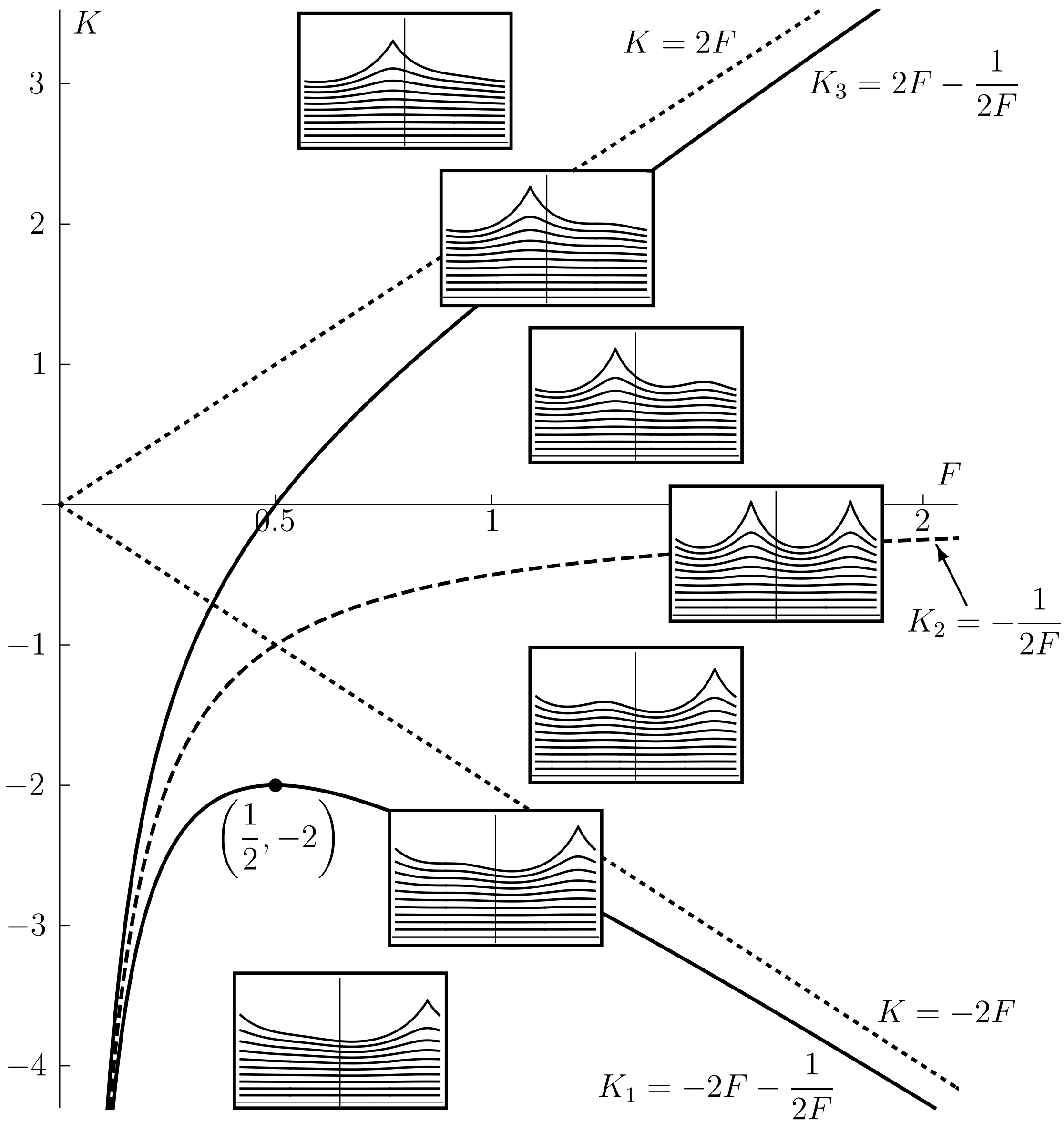

Figure 2.10: Plot of the F–K parameter plane showing how the three curves $K = K_1$, $K = K_2$ and $K = K_3$ given by (2.40) divide the plane into the four regions $K < K_1$, $K_1 < K < K_2$, $K_2 < K < K_3$ and $K > K_3$ in which the behaviour of the film thickness h (typical examples of which are sketched in the insets) is qualitatively different. In addition, the asymptotes of $K = K_1$ and $K = K_3$ as $F \to \infty$, namely $K = \mp 2F$, are plotted with dotted lines.

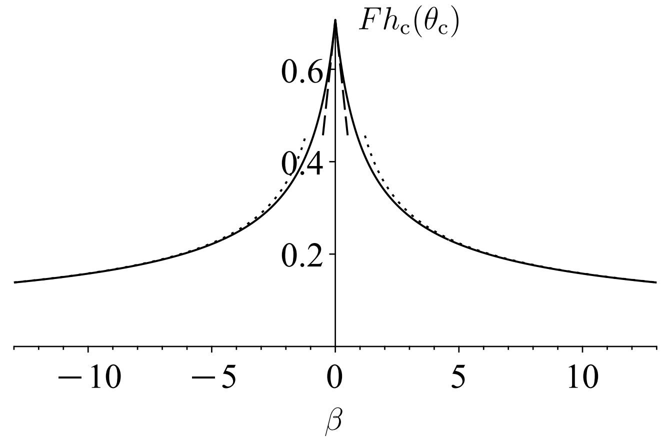

Figure 2.11: Plot of the scaled thickness of the critical film at the corner, $Fh_c(\theta_c)$, given by (2.41) as a function of β. The asymptotic behaviours of $Fh_c(\theta_c)$ in the limits $\beta \to 0^+$ given by (2.43) and $\beta \to \pm\infty$ given by (2.44) are plotted with dashed and dotted lines, respectively.

$Fh_c(\theta_c)$ is a monotonically decreasing function of $|\beta|$ satisfying

$$Fh_c(\theta_c) = \frac{1}{\sqrt{2}} - \frac{1}{2}|\beta| + \mathcal{O}(\beta^2) \to \frac{1}{\sqrt{2}}^{-} \quad \text{as} \quad \beta \to 0 \tag{2.43}$$

and

$$Fh_c(\theta_c) \sim \frac{1}{2\sqrt{|\beta|}} \to 0^+ \quad \text{as} \quad \beta \to \infty. \tag{2.44}$$

As mentioned in Section 2.3, in the special case $FK = -1/2$, corresponding to $K = K_2$ (i.e. $\beta = 0$) the behaviour of the film is due only to the rotation of the cylinder and the far-field airflow. Clearly this situation is closely analogous to that at leading order in the limit of a fast far-field airflow, $F \to \infty$, when $K = 0$ described in Section 2.6. The parameter F (which may now take any non-negative value) may again be scaled out of the problem by writing the solution as $h(\theta) = \hat{h}(\theta)/F$, $Q = \hat{Q}/F$ and $M = \hat{M}/F$, where the solutions for $\hat{h}(\theta)$, $\hat{Q}$ and $\hat{M}$ are given in Section 2.6. In particular, the film thickness h has period π, with two identical maxima at $\theta = 3\pi/4$ and $\theta = -\pi/4$, and two identical minima at $\theta = \pi/4$ and $\theta = -3\pi/4$, and the critical free surface $y = h_c(\theta)$ has two identical corners at $\theta = \theta_c = 3\pi/4$ and $\theta = \theta_c = -\pi/4$ (see, for example, the case $F = 1$ and $K = -1/2$ shown in Figure 2.9(d)).

At leading order in the limit of a strong circulation, $K \to \pm\infty$, the behaviour of the film is due only to the rotation of the cylinder and the circulation of the airflow. In this limit the film is very thin, $h = \mathcal{O}(|K|^{-1/2}) \ll 1$, and both the flux $Q = \mathcal{O}(|K|^{-1/2}) \ll 1$ and the mass $M = \mathcal{O}(|K|^{1/2}) \ll 1$ are correspondingly very small. Thus if we write the leading-order solution as $h(\theta) = \bar{h}(\theta)/(2F|K|)^{1/2}$, $Q = \bar{Q}/(2F|K|)^{1/2}$ and $M = \bar{M}/(2F|K|)^{1/2}$, where barred quantities are $\mathcal{O}(1)$ in the limit $K \to \pm\infty$, then the rescaled film thickness $\bar{h}$ has the form of the solution for h given in (2.18) with $f = \pm\cos\theta$, while from (2.15) and (2.17) the rescaled flux $\bar{Q}$ and the rescaled mass $\bar{M}$ are given by

$$\bar{Q} = \bar{h} \mp \frac{\bar{h}^3}{3}\cos\theta \quad \text{and} \quad \bar{M} = \int_{-\pi}^{\pi} \bar{h}(\theta)\,\mathrm{d}\theta, \tag{2.45}$$

respectively. Thus $\bar{h}(\theta)$, $\bar{Q}$ and $\bar{M}$ are the solutions of the classical coating-flow problem when $K \to \infty$, and the solutions of the mirror image of the classical coating-flow problem in the vertical line $\theta = \pm\pi/2$ (i.e. the solutions of the classical coating-flow problem with the direction of the rotation of the cylinder reversed) when $K \to -\infty$. In particular, the rescaled film thickness $\bar{h}$ has a local maximum at $\theta = 0$ and a local minimum at $\theta = \pi$, and the rescaled critical free surface $y = \bar{h}_{\mathrm{c}}(\theta)$ corresponding to $\bar{Q} = \bar{Q}_{\mathrm{c}} = 2/3$ and $\bar{M} = \bar{M}_{\mathrm{c}} \simeq 4.443$ has a corner at $\theta = \theta_{\mathrm{c}} = 0$ at which $\bar{h}_{\mathrm{c}}(\theta_{\mathrm{c}}) = 1$ when $K \to \infty$, and the mirror image of this behaviour when $K \to -\infty$.

2.8 The mass of fluid on the cylinder

Figure 2.12(a) shows a plot of the mass M of fluid on the cylinder when $K = 0$ given by (2.17) as a function of Q for $0 \le Q \le Q_{\mathrm{c}}$ for a range of values of F, showing that M increases monotonically (almost linearly) with Q. Since, as Figure 2.12(a) shows, M depends only rather weakly on F, Figure 2.12(b) shows a plot of the difference $M - M_0$ between M when $K = 0$ and the mass of fluid in the absence of an airflow (i.e. in the corresponding classical coating-flow problem), denoted by M_0, also as a function of Q for a range of values of F. In both parts of Figure 2.12, the dots denote the values of the critical mass $M = M_{\mathrm{c}}$ at the critical flux $Q = Q_{\mathrm{c}}$ above which there is no full-film solution. In particular, note that the asymptotic solution for M in the regime $Q \ll 1$ given in (2.30) provides excellent approximations to both M and $M - M_0$, namely

$$M \sim 2\pi Q \quad \text{and} \quad M - M_0 \sim \frac{4\pi}{3}\left[(1 + 2FK)^2 + 4F^4 - 1\right] Q^5, \tag{2.46}$$

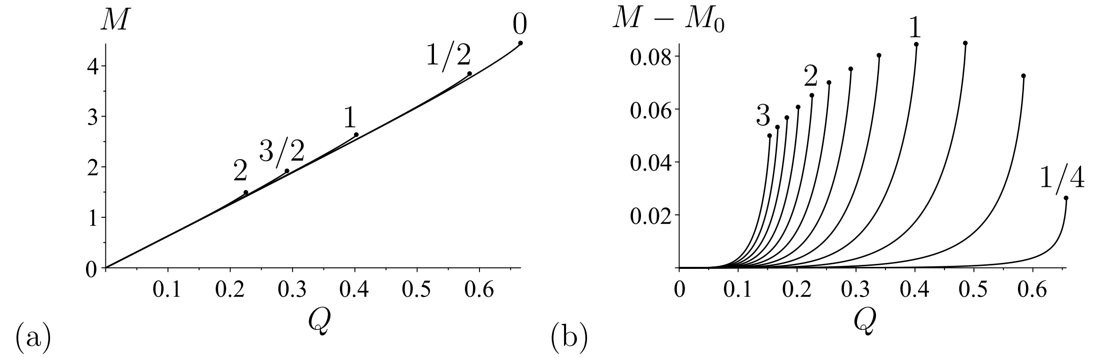

Figure 2.12: (a) Plot of the mass M of fluid on the cylinder when $K = 0$ given by (2.17) as a function of Q for $0 \leq Q \leq Q_{\mathrm{c}}$ for $F = 0$, $1/2$, 1, $3/2$, 2. (b) Plot of the difference $M - M_0$ between M when $K = 0$ and the mass of fluid in the absence of an airflow, M_0, as a function of Q for $F = 0$, $1/4$, $1/2$, $\ldots$, 3. In both parts of the figure, the dots denote the values of $M = M_{\mathrm{c}}$ at $Q = Q_{\mathrm{c}}$ above which there is no full-film solution.

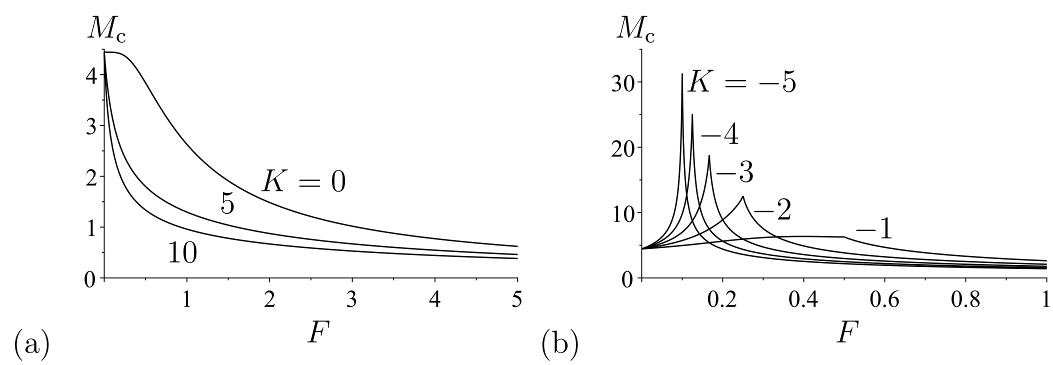

Figure 2.13: Plot of the critical mass of fluid on the cylinder, M_{c}, given by (2.27) as a function of F for (a) $K = 0$, 5, 10 and (b) $K = -5$, -4, $\ldots$, -1.

over the entire range of values of Q (i.e. for $0 \leq Q \leq Q_{\mathrm{c}}$).

Figures 2.13 and 2.14 show plots of the critical mass of fluid on the cylinder, M_{c}, given by (2.27) as a function of F for a range of values of K and as a function of K for a range of values of F, respectively. Figures 2.13 and 2.14 show that when $K \geq 0$, M_{c} decreases monotonically with F and K (i.e. the maximum mass of fluid that can be supported on the cylinder is always less than that in classical coating flow), but that when $K < 0$, M_{c} increases monotonically to a corner at $FK = -1/2$ at which $M_{\mathrm{c}} \simeq 3.141/F \simeq 6.282(-K)$, before decreasing monotonically to zero (i.e. the maximum mass of fluid that can be supported on the cylinder can be greater than that in classical coating flow).

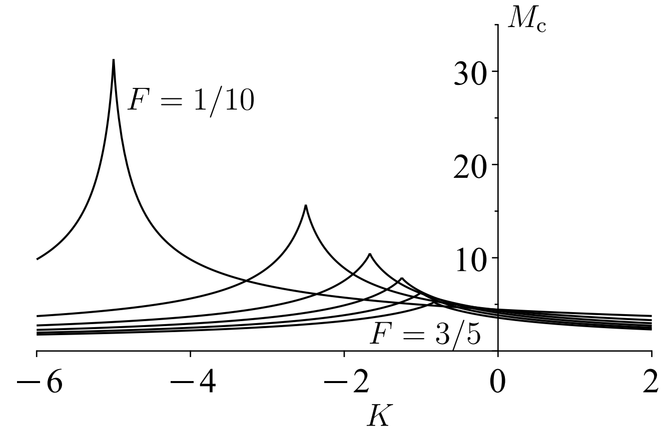

Figure 2.14: Plot of the critical mass of fluid on the cylinder, M_c, given by (2.27) as a function of K for $F = 1/10$, $1/5$, ..., $3/5$.

2.9 Stability

The stability of the steady two-dimensional full-film solutions obtained in the present work to both two-dimensional and three-dimensional (i.e. axial) disturbances is of considerable interest. As discussed in Section 1.2 and 1.3, the study by Newell and Viljoen [118] concluded that for long times, the film can grow without bound for certain values of their non-dimensional airflow parameters. In Chapter 3 we shall revisit the analysis of Newell and Viljoen [118] and show that their analysis is largely incorrect due to a number of errors in their calculations.

A full stability analysis of the present steady solutions is outside the scope of the present work, but, as we shall now show, the analysis of O'Brien [122] can be generalised to show that the present subcritical full-film solutions are neutrally stable to two-dimensional disturbances.

Considering the kinematic condition given by (1.12) and perturbing around any of the present steady full-film solutions with a small perturbation with growth rate s of the form $\phi(\theta)\exp(st)$ and linearising yields the equation

$$(1 - h^2 f)\phi' + [s - (h^2 f)']\phi = 0. \tag{2.47}$$

Solving (2.47) by using an integrating factor given by

$$\eta = \exp\left(\int \frac{s - (h^2 f)'}{1 - h^2 f}\, \mathrm{d}\theta\right) \tag{2.48}$$

yields the solution

$$\phi \propto \frac{1}{1-h^2 f} \exp\left(-s \int \frac{1}{1-h^2 f} \mathrm{d}\theta\right). \tag{2.49}$$

Since, as previously remarked, the present subcritical full-film solutions satisfy $h^2 f < 1$, the integrand in (2.49) is positive, and so, since ϕ must be 2π-periodic in θ, we deduce that the growth rate s must be purely imaginary, i.e. the present subcritical full-film solutions are neutrally stable to two-dimensional disturbances. This is, of course, only a rather limited result, but it at least provides a starting point for future work on the stability of the present steady solutions for coating flow in the presence of an airflow.

2.10 Conclusions

In Chapter 2 we undertook a detailed analysis of steady coating flow in the presence of an irrotational airflow with circulation and showed that the presence of the airflow can result in qualitatively different behaviour of the fluid film from that in classical coating flow. We found that, as in classical coating flow, full-film solutions are possible only when the flux Q and mass M of fluid do not exceed critical values Q_{c} and M_{c}, which we determined in terms of the parameters F and K representing the speed of the far-field airflow and the circulation of the airflow, respectively. In particular, equations (2.34) and (2.42) are explicit expressions for Q_{c} in the special case of no circulation $K = 0$ and in the general case of non-zero circulation $K \neq 0$, respectively.

The qualitative changes in the behaviour of the film thickness as F and K are varied are summarised in Figure 2.10 and illustrated in Figure 2.15. Specifically, Figure 2.10 shows how the three curves $K = K_1$, $K = K_2$ and $K = K_3$ given by (2.40) divide the F–K parameter plane into the four regions $K < K_1$, $K_1 < K < K_2$, $K_2 < K < K_3$ and $K > K_3$ in which the behaviour of the film thickness is qualitatively different. In particular, the film thickness can have as many as four stationary points and, in general, has neither top-to-bottom nor right-to-left symmetry (in contrast to two stationary points and top-to-bottom symmetry in classical coating flow). It should be noted that the behaviour summarised in Figure 2.10 is qualitatively different from that in the corresponding problem of coating flow in the presence of a uniform shear stress on the free surface of the film, in which the film thickness only ever has two stationary points. In addition, when the circulation of the airflow is anticlockwise (i.e. in the same direction as the rotation of the cylinder) the maximum mass of fluid that can be supported on the cylinder is always less than that in classical coating flow, whereas when the circulation is clockwise the maximum mass of fluid can be greater than that in classical coating flow. However, whatever the speed of the far-field airflow and the circulation of the airflow (i.e. whatever the values of F and K), the azimuthal velocity of the film is always in the direction of the rotation of the cylinder.

Figure 2.15 shows examples of both critical and subcritical free surfaces on the rotating cylinder, including three examples with one corner in the critical free surface (Figures 2.15(a)–(c)) and one example in the special case $FK = -1/2$ with two corners in the critical free surface (Figures 2.15(d)), and examples for which the critical flux Q_{c} and the critical mass M_{c} are larger (Figures 2.15(b, d)) and smaller (Figure 2.15(c)) than the critical flux $Q_{\mathrm{c}} = 2/3$ and the critical mass $M_{\mathrm{c}} = 4.443$ for classical coating flow (Figure 2.15(a)).

In the present work we assumed that, since the film is thin, the airflow is unaffected by the presence of the film. In reality, this will not always be the case. For example, as discussed in Section 1.2, the numerical investigation of a thin rivulet of viscous fluid on a stationary cylinder in the presence of an airflow by Taylor and Robertson [163] showed that the presence of the rivulet on the upper half of the cylinder can deflect the corresponding boundary layer further from the horizontal centre line of the cylinder, which reduces the interaction between the boundary layers in the wake in the downstream side of the cylinder, and in particular, reduces the formation of vortices. However, this is beyond the scope of the current work and determining the influence of the shape of the film on the airflow remains an open problem.

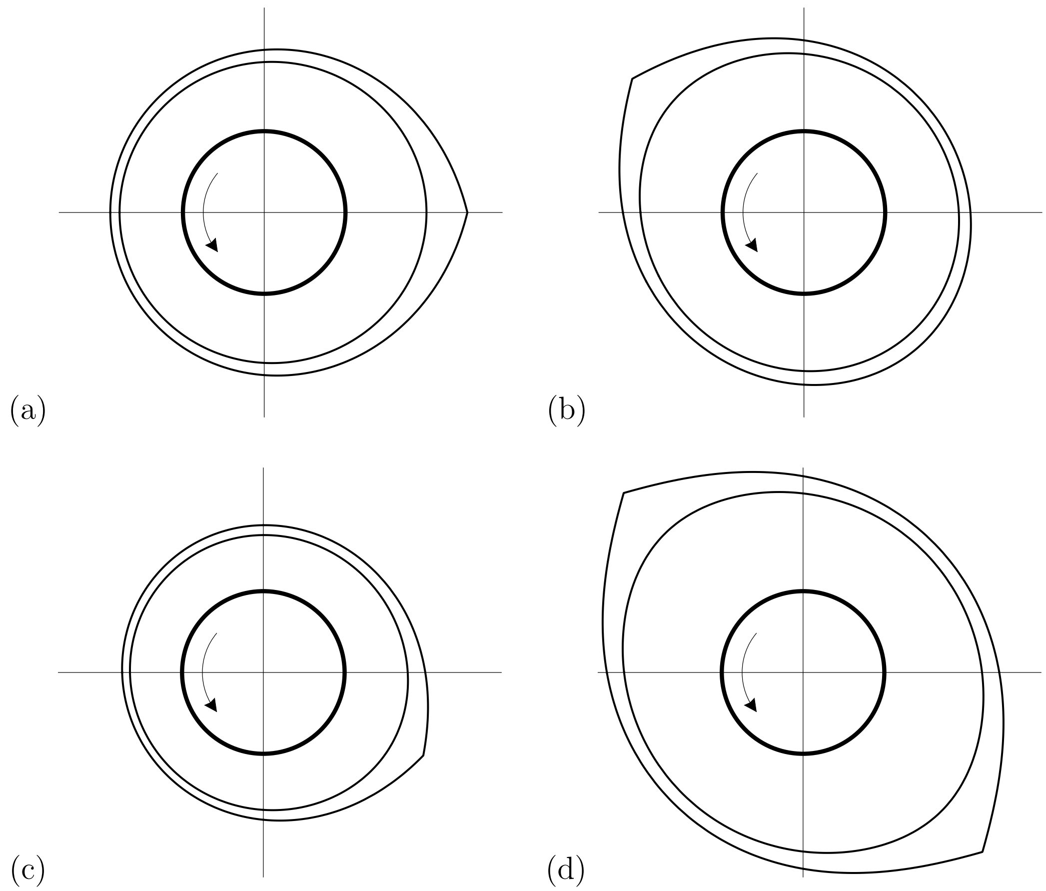

Figure 2.15: Examples of both critical and subcritical free surfaces on the rotating cylinder, for (a) $F = 0$ and $K = 0$ (i.e. classical coating flow) ($\theta_{\mathrm{c}} = 0$, $Q_{\mathrm{c}} = 2/3$, $M_{\mathrm{c}} \simeq 4.443$), (b) $F = 1/2$ and $K = -7/5$ ($\theta_{\mathrm{c}} \simeq 0.790\pi$, $Q_{\mathrm{c}} \simeq 0.745$, $M_{\mathrm{c}} \simeq 4.859$), (c) $F = 1/2$ and $K = 1/4$ ($\theta_{\mathrm{c}} \simeq -0.152\pi$, $Q_{\mathrm{c}} \simeq 0.541$, $M_{\mathrm{c}} \simeq 3.559$), and (d) $F = 1/2$ and $K = -1$ ($\theta_{\mathrm{c}} = 3\pi/4$ and $-\pi/4$, $Q_{\mathrm{c}} \simeq 0.943$, $M_{\mathrm{c}} \simeq 6.283$), with $Q = Q_{\mathrm{c}}$ and $Q = 0.85Q_{\mathrm{c}}$ in each case. All of the parts of the figure are drawn on the same scale, but, for clarity the thicknesses of the fluid films are exaggerated.

Chapter 3

Unsteady coating flow of a thin film subject to an irrotational airflow

3.1 Introduction

In this chapter we investigate the unsteady two-dimensional coating flow of an initially uniform thin film of fluid on the outside of a rotating horizontal cylinder in the presence of surface-tension effects and a non-uniform pressure, given by (1.43), due to an external irrotational airflow with circulation.

As discussed in Section 1.3, Hinch and Kelmanson [61] analysed the corresponding problem in the absence of an external airflow in the case in which the effects of gravity and surface tension are weak compared with those of viscous shear. In particular, they showed that at very large times the asymptotic solution (1.64) decays to a steady state in which the thickness of the film exhibits a gravity-induced phase lag relative to the solid cylinder of the form (1.58). Also discussed in Section 1.2 and 1.3, was the investigation by Newell and Viljoen [118] who, motivated by the application of the operation of a novel rotary pesticide applicator for crops, extended the analysis of Hinch and Kelmanson [61] to include the effects of an irrotational airflow passing over the cylinder. Newell and Viljoen [118] incorrectly concluded that the film is conditionally unstable. In this chapter we begin by correcting the analysis of Newell and Viljoen [118] to show that the film is in fact unconditionally stable, followed by a description of the evolution of the initially uniform film.

3.2 Problem Formulation

We return to the problem described in Section 2.2 and sketched in Figure 2.1. In particular, solving (1.24) subject to (2.6) implies that the pressure is independent of y so that $p = p(\theta, t)$ is given by (2.6) throughout the film. We begin by rewriting the pressure in the film (2.6) and the flux $Q = Q(\theta, t)$ given by (2.8) in dimensional variables, so that

$$p^* = p^*_\infty + \frac{\sigma^*}{a^*} - \frac{\sigma^*}{a^{*2}}\left(\frac{\partial^2 h^*}{\partial \theta^2} + h^*\right) + \frac{\rho^*_{\mathrm{a}}}{2}\left[U^{*2}_\infty - \left(2U^*_\infty \sin\theta - \frac{\kappa^*}{2\pi a^*}\right)^2\right] \tag{3.1}$$

and

$$Q^* = a^*\Omega^* h^* - \frac{h^{*3}}{3\mu^*}\left(\rho^* g^* \cos\theta + \frac{1}{a^*}\frac{\partial p^*}{\partial \theta}\right), \tag{3.2}$$

respectively. In this chapter, we will again non-dimensionalise (3.1) and (3.2) with (2.3), however, in order to be consistent with Hinch and Kelmanson [61] and Newell and Viljoen [118], so that we may easily compare equations and results, we redefine the characteristic film thickness H to be given by the (constant) average film thickness so that now

$$H^* = \frac{1}{2\pi}\int_0^{2\pi} h^*(\theta, t^*)\mathrm{d}\theta \tag{3.3}$$

and, in addition to the parameters F and K defined by (2.12), we also use the parameters γ given by (1.59) and $\hat{\alpha}$ given by (1.62), which satisfy the regime (1.63). Hence, the pressure (3.1) becomes

$$p = -\frac{\hat{\alpha}}{\gamma}\left(\frac{\partial^2 h}{\partial \theta^2} + h\right) + \frac{F^2}{2} - \frac{1}{2}\left(2F\sin\theta - K\right)^2, \tag{3.4}$$

and the flux (3.2) becomes

$$Q = h - \gamma h^3\left(\cos\theta + \frac{\partial p}{\partial \theta}\right), \tag{3.5}$$

that is,

$$Q = h - \gamma h^3 \cos\theta + \hat{\alpha} h^3 \frac{\partial}{\partial\theta}\left(\frac{\partial^2 h}{\partial\theta^2} + h\right) - 2\gamma F h^3 \left(K\cos\theta - F\sin 2\theta\right), \qquad (3.6)$$

and hence from the kinematic condition given by (1.12), the governing evolution equation takes the form

$$\frac{\partial h}{\partial t} + \frac{\partial}{\partial\theta}\left[h - \gamma h^3 \cos\theta + \hat{\alpha} h^3 \frac{\partial}{\partial\theta}\left(\frac{\partial^2 h}{\partial\theta^2} + h\right) - 2\gamma F h^3 (K\cos\theta - F\sin 2\theta)\right] = 0. \qquad (3.7)$$

The evolution equation (3.7) is to be solved subject to periodicity conditions on h and its derivatives, and an initial condition specifying $h(\theta, 0)$.

In the special case of no far-field airflow, $F = 0$, the parameter K appears in (3.4) only in a constant contribution $-K^2/2$ to p, and does not appear in (3.6) or (3.7), showing that the evolution of the film is unaffected by a purely circulatory airflow.

Equation (3.7) is invariant under the transformation

$$\theta \to \theta + \pi, \quad K \to -\left(K + \frac{1}{F}\right) \qquad (F > 0), \qquad (3.8)$$

showing that if a free-surface profile $h(\theta, t)$ is a solution of (3.7) corresponding to a given value of the circulation K then the phase-shifted profile $h(\theta + \pi, t)$ is a solution corresponding to the circulation $-[K + (1/F)]$. Moreover, although equation (3.7) involves all four of the parameters $\hat{\alpha}$, F, K, and γ, for $F \neq 0$ it may be reduced to the form

$$\frac{\partial h}{\partial t} + \frac{\partial}{\partial\theta}\left[h - \hat{\gamma}\beta h^3 \cos\theta + \hat{\alpha} h^3 \frac{\partial}{\partial\theta}\left(\frac{\partial^2 h}{\partial\theta^2} + h\right) + \frac{1}{2}\hat{\gamma} h^3 \sin 2\theta\right] = 0, \qquad (3.9)$$

involving only $\hat{\alpha}$, β defined by (2.38) and $\hat{\gamma}$ defined by

$$\hat{\gamma} = 4F^2\gamma, \qquad (3.10)$$

which may be regarded as a reduced measure of γ, (and we note that, as mentioned in Section 2.7, the transformation of K in (3.8) corresponds simply to $\beta \to -\beta$). Despite this reduction in the number of parameters, it is usually more convenient to use the evolution equation in its original form (3.7), because (3.9) obscures somewhat the dependence of the film flow on the original parameters F and K of the airflow; in particular, (3.7) makes the comparison between our analysis and that of Hinch and Kelmanson [61] in the case $F = K = 0$ more transparent. However, the reduced form (3.9) is useful when the dependence of results on $\hat{\alpha}$ is being discussed.

In the absence of the airflow, $F = K = 0$, equation (3.7) reduces to equation (3.14) of Pukhnachev [137], whose parameters μ and χ are related to $\hat{\alpha}$ and γ by $\mu = 3\gamma$ and $\chi = 3\hat{\alpha}$. Moreover, equations (3.4)–(3.7) reduce to the leading-order versions of equations (35), (52), and (54), respectively, of Evans, Schwartz, and Roy [42], whose parameters Bo and U_Ω are related to $\hat{\alpha}$ and γ by $\mathrm{Bo} = \gamma\bar{h}/(\hat{\alpha}a)$ and $U_\Omega = 1/(3\gamma)$, and to equation (2.13) of Lopes, Thiele, and Hazel [94], whose parameters Ω_λ and Bo_λ are related to $\hat{\alpha}$ and γ by $\Omega_\lambda = 1/(3\gamma)$ and $Bo_\lambda = \gamma/\hat{\alpha}$. Note that the terms in the pressure p in equations (2.2) and (2.3) of Hinch and Kelmanson [61] have the opposite signs from those in (3.2) and (3.1), but this is of no consequence because these differences in sign cancel out in their evolution equation (2.4) (which is identical to the present (3.7) with $F = K = 0$) on which all of their subsequent analysis is based. All of the results in the present work obtained from (3.7) agree with those of Hinch and Kelmanson [61] in the absence of the airflow.

For flow in the presence of the airflow, $F \neq 0$, equations (3.4) and (3.6) reduce to equations (2.11) and (2.15), respectively in the case of steady flow in the absence of capillarity, $\hat{\alpha} = 0$, with $\gamma = 1/3$.

Newell and Viljoen [118] investigated the particular case $\kappa^* = 2\pi a^{*2}\Omega^*$, while allowing U^*_∞ to take values in the range $-a^*\Omega^* \leq U^*_\infty \leq a^*\Omega^*$. Note, however, that, irrespective of whether or not a particular choice of κ^* is made, there are two free parameters associated with the airflow, namely F and K in the present notation, or correspondingly the parameters w and φ in the notation of Newell and Viljoen [118], which are related to F and K by $w = F/K$ and $\varphi = 2K^2$; in the case $\kappa^* = 2\pi a^{*2}\Omega^*$, i.e.

$$w = \frac{F}{K} = \frac{U^*_\infty}{a^*\Omega^*}, \quad \varphi = 2K^2 = \frac{2\rho^*_{\mathrm{a}} a^* \Omega^{*2}}{\rho^* g^*} \, (\geq 0) \tag{3.11}$$

in the present notation. Note that Newell and Viljoen [118] omitted the factor 2 from the definition of their parameter φ, but this appears to be simply a typographical error.

As mentioned in Section 2.9 the work of Newell and Viljoen [118] contains a number of errors. Primarily, Newell and Viljoen [118] (evidently following Hinch and Kelmanson [61]) have the opposite signs on p in their equations (5) and (6) from those in the present (3.2) and (3.1), but unfortunately, unlike for Hinch and Kelmanson [61], these differences in sign do *not* cancel out in their evolution equation (7) (i.e. their version of the present equation (3.7)), leading to their (7) having the incorrect sign on the term due to the airflow, i.e. the term involving their parameter φ. However, as we shall show in what follows, obtaining the correct description of the behaviour of the film is *not* simply a matter of reversing the sign of the term due to the airflow in the analysis of Newell and Viljoen [118].

3.3 Evolution of the film thickness

In this section we correct the asymptotic analysis of Newell and Viljoen [118], who, as we have already described, sought to extend the analysis of Hinch and Kelmanson [61] to include the effect of the airflow.

Hinch and Kelmanson [61] considered the case $\gamma \ll 1$ and $\hat{\alpha} \ll 1$ (in the absence of the airflow, $F = K = 0$), and showed that the film evolves on four different timescales, and they posited a two-timescale expansion of the film thickness to reveal the structure of this evolution. Specifically, as discussed in Section 1.3, Hinch and Kelmanson [61] analysed the evolution of an initially uniform film (so that $h(\theta, 0) = 1$) in the regime (1.63) by seeking a solution of (3.7) with $F = 0$ for h as an expansion in powers of γ:

$$h = 1 + \gamma\psi_1 + \gamma^2\psi_2 + \gamma^3\psi_3 + \mathcal{O}(\gamma^4), \tag{3.12}$$

where the $\psi_i = \psi_i(\theta, t_0, t_1)$ depend on the two timescales $t_0 = t$ and $t_1 = \gamma^2 t$, so that $\partial\psi_i/\partial t = \partial\psi_i/\partial t_0 + \gamma^2\partial\psi_i/\partial t_1$, and the asymptotic solution (3.12) is uniformly valid only for $t < \mathcal{O}(\gamma^{-2})$. Note that the ψ_i satisfy the initial conditions $\psi_i(\theta, 0, 0) = 0$.

Based on the observation that the film thickness h in the absence of the airflow is only weakly dependent on $\hat{\alpha}$, Hinch and Kelmanson [61] make the point that, despite the formal restrictions on $\hat{\alpha}$ in (1.63), in practice their analysis is valid for $\hat{\alpha}$ as large as $\mathcal{O}(1)$. For the present purposes, the main result of Hinch and Kelmanson [61] is that the growth rate of the film thickness s_1 given by (1.61) which again, for $\hat{\alpha} > 0$, is clearly negative, showing that the solution (1.64) is stable in the sense that it decays to a steady state at very large times, and for $\hat{\alpha} = 0$ is clearly zero, showing that the solution (1.64) is neutrally stable in the absence of capillarity. We adopt the same approach to the problem in the presence of the airflow by analysing the evolution equation (3.7) for the film with $F \neq 0$, and, in particular, we obtain the corresponding expression for the growth rate s_1, to understand how the presence of the airflow affects the evolution of the film. On the assumption that in the presence of the airflow the film thickness h is again only weakly dependent on $\hat{\alpha}$, we follow Hinch and Kelmanson [61] and Newell and Viljoen [118] and allow $\hat{\alpha}$ to be as large as $\mathcal{O}(1)$.

Some of the algebraic manipulations involved in obtaining the analytical results presented in the next three subsections are rather lengthy, and so as a check on the accuracy of our results we implemented the entire calculation in two independent ways using the symbolic computational systems Maple [95] and Mathematica [182]. Two simple but important checks on the validity of the present analysis are that in the absence of the airflow, $F = K = 0$, the results obtained reduce to those of Hinch and Kelmanson [61], and that under the transformation (3.8) the free-surface profile $h(\theta, t)$ becomes the phase-shifted profile $h(\theta + \pi, t)$.

3.3.1 Solution for ψ_1

Substituting (3.12) into (3.7) yields

$$\mathcal{L}\psi_1 = -(1 + 2KF)s_{1,0} - 4F^2 c_{2,0} \tag{3.13}$$

at $\mathcal{O}(\gamma)$, where the linear operator $\mathcal{L}$, introduced by Hinch and Kelmanson [61], is defined by

$$\mathcal{L} = \frac{\partial}{\partial t_0} + \frac{\partial}{\partial \theta} + \hat{\alpha}\left(\frac{\partial^4}{\partial \theta^4} + \frac{\partial^2}{\partial \theta^2}\right), \tag{3.14}$$

and $c_{i,j}$ and $s_{i,j}$ are defined by $c_{i,j} = \cos(i\theta - jt_0)$ and $s_{i,j} = \sin(i\theta - jt_0)$. As Hinch and Kelmanson [61] describe, 2π-periodic solutions $\Psi(\theta, t_0, t_1)$ of the equation $\mathcal{L}\Psi = 0$ are of the form

$$\Psi(\theta, t_0, t_1) = \sum_{n=1}^{\infty} \left[A_n(t_1)c_{n,n} + B_n(t_1)s_{n,n}\right] \exp\left[-n^2(n^2 - 1)\hat{\alpha}t_0\right], \tag{3.15}$$

where $A_n(t_1)$ and $B_n(t_1)$ are arbitrary functions of t_1, showing that the nth harmonics $c_{n,n}$ and $s_{n,n}$ $(n = 2,\ 3,\ 4,\ \dots)$ decay exponentially quickly on the fast timescale $\hat{\alpha}t_0$, but that the fundamental $(n = 1)$ modes $c_{1,1}$ and $s_{1,1}$ can decay only slowly via the functions $A_1(t_1)$ and $B_1(t_1)$ on the timescale $t_1 = \gamma^2 t_0$.

The solution of (3.13) is of the form

$$\begin{aligned}\psi_1 = \sum_{n=1}^{\infty} \left[A_{1n}(t_1)c_{n,n} + B_{1n}(t_1)s_{n,n}\right] \exp\left[-n^2(n^2-1)\hat{\alpha}t_0\right] \\ + (1+2KF)c_{1,0} - \frac{2F^2}{1+36\hat{\alpha}^2}(s_{2,0} + 6\hat{\alpha}c_{2,0}),\end{aligned} \tag{3.16}$$

where the $A_{1n}(t_1)$ and $B_{1n}(t_1)$ are required by the initial condition $\psi_1(\theta, 0, 0) = 0$ to satisfy

$$\begin{aligned}
&A_{11}(0) = -(1+2KF), && B_{11}(0) = 0, \\
&A_{12}(0) = \frac{12F^2\hat{\alpha}}{1+36\hat{\alpha}^2}, && B_{12}(0) = \frac{2F^2}{1+36\hat{\alpha}^2}, \\
&A_{1n}(0) = 0, && B_{1n}(0) = 0 \qquad \text{for} \quad n = 3, 4, 5, \dots.
\end{aligned} \tag{3.17}$$

Since the contributions from the higher modes $(n \geq 2)$ are non-negligible only for small times, we may replace $A_{1n}(t_1)$ and $B_{1n}(t_1)$ with $A_{1n}(0)$ and $B_{1n}(0)$ for $n \geq 2$ (but not for $n = 1$). Thus (3.16) becomes, with the subscripts omitted from A_{11} and B_{11} for clarity,

$$\begin{aligned}\psi_1 = A(t_1)c_{1,1} + B(t_1)s_{1,1} + (1+2KF)c_{1,0} \\ - \frac{2F^2}{1+36\hat{\alpha}^2}\Big[(s_{2,0} + 6\hat{\alpha}c_{2,0}) - (s_{2,2} + 6\hat{\alpha}c_{2,2})\exp(-12\hat{\alpha}t_0)\Big],\end{aligned} \tag{3.18}$$

where, from (3.17), $A(t_1)$ and $B(t_1)$ satisfy $A(0) = -(1+2KF)$ and $B(0) = 0$. In Section 3.3.3 we shall determine A and B by considering secular terms at $\mathcal{O}(\gamma^3)$.

Note that the solution for ψ_1 given by (3.18) is in agreement with the solution for ψ_1 given by equations (9) and (10) of Newell and Viljoen [118]; also in the absence of the airflow, $F = K = 0$, it reduces to the solution for ψ_1 in Hinch and Kelmanson [61] given by the $\mathcal{O}(\gamma)$ term in (1.64).

Since modes with $n \geq 2$ decay exponentially quickly on the timescale t_0, henceforth we follow Hinch and Kelmanson [61] and Newell and Viljoen [118] in dropping them when we consider higher-order terms in γ.

3.3.2 Solution for ψ_2

At $\mathcal{O}(\gamma^2)$ equation (3.7) gives

$$\begin{aligned}\mathcal{L}\psi_2 = &-\frac{3F^2\big\{\big[A(t_1)-6\hat{\alpha}B(t_1)\big]c_{1,-1}-\big[6\hat{\alpha}A(t_1)+B(t_1)\big]s_{1,-1}\big\}}{1+36\hat{\alpha}^2}\\ &-\frac{6F^2\big(1+2KF\big)\big(c_{1,0}-6\hat{\alpha}s_{1,0}\big)}{1+36\hat{\alpha}^2}-3\big(1+2KF\big)^2s_{2,0}\\ &+3\big(1+2KF\big)\big[B(t_1)c_{2,1}-A(t_1)s_{2,1}\big]-\frac{18F^2\big(1+2KF\big)\big[c_{3,0}-6\hat{\alpha}s_{3,0}\big]}{1+36\hat{\alpha}^2}\\ &-\frac{9F^2\big\{\big[A(t_1)+6\hat{\alpha}B(t_1)\big]c_{3,1}-\big[6\hat{\alpha}A(t_1)-B(t_1)\big]s_{3,1}\big\}}{1+36\hat{\alpha}^2}\\ &+\frac{24F^4\big[12\hat{\alpha}c_{4,0}+\big(1-36\hat{\alpha}^2\big)s_{4,0}\big]}{\big(1+36\hat{\alpha}^2\big)^2}.\end{aligned} \tag{3.19}$$

The solution of (3.19) may be written as a sum $\psi_2 = \psi_{2\mathrm{s}} + \psi_{2\mathrm{u}}$ of a steady part $\psi_{2\mathrm{s}}$ and an unsteady part $\psi_{2\mathrm{u}}$, where

$$\begin{aligned}\psi_{2\mathrm{s}} = &-\frac{6F^2\big(1+2KF\big)\big(6\hat{\alpha}c_{1,0}+s_{1,0}\big)}{1+36\hat{\alpha}^2}+\frac{3\big(1+2KF\big)^2\big(c_{2,0}-6\hat{\alpha}s_{2,0}\big)}{2\big(1+36\hat{\alpha}^2\big)}\\ &-\frac{6F^2\big(1+2KF\big)\big[30\hat{\alpha}c_{3,0}+(1-144\hat{\alpha}^2)s_{3,0}\big]}{\big(1+36\hat{\alpha}^2\big)\big(1+576\hat{\alpha}^2\big)}\\ &-\frac{6F^4\big[\big(1-756\hat{\alpha}^2\big)c_{4,0}-72\hat{\alpha}\big(1-30\hat{\alpha}^2\big)s_{4,0}\big]}{\big(1+36\hat{\alpha}^2\big)^2\big(1+3600\hat{\alpha}^2\big)}\end{aligned} \tag{3.20}$$

and

$$\begin{aligned}\psi_{2\mathrm{u}} = &-\frac{3F^2\big\{\big[6\hat{\alpha}A(t_1)+B(t_1)\big]c_{1,-1}+\big[A(t_1)-6\hat{\alpha}B(t_1)\big]s_{1,-1}\big\}}{2\big(1+36\hat{\alpha}^2\big)}\\ &+\frac{3\big(1+2KF\big)\big\{\big[A(t_1)+12\hat{\alpha}B(t_1)\big]c_{2,1}-\big[12\hat{\alpha}A(t_1)-B(t_1)\big]s_{2,1}\big\}}{1+144\hat{\alpha}^2}\\ &-\frac{9F^2\big\{\big[42\hat{\alpha}A(t_1)-\big(1-216\hat{\alpha}^2\big)B(t_1)\big]c_{3,1}+\big[\big(1-216\hat{\alpha}^2\big)A(t_1)+42\hat{\alpha}B(t_1)\big]s_{3,1}\big\}}{2\big(1+36\hat{\alpha}^2\big)\big(1+1296\hat{\alpha}^2\big)}.\end{aligned} \tag{3.21}$$

Note that the solution for ψ_2 given by equations (3.20) and (3.21) does *not* agree with that given by equations (11) and (12) of Newell and Viljoen [118], and moreover that, as previously pointed out, obtaining the correct solution for ψ_2 is not simply a matter of reversing the sign of the term due to the airflow in their solution.

However, in the absence of the airflow, $F = K = 0$, both of these solutions reduce to that given by equation (3.5) of Hinch and Kelmanson [61], as they should.

3.3.3 Solution for s_1

At $\mathcal{O}(\gamma^3)$ equation (3.7) gives

$$\begin{aligned}\mathcal{L}\psi_3 = &-3\frac{\partial}{\partial\theta}\left\{\left(\psi_1^2+\psi_2\right)\left[\hat{\alpha}\frac{\partial\psi_1}{\partial\theta}+\hat{\alpha}\frac{\partial^3\psi_1}{\partial\theta^3}+2F^2\sin 2\theta-(1+2FK)\cos\theta\right]\right\}\\ &-3\hat{\alpha}\frac{\partial}{\partial\theta}\left[\psi_1\left(\frac{\partial\psi_2}{\partial\theta}+\frac{\partial^3\psi_2}{\partial\theta^3}\right)\right]-\frac{\partial\psi_1}{\partial t_1},\end{aligned} \tag{3.22}$$

with ψ_1 and ψ_2 given by (3.18), (3.20) and (3.21).

The expanded form of (3.22), omitted for brevity, involves secular terms $s_{1,1}$ and $c_{1,1}$; setting the coefficients of these terms to zero leads to a pair of ordinary differential equations for $A(t_1)$ and $B(t_1)$, namely

$$\frac{\mathrm{d}A}{\mathrm{d}t_1} = s_1A + s_2B, \tag{3.23}$$
$$\frac{\mathrm{d}B}{\mathrm{d}t_1} = -s_2A + s_1B, \tag{3.24}$$

where the real constants s_1 and s_2 are given by

$$s_1 = -81\hat{\alpha}\left(\frac{10F^4}{(1+36\hat{\alpha}^2)(1+1296\hat{\alpha}^2)}+\frac{(1+2KF)^2}{1+144\hat{\alpha}^2}\right)\leq 0 \tag{3.25}$$

and

$$s_2 = \frac{30(1+324\hat{\alpha}^2)F^4}{(1+36\hat{\alpha}^2)(1+1296\hat{\alpha}^2)}+\frac{3(5+72\hat{\alpha}^2)(1+2KF)^2}{2(1+144\hat{\alpha}^2)}\geq 0. \tag{3.26}$$

Note that these expressions for s_1 and s_2 are invariant under the transformation of K given in (3.8), which provides a check on their validity. The solution of (3.23) and (3.24) subject to the initial conditions $A(0) = -(1 + 2KF)$ and $B(0) = 0$ is simply

$$A(t_1) = -(1+2KF)\exp(s_1t_1)\cos(s_2t_1), \tag{3.27}$$
$$B(t_1) = (1+2KF)\exp(s_1t_1)\sin(s_2t_1). \tag{3.28}$$

equation (3.25) shows that for $\hat{\alpha} > 0$ the growth rate of the solution, s_1, is always negative, and so we arrive at our main result, namely that the solution (3.12) for h to $\mathcal{O}(\gamma^3)$ is unconditionally stable, decaying exponentially quickly like $\exp(s_1 t_1)$ to a steady state at very large times. In particular, in the limit of a slow airflow, $F \to 0$,

$$s_1 = -\frac{81\hat{\alpha}}{1+144\hat{\alpha}^2} - \frac{324K\hat{\alpha}F}{1+144\hat{\alpha}^2} + \mathcal{O}(F^2) \to -\frac{81\hat{\alpha}}{1+144\hat{\alpha}^2} \leq 0, \tag{3.29}$$

in the regime of a fast airflow, $F \gg 1$,

$$s_1 = -\frac{810\hat{\alpha}F^4}{(1+36\hat{\alpha}^2)(1+1296\hat{\alpha}^2)} + \mathcal{O}(F^2) \to -\infty, \tag{3.30}$$

in the case of no circulation, $K = 0$,

$$s_1 = -81\hat{\alpha}\left(\frac{10F^4}{(1+36\hat{\alpha}^2)(1+1296\hat{\alpha}^2)} + \frac{1}{1+144\hat{\alpha}^2}\right) \leq 0, \tag{3.31}$$

and in the regime of strong circulation, $|K| \gg 1$,

$$s_1 = -\frac{324\hat{\alpha}F^2}{1+144\hat{\alpha}^2}K^2 + \mathcal{O}(K) \to -\infty. \tag{3.32}$$

Furthermore, in the regime of weak capillarity, $\hat{\alpha} \ll 1$,

$$s_1 = -81\left[(1+2KF)^2 + 10F^4\right]\hat{\alpha} + \mathcal{O}(\hat{\alpha}^3) \to 0^-, \tag{3.33}$$

which is consistent with the conclusion of the limited stability analysis in Section 2.9 that in the absence of capillarity, $\hat{\alpha} = 0$, the solution is neutrally stable (i.e. $s_1 = 0$).

Figure 3.1 shows plots of s_1 as a function of F for several values of K for the values of $\hat{\alpha}$ considered by Hinch and Kelmanson [61] and Newell and Viljoen [118], namely $\hat{\alpha} = 0.0048$ and $\hat{\alpha} = 0.058$. As Figure 3.1 illustrates, s_1 decreases monotonically with F when $K \geq 0$, but first increases to a negative maximum before decreasing monotonically when $K < 0$; in particular, the behaviour of s_1 is consistent with the asymptotic results (3.29)–(3.33). The dashed curves in Figure 3.1 show the locus of the maximum of s_1 as K varies from $-\infty$, corresponding to

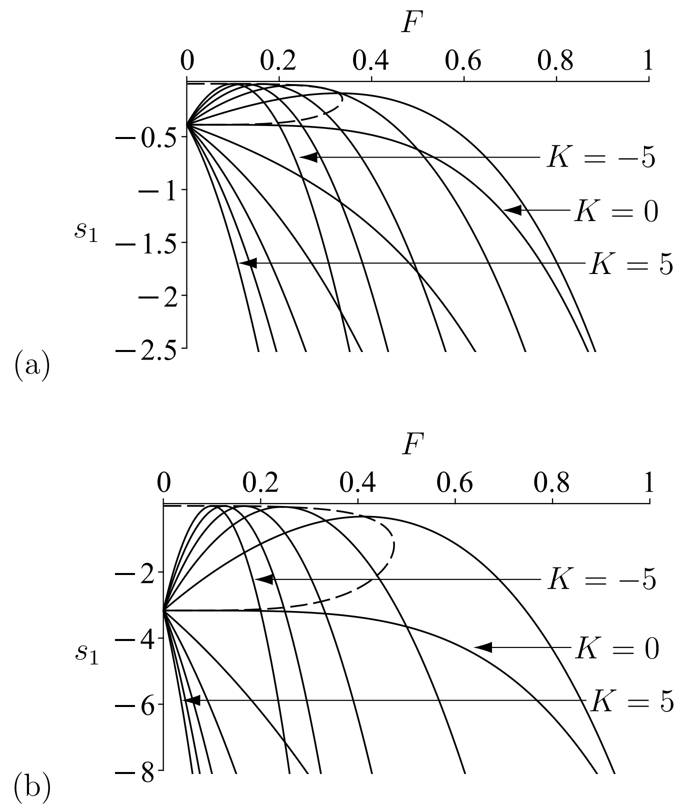

Figure 3.1: Plot of the growth rate s_1 given by (3.25) as a function of F for $K = -5$, -4, -3, $\ldots$, 5 for the values of $\hat{\alpha}$ considered by Hinch and Kelmanson [61] and Newell and Viljoen [118], namely (a) $\hat{\alpha} = 0.0048$ and (b) $\hat{\alpha} = 0.058$. The dashed curves show the locus of the maximum of s_1 as K varies from $-\infty$ [corresponding to the point $(F, s_1) = (0, 0)$] to 0 [corresponding to the point $(F, s_1) = \big(0, -81\hat{\alpha}/(1 + 144\hat{\alpha}^2)\big)$].

the point $(F, s_1) = (0, 0)$, to 0, corresponding to the point

$$(F, s_1) = \left(0, -\frac{81\hat{\alpha}}{1 + 144\hat{\alpha}^2}\right), \tag{3.34}$$

confirming that $s_1 \leq 0$, and hence that the solution is unconditionally stable, for all values of F (≥ 0) and K.

Equations (3.25) and (3.26) show that s_1 and s_2 depend on all three of the parameters $\hat{\alpha}$, F, and K; however, the behaviour of s_1 and s_2 can be seen more clearly if (3.25) and (3.26) are instead written as equations for the scaled quantities

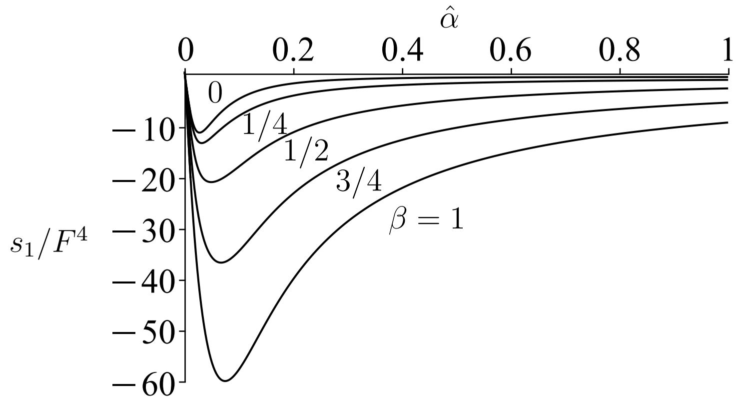

Figure 3.2: Plot of the scaled growth rate s_1/F^4 given by (3.35) as a function of $\hat{\alpha}$ for $\beta = 0$, 1/4, 1/2, 3/4 and 1, where $\beta = (1 + 2KF)/(4F^2)$.

s_1/F^4 and s_2/F^4, which depend on just the two parameters $\hat{\alpha}$ and β:

$$\frac{s_1}{F^4} = -162\hat{\alpha}\left(\frac{5}{(1+36\hat{\alpha}^2)(1+1296\hat{\alpha}^2)} + \frac{8\beta^2}{1+144\hat{\alpha}^2}\right) \leq 0 \tag{3.35}$$

and

$$\frac{s_2}{F^4} = \frac{30(1+324\hat{\alpha}^2)}{(1+36\hat{\alpha}^2)(1+1296\hat{\alpha}^2)} + \frac{24(5+72\hat{\alpha}^2)\beta^2}{1+144\hat{\alpha}^2} \geq 0. \tag{3.36}$$

Figure 3.2 shows the scaled growth rate s_1/F^4 as a function of $\hat{\alpha}$ for a range of values of β, the collapse of the results onto curves of constant β being a consequence of the reduction from three parameters to two. In all cases s_1/F^4 decreases with $\hat{\alpha}$ from 0 to a minimum value before increasing monotonically to 0.

Note that the expression for s_1 given by equation (3.25) does *not* agree with that given by equation (13) of Newell and Viljoen [118], and moreover that, as previously pointed out, obtaining the correct solution for s_1 is not simply a matter of reversing the sign of the term due to the airflow in their solution. However, in the absence of the airflow, $F = K = 0$, it reduces to (1.61), that is, to equation (3.10) of Hinch and Kelmanson [61], as it should. Confirmation that the result of Newell and Viljoen [118] is erroneous comes from the fact that their expression for s_1 does not agree with the equation (3.10) of Hinch and Kelmanson [61] when $\varphi = 0$ (due, we believe, to a double-counting of terms of the types $c_{1,1}c_{n,0}^2 + c_{1,1}s_{n,0}^2 = c_{1,1}$ and $s_{1,1}c_{n,0}^2 + s_{1,1}s_{n,0}^2 = s_{1,1}$), and so is in error even in the absence of the airflow.

3.3.4 Evolution of the free surface of the film

To $\mathcal{O}(\gamma)$ we have $h = 1 + \gamma\psi_1$, and so to $\mathcal{O}(\epsilon\gamma)$, where again $\epsilon = H/a \ll 1$, the free surface has the form $r = 1 + \epsilon(1 + \gamma\psi_1)$, that is,

$$r = 1 + \epsilon + \epsilon\gamma\Big\{(1 + 2KF)\Big(c_{1,0} - [c_{1,1}\cos(s_2 t_1) - s_{1,1}\sin(s_2 t_1)]\exp(s_1 t_1)\Big) - \frac{2F^2}{1 + 36\hat{\alpha}^2}\left[(s_{2,0} + 6\hat{\alpha}c_{2,0}) - (s_{2,2} + 6\hat{\alpha}c_{2,2})\exp(-12\hat{\alpha}t_0)\right]\Big\}, \tag{3.37}$$

where r has been scaled with a. The free surface (3.37) oscillates temporally; for $\hat{\alpha} = 0$ the amplitude of the oscillation is finite for all t, whereas for $\hat{\alpha} > 0$ the amplitude decays to zero in the limit $t \to \infty$, and the free surface approaches the steady profile

$$r = 1 + \epsilon + \epsilon\gamma\Big[(1 + 2KF)c_{1,0} - \frac{2F^2}{1 + 36\hat{\alpha}^2}(s_{2,0} + 6\hat{\alpha}c_{2,0})\Big]. \tag{3.38}$$

As Figure 3.2 shows, for each β there is a unique value of $\hat{\alpha}$ corresponding to the minimum of s_1 (i.e. a special value of the surface tension) such that (3.37) approaches (3.38) quickest: if $\hat{\alpha}$ is larger or smaller than this (i.e. if surface tension is stronger or weaker than this special value) then the approach is slower.

As Hinch and Kelmanson [61] pointed out, in the absence of the airflow, $F = K = 0$, the free surface (3.37) is a circular cylinder of radius $1 + \epsilon$ whose centre is offset from the axis of the solid cylinder by ϵd at any instant, where d is given by (1.58) and $\hat{A} = \hat{A}(t_1)$ and $\hat{B} = \hat{B}(t_1)$ correspond to A and B in (3.27) and (3.28) with $F = 0$; thus for $\hat{\alpha} > 0$ the centre of the circular free surface spirals around the point $(\epsilon\gamma, 0)$, approaching it in the limit $t \to \infty$. Moreover, rewriting the term $c_{1,1}\cos(s_2 t_1) - s_{1,1}\sin(s_2 t_1)$ in (3.37) with $F = 0$ in the form $\cos[\theta - (t_0 - s_2 t_1)]$ shows that the free surface lags the solid cylinder by the amount $s_2 t_1$.

In the presence of the airflow the occurrence of the terms involving $c_{2,0}$ and $s_{2,0}$ (i.e. $\cos 2\theta$ and $\sin 2\theta$) in (3.37) and (3.38) means that the free surface, while still, of course, a cylinder, is no longer simply circular, and that it is no longer possible to identify a uniquely defined lag of the free surface relative to the solid cylinder.

Figure 3.3 shows examples of snapshots of free surfaces given by (3.37) at various times, comparing a case in the absence of the airflow, $F = K = 0$, with cases with far-field airflow $F = 1$ and positive, negative or zero air circulation K, all plotted for $\hat{\alpha} = 0$ and $\gamma = 1/15$ (the latter value being chosen for illustrative

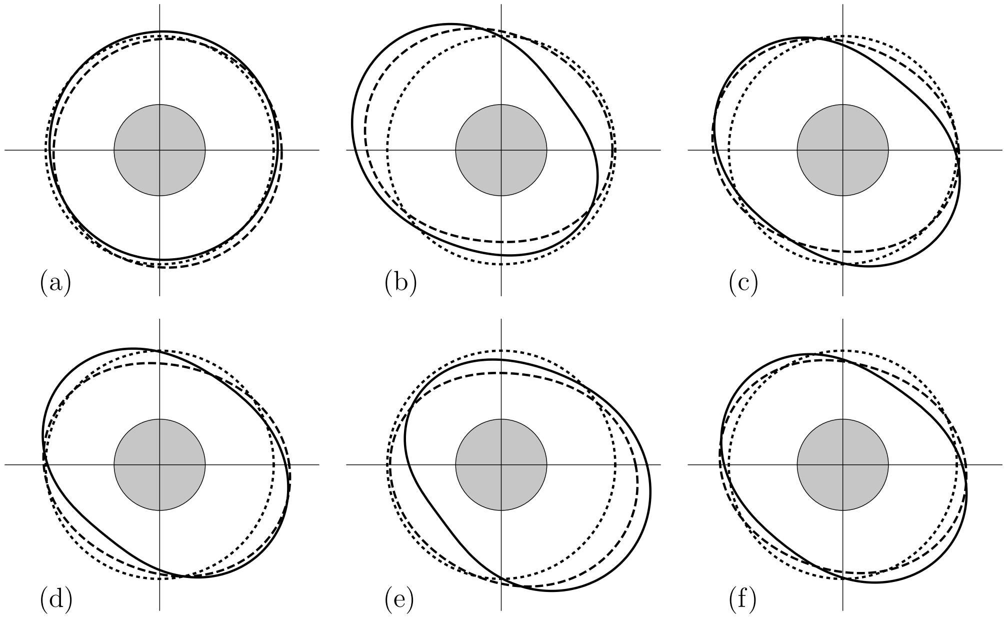

Figure 3.3: Snapshots of free surfaces to $\mathcal{O}(\epsilon\gamma)$ in the cases (a) $F = K = 0$, (b) $F = 1$, $K = -2$, (c) $F = 1$, $K = -1$, (d) $F = 1$, $K = 0$, (e) $F = 1$, $K = 1$, (f) $F = 1$, $K = 2$, with $\hat{\alpha} = 0$ and $\gamma = 1/15$ in each case, at times $t_0 = 0$ (dotted curves), $t_0 = 2.5$ (dashed curves), and $t_0 = 5$ (full curves). The film thickness is exaggerated for clarity.

purposes). Figure 3.3 illustrates the effect of the airflow in both distorting the film and modifying its offset from the centre of the solid cylinder. Figure 3.4 shows corresponding plots for $\hat{\alpha} = 1/15$ (and again with $\gamma = 1/15$), illustrating the tendency of capillarity to suppress the distortion of the film. The largest time shown in Figures 3.3 and 3.4, namely $t_0 = 5$, was chosen simply because the free surfaces in Figure 3.4 (but not those in Figure 3.3) are close to their large-time asymptotic state (3.38) by this time, and change little thereafter.

The successive parts of both Figure 3.3 and Figure 3.4 correspond to the values $\beta = \infty$, $-3/4$, $-1/4$, $1/4$, $3/4$, and $5/4$, respectively, and therefore parts (b) and (e) and parts (c) and (d) provide examples of the phase shift of π under the transformation (3.8), mentioned in Section 3.2; for example, the value of r given by (3.37) at any position θ at time t in Figure 3.3(b) is the same as the value of r at position $\theta + \pi$ at time t in Figure 3.3(e).

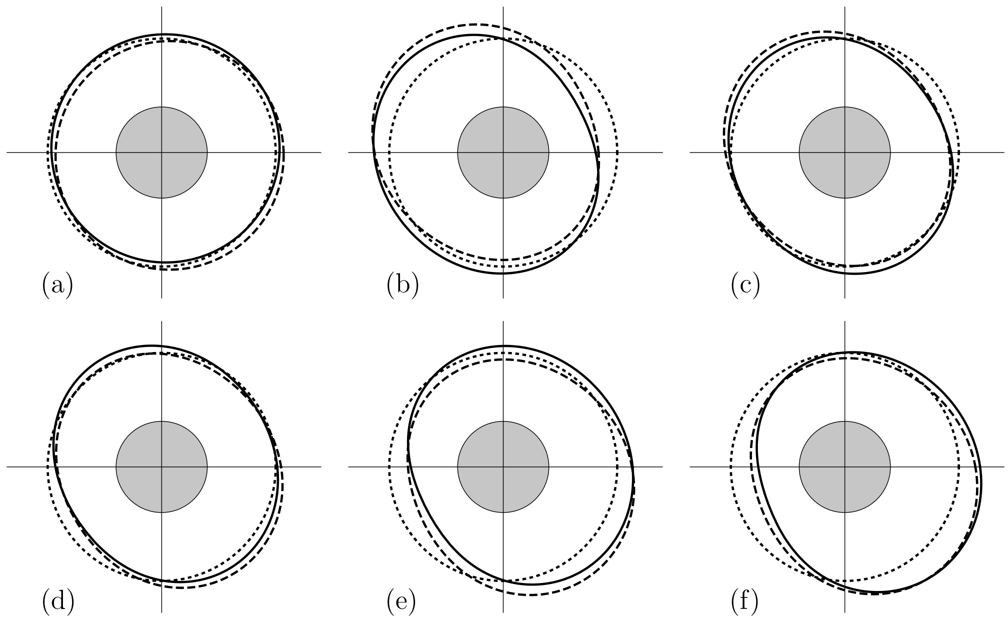

Figure 3.4: Snapshots of free surfaces to $\mathcal{O}(\epsilon\gamma)$ in the cases (a) $F = K = 0$, (b) $F = 1$, $K = -2$, (c) $F = 1$, $K = -1$, (d) $F = 1$, $K = 0$, (e) $F = 1$, $K = 1$, (f) $F = 1$, $K = 2$, with $\hat{\alpha} = 1/15$ and $\gamma = 1/15$ in each case, at times $t_0 = 0$ (dotted curves), $t_0 = 2.5$ (dashed curves), and $t_0 = 5$ (full curves). The film thickness is exaggerated for clarity.

3.4 Conclusions

In this chapter we corrected the analysis of Newell and Viljoen [118] of unsteady two-dimensional coating flow of a thin film of a viscous fluid on the outside of a uniformly rotating solid horizontal circular cylinder in the presence of a steady two-dimensional irrotational airflow with circulation, in the case in which the effects of gravity and of capillarity are weak compared with those of viscous shear. In contrast with the claim of Newell and Viljoen [118] that the solution is unstable for certain values of the physical parameters, we found that the growth rate s_1, given by (3.25) in terms of the parameters F, K, and $\hat{\alpha}$ representing the speed of the far-field airflow, the circulation of the airflow, and surface tension, respectively, is always non-positive, and so the solution for h to $\mathcal{O}(\gamma^3)$ is unconditionally stable.

From their study Newell and Viljoen [118] drew five conclusions concerning the operation of the novel rotary pesticide applicator for crops described in Section 1.2. These conclusions, quoted directly from Newell and Viljoen [118], with additional text added for clarity written inside square brackets [·], are

1. "*A stability condition was derived,* [namely equation] (13) [of Newell and Viljoen [118]], *which can be used to find stable operating conditions for our pesticide applicator. The stability condition depends explicitly on system parameters; therefore, one can explore how constitutive modifications of the pesticide solution to adjust the viscosity or surface tension will affect the stability.*"

2. "*An analytical solution* [namely equation] (19) [of Newell and Viljoen [118]], *is derived for the nonsteady state model derived from $\mathcal{O}(\epsilon)$ lubrication theory,* [given by equation] (14) [of Newell and Viljoen [118]] *for the initial data $h(\theta, 0) = 1$. The series solution, for the special case $\hat{\alpha} = \varphi = 0$, matches the analytical solution very well.*"

3. "*The film is more stable to negative air velocity. To satisfy this condition, the roller must approach the weed, while the roller rotates from below up toward the plant, thus contacting the leaves from below.*"

4. "*A practical consequence of conclusion 3 is that the pesticide will mostly be applied to the abaxial (underneath) leaf surface; thence, the fluid must be modified to adhere to the leaf and minimise dripping.*"

5. "*Since systemic pesticides are transported in the plant's phloem, uptake through the epidermis is important. Although not experimentally confirmed, there is strong evidence that uptake rates from the abaxial side are higher than from the adaxial surface. Knoche and Bukovac [83] measured uptake rates of gibberellic acid by sour cherry leaves and found that uptake rates were significantly higher on the abaxial side (see their Table III). Therefore, it may be a more effective practice to apply the active ingredient to the abaxial leaf surface.*"

Unfortunately their erroneous prediction of instability renders their first conclusion incorrect and their third, fourth and fifth conclusions moot; their second conclusion is correct but concerns only the case of no airflow, and so provides no new information about the use of the applicator. On a more positive note, however, the successful use of the pesticide applicator depends on the film being stable — and our results show that this is always the case in the regime considered.

Chapter 4

Porous squeeze-film flow

In this chapter we describe the behaviour of the axisymmetric squeeze-film flow of a thin layer of fluid in a gap between a flat impermeable bearing moving under a prescribed constant load and a flat thin porous bed, the base of which is open to the atmosphere. In particular, we derive an implicit expression for the fluid gap thickness, an explicit expression for the contact time of the bearing and the porous bed, calculate the particle paths and penetration depths of fluid particles in the porous bed, and analyse their behaviour in the limits of small and large permeability.

As discussed in Section 1.4, the porous squeeze film problem has been well studied due to its applicability to many practical situations. For example, the analysis of the present problem, in which the base of the porous bed is open to the atmosphere, is particularly relevant to the understanding of fluid flow in porous gas bearings and filters. However, in this chapter we describe the porous squeeze-film problem as generally as possible, with no particular application in mind, with the knowledge that the general analysis can be applied to these practical situations.

4.1 Problem formulation

With respect to the axisymmetric cylindrical polar coordinates (r^*, z^*), we consider the pressure-driven porous squeeze-film problem as shown in Figure 4.1. In particular, we consider the unsteady flow of a thin film of Newtonian fluid with constant viscosity μ^* and density ρ^* in the thin gap between a flat impermeable bearing and a flat porous bed. The thickness of the fluid gap at time t^* with initial

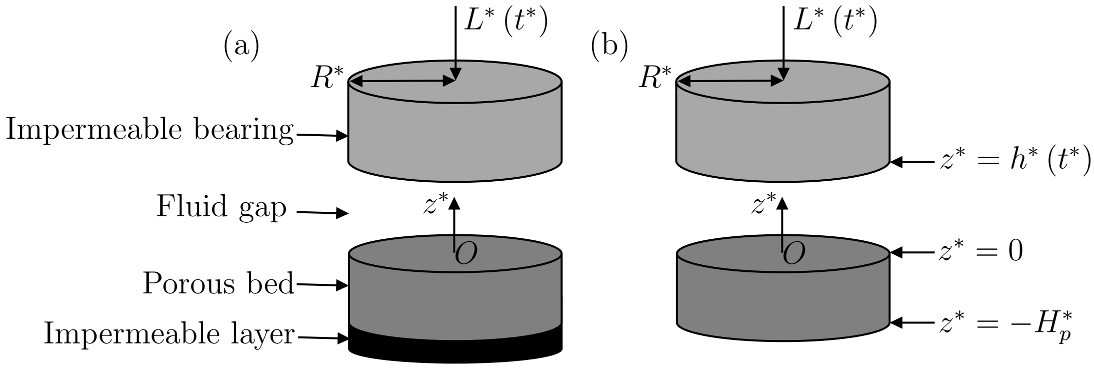

Figure 4.1: The setup of the axisymmetric porous squeeze-film problem where either (a) there is an impermeable layer below the porous bed (the "closed-base configuration") or (b) the base of the porous bed is open to the atmosphere (the "open-base configuration").

bearing height $h^*(0) = H_{\mathrm{f}}^*$ is denoted by $h^* = h^*(t^*)$. The thickness of the porous bed is H_p^* and the bearing and porous bed both have radius R^*. The porous bed is fully saturated in fluid at $t^* = 0$ and has constant permeability k^* and porosity $0 \leq \phi \leq 1$, where, as discussed in Section 1.4, $\phi = V_{\mathrm{p}}^*/V_{\mathrm{bed}}^*$, where V_{p}^* is the total volume of empty space within the pores of the porous bed and V_{bed}^* is the total volume of the bed. A prescribed load $L^*(t^*) > 0$ which acts vertically downwards is applied to the bearing, pushing the bearing towards the porous bed. As discussed in Section 1.4, in the case of an impermeable bed, a theoretically infinite time is required to squeeze all of the fluid out of the gap into the region beyond $r^* = R^*$ (see, for example, [50]). However, if the bed is porous, then all of the fluid is squeezed out of the gap into either the porous bed through the interface $z^* = 0$ or the region beyond $r^* = R^*$ in a finite time, and hence a finite contact time $t^* = t_{\mathrm{c}}^*$ between the bearing and porous bed is achieved. At the base of the porous bed $z^* = -H_{\mathrm{p}}^*$, there may be either an impermeable layer stopping fluid flowing out of the base of the porous bed or the base of the porous bed is open to the atmosphere as shown in Figure 4.1(a) and 4.1(b), respectively. We shall henceforth refer to the problem described in Figure 4.1(a) as the "closed-base configuration" and the problem described in Figure 4.1(b) as the "open-base configuration".

As discussed in Section 1.4, the closed-base configuration has been considered previously by, for example, Wu [186], Murti [111], Knox et al. [86], Karmakar and Raja Sekhar [75] and Venerus [169], whilst open-base configuration has been considered previously by, for example, Murti [112], Verma [170] and Venerus [169].

Many previous works on these problems derive equations for the fluid gap thickness, velocity and pressure in the fluid gap, and Darcy velocity and Darcy pressure in the porous bed, and then analyse their behaviour as the permeability or slip length are varied. There has been less work analysing the finite contact time t^*_{c}, the particles paths, and the penetration depths of fluid particles initially situated in either the fluid gap or porous bed. As discussed in Section 1.4, for the closed-base configuration, Knox et al. [86] derived expressions for the finite contact time and investigated the particle paths of fluid particles initially situated in either the fluid gap or porous bed, and investigated their behaviour in the limits of small and large permeability. For the purpose of comparison, a brief outline of the results for the closed-base configuration is presented in Section 4.5. In Section 4.6 we will investigate the finite contact time and particle paths for the open-base configuration, and the corresponding two-dimensional problem is treated briefly in Appendix E.

4.2 Governing equations

The governing equations in the fluid gap ($0 \leq z^* \leq h^*$) are the continuity equation (1.2) and Navier–Stokes equation (1.3), where $\mathbf{u}^* = (u^*, w^*)$ is the fluid velocity in the fluid gap with radial component $u^* = u^*(r^*, z^*, t^*)$ and vertical component $w^* = w^*(r^*, z^*, t^*)$, the fluid pressure is denoted by $p^* = p(r^*, z^*, t^*)$ and $\mathbf{g}^* = (0, -g^*)$ is the constant acceleration due to gravity.

The governing equations in the porous bed ($-H^*_{\mathrm{p}} \leq z^* \leq 0$), with Darcy velocity $\mathbf{U}^* = (U^*, W^*)$ with radial component $U^* = U^*(r^*, z^*, t^*)$ and vertical component $W^* = W^*(r^*, z^*, t^*)$ and Darcy pressure $P^* = P^*(r^*, z^*, t^*)$, are the continuity equation given by

$$\nabla^* \cdot \mathbf{U}^* = 0 \tag{4.1}$$

and Darcy's law given by (1.65). As we will see in what follows, qualitatively different behaviour occurs for small and large values of the permeability k^*.

The averaging process employed by Whitaker [175] to derive Darcy's law assumes that macroscopic length scales of the porous medium, e.g. which are of the order of $\mathcal{O}(H^*_{\mathrm{p}})$, are much larger than the microscopic length scales associated with the pore length scales, which are of the order of $\mathcal{O}(k^{*1/2})$ (this is also the case in most practical applications of flow through a porous medium). Therefore Darcy's law is valid only for $k^*/H_\mathrm{p}^{*2} \ll 1$. Despite this limitation, in order to obtain a full description of the problem mathematically, we shall investigate both the limits of small and large dimensionless permeability $k^*/H_\mathrm{p}^{*2} \to 0$ and $k^*/H_\mathrm{p}^{*2} \to \infty$, respectively, throughout this chapter, whilst bearing in mind that $k^*/H_\mathrm{p}^{*2} \to 0$ is the most physically relevant limit. This is also the case for the slip length $l_\mathrm{s}^* = k^{*1/2}/\alpha$ which is of the same size as the microscopic length scales associated with the pore length scales ($\mathcal{O}(k^{*1/2})$). Hence the limit $l_\mathrm{s}^*/H_\mathrm{p}^* \to 0$ is again the most physically relevant limit, however in order to obtain a full description of the problem mathematically, we shall again investigate both limits of small and large dimensionless slip length.

4.2.1 Equation of motion of the bearing

From Newton's second law of motion, we derive the equation of motion for the bearing, given by

$$L^* = F_z^* - M^* \frac{\mathrm{d}^2 h^*}{\mathrm{d}t^{*2}}, \tag{4.2}$$

where the net force F_z^* exerted on the bearing by the fluid in the z^*-direction is given by

$$F_z^* = 2\pi \int_0^{R^*} \left(p^* - 2\mu^* \frac{\partial w^*}{\partial z^*} \right) r^* \Bigg|_{z^*=h^*} \mathrm{d}r^*, \tag{4.3}$$

and M^* is the mass of bearing.

4.2.2 Boundary conditions

The no-slip and no-penetration conditions at the bearing are

$$u^* = 0, \quad w^* = \frac{\mathrm{d}h^*}{\mathrm{d}t^*} \tag{4.4}$$

on $z^* = h^*$. Continuity of mass at the interface between the fluid gap and porous bed requires

$$w^* = W^* \tag{4.5}$$

on $z^* = 0$, and continuity of normal stress requires

$$-p^* + 2\mu^* \frac{\partial u^*}{\partial z^*} = -P^* \tag{4.6}$$

on $z^* = 0$. As described in Section 1.4, the interface between the fluid gap and porous bed we also impose the Beavers–Joseph condition (1.69).

Below the porous bed at $z^* = -H_\mathrm{p}^*$ in the closed-base configuration we impose the no-penetration condition, i.e.

$$W^* = 0 \tag{4.7}$$

on $z^* = -H_\mathrm{p}^*$. On the other hand, in the open-base configuration we impose a condition of ambient pressure, and so, without loss of generality, we impose

$$P^* = 0 \tag{4.8}$$

on $z^* = -H_\mathrm{p}^*$. At the outer edge of the fluid located at $r^* = R^*$ the pressure in the fluid gap takes the ambient value, and hence, without loss of generality, we impose

$$p^* = 0 \tag{4.9}$$

at $r^* = R^*$, and since the fluid pressure is axisymmetric and smooth we require

$$\frac{\partial p^*}{\partial r^*} = 0 \tag{4.10}$$

at $r^* = 0$. Note that to solve the current problem we would, in general, require an additional boundary condition, for example a specification of the Darcy pressure at $r^* = R^*$. However, as we shall show subsequently, since the porous bed and fluid gap are thin, we do not need to specify another boundary condition in order to close the problem.

4.3 Thin-film approximation

Henceforth we will consider the fluid gap and porous bed to be thin, i.e. the fluid gap and porous bed both have aspect ratio $\epsilon = H_\mathrm{p}^*/R^* \ll 1$. As we shall see, making this approximation leads to significant simplifications in the governing equations at leading order in the limit $\epsilon \to 0$.

4.3.1 Non-dimensionalisation

We now non-dimensionalise the variables according to

$$r^* = R^* r, \quad z^* = H_{\mathrm{p}}^* z, \quad t^* = \frac{R^*}{V^*} t, \quad h^* = H_{\mathrm{p}}^* h, \quad k^* = H_{\mathrm{p}}^{*2} \hat{k}, \quad l_{\mathrm{s}}^* = H_{\mathrm{p}}^* l_{\mathrm{s}},$$

$$u^* = V u, \quad w^* = \frac{H_{\mathrm{p}}^* V^*}{R^*} w, \quad U^* = V^* U, \quad W^* = \frac{H_{\mathrm{p}}^* V}{R^*} W,$$

$$p^* = \frac{\mu^* V^* R^*}{H_{\mathrm{p}}^{*2}} p, \quad P^* = \frac{\mu^* V^* R^*}{H_{\mathrm{p}}^{*2}} P, \quad L^* = L_0^* L, \quad d = H_{\mathrm{f}}^* / H_{\mathrm{p}}^*, \tag{4.11}$$

where $h(0) = d$ is the initial thickness of the fluid gap, V^*, $\mu^* V^* R^* / H_{\mathrm{p}}^{*2}$ and L_0^* are appropriate characteristic scales for the velocity, pressure and load where

$$V^* = \frac{H_{\mathrm{p}}^{*2} L_0^*}{\mu^* R^{*3}}. \tag{4.12}$$

4.3.2 Leading-order governing equations

Subject to the scalings (4.11), in the fluid gap $0 \leq z \leq h$, the governing equations (1.2) and (1.3) at leading order in the limit $\epsilon \to 0$, neglecting body forces, become

$$\frac{1}{r} \frac{\partial}{\partial r}(r u) + \frac{\partial w}{\partial z} = 0, \tag{4.13}$$

$$\frac{\partial p}{\partial r} = \frac{\partial^2 u}{\partial z^2}, \tag{4.14}$$

$$\frac{\partial p}{\partial z} = 0, \tag{4.15}$$

and hence

$$p = p(r, t). \tag{4.16}$$

In the porous bed $-1 \leq z \leq 0$, the Darcy equation (1.65) becomes

$$\mathbf{U} = (U, W) = -\hat{k} \left(\frac{\partial P}{\partial r}, \frac{1}{\epsilon^2} \frac{\partial P}{\partial z} \right), \tag{4.17}$$

where the Darcy pressure P satisfies Laplace's equation

$$\frac{1}{r} \frac{\partial}{\partial r} \left(r \frac{\partial P}{\partial r} \right) + \frac{1}{\epsilon^2} \frac{\partial^2 P}{\partial z^2} = 0, \tag{4.18}$$

which at leading order in the limit $\epsilon \to 0$ reduces to

$$\frac{\partial^2 P}{\partial z^2} = 0. \tag{4.19}$$

Since the fluid layer is thin, at leading order in the limit $\epsilon \to 0$ the equation of motion (4.2) becomes the load condition $L = F_z$, where

$$L = 2\pi \int_0^1 pr \, \mathrm{d}r. \tag{4.20}$$

We may either consider a time dependent or constant load L. In the case of a constant load, for simplicity we will choose the value of the constant (dimensional) load to be $L^* = L_0^* > 0$, corresponding to taking the constant (dimensionless) load to be equal to unity, i.e. $L_0 = 1$, without loss of generality. We shall, however, retain the constant (dimensionless) load L_0 explicitly in what follows for clarity of presentation. The boundary conditions (4.4)–(4.6) become

$$u = 0, \quad w = \frac{\mathrm{d}h}{\mathrm{d}t} \tag{4.21}$$

on $z = h$,

$$w = W \tag{4.22}$$

on $z = 0$,

$$P = p \tag{4.23}$$

on $z = 0$. On the boundary between the porous bed and the fluid gap the Beavers–Joseph condition (1.69) becomes

$$u - \delta U = \frac{\hat{k}^{\frac{1}{2}}}{\alpha} \frac{\partial u}{\partial z} \tag{4.24}$$

on $z = 0$, where we have introduced the non-dimensional parameter δ which may either take the value $\delta = 1$ corresponding to the Beavers–Joseph condition or $\delta = 0$ corresponding to the Saffman condition (1.70), with slip length

$$l_{\mathrm{s}} = \frac{\hat{k}^{\frac{1}{2}}}{\alpha}. \tag{4.25}$$

In the limit $l_s \to 0$ with $\delta = 1$ (4.24) reduces to the no-slip condition relative to the fluid in the porous bed given by

$$u = U \tag{4.26}$$

on $z = 0$, and when $\delta = 0$ (4.24) reduces to the no-slip condition relative to the solid which makes up the porous bed given by

$$u = 0 \tag{4.27}$$

on $z = 0$. In the limit $l_s \to \infty$ both the Beavers–Joseph condition (4.24) and Saffman condition (i.e. irrespective of the value of δ) become the zero-shear condition given by

$$\frac{\partial u}{\partial z} = 0 \tag{4.28}$$

on $z = 0$. If there is an impermeable layer below the porous bed, as in the closed-base configuration, then (4.7) becomes

$$W = 0 \tag{4.29}$$

on $z = -1$, while if the base of the porous bed is open to the atmosphere, as in the open-base configuration, then (4.8) becomes

$$P = 0 \tag{4.30}$$

on $z = -1$. Finally (4.9) and (4.10) become

$$p = 0 \tag{4.31}$$

at $r = 1$, and

$$\frac{\partial p}{\partial r} = 0 \tag{4.32}$$

at $r = 0$, respectively.

4.4 Particle paths

Integrating the velocity $\boldsymbol{u} = (u, w)$ with respect to t yields the position of a particle of fluid $\boldsymbol{r} = (r(t), z(t))$. Therefore, the path $(r, z) = (r(t), z(t))$ taken by a fluid particle initially situated at a point (r_0, z_0) within either the fluid gap or porous bed (such that $0 \leq r_0 \leq 1$ and $-1 \leq z_0 \leq d$) is determined by the ordinary differential equations

$$\frac{\mathrm{d}r}{\mathrm{d}t} = u, \quad \frac{\mathrm{d}z}{\mathrm{d}t} = w \tag{4.33}$$

in the fluid gap and by

$$\frac{\mathrm{d}r}{\mathrm{d}t} = \frac{U}{\phi}, \quad \frac{\mathrm{d}z}{\mathrm{d}t} = \frac{W}{\phi} \tag{4.34}$$

in the porous bed, where, as mentioned in Section 1.4, $0 \leq \phi \leq 1$ is the porosity of the porous bed and $\boldsymbol{U}/\phi$ is the true fluid velocity within the pores of the porous bed. Equations (4.33)–(4.34) are solved subject to the initial conditions

$$r(0) = r_0 \quad z(0) = z_0 \tag{4.35}$$

when $h(0) = d$.

4.5 Closed-base configuration

In this section, for the purpose of comparison with the open-base configuration described in Section 4.6, we shall briefly describe the work of Knox et al. [86] which considered the axisymmetric porous squeeze-film problem for the closed-base configuration, as shown in Figure 4.1(a). In particular, we shall describe the derivation of the equations that govern the fluid velocity, fluid pressure, Darcy velocity, Darcy pressure, fluid gap thickness, contact time and particle paths. We shall also describe the behaviour of the contact time and particle paths in the limit of small and large permeability $\hat{k} \to 0$ and $\hat{k} \to \infty$, respectively.

4.5.1 Darcy pressure and velocity

We begin by solving Laplace's equation at leading order (4.19) subject to (4.23) and (4.29) yielding the leading-order Darcy pressure to be

$$P = p(r, t). \tag{4.36}$$

The Darcy pressure is therefore independent of z at leading order and dependence on z first appears at $\mathcal{O}(\epsilon^2)$. We seek a solution of (4.18) of the form

$$P = p(r,t) + \epsilon^2 P_1(r,z,t) + \mathcal{O}(\epsilon^4) \tag{4.37}$$

to find the dependence of P on z. Substituting (4.37) into (4.18) and applying the no-penetration condition (4.29) we find that

$$\frac{\partial P_1}{\partial z} = -\frac{(1+z)}{r}\frac{\partial}{\partial r}\left(r\frac{\partial p}{\partial r}\right). \tag{4.38}$$

Substituting (4.37) and (4.38) into the (4.17) we find that the Darcy velocity at leading order in ϵ is given by

$$\mathbf{U} = -\hat{k}\left(\frac{\partial p}{\partial r}, -\frac{(1+z)}{r}\frac{\partial}{\partial r}\left(r\frac{\partial p}{\partial r}\right)\right). \tag{4.39}$$

4.5.2 Fluid pressure and velocity

For the closed-base configuration, with constant load L_0, the fluid pressure is given by

$$p = \frac{2L_0}{\pi}(1-r^2). \tag{4.40}$$

Substituting (4.40) into (4.39) gives the Darcy velocity

$$\mathbf{U} = (U, W) = \frac{4L_0\hat{k}}{\pi}(r, -2(1+z)), \tag{4.41}$$

which is independent of both α and δ, and so remains unchanged regardless of the choice of boundary condition at the interface $z = 0$. The radial fluid velocity is given by

$$u = \frac{2L_0(h-z)[(\hat{k}^{\frac{1}{2}} + \alpha h)z + \hat{k}^{\frac{1}{2}}(h + 2\delta\alpha\hat{k}^{\frac{1}{2}})]r}{\pi(\hat{k}^{\frac{1}{2}} + \alpha h)} \tag{4.42}$$

and the vertical fluid velocity is given by

$$w = -\frac{2L_0[2(\hat{k}^{\frac{1}{2}} + \alpha h)(6\hat{k} - z^3) + 3\alpha(h^2 - 2\delta\hat{k})z^2 + 6\hat{k}^{\frac{1}{2}}h(h + 2\delta\alpha\hat{k}^{\frac{1}{2}})z]}{3\pi(\hat{k}^{\frac{1}{2}} + \alpha h)}. \tag{4.43}$$

Hence, for the closed-base configuration, both U and u are linear in r, however, W and w are independent of r.

4.5.3 Fluid gap thickness and contact time

In this subsection, we present the equations for the fluid gap thickness and finite contact time in the case of the closed-base configuration as shown in Figure 4.1(a). We also present the leading-order finite contact times in the limits of small and large permeability $\hat{k}$.

The solution for the bearing height $h(t)$ is given implicitly by

$$t = -\frac{3\pi}{2L_0}\int_d^h \frac{\alpha s + \hat{k}^{\frac{1}{2}}}{s^2(\alpha s^2 + 4\hat{k}^{\frac{1}{2}}s + 6\delta\alpha\hat{k}) + 12\hat{k}(\alpha s + \hat{k}^{\frac{1}{2}})}\,\mathrm{d}s. \tag{4.44}$$

In the case of an impermeable bed for which $\hat{k} = 0$, the fluid gap thickness is given explicitly by

$$h(t) = \left(\frac{3\pi d^2}{3\pi + 4d^2 L_0 t}\right)^{\frac{1}{2}}, \tag{4.45}$$

which in the limit of large time becomes

$$h(t) \sim \left(\frac{3\pi}{4L_0 t}\right)^{\frac{1}{2}} \to 0 \tag{4.46}$$

as $t \to \infty$, confirming that, as mentioned previously, infinite time is required for the bearing to squeeze all of the fluid from the gap.

Putting $h = 0$ in (4.44) gives the expression for the finite contact time t_c given by

$$t_\mathrm{c} = \frac{3\pi}{2L_0}\int_0^d \frac{\alpha s + \hat{k}^{\frac{1}{2}}}{s^2(\alpha s^2 + 4\hat{k}^{\frac{1}{2}}s + 6\alpha\hat{k}) + 12\hat{k}(\alpha s + \hat{k}^{\frac{1}{2}})}\,\mathrm{d}s. \tag{4.47}$$

Figure 4.2 shows a plot of t_c as a function of $\hat{k}$ and Figure 4.3 shows a more detailed view of t_c as a function of $\hat{k}$ for both small and large $\hat{k}$, where t_c given by (4.47) was calculated numerically (using the default numerical integration tool `int` of the symbolic and numerical mathematics package MAPLE [95]). In particular, Figure 4.2 shows that t_c decreases as $\hat{k}$ increases and Figure 4.3(a) and 4.3(b) show that t_c increases as α increases for small values of $\hat{k}$, but that it decreases as α increases for large values of $\hat{k}$. Knox et al. [86] explains this change in behaviour of t_c as α increases for small and large values of $\hat{k}$ by showing that, for small values of $\hat{k}$, the radial fluid velocity u decreases as α increases (i.e. as l_s decreases), which decreases the fluid volume flux out of the gap into the region beyond $r = 1$, denoted by Q_out. The fluid volume flux into the porous bed, through the interface

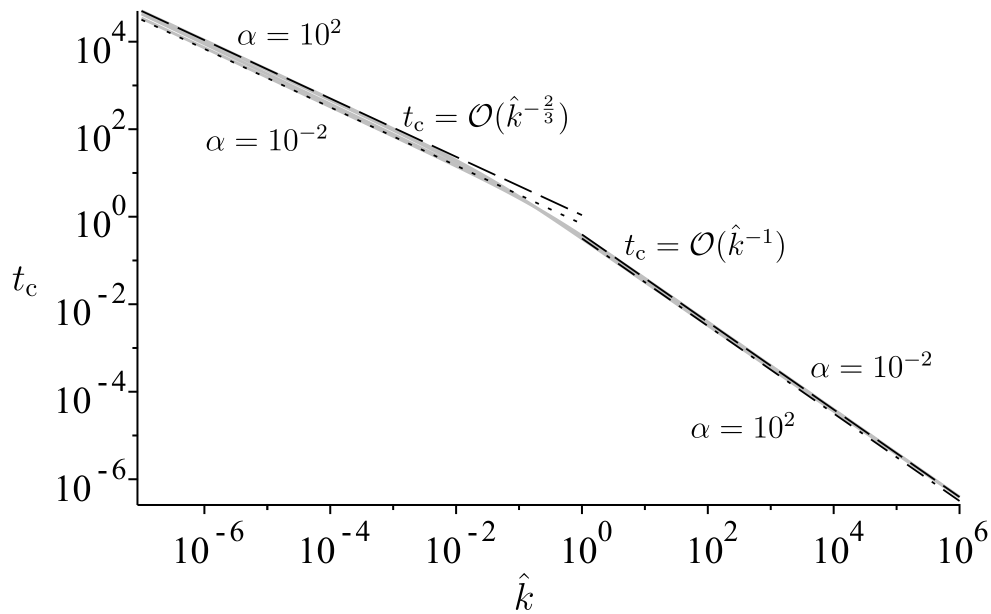

Figure 4.2: Log-log plot of the contact time t_c (solid lines) in the closed-base configuration given by (4.47) as a function of $\hat{k}$ with $\alpha = 10^{-2}, 10^{-1}, 1, 10$, $d = 1$, the contact time in the limit of small $\hat{k}$ given by (4.49) (dashed line) in the case $\alpha = \mathcal{O}(1)$ and (4.52) in the case $\alpha \to 0$ (dotted line) and in the limit of large $\hat{k}$ given by (4.54) (dashed line) in the case $\alpha = \mathcal{O}(1)$ and (4.56) in the case $\alpha \to \infty$ (dash-dot line) for $d = 1$. Based on Figure 2 of Knox et al. [86].

$z = 0$, denoted by $Q_{\text{bed}} = -8L_0\hat{k}$ is constant and independent of α. Therefore a decrease in Q_{out} causes the time taken for the fluid gap to reduce to a thickness h to increase, consistent with Figure 4.3(a). For large values of $\hat{k}$, however, Knox et al. [86] showed that the radial fluid velocity increases as α increases, hence increasing Q_{out} and causing the time taken for the fluid gap to reduce to a thickness h to decrease, consistent with Figure 4.3(b).

(a) Contact time in the limit $\hat{k} \to 0$

In the limit of small permeability $\hat{k} \to 0$, the contact time (4.47) is given by

$$t_c = \frac{\pi^2}{\sqrt{3}L_0(12\hat{k})^{\frac{2}{3}}} - \frac{\pi}{8L_0\alpha\hat{k}^{\frac{1}{2}}} + \mathcal{O}(\hat{k}^{-\frac{1}{3}}), \tag{4.48}$$

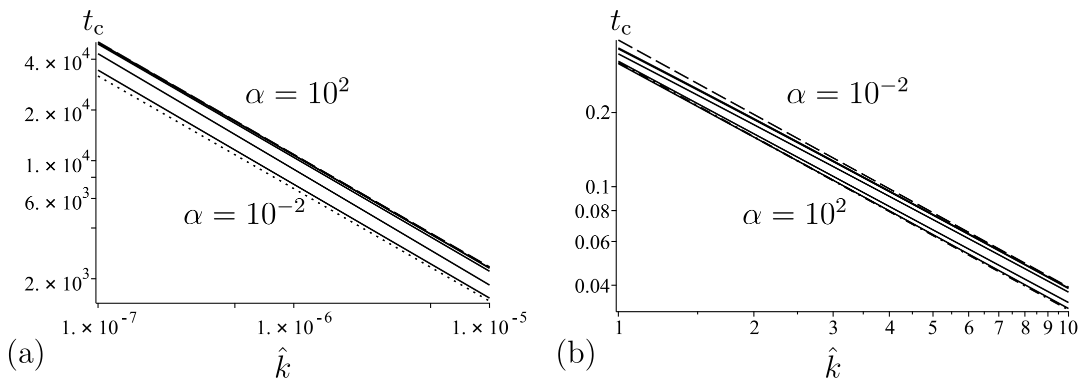

Figure 4.3: Detailed view of Figure 4.2 for (a) small values of $\hat{k}$ and (b) large values of $\hat{k}$.

and so, in particular, the leading-order contact time in the limit $\hat{k} \to 0$ is

$$t_c \sim \frac{\pi^2}{\sqrt{3}L_0(12\hat{k})^{\frac{2}{3}}} \gg 1. \tag{4.49}$$

The Beavers–Joseph constant α appears at first order in (4.48) and shows that increasing the slip length l_s (i.e. decreasing α) decreases the contact time. Furthermore, by comparing the leading and first order terms in (4.48) we can see that the expansion only remains uniformly valid provided that

$$\alpha \gg \hat{k}^{\frac{1}{6}}. \tag{4.50}$$

In the case $\alpha \leq \mathcal{O}(k^{1/6})$ we can find a different asymptotic expansion.

By inspection of (4.49) we find that, in order to obtain a finite, leading-order contact time, we must go to long times, i.e. $t = \mathcal{O}(\hat{k}^{-2/3})$. Hence, we rescale t and h with

$$t = (12\hat{k})^{-\frac{2}{3}}T, \quad h = (12\hat{k})^{\frac{1}{3}}H, \tag{4.51}$$

where T and H are $\mathcal{O}(1)$ in the limit $\hat{k} \to 0$, and expand (4.47) in the limit $\hat{k} \to 0$ in the case $\alpha = 0$. Reintroducing the scalings given by (4.51) yields at leading order

$$t_c \sim \frac{\pi^2}{4\sqrt{3}\left(3\hat{k}\right)^{\frac{2}{3}} L_0} \gg 1 \tag{4.52}$$

as $\hat{k} \to 0$. The contact time (4.52) was not reported by Knox et al. [86] and so is given here for the first time. Furthermore, comparing (4.52) with the contact time given by (4.49) we see that the latter is larger by a factor $2^{2/3}$ (> 1), and hence in the limit $\hat{k} \to 0$, the effect of increasing the slip length is to increase Q_{out}, and hence to decrease t_{c}.

Figure 4.2 shows that the asymptotic expansions (4.49) and (4.52) agree well with the exact expression (4.47), and Figure 4.3(a) shows that (4.49) agrees well with (4.47) for $\alpha = \mathcal{O}(1)$ and $\alpha \to \infty$ and (4.52) agrees well with (4.47) in the limit $l_{\text{s}} \to \infty$ (i.e. in the limit $\alpha \to 0$).

(b) Contact time in the limit $\hat{k} \to \infty$

In the limit of large permeability $\hat{k} \to \infty$, the contact time given by (4.47) is given by

$$t_{\text{c}} = \frac{\pi d}{8L_0\hat{k}} - \frac{\pi\delta\alpha d^3}{48\hat{k}^{\frac{3}{2}}} + \mathcal{O}(\hat{k}^{-2}), \tag{4.53}$$

and so, in particular, the leading-order contact time in the limit $\hat{k} \to \infty$ is given by

$$t_{\text{c}} \sim \frac{\pi d}{8L_0\hat{k}} \ll 1. \tag{4.54}$$

The Beavers–Joseph constant α appears at first order in (4.53) and shows that increasing the slip length l_{s} (i.e. decreasing α) increases the contact time. Furthermore, by comparing the leading and first order terms in (4.53) we see that the expansion only remains uniformly valid provided that

$$\alpha \ll \hat{k}^{\frac{1}{2}}. \tag{4.55}$$

In the case $\alpha \geq \mathcal{O}(k^{1/2})$, Knox [84] showed that

$$t_{\text{c}} \sim \frac{\pi}{4\hat{k}L_0} \ln\left(\frac{d+2}{2}\right) \ll 1. \tag{4.56}$$

Furthermore, comparing (4.56) with the contact time given by (4.54) we see that the latter is larger by a factor $d/2\ln\left((d+2)/2\right)$ (> 1), and hence in the limit $\hat{k} \to \infty$, the effect of increasing the slip length from $l_{\text{s}} = 0$ decreases Q_{out}, and hence increases the contact time t_{c}.

Figure 4.2 shows that the leading-order asymptotic solutions (4.54) and (4.56) agree well with the exact expression (4.47), and Figure 4.3(b) shows that (4.54) agrees well with (4.47) for $\alpha = \mathcal{O}(1)$ and $\alpha \to 0$ and (4.56) agrees well with (4.47) in the limit $l_s \to 0$ (i.e. in the limit $\alpha \to \infty$).

4.5.4 Particle paths

In this section we briefly describe the behaviour of the particle paths for the closed-base configuration.

Figures 4.4(a)–(c) show the particle paths (r, z) taken by fluid particles with initial positions (r_0, z_0) at $t = 0$ for three different values of the permeability $\hat{k}$. In particular, Figure 4.4 shows the particle paths in the case of an impermeable bed for which $\hat{k} = 0$, showing that, in this case no particles are able to flow within or into the impermeable bed and eventually all particles flow out of the gap into the region beyond $r = 1$. Figure 4.4(b) and 4.4(c) show the behaviour of the particle paths for small and large values of the permeability $\hat{k}$, respectively. In particular, Figure 4.4(b) and 4.4(c) show that fluid particles initially situated in the fluid gap can either flow out of the gap into the region beyond $r = 1$ or into the porous bed, after which they may either remain in the porous bed or flow out of the porous bed, into the region beyond $r = 1$. Additionally, Figure 4.4(b) and 4.4(c) also show that as $\hat{k}$ increases more particles initially situated in the fluid gap flow into the porous bed. This is quantified by the "watershed curve", plotted in a dashed line in Figure 4.4(b) and 4.4(c), which divides the fluid gap into two distinct regions such that fluid particles initially situated to the left of the watershed curve will flow out of the gap into the porous bed, and fluid particles initially situated to the right of the watershed curve will flow out of the gap into the region beyond $r = 1$. If a particle is squeezed from the fluid gap into the porous bed, then it will cross the interface $z = 0$ at some point $(r, 0) = (\hat{r}, 0)$, where $\hat{r} = \hat{r}(r_0, z_0)$ at $t = \hat{t}$ $(h = \hat{h})$, and hence the watershed curve, which divides the fluid gap into two regions for which particles are either squeezed into the porous bed $(\hat{r} < 1)$ or out into the region beyond $r = 1$, is given by the curve $\hat{r} = 1$. The watershed curve is therefore found by solving (4.33) and (4.34) numerically backwards in time from $h = \hat{h}$ to $h = d$ and then evaluating the solution when $h = d$ yields the initial position of the fluid particle (r_0, z_0). This process is repeated for $0 \leq \hat{h} \leq d$, resulting in the watershed curve $\hat{r} = 1$.

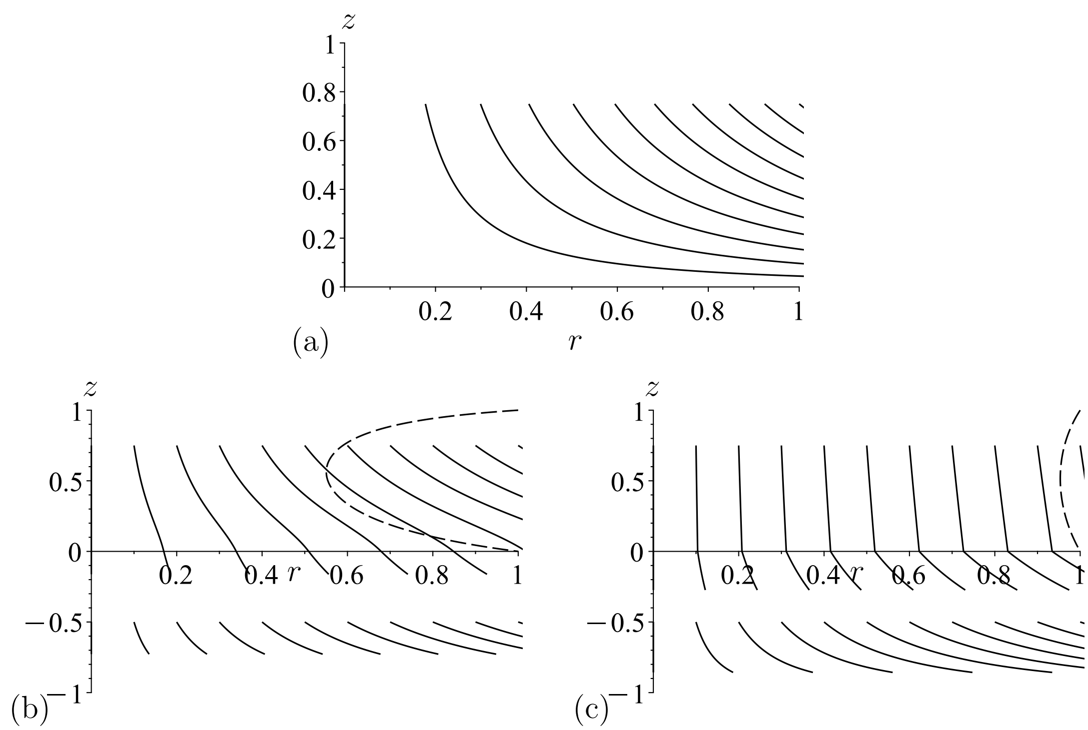

Figure 4.4: Plot of fluid particle paths (r, z) in solid lines given by (4.33)–(4.34) with initial positions $(r_0, z_0) = (0, 0.75)$, $(0.1, 0.75)$, $(0.2, 0.75)$,..., $(1, 0.75)$ in the fluid gap and $(r_0, z_0) = (0, -0.5)$, $(0.1, -0.5)$, $(0.2, -0.5)$,..., $(1, -0.5)$. The permeability in (a) is $\hat{k} = 0$, (b) is $\hat{k} = 0.01$ and (c) is $\hat{k} = 5$. In all plots, $\phi = 0.75$ $\alpha = 1$ and $d = 1$. The watershed curve in (b, c) is plotted with dashed line.

4.6 Open-base configuration

In this section, we consider the porous squeeze-film problem for which the base of the porous bed is open to the atmosphere, as shown in Figure 4.1(b), so that now instead of the no-penetration condition (4.29), we impose the condition of ambient pressure (4.30) at the base of the porous bed.

Solving Laplace's equation (4.19) at leading order, subject to (4.23) and (4.30) yields the Darcy pressure

$$P = p(r, t)(z + 1). \tag{4.57}$$

This solution for the Darcy pressure (4.57) leads to the Darcy velocity given by

$$\boldsymbol{U} = -\hat{k}\left(\frac{\partial p}{\partial r}(z + 1), \frac{p}{\epsilon^2}\right). \tag{4.58}$$

Hence by continuity of vertical velocity (4.22), at leading order in ϵ, the vertical velocity in the fluid gap is given by

$$w = -\frac{\hat{k}p}{\epsilon^2}. \tag{4.59}$$

Therefore in both the fluid gap and porous bed, the radial velocities are $u = \mathcal{O}(1)$ and $U = \mathcal{O}(1)$, however, the vertical velocities are $w = \mathcal{O}(\epsilon^{-2}) \gg 1$ and $W = \mathcal{O}(\epsilon^{-2}) \gg 1$. Physically, the leading-order problem corresponds to the flow in both the fluid gap and porous bed being entirely in the vertical direction. Using (4.21) and the load condition (4.20) subject to a constant load L_0, yields a leading-order expression for the contact time given by

$$t_{\mathrm{c}} = \frac{d\pi}{\hat{k}L_0}\epsilon^2 \ll 1, \tag{4.60}$$

i.e. all of the fluid is squeezed out of the fluid gap extremely quickly. Hence, if the permeability is of the same order as that considered in the closed-base configuration, at leading order in ϵ, there is no flow in the radial direction in the fluid gap or porous bed, and the bearing and porous bed come into contact very quickly ($t_{\mathrm{c}} = \mathcal{O}(\epsilon^2)$). However, when the permeability is much smaller than this, the vertical velocity in the porous bed is greatly reduced and contact occurs on a much longer timescale. Specifically, we consider the scaling

$$k^* = \frac{H_{\mathrm{p}}^{*4}}{R^{*2}}k = \epsilon^2 H_{\mathrm{p}}^2 k, \tag{4.61}$$

so that $\hat{k} = \epsilon^2 k$, i.e. the porous bed has been made a factor of ϵ^2 less permeable than that considered for the closed-base configuration in Section 4.5.

An immediate effect of the rescaling (4.61) is to make the radial Darcy velocity negligible at leading order in ϵ, i.e.

$$(U, W) = -k\left(\epsilon^2\frac{\partial P}{\partial r}, \frac{\partial P}{\partial z}\right), \tag{4.62}$$

which at leading order in $\epsilon \to 0$ gives the radial and vertical Darcy velocities

$$U = 0 \quad \text{and} \quad W = -k\frac{\partial P}{\partial z} = -kp. \tag{4.63}$$

The rescaling of the permeability (4.61) also has the immediate consequence of promoting the slip length to higher order, i.e. $l_{\mathrm{s}}^* = \mathcal{O}(\epsilon) \ll 1$, and hence the Beavers–Joseph condition (4.24) reduces to the no-slip condition at leading order. In order to retain the effect of velocity slip at leading order, we must rescale the Beavers–Joseph constant such that $\alpha = \epsilon\bar{\alpha}$, so that now the slip length is given by $l_{\mathrm{s}}^* = H_{\mathrm{p}}^* k^{1/2}/\bar{\alpha}$, which we non-dimensionalise with $l_{\mathrm{s}}^* = H_{\mathrm{p}}^*\bar{l}_{\mathrm{s}}$, so that the non-dimensional slip length is now given by

$$\bar{l}_{\mathrm{s}} = \frac{k^{\frac{1}{2}}}{\bar{\alpha}}. \tag{4.64}$$

Therefore, with $U = 0$ and the slip length given by (4.64), at leading order in ϵ, the Beavers–Joseph condition (4.24) reduces to the Saffman condition given by

$$u = \frac{k^{\frac{1}{2}}}{\bar{\alpha}}\frac{\partial u}{\partial z} \tag{4.65}$$

on $z = 0$.

4.6.1 Unsteady Reynolds equation

Integrating (4.14) twice with respect to z, subject to the no-slip condition at the bearing (4.21) and the Saffman condition (4.65) gives the radial fluid velocity

$$u = \frac{(z-h)(z(k^{\frac{1}{2}} + \bar{\alpha}h) + k^{\frac{1}{2}}h)}{2(k^{\frac{1}{2}} + \bar{\alpha}h)}\frac{\partial p}{\partial r}. \tag{4.66}$$

Integrating (4.13) with respect to z, subject to (4.22) gives the vertical fluid velocity

$$w = -\frac{z(2k^{\frac{1}{2}}(z^2 - 3h^2) + \bar{\alpha}h(2z^2 - 3zh))}{12r(k^{\frac{1}{2}} + \bar{\alpha}h)}\frac{\partial}{\partial r}\left(r\frac{\partial p}{\partial r}\right) - kp. \tag{4.67}$$

Using (4.21) and (4.67) we derive the unsteady Reynolds equation given by

$$\frac{\mathrm{d}h}{\mathrm{d}t} = \frac{h^3(4k^{\frac{1}{2}} + \bar{\alpha}h)}{12r(k^{\frac{1}{2}} + \bar{\alpha}h)}\frac{\partial}{\partial r}\left(r\frac{\partial p}{\partial r}\right) - kp. \tag{4.68}$$

4.6.2 Fluid pressure and load condition

Equation (4.68) is a partial differential equation for the fluid pressure p which we can solve subject to (4.31) and (4.32) to obtain the solution

$$p = \frac{1}{k}\frac{\mathrm{d}h}{\mathrm{d}t}\left[\frac{I_0\left(\eta r\right)}{I_0\left(\eta\right)} - 1\right], \tag{4.69}$$

where I_ν is the modified Bessel function of order ν and we have defined $\eta = \eta(h)$ according to

$$\eta = \left(\frac{12k(k^{\frac{1}{2}} + \bar{\alpha}h)}{h^3(4k^{\frac{1}{2}} + \bar{\alpha}h)}\right)^{\frac{1}{2}}. \tag{4.70}$$

Note that η depends on t via $h(t)$. The equation for the pressure (4.69) coincides with, for example, equation (14) of Murti [112], equation (24) of Verma [170] and equation (3.1) of Venerus [169], in their own notation and subject to their own (different) scalings, all of whom considered the open-base porous squeeze film problem.

The function η can be conveniently re-written in the form

$$\eta = \left(\frac{12k(\bar{l}_\mathrm{s} + h)}{h^3(4\bar{l}_\mathrm{s} + h)}\right)^{\frac{1}{2}}, \tag{4.71}$$

which, in the limit of no slip $\bar{l}_\mathrm{s} \to 0$ (i.e. in the limit $\bar{\alpha} \to \infty$) yields

$$\eta \to \left(\frac{12k}{h^3}\right)^{\frac{1}{2}}, \tag{4.72}$$

and in the limit of large slip, i.e. $\bar{l}_\mathrm{s} \to \infty$ (i.e. in the limit $\bar{\alpha} \to 0$) yields

$$\eta \to \left(\frac{3k}{h^3}\right)^{\frac{1}{2}}. \tag{4.73}$$

By substituting (4.69) into the load condition (4.20) we have

$$L = -\frac{\pi}{k}\frac{\mathrm{d}h}{\mathrm{d}t}\frac{I_0(\eta)}{I_2(\eta)}. \tag{4.74}$$

For simplicity in the remainder of this chapter, we concentrate on the case of constant load $L = L_0$, Hence rearranging (4.74) yields

$$\frac{\mathrm{d}h}{\mathrm{d}t} = -\frac{kL_0}{\pi}\frac{I_0(\eta)}{I_2(\eta)}. \tag{4.75}$$

If we substitute (4.75) into (4.69) we obtain the fluid pressure given by

$$p = \frac{L_0}{\pi}\left[\frac{I_0(\eta) - I_0(\eta r)}{I_2(\eta)}\right], \tag{4.76}$$

showing that, unlike the pressure for the closed-base configuration (4.40), the pressure (4.76) now depends on k as well as r and t. Note that in the limit $\eta \to 0$, the fluid pressure p in (4.76) is exactly as in (4.40). This limit corresponds to either $k \to 0$ for fixed h or $h \to \infty$ for fixed k in η. In this limit, the porous bed is effectively impermeable, and so as the bearing closes, the fluid near $r = 0$ cannot flow out of the gap easily, so the maximum pressure occurs in this region. The fluid near $r = 1$, however, can flow out of the gap easily into the region beyond $r = 1$, so the minimum pressure occurs in this region, as it tends to its ambient value $p = 0$, resulting in the parabolic profile for the pressure of the form (4.40). Furthermore, in the limit $\eta \to \infty$

$$p \to \frac{L_0}{\pi}\left(1 - \frac{1}{\sqrt{r}}\exp(-\eta(1-r))\right) \sim \frac{L_0}{\pi}, \tag{4.77}$$

which corresponds to $k \to \infty$ for fixed h or $h \to 0$ for fixed k in η. In this limit, the porous bed is extremely permeable, and so as the bearing closes, there is little resistance across the entire gap from $r = 0$ to $r = 1$. The pressure is therefore uniform throughout the gap, except from in an exponentially small region near $r = 1$. In this small region, the fluid can flow out of the gap easily into the region beyond $r = 1$ and the pressure tends to its ambient value $p = 0$. Figure 4.5 shows a plot of the scaled fluid pressure for various values of η, as well as the asymptotic behaviour of the pressure in the limits $\eta \to 0$ and $\eta \to \infty$ given by (4.40) and (4.77), respectively. In particular, Figure 4.5 shows that the pressure is always highest at $r = 0$ and reduces monotonically to its ambient value $p = 0$ as r approaches $r = 1$. Substituting the fluid pressure (4.76) into the equations for

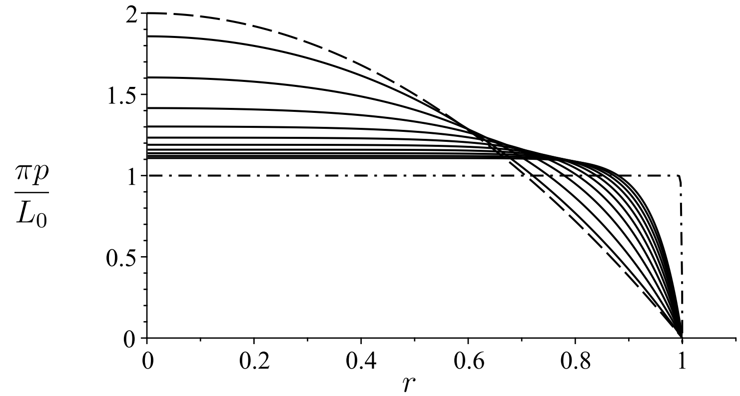

Figure 4.5: The scaled fluid pressure $\pi p/L_0$ given by (4.76) where $\eta = 2, 4, \ldots, 20$ are plotted with solid lines, the limit $\eta \to 0$, given by (4.40) is plotted with a dashed line and the limit $\eta \to \infty$, given by (4.77) is plotted with a dash-dot line for $\eta = 1000$.

the radial and vertical fluid velocities (4.66) and (4.67) yields

$$u = \frac{L_0(h-z)[(k^{\frac{1}{2}} + \bar{\alpha}h)z + hk^{\frac{1}{2}}\eta^2 I_1(\eta r)]}{2\pi(k^{\frac{1}{2}} + \bar{\alpha}h)I_2(\eta)} \tag{4.78}$$

and

$$w = -\frac{L_0\eta}{\pi I_2(\eta)}\left[\frac{z\eta^2 I_0(\eta r)\left(3h^2(2k^{\frac{1}{2}} + \bar{\alpha}) - 2z^2(k^{\frac{1}{2}} + \bar{\alpha}h)\right)}{12(k^{\frac{1}{2}} + \bar{\alpha}h)} - k + kI_0(\eta)\right]. \tag{4.79}$$

The vertical Darcy velocity (4.63) is now given by

$$W = -\frac{kL_0}{\pi}\left[\frac{I_0(\eta) - I_0(\eta r)}{I_2(\eta)}\right]. \tag{4.80}$$

4.6.3 Fluid gap thickness and contact time

In this subsection, we derive equations for the fluid gap thickness and contact time in the case of the open-base configuration as shown in Figure 4.1(b). We then derive asymptotic expansions for the finite contact times in the limits of small and large permeability.

Integration of (4.75) with respect to t shows that the solution for $h(t)$ is given implicitly by

$$t = -\frac{\pi}{L_0 k} \int_d^h \frac{I_2(\eta(s))}{I_0(\eta(s))} \, \mathrm{d}s, \tag{4.81}$$

where s is a dummy variable of integration for h in η. In the case of an impermeable layer, for which $k = 0$, the solution for the fluid gap thickness is given explicitly by (4.45). Figure 4.6 shows the fluid gap thickness h as a function of t given by equation (4.81), for various values of k and $\bar{\alpha}$, calculated numerically (using the default numerical integration tool `int` of the symbolic and numerical mathematics package MAPLE [95]). In particular, Figure 4.6(a) shows that as k increases, the time taken for the fluid gap to reduce to a thickness h decreases, and that when $k \neq 0$, i.e. the porous bed is permeable, all of the fluid is squeezed out of the gap in a finite time t_{c}. Figure 4.6(b) and 4.6(c) show that for both small and large values of k, the time taken for the fluid gap to reduce to a thickness h increases. Putting $h = 0$ in (4.81) gives an expression for the contact time t_{c} given by

$$t_{\mathrm{c}} = \frac{\pi}{L_0 k} \int_0^d \frac{I_2(\eta(s))}{I_0(\eta(s))} \, \mathrm{d}s. \tag{4.82}$$

Figure 4.7 shows a plot of t_{c} as a function of k and Figure 4.8 shows a more detailed view of t_{c} as a function of k for both small and large k. In particular, Figure 4.7 shows that the contact time t_{c} decreases as k increases, in agreement with Figure 4.6(a). Figure 4.8(a) and 4.8(b) show that t_{c} increases as $\bar{\alpha}$ increases, in agreement with Figure 4.6(a) and 4.6(b) for both small and large values of k, respectively. The behaviour of the fluid gap thickness $h(t)$ and contact time t_{c} as k increases is in accord with physical intuition, as increasing the permeability allows fluid to flow through the porous bed quicker, and as a result allows the fluid gap to drain quicker.

The behaviour of the fluid gap thickness $h(t)$ and the contact time t_{c} as $\bar{\alpha}$ varies is not as simple and requires a more detailed explanation. To explain this behaviour, we shall examine the radial fluid velocity u. Figure 4.9 shows plots of the radial fluid gap velocity u as a function of z for $0 \leq z \leq h$ at $r = 1/4$ when $h = 1/2$ for small and large values of the permeability k, and increasing values of the Beavers–Joseph constant $\bar{\alpha}$. Figure 4.9 shows that the fastest flow in the fluid gap occurs for small values of the permeability and that increasing $\bar{\alpha}$ (i.e. decreasing $\bar{l}_{\mathrm{s}}$) decreases the radial velocity u for both small and large values of the permeability. This decrease in the radial velocity u as $\bar{\alpha}$ increases, decreases the

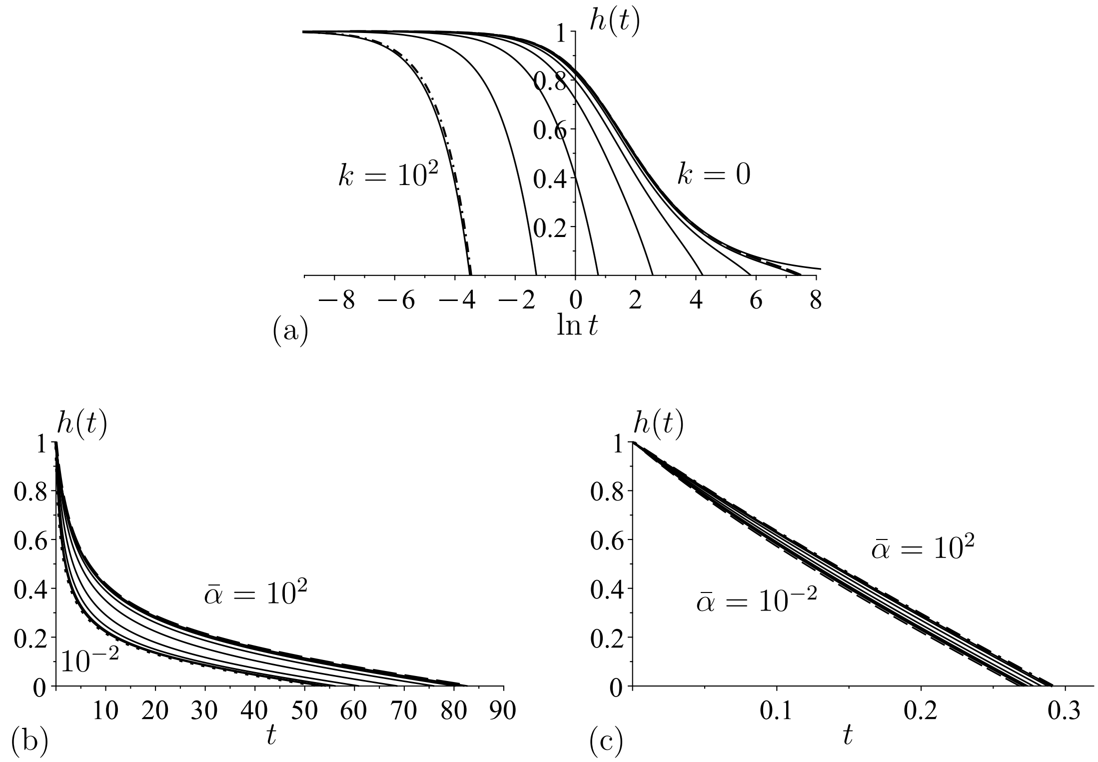

Figure 4.6: Plots of the fluid gap thickness $h(t)$ as a function of t for (a) $k = 0, 10^{-4}, 10^{-3}, \ldots, 10^2$ with the asymptotic solutions in the limits $k \to 0$ and $k \to \infty$ plotted in dash and dash-dot lines given by (4.111) and (4.119), respectively, $\bar{\alpha} = 1$, (b) $k = 10^{-2}$, $\bar{\alpha} = 10^{-2}, 10^{-3/2}, \ldots, 10^2$ with the asymptotic solutions in the limit $k \to 0$ in the case $\bar{\alpha} = \mathcal{O}(1)$ and $\bar{\alpha} = 0$ plotted in dash and dotted lines given by (4.111) and (4.118), respectively and (c) $k = 10^2$, $\bar{\alpha} = 10^{-2}, 10^{-3/2}, \ldots, 10^2$ with the asymptotic solutions in the limit $k \to \infty$ in the case $\bar{\alpha} = \mathcal{O}(1)$ and $\bar{\alpha} \to \infty$ plotted in dash and dash-dot lines given by (4.119) and (4.122), respectively.

volume flux out of the gap into the region beyond $r = 1$, denoted by Q_{out} and given by

$$Q_{\mathrm{out}} = 2\pi \left[\int_0^h ur \mathrm{d}z \right]_{r=1} = \frac{L_0 h^3 \eta^2 I_1(\eta)(4k^{\frac{1}{2}} + \bar{\alpha}h)}{6 I_2(\eta)(k^{\frac{1}{2}} + \bar{\alpha}h)}. \tag{4.83}$$

The volume flux out of the fluid gap into the porous bed, denoted by Q_{bed}, is given by

$$Q_{\mathrm{bed}} = 2\pi \left[\int_0^1 wr \mathrm{d}r \right]_{z=0} = -L_0 k \eta = -\left(\frac{12 L_0^2 k^3 (k^{\frac{1}{2}} + \bar{\alpha}h)}{h^3 (4k^{\frac{1}{2}} + \bar{\alpha}h)} \right)^{\frac{1}{2}}, \tag{4.84}$$

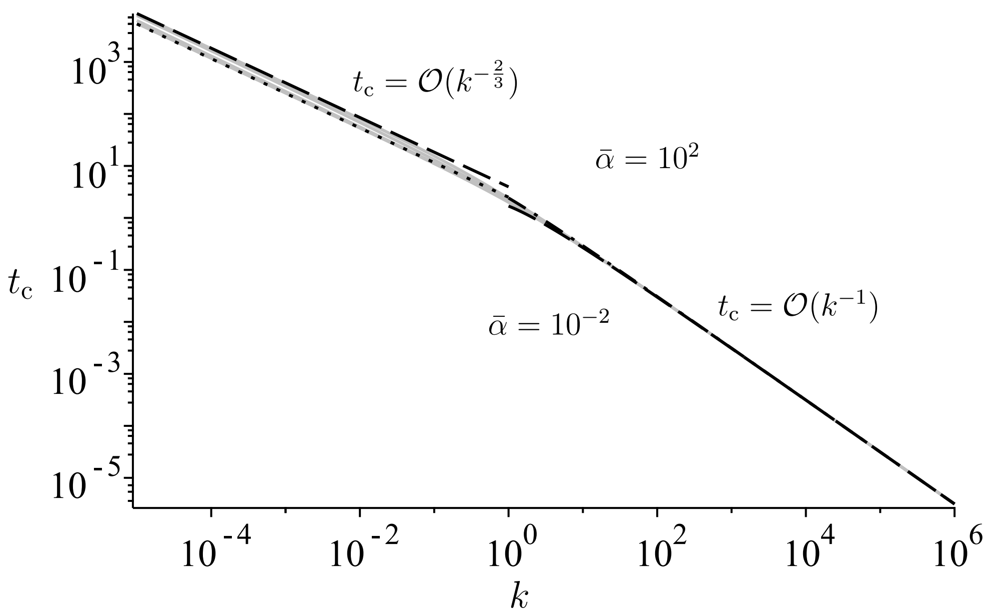

Figure 4.7: Log-log plots of the contact time t_c as a function of k (solid lines) for the open-base configuration given by (4.82) with $\alpha = 10^{-2}, 10^{-1}, 1, 10$, $d = 1$, the contact time in the limit of small k given by (4.110) (dashed line) in the case $\alpha = \mathcal{O}(1)$ and (4.117) in the case $\alpha \to 0$ (dotted line) and in the limit of large k given by (4.120) (dashed line) in the case $\alpha = \mathcal{O}(1)$ and (4.123) in the case $\alpha \to \infty$ (dash-dotted line) for $d = 1$.

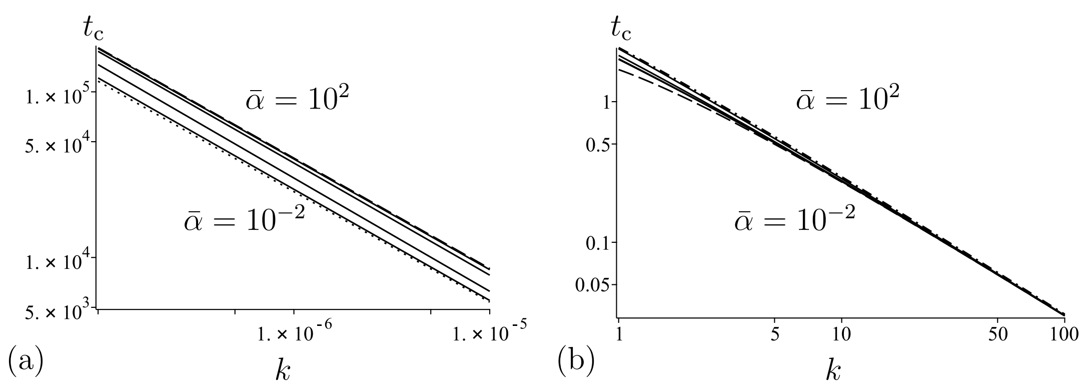

Figure 4.8: Detailed view of Figure 4.7 for (a) small values of k and (b) large values of k.

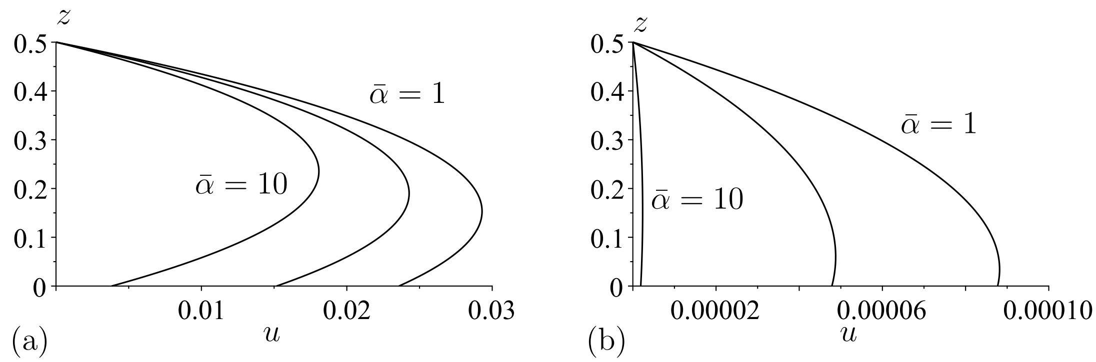

Figure 4.9: Plots of the radial fluid velocity u given by (4.78) as a function of z for $0 \leq z \leq h$ at $r = 1/4$ when $h = 1/2$ for $\bar{\alpha} = 1, 2$ and 10 with (a) $k = 10^{-1}$ and (b) $k = 10$.

such that

$$\frac{\partial Q_{\mathrm{bed}}}{\partial \bar{\alpha}} = -\left(\frac{27L_0^2k^4}{h(4k^{\frac{1}{2}} + \bar{\alpha}h)^3(k^{\frac{1}{2}} + \bar{\alpha}h)}\right) < 0, \tag{4.85}$$

showing that Q_{bed} is also a decreasing function of $\bar{\alpha}$. Since, as $\bar{\alpha}$ increases, both Q_{out} and Q_{bed} decrease, the time required for the fluid gap to decrease to a thickness h must increase (i.e. the reduction in fluid gap thickness must be slower), as $\bar{\alpha}$ increases. This is confirmed by Figure 4.6(b) and 4.6(c) which show that for both small and large values of k, the time taken for the fluid gap to reduce to a thickness h increases as $\bar{\alpha}$ increases. This is qualitatively different behaviour from that in the closed-base configuration, which, as discussed in Section 4.5, the time taken for the fluid gap to reduce to a thickness h decreases for small $\hat{k}$ but increases for large $\hat{k}$ as α increases.

(a) Contact time in the limit $k \to 0$

This subsection contains the derivation of the contact times in the limit of small permeability $k \to 0$.

In the limit $k \to 0$ we seek a perturbation solution to (4.75) of the form

$$h = h_0 + k^{\frac{1}{2}}h_1 + kh_2 + \mathcal{O}(k^{\frac{3}{2}}) \tag{4.86}$$

and expand (4.75) up to order k to find at $\mathcal{O}(1)$

$$\frac{\mathrm{d}h_0}{\mathrm{d}t} = -\frac{2L_0h_0^3}{3\pi}, \tag{4.87}$$

at $\mathcal{O}(k^{1/2})$

$$\frac{\mathrm{d}h_1}{\mathrm{d}h_0} = \frac{3(1+\bar{\alpha}h_1)}{h_0\bar{\alpha}} \tag{4.88}$$

and at $\mathcal{O}(k)$

$$\frac{\mathrm{d}h_2}{\mathrm{d}h_0} = \frac{\bar{\alpha}^2(3h_0^2h_2 + 3h_0h_1^2 + 2) + 6\bar{\alpha}h_0h_1 - 3h_0}{h_0^3\bar{\alpha}}. \tag{4.89}$$

We can solve (4.87)–(4.89) subject to the boundary conditions

$$h_0(0) = d,\;\; h_1(0) = h_2(0) = 0 \tag{4.90}$$

to obtain

$$h_0(t) = \frac{\sqrt{3\pi}d}{(4L_0d^2t + 3\pi)^{\frac{1}{2}}}, \tag{4.91}$$

$$h_1(t) = \frac{h_0^3 - d^3}{d^3\bar{\alpha}}, \tag{4.92}$$

$$h_2(t) = \frac{3h_0^5}{2d^6\bar{\alpha}^2} - \frac{2}{5h_0^2} + \frac{3}{2h_0\bar{\alpha}^2} - \frac{h_0^3}{d^3}\left(\frac{3}{d\bar{\alpha}^2} - \frac{2}{5d^2}\right). \tag{4.93}$$

The asymptotic behaviour of (4.91)–(4.93) as $t \to \infty$, namely

$$h_0(t) \sim \left(\frac{3\pi}{4L_0t}\right)^{\frac{1}{2}} \to 0, \quad h_1(t) \sim -\frac{1}{\bar{\alpha}}, \quad h_2(t) \sim -\frac{2}{5h_0^2} \sim -\frac{8L_0t}{15\pi} \to -\infty \tag{4.94}$$

shows that the expansion (4.86) is not uniformly valid for all t. Comparing leading- and first-order terms suggests that the expansion remains uniformly valid provided that

$$t \ll \frac{\bar{\alpha}^2}{L_0k}, \quad \text{i.e.} \quad t = \mathcal{O}(k^{-1}). \tag{4.95}$$

However, comparing the first and second order terms we can see that the expansion actually only remains uniformly valid provided that

$$t \ll \frac{1}{L_0\bar{\alpha}k^{\frac{1}{2}}} \quad \text{i.e.} \quad t = \mathcal{O}(k^{-\frac{1}{2}}). \tag{4.96}$$

Therefore, in order to obtain a uniformly-valid expansion for intermediate times $t = \mathcal{O}(k^{-1/2})$, for which $h = \mathcal{O}(k^{1/4})$, we re-scale t and h according to

$$t = k^{-\frac{1}{2}}\bar{t}, \quad h = k^{\frac{1}{4}}\bar{h}, \tag{4.97}$$

where $\bar{t}$ and $\bar{h}$ are $\mathcal{O}(1)$ in the limit $k \to 0$. Substituting these scalings into (4.75) and seeking a solution of the form

$$\bar{h} = \bar{h}_0 + k^{1/4}\bar{h}_1 + \mathcal{O}(k^{1/2}) \tag{4.98}$$

we find at leading- and first-order

$$\frac{\mathrm{d}\bar{h}_0}{\mathrm{d}\bar{t}} = -\frac{2L_0\bar{h}_0^3}{3\pi}, \tag{4.99}$$

$$\frac{\mathrm{d}\bar{h}_1}{\mathrm{d}\bar{h}_0} = \frac{3\bar{h}_1}{\bar{h}_0} + \frac{3}{\bar{h}_0\bar{\alpha}} + \frac{2}{\bar{h}_0^3}. \tag{4.100}$$

Solving (4.99) and (4.100) subject to the appropriate matching conditions $\bar{h}_0 \to \infty$ and $\bar{h}_1 \to -1/\bar{\alpha}$ as $\bar{t} \to 0$ gives

$$\bar{h}_0 = \frac{\sqrt{3\pi}d}{(4L_0d^2\bar{t} + 3\pi)^{\frac{1}{2}}} \tag{4.101}$$

and

$$\bar{h}_1 = -\frac{(8L_0\bar{\alpha}\bar{t} + 15\pi)}{15\bar{\alpha}\pi}. \tag{4.102}$$

The asymptotic behaviour of (4.101) and (4.102) as $t \to \infty$, namely

$$\bar{h}_0 \sim \left(\frac{3\pi}{4L_0\bar{t}}\right)^{\frac{1}{2}} \to 0, \quad \bar{h}_1 \sim -\frac{8L_0\bar{t}}{15\pi} \to -\infty \tag{4.103}$$

as $\bar{t} \to \infty$ shows that the expansion (4.98) is not uniformly valid for all t. Comparing leading- and first-order terms suggests that the expansion remains uniformly valid provided that

$$\bar{t} \ll \frac{1}{L_0k^{\frac{1}{6}}}, \quad \text{i.e. } t \ll \frac{1}{L_0k^{\frac{2}{3}}}. \tag{4.104}$$

Therefore, in order to obtain a uniformly-valid expansion for long times $t = \mathcal{O}(k^{-2/3})$, for which $h = \mathcal{O}(k^{1/3})$, we re-scale t and h subject to

$$t = k^{-\frac{2}{3}}T, \quad h = k^{\frac{1}{3}}H, \tag{4.105}$$

where T and H are $\mathcal{O}(1)$ in the limit $k \to 0$. Hence seeking a solution to (4.75) subject to the long-time scalings given by (4.105) of the form $H = H_0 + \mathcal{O}(k^{1/6})$

yields

$$\frac{\mathrm{d}H_0}{\mathrm{d}T} = -\frac{L_0 I_0\left(2\sqrt{3}H_0^{-\frac{3}{2}}\right)}{\pi I_2\left(2\sqrt{3}H_0^{-\frac{3}{2}}\right)}, \tag{4.106}$$

which is separable and leads to

$$T = \frac{\pi}{L_0}\int_{H_0(T)}^{\infty} \frac{I_2\left(2\sqrt{3}s^{-\frac{3}{2}}\right)}{I_0\left(2\sqrt{3}s^{-\frac{3}{2}}\right)}\ \mathrm{d}s + \mathcal{O}(k^{\frac{1}{6}}). \tag{4.107}$$

Hence the contact time T_c, when $H_0 = 0$, is given by

$$T_\mathrm{c} = \frac{\pi}{L_0}\int_{0}^{\infty} \frac{I_2\left(2\sqrt{3}s^{-\frac{3}{2}}\right)}{I_0\left(2\sqrt{3}s^{-\frac{3}{2}}\right)}\ \mathrm{d}s + \mathcal{O}(k^{\frac{1}{6}}). \tag{4.108}$$

Evaluating (4.108) numerically and reintroducing the scaling from (4.105) gives

$$t_\mathrm{c} = \frac{1.26139\pi}{L_0 k^{\frac{2}{3}}} - \frac{\pi}{\bar{\alpha} L_0 k^{\frac{1}{2}}} + \mathcal{O}(k^{-\frac{1}{3}}), \tag{4.109}$$

to 5 decimal places. Hence the leading-order contact time in the limit $k \to 0$ given by

$$t_\mathrm{c} \sim \frac{1.26139\pi}{k^{\frac{2}{3}} L_0} \gg 1 \tag{4.110}$$

remains uniformly valid up to the contact time $t_\mathrm{c} = T_\mathrm{c} k^{-2/3}$ where $T_\mathrm{c} \simeq 1.26139$ satisfies $H_0 = (T_\mathrm{c}) = 0$.

A uniformly-valid leading-order composite solution for the time t in the limit $k \to 0$ can be obtained using (4.107) and the leading-order solution (4.91), subject to the long time scalings (4.105). This uniformly-valid leading-order composite solution for the time t is given by

$$t(h) = -\frac{3\pi}{4L_0 d^2} + \frac{\pi}{k^{\frac{2}{3}} L_0}\int_{h/k^{\frac{1}{3}}}^{\infty} \frac{I_2\left(2\sqrt{3}s^{-\frac{3}{2}}\right)}{I_0\left(2\sqrt{3}s^{-\frac{3}{2}}\right)}\ \mathrm{d}s. \tag{4.111}$$

The Beavers–Joseph constant $\bar{\alpha}$ appears at first order in (4.109) and shows that increasing the slip length $\bar{l}_\mathrm{s}$ (i.e. decreasing $\bar{\alpha}$) decreases the contact time. Furthermore, comparing the leading and first order terms in (4.109) we can see that the expansion only remains uniformly valid provided that

$$\bar{\alpha} \gg k^{\frac{1}{6}}. \tag{4.112}$$

In the case in which $\bar{\alpha} \leq \mathcal{O}(k^{1/6})$ we can find another asymptotic expansion.

Setting $\bar{\alpha} = 0$ in (4.82) we carry out the same asymptotic analysis as before and find that (4.75) at leading order in the limit of small k becomes

$$\frac{\mathrm{d}h_0}{\mathrm{d}t} = -\frac{8L_0 h_0^3}{3\pi}. \tag{4.113}$$

Now, again for long times we must rescale t and h with (4.105). Hence seeking a solution to (4.75) with the scalings given by (4.105) of the form $H = H_0 + \mathcal{O}(k^{1/6})$ yields at leading order

$$\frac{\mathrm{d}H_0}{\mathrm{d}T} = -\frac{L_0 I_0\left(\sqrt{3}H_0^{-\frac{3}{2}}\right)}{\pi I_2\left(\sqrt{3}H_0^{-\frac{3}{2}}\right)}, \tag{4.114}$$

which is separable and leads to

$$T = \frac{\pi}{L_0}\int_{H_0}^{\infty} \frac{I_2\left(\sqrt{3}s^{-\frac{3}{2}}\right)}{I_0\left(\sqrt{3}s^{-\frac{3}{2}}\right)}\ \mathrm{d}s, \tag{4.115}$$

which when $H_0 = 0$ gives the contact time

$$T_{\mathrm{c}} = \frac{\pi}{L_0}\int_{0}^{\infty} \frac{I_2\left(\sqrt{3}s^{-\frac{3}{2}}\right)}{I_0\left(\sqrt{3}s^{-\frac{3}{2}}\right)}\ \mathrm{d}s. \tag{4.116}$$

Evaluating (4.116) numerically and reintroducing the scaling from (4.105), gives the small k leading-order asymptotic solution for the contact time in the case $\bar{\alpha} \leq \mathcal{O}(k^{1/6})$ given by

$$t_{\mathrm{c}} \sim \frac{0.79463\pi}{k^{\frac{2}{3}}L_0} \gg 1 \tag{4.117}$$

to 5 decimal places. Hence for $k \to 0$ in the case $\bar{\alpha} \leq \mathcal{O}(k^{1/6})$, the leading-order solution (4.117) remains uniformly valid up to the contact time $t_{\mathrm{c}} = T_{\mathrm{c}}k^{-2/3}$ where $T_{\mathrm{c}} \simeq 0.79463$ satisfies $H_0(T_{\mathrm{c}}) = 0$. A uniformly-valid leading-order asymptotic solution for the time t in the limit $k \to 0$ in the case $\bar{\alpha} \leq \mathcal{O}(k^{1/6})$ can again be obtained from (4.115) and (4.113) subject to (4.105). This uniformly-valid leading-order asymptotic solution for the time t is given by

$$t(h) = -\frac{3\pi}{16L_0d^2} + \frac{\pi}{k^{\frac{2}{3}}L_0}\int_{\frac{h}{k^{\frac{1}{3}}}}^{\infty} \frac{I_2\left(\sqrt{3}s^{-\frac{3}{2}}\right)}{I_0\left(\sqrt{3}s^{-\frac{3}{2}}\right)}\ \mathrm{d}s. \tag{4.118}$$

Comparing (4.117) with the contact time given by (4.110), we see that the latter is larger than the former by a factor of 1.5874 (> 1), and hence in the limit $k \to 0$, the effect of increasing the slip length is to decrease Q_{out}, and hence to decrease t_{c}.

Figure 4.7 shows that the leading-order asymptotic solutions for the contact time (4.110) and (4.117) agree well with the the exact expression (4.82) in the limit $k \to 0$ and Figure 4.8(a) shows that (4.110) agrees well with (4.82) for $\bar{\alpha} = \mathcal{O}(1)$ and $\bar{\alpha} \gg 1$ and (4.117) agrees well with (4.82) in the limit $\bar{l}_{\mathrm{s}} \to \infty$ (i.e. in the limit $\alpha \to 0$).

(b) Contact time in the limit $k \to \infty$

This subsection contains the derivation of the contact times in the limit of large permeability $k \to \infty$.

Expanding (4.81) in the limit $k \to \infty$ with $\bar{\alpha} = \mathcal{O}(1)$ yields

$$t = \frac{\pi}{L_0k}(d-h) - \frac{4\pi(d^{\frac{5}{2}} - h^{\frac{5}{2}})}{5\sqrt{3}L_0k^{\frac{3}{2}}} + \frac{\pi\left[6\sqrt{3}\bar{\alpha}(d^{\frac{7}{2}} - h^{\frac{7}{2}}) - 7\left(d^4 - h^4\right)\right]}{84L_0k^2} + \mathcal{O}\left(k^{-\frac{5}{2}}\right), \tag{4.119}$$

which, when $h = 0$, gives a contact time of

$$t_{\mathrm{c}} = \frac{\pi d}{L_0k} - \frac{4\pi d^{\frac{5}{2}}}{5\sqrt{3}L_0k^{\frac{3}{2}}} + \frac{\pi\left(6\sqrt{3}d^{\frac{7}{2}}\bar{\alpha} + 7d^4\right)}{84L_0k^2} + \mathcal{O}(k^{-\frac{5}{2}}). \tag{4.120}$$

The Beavers–Joseph constant appears at second order in the limit of large k in asymptotic expansions for the film thickness and contact time (4.119) and (4.120), respectively, showing that, as the slip length $\bar{l}_{\mathrm{s}}$ increases (i.e. as $\bar{\alpha}$ decreases), the contact time decreases. Furthermore, comparing the first order and second order terms in (4.120) we can see that the expansion only remains uniformly valid provided that

$$\bar{\alpha} \ll k^{\frac{1}{2}}. \tag{4.121}$$

In the case in which $\bar{\alpha} \geq \mathcal{O}(k^{1/2})$ we can find another asymptotic expansion.

In this case we take the limit $\bar{\alpha} \to \infty$ in η (given by (4.72)) in (4.119) and (4.120) and seek an asymptotic expansion in the limit $k \to \infty$ giving, to second order, the implicit asymptotic expansion for the fluid gap thickness

$$t(h) = \frac{\pi(d-h)}{L_0 k} - \frac{2\pi\left(d^{\frac{5}{2}} - h^{\frac{5}{2}}\right)}{5\sqrt{3}L_0 k^{\frac{3}{2}}} + \frac{\pi\left(d^4 - h^4\right)}{48 L_0 k^2} + \mathcal{O}\left(k^{-\frac{5}{2}}\right) \tag{4.122}$$

and contact time

$$t_{\mathrm{c}} = \frac{\pi d}{L_0 k} - \frac{2\pi d^{\frac{5}{2}}}{5\sqrt{3}L_0 k^{\frac{3}{2}}} + \frac{\pi d^4}{48 L_0 k^2} + \mathcal{O}(k^{-\frac{5}{2}}), \tag{4.123}$$

in the limit $k \to \infty$. In this limit, the leading-order contact time

$$t_{\mathrm{c}} \sim \frac{\pi d}{L_0 k}, \tag{4.124}$$

is therefore valid for all $\bar{\alpha}$, however, the first order term in (4.120) is valid only in the case $\bar{\alpha} \ll \mathcal{O}(k)$ and in (4.123) is valid only in the case $\bar{\alpha} \geq \mathcal{O}(k)$. Figure 4.7 shows that the leading-order asymptotic solution (4.124) agrees well with the solution (4.82) in the limit $k \to \infty$ for all $\bar{\alpha}$ and Figure 4.8(b) shows that the asymptotic expansion (4.120) to first order agrees well with the solution (4.82) for $\bar{\alpha} = \mathcal{O}(1)$ and $\bar{\alpha} \to 0$ and the asymptotic expansion (4.123) to first order agrees well with the solution (4.82) in the limit $\bar{l}_{\mathrm{s}} \to 0$ (i.e. in the limit $\bar{\alpha} \to \infty$).

4.6.4 Particle paths and penetration depths

In this section we consider the particle paths and penetration depths of fluid particles situated in the fluid and porous bed as the fluid gap thickness reduces from $h(0) = d$ to $h(t_{\mathrm{c}}) = 0$. In particular, we investigate the behaviour of the particle paths in the limit of small and large k and determine the corresponding watershed curves (as defined in Section 4.5.4) and "escape curves", the latter of which divides the fluid gap and/or porous bed into two distinct regions. In particular, fluid particles initially situated below the escape curve will flow out of the base of the porous bed into the region beyond $z = -1$ by the time $t = t_{\mathrm{c}}$, whereas fluid particles initially situated above the escape curve will not flow out of the base of the porous bed into the region beyond $z = -1$ by the time $t = t_{\mathrm{c}}$.

We can eliminate t from (4.33) and (4.34) using (4.75) so that the particle paths are determined by the following ordinary differential equations:

$$\frac{\mathrm{d}r}{\mathrm{d}h} = \frac{6(h-z)(z(k^{\frac{1}{2}}+\bar{\alpha}h)+k^{\frac{1}{2}}h)I_1(\eta r)}{h^3(4k^{\frac{1}{2}}+\bar{\alpha}h)\eta I_0(\eta)}, \tag{4.125}$$

$$\frac{\mathrm{d}z}{\mathrm{d}h} = 1 - \frac{(h-z)^2(2z(k^{\frac{1}{2}}+\bar{\alpha}h)+h(4k^{\frac{1}{2}}+\bar{\alpha}h))I_0(\eta r)}{h^3(4k^{\frac{1}{2}}+\bar{\alpha}h)I_0(\eta)} \tag{4.126}$$

in the fluid gap for $0 \le z \le h$ and

$$\frac{\mathrm{d}r}{\mathrm{d}h} = 0, \tag{4.127}$$

$$\frac{\mathrm{d}z}{\mathrm{d}h} = \frac{1}{\phi}\left[1 - \frac{I_0(\eta r)}{I_0(\eta)}\right] \tag{4.128}$$

in the porous bed for $-1 \le z \le 0$. Equations (4.125)–(4.128) are solved subject to the initial conditions (4.35). In particular, if a fluid particle is initially situated in the fluid gap ($0 \le z_0 \le d$) then (4.125) and (4.126) are solved subject to (4.35) and (4.127) and (4.128) are solved subject to $(r, z) = (\hat{r}, 0)$ at some bearing height $h = \hat{h}$ at which the fluid particle crosses the interface $z = 0$. Hence, for a fluid particle initially situated in the fluid gap, (4.127) and (4.128) have solutions

$$r = \hat{r}, \tag{4.129}$$

$$z = -\frac{1}{\phi}\left[\hat{h} - h - \int_h^{h^*} \frac{I_0(\eta(s)\hat{r})}{I_0(\eta(s))}\,\mathrm{d}s\right]. \tag{4.130}$$

For a fluid particle initially situated in the porous bed ($-1 \le z_0 < 0$) then (4.127) and (4.128) are solved subject to (4.35). In particular, for a fluid particle initially situated in the porous bed, (4.127) and (4.128) have solutions

$$r = r_0, \tag{4.131}$$

$$z - z_0 = -\frac{1}{\phi}\left[d - h - \int_h^{d} \frac{I_0(\eta(s)r_0)}{I_0(\eta(s))}\,\mathrm{d}s\right]. \tag{4.132}$$

For $k \neq 0$ the differential equations (4.125)–(4.128) are solved numerically subject to the initial conditions (4.35). Figures 4.10(a)–(d) show the particle paths as the fluid gap thickness reduces from $h(0) = d$ to $h(t_c) = 0$. In particular,

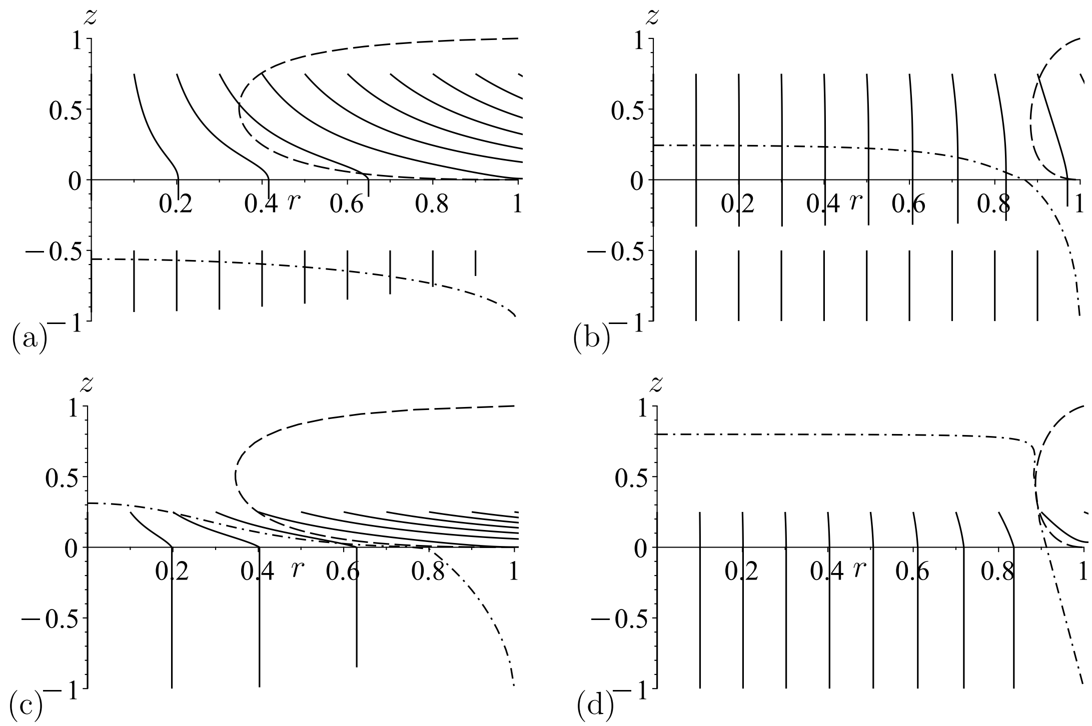

Figure 4.10: Plot of fluid particle paths (r, z) in solid lines given by (4.125)–(4.128) with initial positions in (a, b) $(r_0, z_0) = (0, 0.75)$, $(0.1, 0.75)$, $(0.2, 0.75)$, $\ldots$, $(1, 0.75)$ in the fluid gap and $(r_0, z_0) = (0, -0.5)$, $(0.1, -0.5)$, $(0.2, -0.5)$, $\ldots$, $(1, -0.5)$ in the porous bed and in (c, d) $(r_0, z_0) = (0, 0.2)$, $(0.1, 0.2)$, $(0.2, 0.2)$, $\ldots$, $(1, 0.2)$ in the fluid gap. The permeability in (a, c) is $k = 0.01$ and in (b, d) is $k = 5$. The porosity in (a, b) is $\phi = 0.75$ and in (c, d) is $\phi = 0.2$. In all plots, $\bar{\alpha} = 1$ and $d = 1$ and the watershed and escape curves are plotted with dashed and dash-dot lines, respectively.

Figures 4.10(a)–(d) show that particles initially situated in the fluid gap are either squeezed into the porous bed, or out of the gap, into the region beyond $r = 1$. Since the leading-order radial velocity in the porous bed is zero, i.e. $U = 0$, the particle paths in the porous bed are always vertical, and hence as Figures 4.10(a)–(d) show, fluid particles initially situated in either the fluid gap or the porous bed can only either remain the porous bed or escape into the region beyond $z = -1$.

Since the vertical Darcy velocity $W = -kp$ is always less than or equal to zero (p is always non-negative as can be seen from Figure 4.5), fluid particles that are initially situated in the fluid gap that are squeezed into the porous bed can never re-enter the fluid gap, and similarly, fluid particles that are initially situated in the porous bed can never enter the fluid gap. Figures 4.10(a)–(d) also show that as the

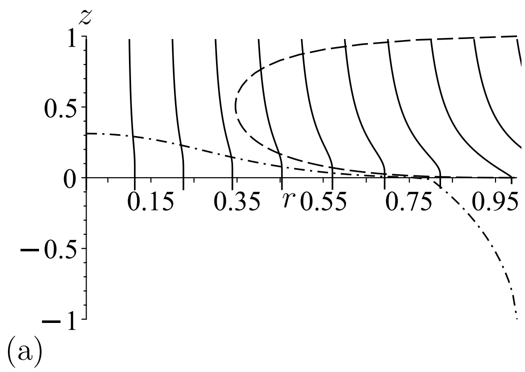

Figure 4.11: Plot of fluid particle paths (r, z) in solid lines given by (4.125)–(4.128) with initial positions (a) $(r_0, z_0) = (0, 0.98)$, $(0.1, 0.98)$, $(0.2, 0.98)$, $\ldots$, $(1, 0.98)$ and in (b) $(r_0, z_0) = (0, 1)$, $(0.1, 1)$, $(0.2, 1)$, $\ldots$, $(1, 1)$. The permeability and porosity in both (a) and (b) are $k = 0.01$ and $\phi = 0.2$, respectively. In all plots $\bar{\alpha} = 1$ and $d = 1$. The watershed and escape curves are plotted with dashed and dash-dot lines, respectively.

permeability becomes large, the vertical fluid velocity w dominates the radial fluid velocity u and the particle paths in the fluid gap follow an increasingly vertical and less curved path from the fluid gap into the porous bed.

As described previously, the watershed curves, found by solving (4.125) and (4.126) numerically backwards in time, to find the curve $\hat{r} = 1$, are plotted with dashed lines in Figures 4.10(a)–(d), divide the fluid gap into two distinct regions, namely, fluid particles initially situated to the left of the watershed curve will be squeezed down into the porous bed, whilst fluid particles initially situated to the right of the watershed curve will be squeezed out of the gap into the region beyond $r = 1$. Figure 4.12(a) shows a series of watershed curves for various values of k. In particular, Figure 4.12 shows that as the permeability k increases, the region to the right of the watershed curve becomes smaller indicating that more fluid enters the porous bed and less out of the gap into the region beyond $r = 1$. This behaviour is qualitatively similar to the behaviour of the watershed curves plotted in Figure 4.4 for the closed-base configuration.

The escape curves plotted with dash-dot lines in Figures 4.10(a)–(d) divide the fluid gap and/or porous bed into two regions, namely, fluid particles initially situated above escape curve will remain in the porous bed after squeezing has ended whilst fluid particles initially situated below the escape curve will escape out of the base of the porous bed into the region beyond $z = -1$. If a particle

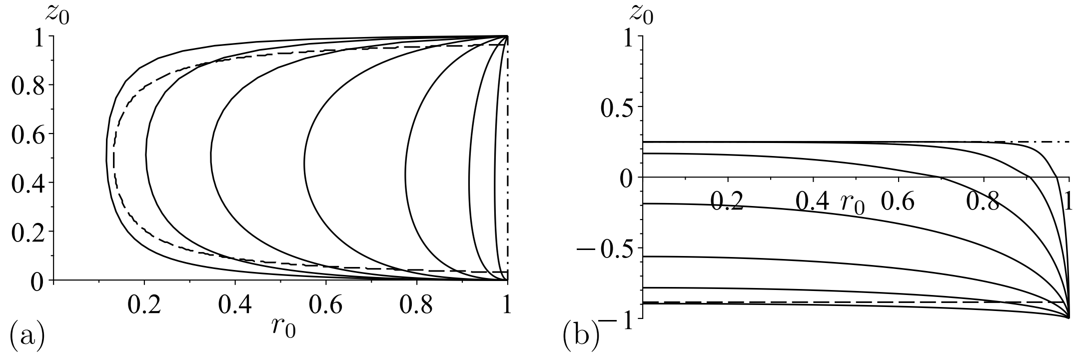

Figure 4.12: Plots of (a) a series of watershed curves in solid lines with the leading-order asymptotic solution in the limit $k \to 0$ in a dashed line given by (4.147) with $k = 10^{-4}$ and the leading-order asymptotic solution in the limit $k \to \infty$ in a dash-dot line given by $r = 1$ and (b) a series of escape curves plotted with the leading-order asymptotic solution in the limit $k \to 0$ in a dashed line given by (4.158) with $k = 10^{-4}$ and the leading-order asymptotic solution in the limit $k \to \infty$ in a dash-dot line given by (4.164) for $\phi = 0.75$. Both figures are plotted for $k = 10^{-4}, 10^{-3}, \ldots, 10^{2}$, $d = 1$ and $\bar{\alpha} = 1$.

is squeezed out of the porous bed then it will cross the interface $z = -1$ at some point $(r, -1) = (\tilde{r}, -1)$, where $\tilde{r} = \tilde{r}(r_0, z_0)$ at $t = \tilde{t}$ ($h = \tilde{h}(\tilde{t})$), and hence the escape curve can be calculated by solving (4.125)–(4.128) numerically backwards in time from $h = 0$ to $h = d$ and evaluating the solution at $z = -1$ and $h = d$ yields the initial position of the fluid particle (r_0, z_0). Figure 4.12(b) shows a series of escape curves for various values of k. In particular, Figure 4.12(b) shows that as the permeability k increases, the region below the escape curve becomes larger, indicating that more fluid is able to escape out of the base of the porous bed into the region beyond $z = -1$ and less fluid remains trapped.

Figure 4.11(a) shows the particle paths of particles initially situated close to the impermeable bearing at $z_0 = 0.98$ and Figure 4.11(b) shows the particle paths of particles initially situated at the impermeable bearing $z_0 = d = 1$. In particular, Figure 4.11(a) shows that particles initially situated above the watershed curve will still make it to the porous bed when $t = t_c$, whilst particles situated in the region to the right of the watershed curve will flow out into the region beyond $r = 1$. Furthermore, Figure 4.11 (b) shows that, due to the no-slip condition, particles initially situated on the impermeable bearing at $h(0) = d$ will remain on the bearing and travel vertically downwards to $h(t_c) = 0$.

The effect of the porosity ϕ can be seen by comparing Figure 4.10(a) and

4.10(b) plotted for $\phi = 0.75$ with Figure 4.10(c) and 4.10(d) plotted for $\phi = 0.2$. In particular, the region below the escape curve in Figure 4.10(a) is smaller than the region below the escape curve in Figure 4.10(c) (both plotted for $k = 0.01$) and the same for Figures 4.10(b) and 4.10(d) (both plotted for $k = 5$), respectively. This shows that if k remains unchanged and ϕ is decreased more fluid has escaped out of the base of the porous bed when $h(t_\mathrm{c}) = 0$. As mentioned in Section 1.4, the porosity ϕ is the proportion of volume of empty space within the porous bed to the total volume of the porous bed, and hence is a measure only of how much fluid the porous bed can retain rather than how easily the fluid can flow through the porous bed, the latter of which is measured by the permeability k only. Therefore, as the porosity ϕ increases, more fluid is retained in the porous bed, and hence less escapes out of the base into the region beyond $z = -1$, which in turn decreases the size of the region below the escape curve, as seen by comparing Figures 4.10(a) and 4.10(b) with Figures 4.10(c) and 4.10(d).

The penetration depth $z_\mathrm{pen} = z(t_\mathrm{c}) < 0$ of a fluid particle either initially situated in the fluid gap or porous bed is also considered. For a particle initially situated in the fluid gap $0 < z_0 < d$, we evaluate (4.130) at $h = 0$ to find

$$z_\mathrm{pen} = -\frac{1}{\phi}\left[\hat{h} - \int_0^{\hat{h}} \frac{I_0(\eta(s)\hat{r})}{I_0(\eta(s))}\,\mathrm{d}s\right], \tag{4.133}$$

and similarly for a fluid particle initially situated in the porous bed $-1 \le z_0 < 0$ we find

$$z_\mathrm{pen} - z_0 = -\frac{1}{\phi}\left[d - \int_0^{d} \frac{I_0(\eta(s)r_0)}{I_0(\eta(s))}\,\mathrm{d}s\right]. \tag{4.134}$$

Figure 4.13(a) and 4.13(b) show z_pen for fluid particles initially situated in the fluid gap $0 < z_0 < d$ as a function of k for small and large values of k, respectively. In particular, Figure 4.13(a) shows that for small values of the permeability the absolute value of the penetration depth $|z_\mathrm{pen}|$ decreases as k decreases and as z_0 increases, however, the effect of z_0 becomes less pronounced as k decreases. Figure 4.13(b) shows that for large values of the permeability, the absolute value of the penetration depth $|z_\mathrm{pen}|$ decreases as k decreases and as z_0 increases. Unlike for small values, for large values of the permeability, Figure 4.13(b) also shows that the effect of the permeability becomes less pronounced as k increases.

Figure 4.14(a) and 4.14(b) show $z_\mathrm{pen} - z_0$ as a function of k for small and large values of k, respectively for fluid particles initially situated in the porous

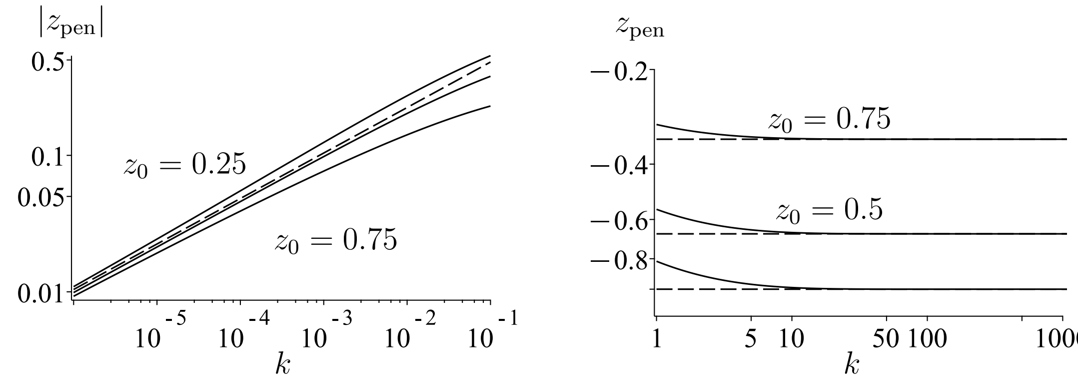

Figure 4.13: (a) A log-log plot of $|z_{\rm pen}|$ as a function of k given by (4.125)–(4.128) subject to $(r_0, z_0) = (0.5k^{1/4}, 0.25)$, $(0.5k^{1/4}, 0.5)$ and $(0.5k^{1/4}, 0.75)$ in solid lines and the leading-order solution in the limit $k \to 0$ given by (4.151) in a dashed line, (b) a log-log plot of $|z_{\rm pen}|$ as a function of k given by (4.125)–(4.128) subject to $(r_0, z_0) = (0.5, 0.25)$, $(0.5, 0.5)$ and $(0.5, 0.75)$ in solid lines and the leading-order solution in the limit $k \to \infty$ given by (4.163) in a dashed line. In all plots $\phi = 0.75$ and $d = 1$

bed $-1 < z_0 < 0$. In particular, Figure 4.14(a) shows that for small values of the permeability, $|z_{\rm pen} - z_0|$ decreases as k decreases and increases as the initial radial position r_0 decreases, however, the effect of r_0 becomes less pronounced as k decreases. For large values of the permeability, Figure 4.14(b) shows that $|z_{\rm pen} - z_0|$ decreases as k decreases and increases as the initial radial position r_0 decreases, however, the effect of r_0 becomes less pronounced as k increases. Figure 4.14(b) also shows that the effect of the permeability becomes less pronounced as k increases.

(a) Asymptotic limit $k \to 0$

(i) Particles initially situated in the fluid gap $0 < z_0 \leq d$

In the case $k = 0$, for which the porous bed is impermeable, equations (4.125) and (4.126) reduce to

$$\frac{dr}{dh} = -\frac{3rz(h - z)}{h^3} \tag{4.135}$$

and

$$\frac{dz}{dh} = -\frac{z^2(2z - 3h)}{h^3}, \tag{4.136}$$

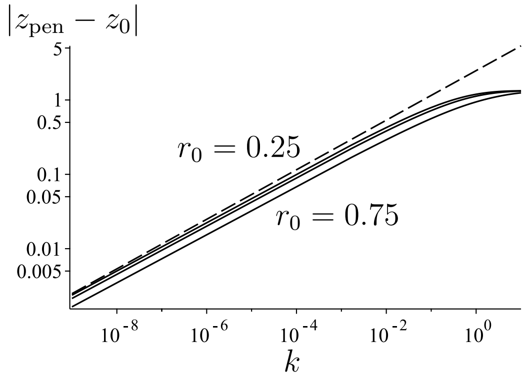

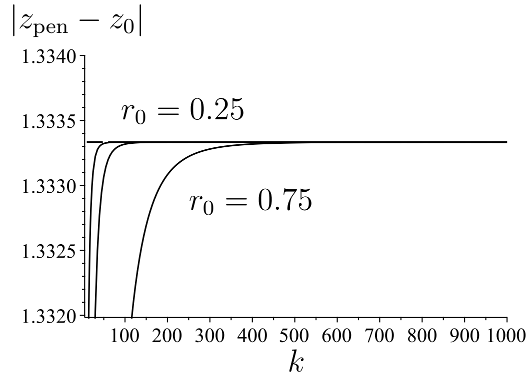

Figure 4.14: Plots of (a) showing a log-log plot of $|z_{\text{pen}} - z_0|$ as a function of k given by (4.125)–(4.128) subject to $r_0 = 0.25, 0.5, 0.75$ in solid lines and the leading-order solution in the limit $k \to 0$ given by (4.157) in a dashed line, (b) $|z_{\text{pen}} - z_0|$ as a function of k given by (4.125)–(4.128) subject to $r_0 = 0.25, 0.5, 0.75$ in solid lines and the leading-order solution in the limit $k \to \infty$ given by (4.166) in a dashed line. In all plots $\bar{\alpha} = 1$, $\phi = 0.75$ and $d = 1$

which when solved subject to (4.35) give the solutions for an impermeable bed given by

$$r = r_0 \left(\frac{4dz_0(d - z_0) + (d - 2z_0)^2 h}{d^2 h} \right)^{\frac{3}{4}}, \tag{4.137}$$

$$z = \frac{h}{2} \left[1 - (d - 2z_0) \left(\frac{h}{4dz_0(d - z_0) + h(d - 2z_0)^2} \right)^{\frac{1}{2}} \right] \tag{4.138}$$

for $z_0 \geq 0$. As shown in Section 4.6.3, in the limit $k \to 0$, the porous bed remains impermeable for short and intermediate times and only for long times $t = \mathcal{O}(k^{-2/3})$ does the effect of the permeability appear at leading order. Knox et al. [86] showed that for long times, when $t = \mathcal{O}(k^{-2/3})$ and $h = \mathcal{O}(k^{1/3})$, the solution for an impermeable bed behaves like

$$r \sim r_0 \left(\frac{4(d - z_0)z_0}{hd} \right)^{\frac{3}{4}} = \mathcal{O} \left(\frac{r_0((d - z_0)z_0)^{\frac{3}{4}}}{k^{\frac{1}{4}}} \right) \tag{4.139}$$

and

$$z \sim \frac{h}{2} = \mathcal{O}(k^{\frac{1}{3}}), \tag{4.140}$$

which shows that particles with initial positions near the axis $r = 0$ (with $r_0 = \mathcal{O}(k^{1/4})$) or near the porous bed or bearing (with $z_0 = \mathcal{O}(k^{1/3})$ or $d - z_0 = \mathcal{O}(k^{1/3})$) have not flowed out of the gap beyond $r = 1$ at long times. In order to determine the behaviour of the particle paths in the limit $k \to 0$ for long times we rescale r_0, z, h and t according to

$$r_0 = R_0 k^{\frac{1}{4}}, \quad z = Zk^{\frac{1}{3}}, \quad h = Hk^{\frac{1}{3}}, \quad t = Tk^{-\frac{2}{3}}, \tag{4.141}$$

where R_0, Z, H, and T are $\mathcal{O}(1)$ in the limit $k \to 0$. Using these scalings the particle path equations in the fluid gap (4.125) and (4.126) become at leading order

$$\frac{\mathrm{d}r}{\mathrm{d}H} = -\frac{\sqrt{3}Z(H-Z)I_1(\sqrt{12H^{-3}}r)}{\sqrt{H^3}I_0(\sqrt{12H^{-3}})}, \tag{4.142}$$

$$\frac{\mathrm{d}Z}{\mathrm{d}H} = 1 - \frac{(H-z)^2(H+2Z)I_0(\sqrt{12H^{-3}}r)}{H^3 I_0(\sqrt{12H^{-3}})}. \tag{4.143}$$

The solutions of (4.142) and (4.143) must match with the $h \to 0$ limits of (4.137) and (4.138) as $H \to \infty$ given by

$$r \sim R_0 \left(\frac{4(d-z_0)z_0}{Hd} \right)^{\frac{3}{4}} \to 0 \tag{4.144}$$

as $H \to \infty$ and

$$Z \sim \frac{H}{2} \to \infty \tag{4.145}$$

as $H \to \infty$, respectively. To find the vertical position of the fluid particle $Z(T)$, which is independent of the initial position z_0, we solve (4.143) numerically as an initial value problem, shooting from $Z = 0$ at the unknown value of the fluid gap thickness $H = \hat{H}$ at which the particle crosses the interface $Z = 0$ to $Z = H_\infty/2$, where $H_\infty \gg 1$ is some large value which we use to approximate the matching condition (4.145). This procedure leads to the approximate value $H^* \simeq 0.7856$ (to 4 decimal places) calculated with $H_\infty = 10^8$. In the case of the closed-base configuration (with permeability $\hat{k}$), Knox et al. [86] found the corresponding value to be $\hat{H} \simeq 0.4958$. The leading-order radial position of the fluid particle is found by solving (4.142) numerically from $H = 0$ to $H = \hat{H}$, at $r = \hat{r}$, where again, $\hat{r}$ is the radial position at which the fluid particle crosses the interface $Z = 0$. If we follow this procedure with $\hat{r} = 1$, we can derive a leading-order asymptotic solution for the watershed curve in the limit $k \to 0$. This numerically calculated solution is plotted in Figure 4.15 along with its asymptotic behaviour for large H

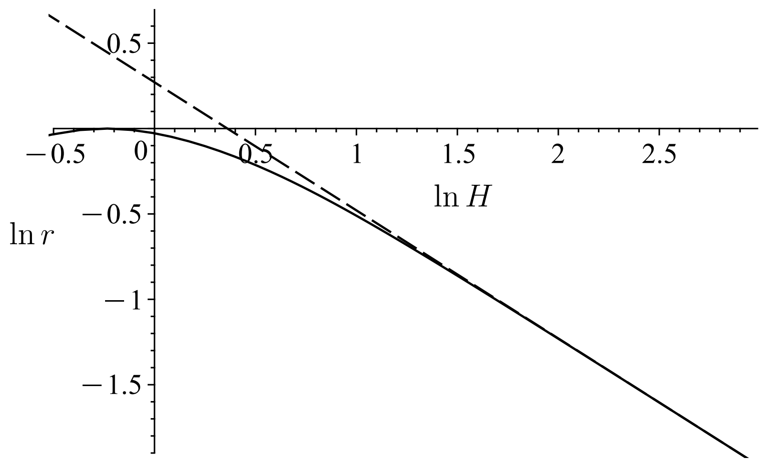

Figure 4.15: Plot of $\ln r$, where r is the numerically calculated solution of (4.142) for $\hat{r} = 1$, as a function of $\ln H$. The large H asymptotic behaviour given by (4.146) is plotted in a dashed line.

given by

$$r \sim 1.3111 H^{-\frac{3}{4}}, \tag{4.146}$$

to 4 decimal places. In the case of the closed-base configuration (with permeability $\hat{k}$), Knox et al. [86] found that the corresponding coefficient of $H^{-3/4}$ in the corresponding version of equation (4.146) to be 1.0708. Therefore, imposing the matching condition (4.144) yields the leading-order asymptotic solution for the watershed curve in the limit $k \to 0$ given by

$$r_0 = 1.3111 k^{\frac{1}{4}} \left(\frac{d}{4(d - z_0) z_0} \right)^{\frac{3}{4}}. \tag{4.147}$$

This leading-order asymptotic solution for the watershed curve in the limit $k \to 0$ is plotted in Figure 4.12(a). In particular, Figure 4.12(a) shows that the leading-order asymptotic watershed curve compares well with the numerical solution for $z_0 = \mathcal{O}(1)$, but does not perform well for $z_0 = \mathcal{O}(k^{1/3}) \ll 1$ or $d - z_0 = \mathcal{O}(k^{1/3}) \ll 1$, i.e. for particles initially situated near the porous bed or the bearing. It also shows that in this limit, particles situated near the axis will never be squeezed out of the gap into the region beyond $r = 1$ and can only be squeezed into the porous bed through the interface $z = 0$.

In the limit $k \to 0$, we may rescale (4.127) and (4.128) subject to the long-time scalings (4.105) to obtain the leading-order equations of a particle path after it has entered the porous bed ($0 \leq H \leq \hat{H}$) given by

$$\frac{\mathrm{d}R}{\mathrm{d}H} = 0, \tag{4.148}$$

$$\frac{\mathrm{d}Z}{\mathrm{d}H} = \frac{1}{\phi}\left[1 - \frac{I_0(\hat{r}\sqrt{12H^{-3}})}{I_0(\sqrt{12H^{-3}})}\right], \tag{4.149}$$

where we have defined $r = \hat{r} + k^{1/3}R$. Solving (4.148) and (4.149) subject to $R = 0$ and $Z = 0$ at $H = \hat{H}$ gives the solution

$$r = \hat{r} \quad \text{and} \quad z = -\frac{k^{\frac{1}{3}}}{\phi}\left[(\hat{H} - H) - \int_H^{\hat{H}} \frac{I_0(\hat{r}\sqrt{12\xi^{-3}})}{I_0(\sqrt{12\xi^{-3}})}\,\mathrm{d}\xi\right], \tag{4.150}$$

which, setting $H = 0$, gives the leading-order solution for the penetration depth in the limit $k \to 0$, namely

$$z_{\text{pen}} = -\frac{k^{\frac{1}{3}}}{\phi}\left[\hat{H} - \int_0^{\hat{H}} \frac{I_0(\hat{r}\sqrt{12\xi^{-3}})}{I_0(\sqrt{12\xi^{-3}})}\,\mathrm{d}\xi\right]. \tag{4.151}$$

Equation (4.151) shows that $|z_{\text{pen}}| = \mathcal{O}(k^{1/3}) \ll 1$, and so in particular, shows that in the limit $k \to 0$, particles initially situated in the fluid gap will never escape out of the base of the porous bed into the region beyond $z = -1$. Figure 4.13(a) shows plots of the numerically-calculated solution $|z_{\text{pen}}|$ and its leading-order small k asymptotic solution given by (4.151). (using the default numerical differential equation solver `dsolve` and numerical integration tool `int` of the symbolic and numerical mathematics software MAPLE [95]). In particular, as previously mentioned, Figure 4.13 shows $|z_{\text{pen}}|$ becomes less dependent on z_0 as k decreases, in agreement with the leading-order asymptotic solution (4.151) which is dependent on k but independent of z_0.

(ii) Particles initially situated in the porous bed $-1 \leq z_0 < 0$

At leading order for short and intermediate times the particle paths initially situated in the porous bed ($z_0 < 0$) follow the path (r, z), where

$$r = r_0 \tag{4.152}$$

and

$$z - z_0 = -\frac{3k(1 - r_0^2)(h^2 - d^2)}{2\phi d^2 h^2}. \tag{4.153}$$

The particle path solutions given by (4.152) and (4.153) show that the radial positions of the particles do not change while the vertical positions of the fluid particles remain very close to their initial positions z_0 in the limit $k \to 0$ for these times.

For long times, we rescale the variables in (4.127) and (4.128) subject to (4.105) and solve subject to $r = r_0$ and $Z = Z_0$ as $H \to \infty$ leading again to $r = r_0$ throughout the porous bed and

$$\frac{\mathrm{d}Z}{\mathrm{d}H} = \frac{1}{\phi}\left[1 - \frac{1}{I_0(\sqrt{12H^{-3}})}\right], \tag{4.154}$$

which has solution

$$Z - Z_0 = -\frac{1}{\phi}\int_H^\infty 1 - \frac{1}{I_0(\sqrt{12s^{-3}})}\mathrm{d}s. \tag{4.155}$$

Hence when $H = 0$, the penetration depth is given by

$$Z_{\text{pen}} - Z_0 = -\frac{1.86203}{\phi}, \tag{4.156}$$

which with (4.105) reintroduced gives

$$z_{\text{pen}} - z_0 \sim -\frac{1.86203k^{\frac{1}{3}}}{\phi}. \tag{4.157}$$

Equation (4.157) shows that $|z_{\text{pen}} - z_0| = \mathcal{O}(k^{1/3}) \ll 1$, and so, in particular, shows that in the limit $k \to 0$, fluid particles initially situated in the porous bed will stay very close to their initial positions. Figure 4.14 shows plots of the numerically-calculated solution $|z_{\text{pen}} - z_0|$ and its leading-order small k asymptotic solution given by (4.157). In particular, Figure 4.14 shows that for small values of k, the distance between the initial position z_0 of a fluid particle and its penetration depth z_{pen} increases as r_0 decreases, i.e. as the initial position of the fluid particle approaches the origin. Physically, this behaviour is due to less fluid in the fluid gap leaving the gap into the region beyond $r = 1$ as the initial position r_0 approaches the origin, and so more fluid is forced into the porous bed near the origin, which pushes fluid particles initially situated in the porous bed in this region, further down than those initially situated closer to $r_0 = 1$. Figure 4.14 also shows that the small k asymptotic solution given by (4.157) agrees well with the numerically-calculated solution $|z_{\text{pen}}|$, but becomes less accurate as r_0 increases.

Since equation (4.151) shows that fluid particles initially situated in the fluid gap never escape out of the base of the porous bed into the region beyond $z = -1$, the escape curve is calculated by setting $z = -1$ in (4.157) which gives the leading-order asymptotic solution for the escape curve in the limit $k \to 0$

$$z_0 = \frac{1.86203 k^{\frac{1}{3}}}{\phi} - 1. \tag{4.158}$$

Figure 4.12(b) shows the leading-order asymptotic solution (4.158) compared to the numerically-calculated escape curve for $k = 10^{-4}$. In particular, Figure 4.12(b) shows that in the limit $k \to 0$ only particles initially situated close to the base of the porous bed at $z = -1$ are able to escape for long times and that the leading-order asymptotic solution (4.158) agrees well with the numerically-calculated escape curve near $r = 0$ and is less accurate near $r = 1$. Equation (4.158) also shows that if $k = 0$, i.e. the bed is impermeable then the escape curve is $z_0 = -1$ indicating that no particles within the bed can escape out of the base of the bed, as expected.

(b) Asymptotic limit $k \to \infty$

(i) Particles initially situated in the fluid gap $0 < z_0 \leq d$

In this subsection, we describe the leading-order behaviour of the paths of fluid particles initially situated in the fluid gap ($0 \leq z_0 \leq d$) in the limit of large permeability $k \to \infty$.

In the limit $k \to \infty$, the ordinary differential equations (4.125)–(4.128) become

$$\frac{\mathrm{d}r}{\mathrm{d}h} = \frac{6(h-z)z + h}{4h^3\sqrt{3kh^{-3}}r} \mathrm{e}^{-\sqrt{3kh^{-3}}(1-r)} \to 0, \tag{4.159}$$

$$\frac{\mathrm{d}z}{\mathrm{d}h} = 1 - \frac{(h-z)^2(z+2h)}{2h^3\sqrt{r}} \mathrm{e}^{-\sqrt{3kh^{-3}}(1-r)} \to 1 \tag{4.160}$$

for $0 \leq z \leq h$ and

$$\frac{\mathrm{d}r}{\mathrm{d}h} = 0, \quad \frac{\mathrm{d}z}{\mathrm{d}h} = \frac{1}{\phi}\left[1 - \frac{1}{\sqrt{r}} \mathrm{e}^{-\sqrt{\frac{3k}{h^3}}(1-r)}\right] \to \frac{1}{\phi} \tag{4.161}$$

for $-1 \leq z < 0$ at leading order, except for an exponentially small region near $r = 1$.

Solving (4.159)–(4.161) subject to (4.35) and $z = 0$ on $h = \hat{h}$, the solutions for the particle paths in the limit $k \to \infty$ are given by

$$r = r_0 \quad \text{and} \quad z = \begin{cases} h - \hat{h} & \text{for} \quad 0 \leq z \leq h \\ \dfrac{1}{\phi}(h - \hat{h}) & \text{for} \quad -1 \leq z \leq 0, \end{cases} \tag{4.162}$$

where $\hat{h} = d - z_0$ is the bearing height at which the particle path reaches the interface $z = 0$. The vertical fluid velocity $w = \mathcal{O}(k) \ll 1$ is much larger than the radial fluid velocity $u = \mathcal{O}(\mathrm{e}^{-(1-r)\sqrt{k}}) \ll 1$ at leading order in the limit $k \to \infty$, and hence the particle paths are directed vertically from their initial positions $(r, z) = (r_0, z_0)$ to the interface $(r, z) = (r_0, 0)$ when $h = \hat{h}$. This in turn means that the watershed curve in the limit $k \to \infty$ is simply the vertical line $r_0 = 1$, as shown in Figure 4.12. In particular, Figure 4.12 shows that as k becomes large the watershed curves become closer to completely vertical, approaching the asymptotic watershed curve $r_0 = 1$ in the limit $k \to \infty$.

Evaluating the solution for z given by (4.162) at $h = 0$, gives the leading-order penetration depth in the limit $k \to \infty$,

$$z_{\text{pen}} = -\frac{\hat{h}}{\phi} = \mathcal{O}(1). \tag{4.163}$$

Figure 4.13(b) shows plots of the numerically-calculated solution and leading-order large k asymptotic solution z_{pen} given by (4.163). In particular, Figure 4.13(b) shows that the dependence of z_{pen} on k decreases as k increases, in agreement with the leading-order asymptotic solution (4.163) which is $\mathcal{O}(1)$ in the limit $k \to \infty$.

Since $r = \hat{r} = r_0$ throughout for $-1 \leq z \leq h$, evaluating (4.163) at $z_{\text{pen}} = -1$ yields the leading-order expression for the escape curve in the limit $k \to \infty$ to be

$$z_0 = d - \phi. \tag{4.164}$$

Since $0 \leq z_0 \leq 1$, the expression for the escape curve (4.164) is valid when $d \geq \phi$. If we reintroduce dimensional variables to this condition relating the initial bearing height and porosity, then we obtain $H_{\mathrm{f}}^*/H_{\mathrm{p}}^* \geq V_{\mathrm{p}}^*/V_{\mathrm{bed}}^*$ which, by writing $V_{\mathrm{bed}}^* = \pi R^{*2} H_{\mathrm{p}}^*$, becomes $V_{\mathrm{f}}^* = \pi R^{*2} H_{\mathrm{f}}^* \geq V_{\mathrm{p}}^*$, where we have defined V_{f} to be the initial volume of the fluid gap. Therefore, in the limit $k \to \infty$, if the initial volume of the fluid gap V_{f}^* is greater than or equal to the volume of fluid in the porous bed V_{p}^*, then the escape curve given by (4.164) resides in the region $0 \leq z_0 \leq 1$, and all of the fluid initially situated in the porous bed will be squeezed out of the base of the porous bed into the region beyond $z = -1$ when $t = t_{\mathrm{c}}$.

Figure 4.12(b) shows the leading-order escape curve in the limit $k \to \infty$, and in particular, shows that in this limit, any particles that are initially situated above the line $d - \phi$ remain in the porous bed and do not escape out of the base into the region beyond $z = -1$ after all of the fluid has been squeezed out of the gap.

(ii) Particles initially situated in the porous bed $-1 \leq z_0 < 0$

Solving (4.161) subject to the conditions (4.35) yields the solutions for the particle paths for particles initially situated in porous bed to be

$$r = r_0 \quad \text{and} \quad z - z_0 = -\frac{1}{\phi}(d - h). \tag{4.165}$$

Evaluating the solution for z given by (4.165) at $h = 0$, gives the leading-order penetration depth in the limit $k \to \infty$,

$$z_{\mathrm{pen}} = z_0 - \frac{d}{\phi} = \mathcal{O}(1). \tag{4.166}$$

Figure 4.14(b) shows plots of the numerically-calculated solution and the leading-order large k asymptotic solution $|z_{\mathrm{pen}} - z_0|$ given by (4.166). In particular, Figure 4.14(b) shows that the dependence of $|z_{\mathrm{pen}} - z_0|$ on k decreases as k increases, in agreement with the leading-order asymptotic solution (4.166), which is $\mathcal{O}(1)$ in the limit $k \to \infty$.

Evaluating (4.166) at $z_{\mathrm{pen}} = -1$ yields the leading-order expression for the escape curve in the limit $k \to \infty$ to be

$$z_0 = -\left(1 - \frac{d}{\phi}\right). \tag{4.167}$$

Since $-1 \leq z_0 < 0$, the expression for the escape curve (4.167) is valid when $d < \phi$. Again, if we reintroduce dimensional variables to this condition relating the initial bearing height and porosity, we obtain $H_{\mathrm{f}}^*/H_{\mathrm{p}}^* < V_{\mathrm{p}}^*/V_{\mathrm{bed}}^*$ which, by writing $V_{\mathrm{bed}}^* = \pi R^{*2} H_{\mathrm{p}}^*$, becomes $V_{\mathrm{f}}^* = \pi R^{*2} H_{\mathrm{f}}^* < V_{\mathrm{p}}^*$. Therefore, in the limit

$k \to \infty$, if the initial volume of the fluid gap V_f^* is less than the volume of fluid in the porous bed V_p^*, then there is an insufficient volume of fluid in the fluid gap to be able to squeeze all of the fluid out of the base of the porous bed into the region beyond $z = -1$, and so the escape curve given by (4.167) resides in the region $-1 \leq z_0 \leq 0$, and particles initially situated above the escape curve given by (4.167) remain in the porous bed when $t = t_\mathrm{c}$. From (4.167), the fraction of particles initially situated in the porous bed that remain in the porous bed when $t = t_\mathrm{c}$ is equal to $1 - d/\phi$.

4.7 Conclusions

In this chapter we considered the open-base configuration of the axisymmetric porous squeeze-film problem (as shown in Figure 4.1(b)) in which a thin layer of Newtonian fluid within the gap between a flat impermeable bearing moving under a prescribed constant load and a flat porous bed, is forced to either flow out of the side of the gap or into the porous bed. Consequently, the fluid in the porous bed is forced to either flow out of the base of the porous bed or remains in the porous bed when the bearing and porous bed contact, which occurs in a finite time.

The related problem of the closed-base configuration, as shown in Figure 4.1(a), previously described by Knox et al. [86], was briefly described in Section 4.5 for the purpose of comparison with the results of the open-base configuration described in Section 4.6.

In Section 4.6, we derived equations for the Darcy pressure P given by (4.57) and Darcy velocity $\mathbf{U} = (U, W)$ given by (4.63), fluid pressure p given by (4.76), fluid velocity $\mathbf{u} = (u, w)$ given by (4.78)–(4.79), bearing height h at time t given by (4.81), and contact time t_c when $h = 0$ given by (4.82). In addition, we showed that if the permeability of the porous bed in the open-base configuration is the same size as the permeability of the closed-base configuration, then at leading order in the limit $\epsilon \to 0$, the velocity in the fluid gap is entirely vertical, i.e. $w = \mathcal{O}(\epsilon^{-2}) \gg u = \mathcal{O}(1)$, and the contact time $t_\mathrm{c} = \mathcal{O}(\epsilon^2)$, i.e. all of the fluid is squeezed out of the fluid gap extremely quickly. However, when the permeability is much smaller than this, the vertical velocity in the porous bed is greatly reduced and contact occurs on a much longer timescale. Specifically, by introducing the scaling (4.61), the porous bed was made a factor of ϵ^2 less permeable than that considered for the closed-base configuration. This slowed down the vertical Darcy velocity W in the porous bed, and hence the vertical fluid velocity w in the fluid gap, which made the radial fluid velocity and vertical fluid velocity both $\mathcal{O}(1)$, and led to an $\mathcal{O}(1)$ contact time.

The effect of reducing the size of the permeability for the open-base configuration can be seen by comparing the leading-order finite contact times in the limits of small and large permeability for both configurations in dimensional variables. Table 4.1 and Table 4.2 show these dimensional contact times for the closed-base and open-base configurations, respectively, and Table 4.3 shows the dimensional contact time for the open-base configuration divided by the dimensional contact time for the closed-base configuration in the limits of small and large permeability and of $\mathcal{O}(1)$, small, and large slip length. Table 4.3 shows that despite the porous bed for the open-base configuration being less permeable than for the closed-base configuration, the contact time for the open-base configuration is always smaller than the contact time for the closed-base configuration. This may not at first seem in accord with physical intuition, however, by comparing the particle paths shown in Figure 4.4 for the closed-base configuration with those shown in Figure 4.10 for the open-base configuration, it is clear that the fluid in the porous bed, especially near $r = 0$, has much less distance to travel before it is able to leave the porous bed in the open-base configuration compared with the closed-base configuration. Hence, despite the porous bed being less permeable for the open-base configuration than the closed-base configuration, the fluid can flow vertically through and out of the base of the porous bed in the open-base configuration, rather than being redirected by the impermeable layer below the porous bed towards the region beyond $r = 1$ in the closed-base configuration, and so the contact time for the open-base configuration is much less than for the closed-base configuration.

The behaviour of the contact time t_c, for the open-base configuration, as the permeability of the porous bed k and slip-length $\bar{l}_\mathrm{s}$ varied was analysed in Section 4.6.3. We note here that, as discussed in Section 4.2, the limits $k \to 0$ and $\bar{l}_\mathrm{s} \to 0$ correspond to the limit in which the length scale associated with the pores in the porous bed $\mathcal{O}(k^{*1/2})$ is much smaller than the length scale associated with porous bed H_p^*, and hence are the most physically relevant. Therefore, in reality, the amount of velocity slip at the interface between the fluid gap and porous bed will always be small. Meanwhile, the limits $k \to \infty$ and $\bar{l}_\mathrm{s} \to \infty$ correspond to the non-physical limit in which $k^{*1/2}/H_\mathrm{p}^* \gg 1$ and the mathematical analysis of this limit is included in this chapter for completeness only. Figure 4.7 shows that

Slip length	Small permeability	Large permeability
$\mathcal{O}(1)$	$\dfrac{\pi^2 R^{*4}\mu^*}{\sqrt{3}(12k^* H_\mathrm{p}^*)^{\frac{2}{3}} L_0^*}$	$\dfrac{\pi\mu^* R^{*4} H_\mathrm{f}^*}{8H_\mathrm{p}^* k^* L_0^*}$
Small	$\dfrac{\pi^2 R^{*4}\mu^*}{\sqrt{3}(12k^* H_\mathrm{p}^*)^{\frac{2}{3}} L_0^*}$	$\dfrac{\pi\mu^* R^{*4}}{4k^* L_0^*}\ln\left(\dfrac{H_\mathrm{f}^* + 2H_\mathrm{p}^*}{2H_\mathrm{p}^*}\right)$
Large	$\dfrac{\pi^2 R^{*4}\mu^*}{4\sqrt{3}(3k^* H_\mathrm{p}^*)^{\frac{2}{3}} L_0^*}$	$\dfrac{\pi\mu^* R^{*4} H_\mathrm{f}^*}{8H_\mathrm{p}^* k^* L_0^*}$

Table 4.1: The leading-order asymptotic expressions for the dimensional contact time for the closed-base configuration t_c^* in the limits of small and large permeability and for $\mathcal{O}(1)$, small, and large slip length.

Slip length	Small permeability	Large permeability
$\mathcal{O}(1)$	$\dfrac{1.26139\pi\mu^*}{L_0^*}\left(\dfrac{R^{*4}H_\mathrm{p}^*}{k^*}\right)^{\frac{2}{3}}$	$\dfrac{\pi\mu^* R^{*2} H_\mathrm{f}^* H_\mathrm{p}^*}{L_0^* k^*}$
Small	$\dfrac{1.26139\pi\mu^*}{L_0^*}\left(\dfrac{R^{*4}H_\mathrm{p}^*}{k^*}\right)^{\frac{2}{3}}$	$\dfrac{\pi\mu^* R^{*2} H_\mathrm{f}^* H_\mathrm{p}^*}{L_0^* k^*}$
Large	$\dfrac{0.79463\pi\mu^*}{L_0^*}\left(\dfrac{R^{*4}H_\mathrm{p}^*}{k^*}\right)^{\frac{2}{3}}$	$\dfrac{\pi\mu^* R^{*2} H_\mathrm{f}^* H_\mathrm{p}^*}{L_0^* k^*}$

Table 4.2: The leading-order asymptotic expressions for the dimensional contact time for the open-base configuration t_c^* in the limits of small and large permeability and for $\mathcal{O}(1)$, small, and large slip length.

Slip length	Small permeability	Large permeability
$\mathcal{O}(1)$	$\dfrac{1.26139\sqrt{3}}{\pi}(\sqrt{12}\epsilon)^{\frac{4}{3}} \ll 1$	$8\epsilon^2 \ll 1$
Small	$\dfrac{1.26139\sqrt{3}}{\pi}(\sqrt{12}\epsilon)^{\frac{4}{3}} \ll 1$	$\dfrac{4d}{\ln\left(\frac{d+2}{2}\right)}\epsilon^2 \ll 1$
Large	$\dfrac{3.17852\sqrt{3}}{\pi}\epsilon^{\frac{4}{3}} \ll 1$	$8\epsilon^2 \ll 1$

Table 4.3: The leading-order expressions for the dimensional contact time for the open-base configuration given by Table 4.2, divided by the corresponding leading-order asymptotic expressions for the dimensional contact time for the closed-base configuration given by Table 4.1, in the limits of small and large permeability and for $\mathcal{O}(1)$, small, and large slip length.

the contact time t_c decreases as the permeability of the porous bed k increases. Furthermore, it was shown that $t_c = \mathcal{O}(k^{-2/3}) \gg 1$ in the limit $k \to 0$ and $t_c = \mathcal{O}(k^{-1}) \ll 1$ in the limit $k \to \infty$. At first order in the limit $k \to 0$ we found that the expansion for t_c given by (4.109) is not uniformly valid in the limit of large slip length $\bar{l}_s \to \infty$ (i.e. in the limit $\bar{\alpha} \to 0$), and so a different leading-order contact time was found in this case given by (4.117). Similarly, at second order in the limit $k \to \infty$ we found that the expansion for t_c given by (4.120) is not uniformly valid in the case of no slip $\bar{l}_s \to 0$ (i.e. in the limit $\bar{\alpha} \to \infty$), and so a different expression for the contact time with the same leading-order behaviour but different first-order behaviour was found in this case given by (4.123). Figure 4.8 shows a more detailed view of t_c as a function of k. In particular, Figure 4.8(a) shows t_c for small values of the permeability which shows that the contact time increases as $\bar{\alpha}$ increases and matches closely with the asymptotic solutions given by (4.109) and (4.117). Figure 4.8(b) shows t_c for large values of the permeability which shows that the contact time increases as $\bar{\alpha}$ increases and matches closely with the asymptotic solutions given by (4.120) and (4.123). This behaviour is qualitatively different from that in the closed-base configuration, for which, the contact time t_c increases as the Beavers–Joseph constant α increases for small values of $\hat{k}$ but decreases as α increases for large values of $\hat{k}$, as shown in Figure 4.2. In the case of the two-dimensional porous squeeze-film problem, treated briefly in Appendix E, the expression for the finite contact time is given by equation (E.7). In particular, the results obtained in Appendix E show that the contact times in the limit of small and large permeability are of the same order of magnitude of those calculated for the corresponding axisymmetric porous squeeze-film problem, i.e. $t_c = \mathcal{O}(k^{-2/3}) \gg 1$ in the limit $k \to 0$ and $k = \mathcal{O}(k^{-1}) \ll 1$ in the limit $k \to \infty$.

The particle paths of fluid particles initially situated in either the fluid gap or the porous bed were also analysed in Chapter 4. Figure 4.4 shows that for the closed-base configuration particles initially situated in the fluid gap may either flow out of the gap into the region beyond $r = 1$ or down into the porous bed, through the interface $z = 0$, whilst fluid particles initially situated in the porous bed can only flow out of the porous bed, into the region beyond $r = 1$. Figure 4.10 shows that for the open-base configuration particles initially situated in the fluid gap may either flow out of the gap into the region beyond $r = 1$ or down into the porous bed, through the interface $z = 0$, whilst particles initially situated in the porous bed can only flow out of the base of the porous bed, into the region beyond

$z = -1$. This is due to the fact that the radial Darcy velocity for the open-base configuration is simply $U = 0$, and so there is no flow in the radial direction within the porous bed in this case.

The watershed curve that divides the fluid gap into a region of fluid particles which flow into the porous bed and a region of fluid particles which flow into the region beyond $r = 1$ was also calculated. The watershed curves in Figure 4.12 show that as k increases more fluid particles initially situated in the fluid gap are able to enter the porous bed and less flow out into the region beyond $r = 1$. In particular, in the limit $k \to 0$ the leading-order solution for the watershed curve shows that only fluid particles initially situated in the fluid gap near the origin will never flow out of the fluid gap into the region beyond $r = 1$, while in the limit $k \to \infty$ the leading-order solution for the watershed curve shows that all of the fluid particles initially situated in the fluid gap flow down into the porous bed.

The penetration depths for the open-base configuration were also analysed. In particular, it was shown that in the limit $k \to 0$, fluid particles initially situated in the fluid gap near $r = 0$, have penetration depths $|z_{\mathrm{pen}}| = \mathcal{O}(k^{1/3}) \ll 1$, and so are never able to escape out of the base of the porous bed. Additionally, for fluid particles initially situated in the porous bed, it was shown that the relative penetration depth $|z_{\mathrm{pen}} - z_0| = \mathcal{O}(k^{1/3}) \ll 1$, and so only particles very close to the base of the porous bed are able to escape out of the base into the region beyond $z = -1$. It was also shown that in the limit $k \to \infty$, fluid particles initially situated in the fluid gap, have relative penetration depths $|z_{\mathrm{pen}} - z_0| = \mathcal{O}(1)$, and so are able to penetrate deep into the porous bed and potentially escape out of the base of the porous bed into the region beyond $z = -1$. Additionally, for fluid particles initially situated in the porous bed, it was shown that the relative penetration depth $|z_{\mathrm{pen}} - z_0| = \mathcal{O}(1)$, and so again are able to penetrate deep into the porous bed and potentially escape out of the base of the porous bed into the region beyond $z = -1$.

The escape curves that divide the fluid gap and porous bed into a region of fluid particles which flow out of the base of the porous bed into the region beyond $z = -1$ and those that remain in the porous bed when $t = t_{\mathrm{c}}$ was also calculated. The escape curves in Figure 4.12 show that as k increases more fluid particles initially situated in either the fluid gap or porous bed are able to escape out of the base of the porous bed and less remain in the porous bed when $t = t_{\mathrm{c}}$. In particular, in the limit $k \to 0$ the leading-order solution for the escape curve shows that only particles initially situated close to the base of the porous bed will escape into the region beyond $z = -1$. In the limit $k \to \infty$, there are two possible solutions for the leading-order escape curve. If the initial bearing height satisfies $d \geq \phi$ (or equivalently $V_{\mathrm{f}}^* \geq V_{\mathrm{p}}^*$), i.e. when the initial volume of the fluid gap is greater than or equal to the volume of fluid in the porous bed, then all of the fluid initially situated in the porous bed will be squeezed out of the base of the porous bed into the region beyond $z = -1$ when $t = t_{\mathrm{c}}$. If, however, the initial bearing height satisfies $d < \phi$ (or equivalently $V_{\mathrm{f}}^* < V_{\mathrm{p}}^*$), i.e. when the initial volume of the fluid gap is less than the volume of fluid in the porous bed, then a fraction of the fluid initially situated in the porous bed, equal to $1 - d/\phi$, will remain in the porous bed when $t = t_{\mathrm{c}}$.

In summary, in this chapter we first compared the behaviour of the fluid gap thickness, contact time and particle paths of the closed-base and open-base configurations. In particular, in the limits of small and large permeability and of small and large slip length, the two configurations exhibit qualitatively different behaviour. For example, in the limit of small permeability, the contact time in the closed-base configuration increases as the slip length decreases, however, in the limit of large permeability, the opposite is true. Conversely, in the limit of small and large permeability, the contact time in the open-base configuration increases as the slip length decreases for all k. We also described in detail the behaviour of the finite contact time, particle paths and penetration depths of the open-base configuration of the porous squeeze-film problem, and showed that it is qualitatively different in the limits of small and large permeability. In particular, in the limit of small permeability, the finite contact time of the bearing and porous bed is large. When the bearing and porous bed contact, most of the fluid particles initially situated in the fluid gap will flow out of the side of the fluid gap. Furthermore, only fluid particles initially situated very close to the base of the porous bed are able to flow out of the base. On the other hand, in the limit of large permeability, the finite contact time of the bearing and porous bed is small. When the bearing and porous bed contact, fluid particles initially situated in the fluid gap will all flow into the porous bed, and none out of the side of the gap. Furthermore, if the initial volume of the fluid gap is greater than or equal to the volume of fluid in the porous bed, fluid particles initially situated in the porous bed will all flow out of the base. If, however, the initial volume of the fluid gap is less than or equal to the volume of fluid in the porous bed, some of the fluid initially situated in the porous bed will remain in the porous bed. Finally, we showed that the contact time in the open-base configuration is always smaller than the contact time in the closed-base configuration, even when the porous bed in the open-base configuration is much less permeable.

Chapter 5

An evaporating rivulet

In this chapter we analyse the flow of an evaporating rivulet using three different models of evaporation. As discussed in Section 1.5, evaporating rivulets occur in practical applications such as heat exchangers, cooling of electronic devices and cooking (for example, rivulets of oil in a frying pan, as shown in Figure 1.5). We will therefore formulate and describe the behaviour of the evaporating rivulet in this chapter without reference to any specific application, but with the knowledge that further understanding of this problem is applicable to practical situations. In particular, we shall describe how the length, semi-width and contact angle of the rivulet vary as the parameters appearing in the problem vary, such as the input flux, the angle of inclination of the substrate, and the parameters of the relevant model of evaporation.

5.1 Problem formulation

As shown in Figure 5.1, consider the steady gravity-driven flow of an evaporating, symmetric, thin rivulet of an incompressible Newtonian fluid with constant density ρ^*, viscosity μ^* and surface tension σ^* over a solid planar substrate inclined at an angle α to the horizontal. In particular, we consider sessile (i.e. with $0 \leq \alpha < \pi/2$), vertical (i.e. with $\alpha = \pi/2$) and pendant (i.e. with $\pi/2 < \alpha \leq \pi$) rivulets. We use Cartesian coordinates (x^*, y^*, z^*), with the x^*-axis down the line of greatest slope, the y^*-axis horizontal and the z^*-axis normal to the substrate at $z^* = 0$. The free surface of the rivulet is at $z^* = h^*(x^*, y^*)$. The rivulet evaporates from its free surface for $x^* > 0$ with an evaporative mass flux denoted by $J^*(x^*, y^*)$. At $x^* = 0$

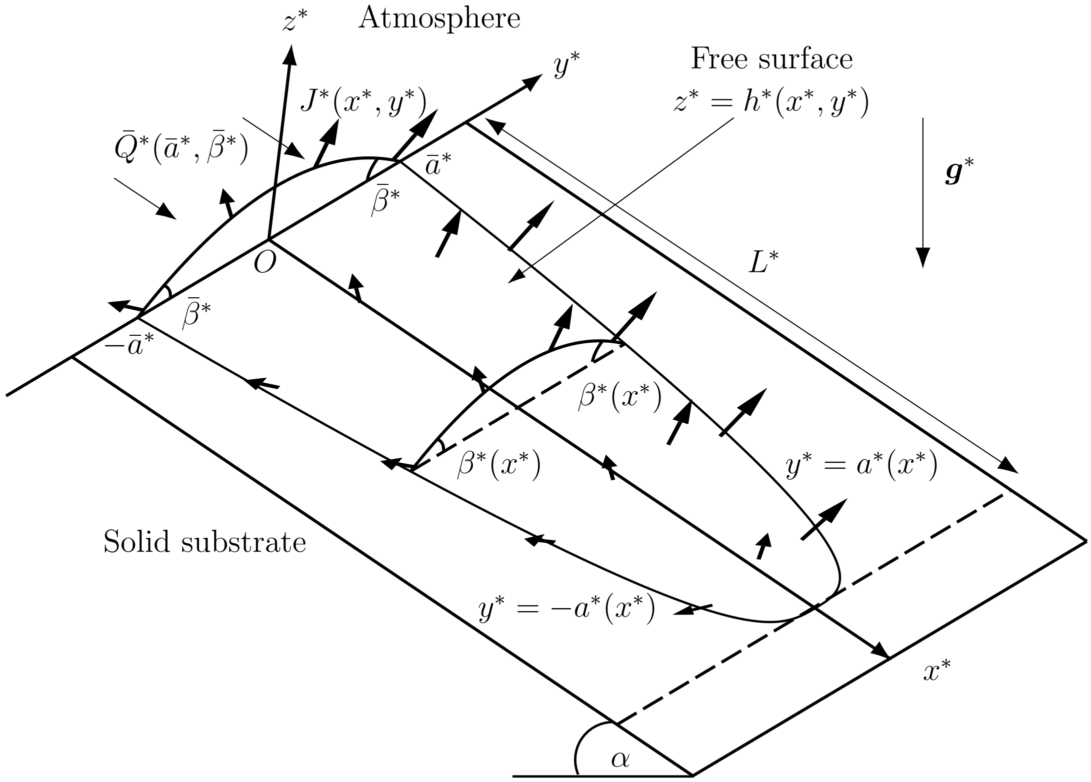

Figure 5.1: Sketch of a thin gravity-driven evaporating rivulet with free surface $z^* = h^*(x^*, y^*)$, contact angle $0 \le \beta^* \le \bar{\beta}^*$ and semi-width $0 \le a^* \le \bar{a}^*$, length L^* and evaporative flux at the free surface $J^*(x^*, y^*)$. The substrate is inclined at an angle $0 \le \alpha \le \pi$ to the horizontal and gravity $\mathbf{g}^*$ acts vertically downwards.

there is a prescribed inlet flux $\bar{Q}^*$. For $x^* > 0$ the non-constant volume flux is $Q^*(x^*)$ $(0 \le Q^* \le \bar{Q}^*)$, the non-constant semi-width is $a^*(x^*)$ $(0 \le a^* \le \bar{a}^*)$ such that $-a^* \le y^* \le a^*$, and the non-constant contact angle is $\beta^*(x^*)$ $(0 \le \beta^* \le \bar{\beta}^*)$, and Q^*, a^* and β^* take the initial values $Q^*(0) = \bar{Q}^*$, $a^*(0) = \bar{a}^*$ and $\beta^*(0) = \bar{\beta}^*$, respectively, at $x^* = 0$. In the present work, for each evaporation model, we will consider both rivulets with a fixed semi-width $a^* = \bar{a}^*$ and decreasing contact angle $\beta^*(x^*)$ $(\le \bar{\beta}^*)$ in $x^* > 0$ and rivulets with a fixed contact angle $\beta^* = \bar{\beta}^*$ and decreasing semi-width $a^*(x^*)$ $(\le \bar{a}^*)$ in $x^* > 0$ (see, for example, Paterson et al. [129]). Eventually, at the "nose" (i.e. the downstream end) of the rivulet, at which $x^* = L^*$, the fluid has evaporated completely. At the nose of the rivulet, $Q^* = 0$, and so, we have the following end conditions, $\beta^*(L^*) = 0$ (in the case of a rivulet with fixed semi-width) or $a^*(L^*) = 0$ (in the case of a rivulet with fixed contact angle).

The atmosphere above the rivulet may consist entirely of vapour or be composed of a mixture of both vapour and passive gas (for example, air) [110]. In this chapter, we will only describe in detail the full derivation for the one-sided model, as it is the most complicated, and for the other two evaporation models, we shall simply assert the form of the evaporative flux. In particular, we shall derive the one-sided model following, for example, Burelbach et al. [22], Ajaev et al. [3, 5, 6], and in the simplest possible case in which Marangoni effects, van der Waals attractions and the effects of vapour recoil are all neglected. In this simplest possible case, the leading order lubrication equations that govern the flow in the rivulet remain the same for all three evaporation models considered in this chapter. We shall therefore subsequently derive the governing equations for the flow in the rivulet with a general evaporative flux J^*, and then consider three possible models for evaporation, and hence choices for J^*. Specifically, we shall consider a constant rate of evaporation, a model inspired by the diffusion-limited model which we term the "pseudo" diffusion-limited model, and the one-sided model.

5.1.1 Governing equations

The continuity equation and steady Navier–Stokes equation for the rivulet are again (1.2) and (1.3), where $\mathbf{u}^* = (u^*(x^*, y^*, z^*), v^*(x^*, y^*, z^*), w^*(x^*, y^*, z^*))$ is the fluid velocity, $p^*(x^*, y^*, z^*)$ is the pressure in the fluid and $\mathbf{g}^* = g^*(\sin\alpha, 0, -\cos\alpha)$ is the gravity vector, with magnitude g^*.

5.1.2 Boundary conditions

At the substrate we impose the no-slip and no-penetration conditions

$$\mathbf{u}^* = \mathbf{0} \tag{5.1}$$

on $z^* = 0$. We also assume no-slip between the fluid and the vapour at the interface

$$(\mathbf{u}^* - \mathbf{u}^{(\mathrm{V})*}) \cdot \mathbf{t}_i^* = 0 \tag{5.2}$$

on $z^* = h^*$. The normal-stress condition is given by

$$J^*(\mathbf{u}^* - \mathbf{u}^{(\mathrm{V})*}) \cdot \mathbf{n}^* - (\mathbf{T}^* - \mathbf{T}^{(\mathrm{V})*}) \cdot \mathbf{n}^* \cdot \mathbf{n}^* = \sigma^* \nabla \cdot \mathbf{n}^* \tag{5.3}$$

on $z^* = h^*$. and the tangential-stress condition is given by

$$J^*(\mathbf{u}^* - \mathbf{u}^{(\mathrm{V})*}) \cdot \mathbf{t}_i^* - (\mathbf{T}^* - \mathbf{T}^{(\mathrm{V})*}) \cdot \mathbf{n}^* \cdot \mathbf{t}_i^* = 0 \tag{5.4}$$

on $z^* = h^*$, where $i = 1, 2$, $\mathbf{T}^* = -p^*\mathbf{I} + 2\mu^*\boldsymbol{\tau}^*$ is the stress tensor of the fluid, $\mathbf{T}^{(\mathrm{V})*} = -p^{(\mathrm{V})*}\mathbf{I} + 2\mu^{(\mathrm{V})*}\boldsymbol{\tau}^{(\mathrm{V})*}$ is the stress tensor of the vapour, with the identity matrix $\mathbf{I}$ and rate-of-strain tensors τ^* and $\tau^{(\mathrm{V})*}$ in the fluid and atmosphere, respectively, $p^{(\mathrm{V})*}$ is the constant pressure in the vapour and $\mu^{(\mathrm{V})*}$ is the constant viscosity of the vapour. The outward unit normal and tangent vectors to the free surface are

$$\mathbf{n}^* = \frac{(-h^*_{x^*}, -h^*_{y^*}, 1)}{\sqrt{1 + {h^*_{x^*}}^2 + {h^*_{y^*}}^2}}, \quad \mathbf{t}_1^* = \frac{(1, 0, h^*_{x^*})}{\sqrt{1 + {h^*_{x^*}}^2}}, \quad \mathbf{t}_2^* = \frac{(0, 1, h^*_{y^*})}{\sqrt{1 + {h^*_{y^*}}^2}}, \tag{5.5}$$

respectively. The mass balance condition at the free surface is given by

$$J^* = \rho^*(\mathbf{u}^* - \mathbf{u}^{(\mathrm{I})*}) \cdot \mathbf{n}^* = \rho^{(\mathrm{V})*}(\mathbf{u}^{(\mathrm{V})*} - \mathbf{u}^{(\mathrm{I})*}) \cdot \mathbf{n}^* \tag{5.6}$$

on $z^* = h^*$, where $\mathbf{u}^{(\mathrm{I})*}$ is the velocity of the interface, $\mathbf{u}^{(\mathrm{V})*}$ is the vapour velocity and $\rho^{(\mathrm{V})*}$ is the constant vapour density. Following Burelbach et al. [22], using (5.2) and (5.6) and considering $\mu^{(V)*} \ll \mu^*$ and $\rho^{(V)*} \ll \rho^*$ (with $\rho^{(V)*}$ retained in (5.6) as it multiplies the vapour velocity, which may be large), the normal stress (5.3) and tangential stress (5.4) conditions reduce to

$$-\frac{J^{*2}}{\rho^{(\mathrm{V})*}} - (p^{(\mathrm{V})*}\mathbf{I} + \mathbf{T}^*) \cdot \mathbf{n}^* \cdot \mathbf{n}^* = \sigma^*\nabla^* \cdot \mathbf{n}^* \tag{5.7}$$

on $z^* = h^*$ and

$$\mathbf{T}^* \cdot \mathbf{n}^* \cdot \mathbf{t}_i^* = 0 \tag{5.8}$$

on $z^* = h^*$ respectively.

Consider a control volume of the rivulet occupying x^* to $x^* + \Delta x^*$. Over a small interval of time Δt^*, a mass $\rho^* Q^* \Delta t^*$ flows in at x^*, a mass $\rho^*(Q^* + \Delta Q^*)\Delta t^*$ flows out at $x^* + \Delta x^*$ and a mass

$$\int_{x^*}^{x^*+\Delta x^*} \int_{-a^*}^{a^*} J^* \, \mathrm{d}y^* \mathrm{d}x^* \, \Delta t^* \tag{5.9}$$

is lost by evaporation at the free surface. For steady flow of a fluid the mass occupying the control volume is constant and therefore

$$\rho^* Q^* \Delta t^* = \rho^*(Q^* + \Delta Q^*)\Delta t^* + \int_{x^*}^{x^*+\Delta x^*} \int_{-a^*(\tilde{x}^*)}^{a^*(\tilde{x}^*)} J^*(\tilde{x}^*, y^*)\ \mathrm{d}y^*\ \mathrm{d}\tilde{x}^*\ \Delta t^*, \quad (5.10)$$

and hence the global mass-balance equation is given by

$$\rho^* \frac{\mathrm{d}Q^*}{\mathrm{d}x^*} = -\int_{-a^*(x^*)}^{a^*(x^*)} J^*(x^*, y^*)\ \mathrm{d}y^*. \quad (5.11)$$

5.2 Thin-film approximation

We consider the rivulet to be thin and slowly varying, such that the length scale in the z^* direction, $\delta\ell^*$, is much smaller than the length scale in the y^* direction, ℓ^*, which in turn is much smaller than the length scale in the x^* direction, ℓ^*/ϵ, so that $\delta\ell^* \ll \ell^* \ll \ell^*/\epsilon$, where $\delta \ll 1$ is the transverse aspect ratio of the rivulet and $\epsilon \ll 1$ is the longitudinal aspect ratio of the rivulet.

5.2.1 Non-dimensionalisation

We non-dimensionalise according to

$$x^* = \frac{\ell^*}{\epsilon}x, \quad L^* = \frac{\ell^*}{\epsilon}L, \quad y^* = \ell^* y, \quad a^* = \ell^* a, \quad z^* = \delta\ell^* z, \quad h^* = \delta\ell^* h, \quad \beta^* = \delta\beta,$$
$$Q^* = \frac{\delta^3\rho^* g^* \ell^{*4}}{\mu^*}Q, \quad u^* = \frac{\delta^2\rho^* g^* \ell^{*2}}{\mu^*}u, \quad v^* = \frac{\epsilon\delta^2\rho^* g^* \ell^{*2}}{\mu^*}v, \quad w^* = \frac{\epsilon\delta^3\rho^* g^* \ell^{*2}}{\mu^*}w,$$
$$p^* = p^{(V)*} + \delta\rho^* g^* \ell^* p, \quad J^* = \hat{J}^* J, \quad (5.12)$$

where $\ell^* = (\sigma^*/\rho^* g^*)^{1/2}$ is the capillary length and $\hat{J}^*$ is a characteristic evaporative flux, whose value depends on the characteristics of the evaporation model considered. We may choose

$$\delta = \bar{\beta}^* \quad \text{and} \quad \epsilon = \frac{\hat{J}^* \mu^*}{\rho^{*2} g^* {\bar{\beta}^*}^3 \ell^{*2}}. \quad (5.13)$$

The choice of δ in (5.13) means that, without loss of generality, we may take $\bar{\beta} = 1$, we shall however retain $\bar{\beta}$ in what follows for clarity of presentation. The assumption that the rivulet is thin requires that the dimensional contact angle $\beta^* \ll 1$ is small, however, the scaled contact angle $\beta > 0$ defined in (5.12) may take any positive value.

5.2.2 Leading-order governing equations

At leading order in $\delta \to 0$ and $\epsilon \to 0$ the governing equations (1.2) and (1.3) become the thin-film equations given by

$$u_x + v_y + w_z = 0, \tag{5.14}$$

$$u_{zz} = -\sin\alpha, \tag{5.15}$$

$$-p_y = 0, \tag{5.16}$$

$$p_z = -\cos\alpha. \tag{5.17}$$

The global mass balance equation (5.11) is given by

$$\frac{\mathrm{d}Q}{\mathrm{d}x} = -\int_{-a(x)}^{+a(x)} J(x,y)\ \mathrm{d}y, \tag{5.18}$$

or, equivalently, by integrating (5.18) with respect to x,

$$Q - \bar{Q} = -\int_0^x \int_{-a(\tilde{x})}^{+a(\tilde{x})} J(\tilde{x},y)\ \mathrm{d}y\ \mathrm{d}\tilde{x}. \tag{5.19}$$

Equation (5.18) (or equivalently (5.19)) is the governing equation that describes the behaviour of the contact angle $\beta(x)$ and the semi-width $a(x)$. However, the problem as stated thus far is not sufficient to determine both $\beta(x)$ and $a(x)$, and hence an additional assumption is required. Therefore, as mentioned previously, for each evaporation model, we shall consider the rivulet to have either a fixed semi-width $a = \bar{a}$ and decreasing contact angle $\beta(x)$ ($\leq \bar{\beta}$) or a fixed contact angle $\beta = \bar{\beta}$ and decreasing semi-width $a(x)$ ($\leq \bar{a}$).

5.2.3 Boundary conditions

At leading order in $\delta \to 0$ and $\epsilon \to 0$, the no-slip and no-penetration conditions (5.1) are given by

$$u = v = w = 0 \tag{5.20}$$

on $z = 0$. On the free surface of the rivulet the normal stress condition (5.7) becomes

$$p = -h_{yy} \tag{5.21}$$

on $z = h$, while the tangential stress condition (5.8) leads to

$$u_z = 0 \tag{5.22}$$

on $z = h$.

5.2.4 Velocity, pressure and film thickness

Solving (5.15) subject to (5.20) and (5.22) gives

$$u = \frac{\sin\alpha}{2}(2hz - z^2). \tag{5.23}$$

Solving (5.17) subject to (5.21) we find

$$p = (h - z)\cos\alpha - h_{yy}. \tag{5.24}$$

Now using (5.16) we find the following differential equation for h

$$(h\cos\alpha - h_{yy})_y = 0, \tag{5.25}$$

which we solve subject to

$$h = 0, \quad h_y = \mp\beta \tag{5.26}$$

at $y = \pm a$. This leads to the solution for the free surface shape, obtained by Duffy and Moffatt [37], given by

$$h = \beta \times \begin{cases} \dfrac{\cosh ma - \cosh my}{m \sinh ma} & 0 \leq \alpha < \dfrac{\pi}{2}, \\ \dfrac{a^2 - y^2}{2a} & \alpha = \dfrac{\pi}{2}, \\ \dfrac{\cos my - \cos ma}{m \sin ma} & \dfrac{\pi}{2} < \alpha \leq \pi, \end{cases} \tag{5.27}$$

where $m = \sqrt{|\cos\alpha|}$. The maximum height of the rivulet which occurs at $y = 0$ is given by

$$h_{\mathrm{m}} = \beta \times \begin{cases} \dfrac{1}{m}\tanh\left(\dfrac{ma}{2}\right) & 0 \le \alpha < \dfrac{\pi}{2}, \\ \dfrac{a}{2} & \alpha = \dfrac{\pi}{2}, \\ \dfrac{1}{m}\tan\left(\dfrac{ma}{2}\right) & \dfrac{\pi}{2} < \alpha \le \pi. \end{cases} \tag{5.28}$$

For sessile and vertical rivulets (i.e. with $0 \le \alpha \le \pi/2$) there is always a physically sensible solution for the free surface (5.27) such that $h \ge 0$. However, for a pendant rivulet (i.e. with $\pi/2 < \alpha \le \pi$), as $ma \to \pi$ the rivulet becomes infinitely deep ($h \to \infty$) and for $ma > \pi$ the solution (5.27) becomes negative such that $h < 0$ for some values of y in the range $-a < y < a$, both of which are not physically sensible, and so we restrict our attention to $0 \le ma < \pi$ only.

Now considering the volume flux along the rivulet given by

$$Q = \int_0^h \int_{-a}^{a} u \; \mathrm{d}y \; \mathrm{d}z, \tag{5.29}$$

which becomes

$$Q = \frac{\beta^3 \sin\alpha}{9m^4} f(ma), \tag{5.30}$$

where the function $f(ma)$, first described by Duffy and Moffatt [37], is given by

$$f(ma) = \begin{cases} 15ma\coth^3 ma - 15\coth^2 ma - 9ma\coth ma + 4 & 0 \le \alpha < \dfrac{\pi}{2}, \\ \frac{12}{35}(ma)^4 & \alpha = \dfrac{\pi}{2}, \\ -15ma\cot^3 ma + 15\cot^2 ma - 9ma\cot ma + 4 & \dfrac{\pi}{2} < \alpha \le \pi. \end{cases} \tag{5.31}$$

As described by Duffy and Moffatt [37], equation (5.31) satisfies $f(ma) \sim 12(ma)^4/35 \to 0$ as $ma \to 0$, $f(ma) \sim 6ma - 11 \to \infty$ as $ma \to \infty$ for $0 \le \alpha \le \pi/2$, and $f(ma) \sim 15\pi(\pi - ma)^{-3} \to \infty$ as $ma \to \pi$ for $\pi/2 < \alpha \le \pi$.

5.2.5 Inlet flux $\bar{Q}$

At the inlet of the rivulet, at $x = 0$, the flux (5.30) takes the initial value

$$\bar{Q} = \frac{\bar{\beta}^3 \sin\alpha}{9m^4} f(m\bar{a}). \tag{5.32}$$

Considering the inlet flux to be a function of α, i.e. $\bar{Q} = \bar{Q}(\alpha)$, if the initial semi-width of the rivulet satisfies $\bar{a} < \pi$, then the inlet flux $\bar{Q}$ is finite for sessile, vertical, and pendant rivulets, i.e. for $0 \leq \alpha \leq \pi$. We henceforth refer to rivulets with initial semi-width $\bar{a} < \pi$ as "narrow" rivulets. In particular, the inlet flux $\bar{Q}(\alpha)$ of a narrow rivulet satisfies

$$\bar{Q} \sim \frac{\bar{\beta}^3 f(\bar{a})}{9}\alpha \to 0^+ \tag{5.33}$$

in the regime $\alpha \ll 1$, and

$$\bar{Q} \sim \frac{\bar{\beta}^3 f(\bar{a})}{9}(\pi - \alpha) \to 0^+ \tag{5.34}$$

as $\alpha \to \pi^-$. If the initial semi-width of the rivulet satisfies $\bar{a} \geq \pi$, then the inlet flux is finite for sessile and vertical rivulets, i.e. $0 \leq \alpha \leq \pi/2$, however for pendant rivulets, the inlet flux remains finite only for $\pi/2 < \alpha < \alpha_{\text{crit}}$. We henceforth refer to rivulets with initial semi-width $\bar{a} \geq \pi$ as "wide" rivulets. The value of α_{crit} is calculated by solving the equation $m\bar{a} = \pi$ (corresponding to $f(m\bar{a}) \to \infty$) for α, which, as described in Section 1.5, is given by (1.81). Beyond $\alpha = \alpha_{\text{crit}}$, the inlet flux becomes negative, i.e. $\bar{Q} < 0$, and since in the present work we consider only $0 \leq Q \leq \bar{Q}$, for wide rivulets, we restrict the range of α to be $0 \leq \alpha < \alpha_{\text{crit}}$. In particular, the inlet flux $\bar{Q}$ of a wide rivulet satisfies (5.33) as $\alpha \to 0^+$, and

$$\bar{Q} \sim \frac{40\bar{\beta}^3\bar{a}^2}{3(\bar{a}^4 - \pi^4)}(\alpha_{\text{crit}} - \alpha)^{-3} \to \infty \tag{5.35}$$

as $\alpha \to \alpha_{\text{crit}}^-$ for $\bar{a} > \pi$ and

$$\bar{Q} \sim \frac{320\bar{\beta}^3}{3\pi^2}(\pi - \alpha)^{-5} \to \infty \tag{5.36}$$

as $\alpha \to \alpha_{\text{crit}}^- = \pi^-$ for $\bar{a} = \pi$.

On the other hand, considering the inlet flux to be a function of the initial semi-width $\bar{a}$, i.e. $\bar{Q} = \bar{Q}(\bar{a})$, for sessile and vertical rivulets the inlet flux is finite for all $0 \leq \bar{a} < \infty$, however for pendant rivulets, the inlet flux remains finite only for $0 \leq \bar{a} < \bar{a}_{\text{crit}}$. The value of $\bar{a}_{\text{crit}}$ is calculated by solving the equation $m\bar{a} = \pi$

(corresponding to $f(m\bar{a}) \to \infty$) for $\bar{a}$, which yields

$$\bar{a}_{\mathrm{crit}} = \frac{\pi}{m}. \tag{5.37}$$

For $\bar{a} > \bar{a}_{\mathrm{crit}}$, the inlet flux becomes negative, i.e. $\bar{Q} < 0$, and since in the present work we consider only $0 \le Q \le \bar{Q}$, for pendant rivulets, we restrict the range of $\bar{a}$ to be $0 \le \bar{a} < \bar{a}_{\mathrm{crit}}$. In particular, for sessile, vertical and pendant rivulets the inlet flux $\bar{Q}$ satisfies

$$\bar{Q} \sim \frac{4\bar{\beta}^3 \sin\alpha}{105}\bar{a}^4 \to 0^+ \tag{5.38}$$

in the regime $\bar{a} \ll 1$. For sessile and vertical rivulets the inlet flux $\bar{Q}$ satisfies

$$\bar{Q} \sim \frac{2\bar{\beta}^3 \sin\alpha}{3m^3}\bar{a} \to \infty \tag{5.39}$$

and

$$\bar{Q} \sim \frac{4\bar{\beta}^3}{105}\bar{a}^4 \to \infty \tag{5.40}$$

in the regime $\bar{a} \gg 1$, respectively. For pendant rivulets the inlet flux $\bar{Q}$ satisfies

$$\bar{Q} \sim \frac{5\pi\bar{\beta}^3 \sin\alpha}{3m^7}(\bar{a}_{\mathrm{crit}} - \bar{a})^{-3} \to \infty \tag{5.41}$$

as $\bar{a} \to \bar{a}_{\mathrm{crit}}^-$.

5.2.6 Area and volume

The area of the base A and volume V of the rivulet are given by

$$A = 2\int_0^L a \,\mathrm{d}x \quad \text{and} \quad V = \int_0^L \int_{-a}^{a} \int_0^h \mathrm{d}z \,\mathrm{d}y \,\mathrm{d}x. \tag{5.42}$$

The volume can be written

$$V = \frac{2}{\cos\alpha}\int_0^L \beta[g(ma) - 1] \,\mathrm{d}x, \tag{5.43}$$

where

$$g(ma) = \begin{cases} ma \coth ma & 0 \leq \alpha < \dfrac{\pi}{2}, \\ 1 & \alpha = \dfrac{\pi}{2}, \\ ma \cot ma & \dfrac{\pi}{2} < \alpha \leq \pi. \end{cases} \tag{5.44}$$

Equations (5.42) and (5.43) coincide with equations (25) and (26) of Alshaikhi et al. [10], who considered the flow of a rivulet over and through a porous substrate, as described in Section 1.5. It is useful to note here that the function $g(ma)$ satisfies $g(ma) = 1 + \mathrm{sgn}(\cos\alpha)(ma)^2/3 + \mathcal{O}(ma)^4$ as $ma \to 0$ i.e. as $\alpha \to \pi/2$. Therefore in the case of a vertical rivulet the expression for the volume (5.43) is given by

$$V = \frac{2}{3}\int_0^L \beta a^2 \, \mathrm{d}x. \tag{5.45}$$

5.3 Evaporation models

In this section we will describe in further detail the three models of evaporation first introduced in Section 1.5 that will be used to model the evaporation of the rivulet, namely, uniform evaporation, the pseudo diffusion-limited model, and the one-sided model.

5.3.1 Uniform evaporation

A simple model for the evaporation of the fluid is to assume the fluid evaporates with a constant and spatially uniform evaporative flux J^*. In this case we may choose $J^* = \hat{J}^*$ in (5.12) so that $J = \hat{J} = 1$, with $\hat{J}$ retained for clarity of presentation.

5.3.2 Pseudo diffusion-limited model

As discussed in Section 1.5, the evaporation of a fluid in a thermally equilibrated state can be governed by the diffusion of vapour in a passive atmosphere (for example, air). This model of evaporation, named the diffusion-limited model, in which the diffusion of vapour in the atmosphere determines the evaporative flux, is often used to model situations in which the fluid is not being heated (see, for example, [34, 69, 96, 24, 89, 149]).

As we will show subsequently, because the rivulet is slowly varying, at leading order the vapour concentration in the atmosphere is governed by the two-dimensional Laplace equation. As we will show, the solution of the two-dimensional Laplace equation cannot satisfy the far-field condition of ambient concentration. Previous works (such as, for example, Yarin et al. [188], Schofield et al. [149], and Haynes and Pradas [59]) overcame this problem by introducing a large (but finite) outer boundary to the atmosphere, at which the concentration takes its ambient value.

In this section (and in Section 5.5), we shall simply assert an evaporative flux with the same functional dependence on y as in Schofield et al. [149]. In doing so, we avoid complications associated with including a large but finite boundary, whilst also retaining the properties of the evaporative flux of the full diffusion-limited model, for example, as will be shown subsequently, the same integrable singularity at the contact line of the rivulet.

5.3.2.1 Diffusion-limited model

To first describe the diffusion-limited model, we consider a rivulet as described in Section 5.1 that evaporates into a surrounding passive atmosphere. The vapour transport into the atmosphere is considered to be quasi steady, and so the vapour concentration in the atmosphere is denoted by $c^* = c^*(x^*, y^*, z^*)$. Following, for example, [34, 69, 96, 24, 89, 149, 147, 59, 189], the concentration in the atmosphere above the rivulet is governed by Laplace's equation given by

$$\nabla^{*2} c^* = 0. \tag{5.46}$$

Since the rivulet is slowly varying, i.e. the length scale in the x^* direction is ℓ^*/ϵ, (5.46) reduces to the two-dimensional Laplace equation given by

$$\frac{\partial^2 c^*}{\partial y^{*2}} + \frac{\partial^2 c^*}{\partial z_{\mathrm{a}}^{*2}} = 0, \tag{5.47}$$

where z_{a}^* is the z^*-coordinate in the atmosphere. At the free surface of the rivulet, the concentration takes the value of the constant saturation concentration c_{sat}^*. Whilst far from the free surface of the rivulet, the concentration takes the value of the constant ambient concentration c_∞. At substrate, outside the rivulet for $y^* > |a^*|$, there is no evaporation, and hence the evaporative flux is zero. We non-dimensionalise according to (5.12) and

$$z_{\mathrm{a}}^* = \ell^* z_{\mathrm{a}} \quad \text{and} \quad c^* = c_\infty^* + (c_{\mathrm{sat}}^* - c_\infty^*)c. \tag{5.48}$$

Hence, at leading order in $\delta \to 0$ and $\epsilon \to 0$, (5.47) becomes

$$\frac{\partial^2 c}{\partial y^2} + \frac{\partial^2 c}{\partial {z_{\mathrm{a}}}^2} = 0. \tag{5.49}$$

At the free surface (which we evaluate at $z_{\mathrm{a}} = 0$ due to the thinness of the rivulet) the concentration takes the value of the constant saturation concentration, and hence

$$c = 1 \tag{5.50}$$

on $z_{\mathrm{a}} = 0$. Far from the rivulet, the concentration takes the value of the constant ambient concentration, and hence

$$c \to 0 \quad \text{as} \quad \sqrt{y^2 + z_{\mathrm{a}}^2} \to \infty. \tag{5.51}$$

At the substrate, outside the rivulet, there is no evaporation, and hence

$$\frac{\partial c}{\partial z_{\mathrm{a}}} = 0 \tag{5.52}$$

on $z_{\mathrm{a}} = 0$ for $|y| > \bar{a}$. The solution of (5.49) clearly satisfies

$$c = \mathcal{O}\left(\ln\left(\sqrt{y^2 + z_{\mathrm{a}}^2}\right)\right) \to \infty \tag{5.53}$$

as $\sqrt{y^2 + z_{\mathrm{a}}^2} \to \infty$. Therefore, the solution of the two-dimensional problem cannot satisfy the far-field condition (5.51). To overcome this problem, the works of, for example, Yarin et al. [188], Schofield et al. [149], and Haynes and Pradas [59], instead of evaluating the condition (5.51) at infinity, they evaluated it at a large (but finite) outer boundary to the atmosphere. For example, Schofield et al. [149] considered the semi-circular outer boundary condition

$$c = 0 \quad \text{for} \quad y^2 + z^2 = \gamma^2, \tag{5.54}$$

where γ is a large (but finite) distance from the origin $y = z_{\mathrm{a}} = 0$. However, note that introducing a large (but finite) outer boundary in this way introduces an additional parameter into the problem, i.e. the solution for c depends on the size and shape of outer boundary. Schofield et al. [149], for example, showed that the evaporative flux is of the form

$$J = -\frac{\partial c}{\partial z}(y, 0) = \frac{1}{\operatorname{arcsinh}(\Psi/a)} \frac{1}{\sqrt{a^2 - y^2}} \quad \text{for} \quad |y| < \bar{a}, \tag{5.55}$$

where the parameter Ψ is a non-dimensional constant which depends on the size of the large (but finite) outer boundary. The evaporative flux given by (5.55) therefore not only depends on y and a, but also the parameter Ψ, and also has the same (integrable) square-root singularity at $|y| = a$ as in the corresponding axisymmetric problem [136]. Note that in the axisymmetric problem, the concentration satisfies Laplace's equation and the far-field condition (5.51), and so there is no need to introduce a large (but finite) outer boundary.

5.3.2.2 Pseudo diffusion-limited model

Motivated by the successful description of the evaporation of ridges (i.e. two-dimensional droplets) of fluid just described in Section 5.3.2.1, in the present work we investigate a rivulet which evaporates according to an evaporative flux of the same (integrable) form as (5.55). Specifically, in order to avoid the complications of the dependence on the size of the domain, we assume that the evaporative flux is given simply by

$$J = \frac{\hat{\jmath}}{\sqrt{a^2 - y^2}}, \tag{5.56}$$

where $\hat{\jmath}$ is a non-dimensional constant. We shall henceforth refer to (5.56) as the evaporative flux of the pseudo diffusion-limited model, in order to distinguish it from the correct form of the evaporative flux given by (5.55). We can, without loss of generality, take $\hat{\jmath} = 1$, but retain $\hat{\jmath}$ in what follows for clarity.

5.3.3 One-sided model

As discussed in Section 1.5, the evaporation of a fluid can also be modelled by the non-equilibrated thermal effects at the free surface of the fluid. This model of evaporation, named the one-sided model, was originally proposed by Burelbach et al. [22], and is often used to model situations in which the substrate, and hence the fluid, is heated (see, for example, [128, 22, 173, 3, 5, 6, 26, 25]).

Following Burelbach et al. [22], we derive the evaporative flux J^* and temperature in the fluid T^* according to the one-sided model in the simplest case in which we neglect Marangoni effects, van der Waals attraction and vapour recoil.

The energy equation for steady flow is given by

$$\mathbf{u}^* \cdot \nabla T^* = \kappa^* \nabla^2 T^*, \tag{5.57}$$

where $T^*(x^*, y^*, z^*)$ is the temperature of the fluid and κ^* is the constant thermal diffusivity. On the substrate we assume constant temperature

$$T^* = T^*_{\mathrm{H}} \tag{5.58}$$

on $z^* = 0$, where $T^*_{\mathrm{H}} > 0$ is the constant temperature of the substrate.

The energy balance condition at the fluid–vapour interface (see, for example, Burelbach et al. [22] and Ajaev [4]) is given by

$$0 = J^* \left[\hat{L}^* + \frac{1}{2} \left[\mathbf{u}^{(\mathrm{V})*} - \mathbf{u}^{(\mathrm{I})*}) \cdot \mathbf{n}^* \right]^2 - \frac{1}{2} \left[(\mathbf{u}^* - \mathbf{u}^{(\mathrm{I})*}) \cdot \mathbf{n}^* \right]^2 \right] + k^* \nabla T^* \cdot \mathbf{n}^*$$
$$- k^{(V)*} \nabla T^* \cdot \mathbf{n}^* + 2\mu^* (\tau^* \cdot \mathbf{n}^*) \cdot (\mathbf{u}^* - \mathbf{u}^{(\mathrm{I})*}) - 2\mu^{(V)*} (\tau^{(V)*} \cdot \mathbf{n}^*) \cdot (\mathbf{u}^{(\mathrm{V})*} - \mathbf{u}^{(\mathrm{I})*}) \tag{5.59}$$

on $z^* = h^*$, where $\hat{L}^*$ is the latent heat of vaporisation, k^* and $k^{(V)*}$ are the constant thermal conductivities of the fluid and vapour, respectively.

We now consider the limiting case in which the thermal conductivity of the vapour is much smaller than that of the fluid [22], i.e.

$$\frac{k^{(V)*}}{k^*} \to 0. \tag{5.60}$$

This limit together with the limits $\rho^{(\mathrm{V})*}/\rho^* \to 0$ and $\mu^{(\mathrm{V})*}/\mu^* \to 0$ applied in Section 5.1 form the "one-sided model" and decouple the dynamics of the fluid from the dynamics of the vapour [22].

Substituting from (5.6) and taking the limit (5.60), the energy balance condition (5.59) becomes

$$J^* \left[\hat{L}^* + \frac{1}{2} \left(\frac{J^*}{\rho^{(V)*}} \right)^2 \right] = -k^* \nabla T^* \cdot \mathbf{n}^*. \tag{5.61}$$

Considering the Hertz-Knudsen-Schrage equation, derived from classical kinetic theory (see, for example, [150, 128, 14, 4, 192]), linearised around the equilibrium temperature at which $T^{(\mathrm{I})*} = T^*_{\mathrm{S}}$, given by

$$J^* = \hat{\alpha}\sqrt{\frac{M^*_{\mathrm{W}}}{2\pi R_{\mathrm{g}} T^*_{\mathrm{S}}}}(p^{(\mathrm{V})*} - p^{(\mathrm{S})*}), \tag{5.62}$$

where $p^{(\mathrm{S})*} = p^{(\mathrm{V})*}(T^*_{\mathrm{S}})$ is the saturation vapour pressure, T^*_{S} is the saturation temperature, $T^{(\mathrm{I})*}$ is the temperature at the free surface, ${M_{\mathrm{W}}}^*$ is the molecular weight of the vapour, and R_{g} is the universal gas constant. Combining (5.62) with the classical Clausius-Clapeyron equation (see, for example, [27, 28, 6, 192]), linearised around the equilibrium temperature, given by

$$p^{(\mathrm{V})*} - p^{(\mathrm{S})*} = \frac{\rho^{(\mathrm{V})*}\hat{L}^*}{T^*_{\mathrm{S}}}(T^{(\mathrm{I})*} - T^*_{\mathrm{S}}), \tag{5.63}$$

yields the linearised constitutive equation given by Burelbach et al. [22], namely

$$J^* = \left(\frac{\hat{\alpha}\rho^{(\mathrm{V})*}\hat{L}^*}{{T^*_{\mathrm{S}}}^{\frac{3}{2}}}\right)\left(\frac{{M_{\mathrm{W}}}^*}{2\pi R_{\mathrm{g}}}\right)^{\frac{1}{2}}(T^{(\mathrm{I})*} - T^*_{\mathrm{S}}), \tag{5.64}$$

where $\hat{\alpha}$ is the accommodation coefficient. The accommodation coefficient is defined as the probability of molecules in the vapour either diffusing into the fluid surface ($\hat{\alpha}$) or being reflected away from the fluid surface ($1 - \hat{\alpha}$), hence the accommodation coefficient lies in the interval $0 \leq \hat{\alpha} \leq 1$, where $\hat{\alpha} = 0$ corresponds to no energy being transferred from the vapour to the fluid and $\hat{\alpha} = 1$ corresponds to the vapour achieving equilibrium with the fluid surface. The value of the accommodation coefficient can depend on many factors including the smoothness of the fluid surface and the composition and pressure in the vapour [72].

Subject to the scalings (5.12) and

$$T^* = \Delta T T + T^*_S, \tag{5.65}$$

where

$$\Delta T^* = T^*_H - T^*_S, \tag{5.66}$$

and the characteristic evaporative flux given by

$$\hat{J}^* = \frac{k^* \Delta T^*}{\hat{L}^* \ell^* \delta} \tag{5.67}$$

at leading order in $\delta \to 0$ and $\epsilon \to 0$, the energy equation (5.57) becomes

$$\frac{\partial^2 T}{\partial z^2} = 0. \tag{5.68}$$

The energy balance condition (5.61) becomes

$$J = -\frac{\partial T}{\partial z} \tag{5.69}$$

on $z = h$. The linearised constitutive equation (5.64) becomes

$$T = KJ \tag{5.70}$$

on $z = h$, where the non-dimensional parameter K, defined by

$$K = \left(\frac{k^* T_S^{*\frac{3}{2}}}{\hat{\alpha} \rho^{(\mathrm{V})*} \hat{L}^{*2} \ell^* \bar{\beta}} \right) \left(\frac{2\pi R_{\mathrm{g}}}{M^*_{\mathrm{W}}} \right)^{\frac{1}{2}}, \tag{5.71}$$

measures the degree of non-equilibrium at the free surface of the rivulet. On the substrate the temperature takes the constant value

$$T = 1 \tag{5.72}$$

on $z = 0$. Solving (5.68) subject to (5.69) and (5.72) yields

$$T = 1 - Jz. \tag{5.73}$$

Substituting (5.70) into (5.73) yields the evaporative flux given by

$$J = \frac{1}{h + K}, \tag{5.74}$$

and hence the temperature (5.73) in the fluid is given by

$$T = 1 - \frac{z}{K + h}. \tag{5.75}$$

In particular, $K \to 0^+$ corresponds to the limit in which the free surface temperature is constant and equal to the saturation temperature and so $T = 0$ on $z = h$. In this limit the evaporative flux becomes large, $J \to \infty$, and so $L \to 0^+$, i.e. the rivulet evaporates immediately. On the other hand, in the limit $K \to \infty$, the evaporative flux becomes small, $J \to 0^+$, and so $L \to \infty$, i.e. the rivulet does not evaporate and is therefore infinitely long.

5.4 Evaporating rivulet: Uniform evaporation

In this section we consider the evaporation rate at the free surface of the fluid to be uniform. Hence, as discussed in Section 5.3.1, we choose $J^* = \hat{J}^*$ in (5.12) so that $J \equiv \hat{J} = 1$, with $\hat{J}$ retained for clarity of presentation. Hence, (5.18) gives the following differential equation

$$\frac{\mathrm{d}Q}{\mathrm{d}x} = -2\hat{J}a(x) \tag{5.76}$$

and equation (5.19) becomes

$$Q - \bar{Q} = -2\hat{J} \int_0^x a(\tilde{x}) \, \mathrm{d}\tilde{x}. \tag{5.77}$$

Substituting (5.30) into (5.76) we obtain the ordinary differential equation for $\beta(x)$ and/or $a(x)$, namely

$$\frac{\sin\alpha}{9m^4} \frac{\mathrm{d}}{\mathrm{d}x} \left[\beta^3 f(ma)\right] = -2\hat{J}a. \tag{5.78}$$

5.4.1 Fixed semi-width $a = \bar{a}$

In this subsection we will consider an evaporating rivulet whose semi-width is fixed with constant value $a = \bar{a}$. In particular, we will describe the behaviour of the contact angle and the variation of the length of narrow, wide, sessile, vertical and pendant rivulets, with respect to the angle of inclination α and initial semi-width $\bar{a}$. We will also derive expressions for the area of the base and volume of the rivulet.

For a rivulet with fixed semi-width, the ordinary differential equation (5.78) becomes

$$\frac{\sin\alpha f(m\bar{a})}{9m^4} \frac{\mathrm{d}}{\mathrm{d}x} \left(\beta^3\right) = -2\hat{J}\bar{a}. \tag{5.79}$$

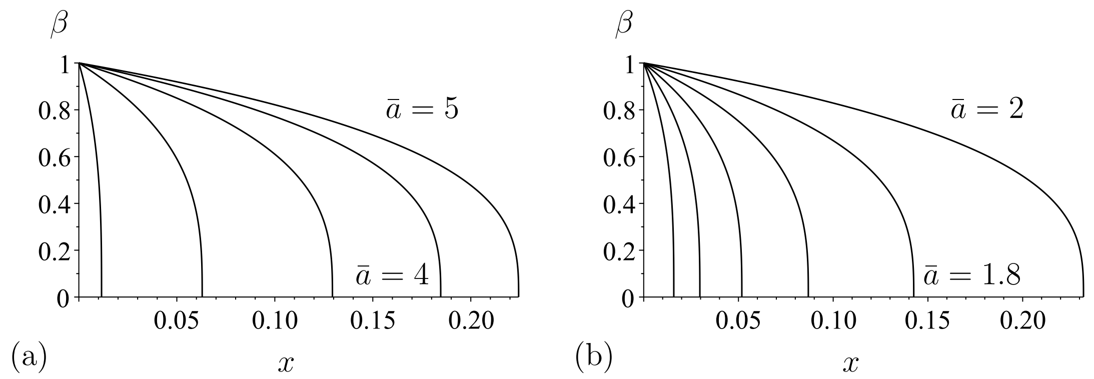

Figure 5.2: Plots of the contact angle β given by (5.81) as a function of x for (a) $\alpha = \pi/4$, $\bar{a} = 1,\ 2,\ \ldots,\ 5$ and (b) $\alpha = 3\pi/4$, $\bar{a} = 1,\ 1.2,\ \ldots,\ 2$, in the case of a rivulet with fixed semi-width and uniform evaporative flux.

Solving (5.79) subject to the initial condition $\beta(0) = \bar{\beta}$ gives

$$\beta = \bar{\beta}\left(1 - \frac{18m^4\hat{J}\bar{a}x}{f(m\bar{a})\bar{\beta}^3\sin\alpha}\right)^{\frac{1}{3}}. \tag{5.80}$$

Using the end condition $\beta(L) = 0$, (5.80) becomes

$$\beta = \bar{\beta}\left(1 - \frac{x}{L}\right)^{\frac{1}{3}} = \bar{\beta}\left(1 - \frac{2\hat{J}\bar{a}x}{\bar{Q}}\right)^{\frac{1}{3}}, \tag{5.81}$$

where the length of the rivulet L is given by

$$L = \frac{\bar{\beta}^3\sin\alpha}{18m^4\hat{J}\bar{a}}f(m\bar{a}) = \frac{\bar{Q}}{2\hat{J}\bar{a}}. \tag{5.82}$$

In the case of a vertical rivulet (5.82) is given by

$$L = \frac{2\bar{\beta}^3\bar{a}^3}{105\hat{J}}. \tag{5.83}$$

Figure 5.2 shows the contact angle given by (5.81) as a function of x for different values of $\bar{a}$ for both a sessile and a pendant rivulet. In particular, Figure 5.2 shows that β decreases from $\beta = \bar{\beta}$ at $x = 0$ to $\beta = 0$ at $x = L$. Furthermore, Figure 5.2 shows that the contact angle β increases as the initial semi-width $\bar{a}$ increases.

5.4.1.1 Rivulet shape

An example of the three-dimensional shape of the rivulet in the case of a vertical rivulet with fixed semi-width is shown in Figure 5.3. Figure 5.3 illustrates that the rivulet has a "square" nose at which its slope in the x-direction becomes large according to $\mathrm{d}h_m/\mathrm{d}x = \mathcal{O}((L-x)^{-2/3}) \to -\infty$ as $x \to L^-$. Hence the assumption that the rivulet is slowly varying in x breaks down locally near the nose. In particular, the contact angle near the nose behaves like

$$\beta \sim \bar{\beta}\left(1 - \frac{x}{L}\right)^{\frac{1}{3}} \to 0^+ \tag{5.84}$$

as $x \to L^-$.

Near $x = 0$ the contact angle behaves like

$$\beta \sim \bar{\beta}\left(1 - \frac{x}{3L}\right) \to \bar{\beta}^-, \tag{5.85}$$

the free surface behaves like

$$h \sim \bar{h}\left(1 - \frac{1}{3L}x\right) \to \bar{h}^-, \tag{5.86}$$

where $\bar{h} = h(0, y)$, and the maximum height of the rivulet behaves like

$$h_{\mathrm{m}} \sim \bar{h}_{\mathrm{m}}\left(1 - \frac{1}{3L}x\right) \to \bar{h}_{\mathrm{m}}^-, \tag{5.87}$$

where $\bar{h}_{\mathrm{m}} = h_{\mathrm{m}}(0)$, as $x \to 0^+$.

5.4.1.2 The length of a narrow rivulet

In the case of a narrow rivulet (i.e. a rivulet with $0 \le \bar{a} < \pi$) with fixed semi-width, Figure 5.4 shows the length L given by (5.82) as a function of α/π for various values of $\bar{a}$. In particular, Figure 5.4 shows that the rivulet length increases from zero at $\alpha = 0$ to a maximum $L = L_{\mathrm{max}}$ at some value $\alpha = \alpha_{\mathrm{max}}$ and then decreases towards zero at $\alpha = \pi$. In particular, the length of a sessile narrow rivulet behaves like

$$L \sim \frac{\bar{\beta}^3 f(\bar{a})}{18\hat{J}\bar{a}}\alpha \to 0^+ \tag{5.88}$$

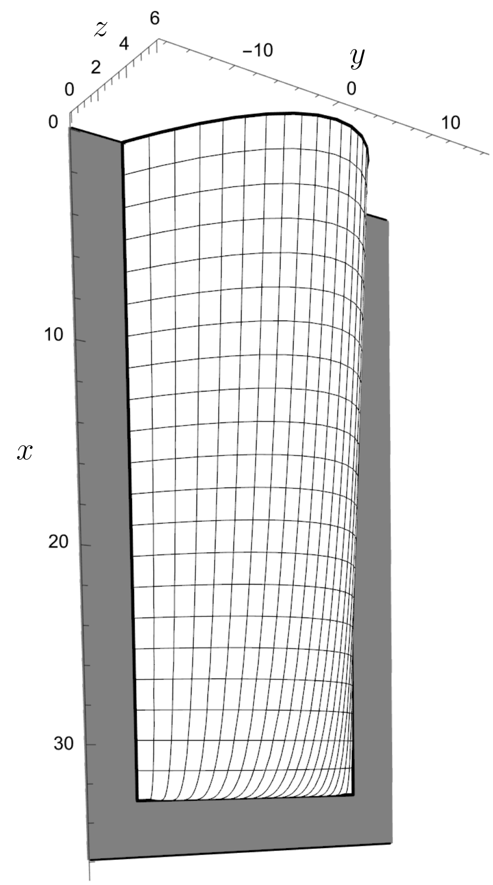

Figure 5.3: Three-dimensional plot of the shape of the rivulet $z = h(x, y)$ given by (5.27), (5.81) and (5.83) in the case of a vertical rivulet with fixed semi-width for $\bar{a} = 12$, $L = 2\bar{a}^3/105 \simeq 32.91$ and $\bar{Q} = 4\bar{a}^4/105 \simeq 789.94$.

in the regime $\alpha \ll 1$. The length of a pendant narrow rivulet behaves like

$$L \sim \frac{\bar{\beta}^3 f(\bar{a})}{18\hat{J}\bar{a}}(\pi - \alpha) \to 0^+ \tag{5.89}$$

as $\alpha \to \pi^-$.

Plots of $\alpha_{\max}$ and $L_{\max}$ as functions of $\bar{a}$ are shown in Figure 5.5. In particular, Figure 5.5 shows that the maximum length of a narrow rivulet with fixed semi-width increases monotonically from $L_{\max} \to 0^+$ and $\alpha_{\max} = \pi/2$ as $\bar{a} \to 0^+$ to $L_{\max} \to \infty$ and $\alpha_{\max} \to \pi^-$ as $\bar{a} \to \pi^-$.

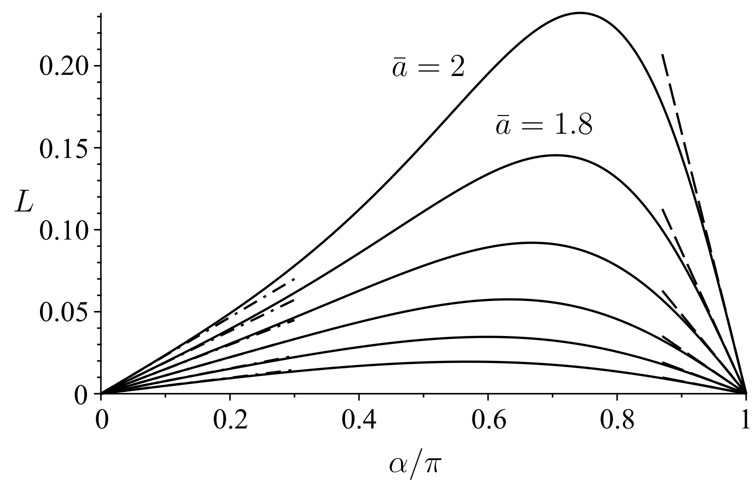

Figure 5.4: Plot of the length L given by (5.82) as a function of α/π and the asymptotic solutions (5.88) and (5.89) in the limits $\alpha \to 0^+$ and $\alpha \to \pi^-$ shown with dash-dotted and dashed lines, respectively, for $\bar{a} = 1, 1.2, 1.4, \ldots, 2$ in the case of a narrow rivulet with fixed semi-width and uniform evaporative flux.

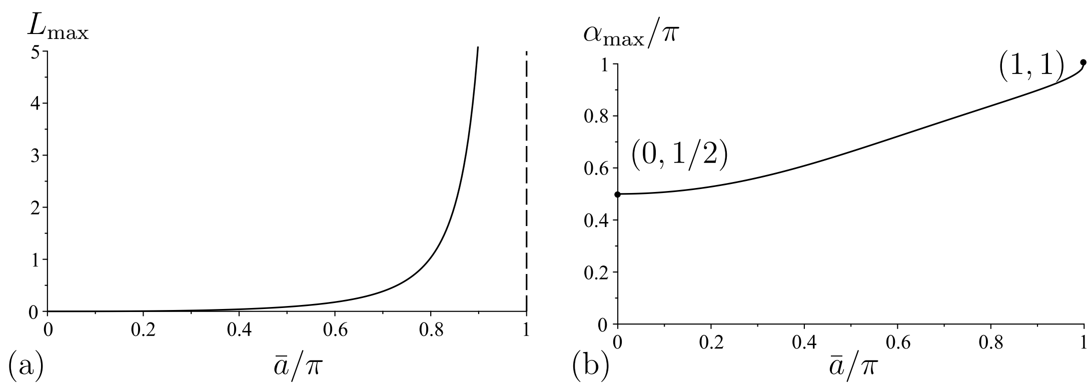

Figure 5.5: Plots of (a) $L_{\max}$ as a function of $\bar{a}/\pi$ and the vertical asymptote at $\bar{a}/\pi = 1$, and (b) $\alpha_{\max}/\pi$ as a function of $\bar{a}/\pi$ in the case of a narrow rivulet with fixed semi-width and uniform evaporative flux.

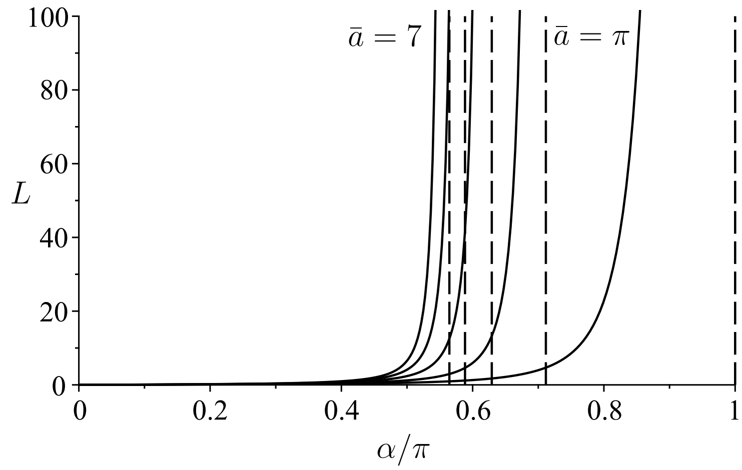

Figure 5.6: Plot of the length L given by (5.82) as a function of α/π and the vertical asymptotes at $\alpha = \alpha_{\mathrm{crit}}$ shown with dashed lines for $\bar{a} = \pi$, 4, 5, 6, 7 in the case of a wide rivulet with fixed semi-width and uniform evaporative flux.

5.4.1.3 The length of a wide rivulet

In the case of a wide rivulet (i.e. a rivulet with $\bar{a} \geq \pi$) with fixed semi-width, Figure 5.6 shows the length L given by (5.82) as a function of α/π for various values of $\bar{a}$. In particular, Figure 5.6 shows that the rivulet length increases from $L \to 0^+$ as $\alpha \to 0^+$ to $L \to \infty$ as $\alpha \to \alpha_{\mathrm{crit}}^-$, where a rivulet with finite length exists only for $0 \leq \alpha < \alpha_{\mathrm{crit}} \leq \pi$. In particular, the length of the rivulet behaves like (5.88) as $\alpha \to 0^+$ and becomes infinitely long according to

$$L \sim \frac{20\bar{\beta}^3\bar{a}}{3\hat{J}(\bar{a}^4 - \pi^4)}(\alpha_{\mathrm{crit}} - \alpha)^{-3} \to \infty \tag{5.90}$$

as $\alpha \to \alpha_{\mathrm{crit}}^-$ for $\bar{a} > \pi$ and

$$L \sim \frac{160\bar{\beta}^3}{3\pi^3\hat{J}}(\pi - \alpha)^{-5} \to \infty \tag{5.91}$$

as $\alpha \to \alpha_{\mathrm{crit}}^- = \pi^-$ for $\bar{a} = \pi$.

5.4.1.4 The rivulet length as $\bar{a}$ varies

The variation of L as a function of $\bar{a}$ for a sessile, vertical and pendant rivulet is shown in Figures 5.7 and 5.8.

In the case of a sessile rivulet, Figure 5.7 shows that the length increases from

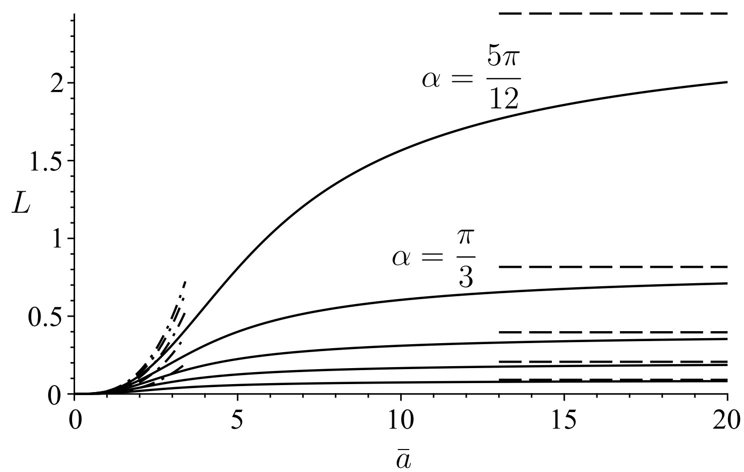

Figure 5.7: Plot of the length L given by (5.82) as a function of $\bar{a}$ and the asymptotic solutions (5.92) and (5.93) in the limits $\bar{a} \to 0^+$ and $\bar{a} \to \infty$ shown with dash-dotted and dashed lines, respectively, for $\alpha = \pi/12$, $\pi/6$, ..., $5\pi/12$, in the case of a sessile rivulet with fixed semi-width and uniform evaporative flux.

$L \to 0^+$ as $\bar{a} \to 0^+$ to a constant value as $\bar{a} \to \infty$. In particular, the length of a sessile rivulet with fixed semi-width behaves like

$$L \sim \frac{2\bar{\beta}^3 \sin\alpha}{105\hat{J}}\bar{a}^3 \to 0^+ \tag{5.92}$$

in the regime $\bar{a} \ll 1$ and approaches the finite value

$$L \sim \frac{\bar{\beta}^3 \sin\alpha}{3\hat{J}m^3} = \mathcal{O}(1) \tag{5.93}$$

as $\bar{a} \to \infty$. Note that the length of the rivulet in the limit $\bar{a} \to \infty$ for a sessile rivulet given by (5.93) corresponds to the length of a two-dimensional (i.e. an infinitely wide) sessile evaporating sheet.

In the case of a vertical rivulet, Figure 5.8 shows that the length increases from $L \to 0^+$ as $\bar{a} \to 0^+$ to $L \to \infty$ as $\bar{a} \to \infty$. In particular, the length of a vertical rivulet with fixed semi-width behaves like (5.92) as $\bar{a} \to 0^+$ and

$$L \sim \frac{2\bar{\beta}^3}{105\hat{J}}\bar{a}^3 \to \infty \tag{5.94}$$

in the regime $\bar{a} \gg 1$.

In the case of a pendant rivulet, Figure 5.8 shows that the length increases

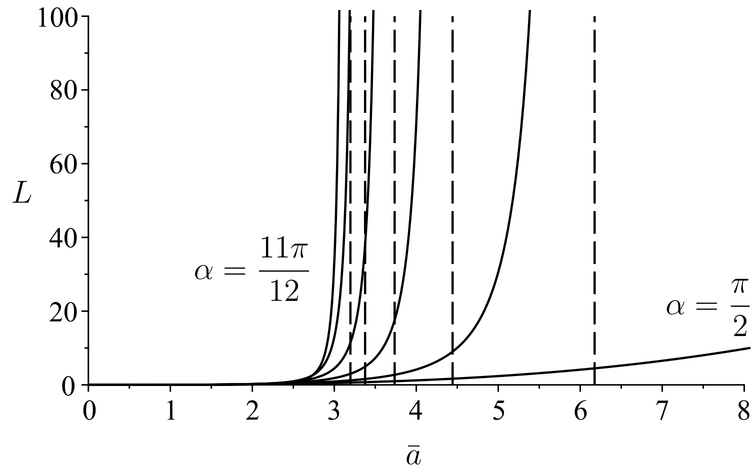

Figure 5.8: Plot of the length L given by (5.82) as a function of $\bar{a}$ and the vertical asymptotes at $\bar{a} = \bar{a}_{\mathrm{crit}} = \pi/m$ shown with dashed lines for $\alpha = \pi/2$, $7\pi/12$, ..., $11\pi/12$, in the case of a pendant rivulet with fixed semi-width and uniform evaporative flux.

from $L \to 0^+$ as $\bar{a} \to 0^+$ to $L \to \infty$ as $\bar{a} \to \bar{a}_{\mathrm{crit}}^-$. In particular, the length of a pendant rivulet with fixed semi-width behaves like (5.92) as $\bar{a} \to 0^+$ and becomes infinitely long according to

$$L \sim \frac{5\bar{\beta}^3 \sin\alpha}{6m^6 \hat{J}} (\bar{a}_{\mathrm{crit}} - \bar{a})^{-3} \to \infty \tag{5.95}$$

as $\bar{a} \to \bar{a}_{\mathrm{crit}}^-$.

5.4.1.5 Area and volume

From (5.42) the area of the base of a rivulet with fixed semi-width is given by

$$A = 2L\bar{a} = \frac{\bar{\beta}^3 \sin\alpha}{9m^4 \hat{J}} f(m\bar{a}) = \frac{\bar{Q}}{\hat{J}}. \tag{5.96}$$

From (5.42) the volume of a rivulet with fixed semi-width is given by

$$V = \frac{3\bar{\beta}L}{2\cos\alpha}[g(m\bar{a}) - 1] = \frac{\bar{\beta}^4 \tan\alpha}{12m^4 \hat{J}\bar{a}} f(m\bar{a})(g(m\bar{a}) - 1) = \frac{3\bar{\beta}\bar{Q}}{4\cos\alpha \hat{J}\bar{a}}(g(m\bar{a}) - 1). \tag{5.97}$$

In the case of a vertical rivulet (5.96) and (5.97) reduce to

$$A = 2L\bar{a} = \frac{4\bar{\beta}^3\bar{a}^4}{105\hat{J}} = \frac{\bar{Q}}{\hat{J}}, \quad V = \frac{\bar{\beta}\bar{a}^2 L}{2} = \frac{\bar{\beta}^4\bar{a}^5}{105\hat{J}} = \frac{\bar{\beta}\bar{a}\bar{Q}}{4\hat{J}}. \tag{5.98}$$

5.4.2 Fixed contact angle $\beta = \bar{\beta}$

In this subsection we will consider an evaporating rivulet whose contact angle is fixed with constant value $\beta = \bar{\beta}$. In particular, we will describe the behaviour of the semi-width and the variation of the length of narrow, wide, sessile, vertical and pendant rivulets, with respect to the angle of inclination α and initial semi-width $\bar{a}$. We will also derive expressions for the area of the base and volume of the rivulet.

For a rivulet with fixed contact angle, the ordinary differential equation (5.78) becomes

$$\frac{\bar{\beta}^3 \sin\alpha}{9m^4}\frac{\mathrm{d}}{\mathrm{d}x}\left(f(ma)\right) = -2\hat{J}a. \tag{5.99}$$

Solving (5.99) subject to the initial condition $a(0) = \bar{a}$ gives the implicit solution for the semi-width

$$F(ma) = F(m\bar{a}) - \frac{18\hat{J}m^3}{\bar{\beta}^3\sin\alpha}x, \tag{5.100}$$

where

$$F(ma) = \int_0^{ma} \frac{f'(M)}{M}\,\mathrm{d}M, \tag{5.101}$$

where $M = m\tilde{a}$. Using the end condition $a(L) = 0$, (5.100) becomes

$$F(ma) = \frac{18\hat{J}m^3}{\bar{\beta}^3\sin\alpha}(L - x), \tag{5.102}$$

where the length of the rivulet is given by

$$L = \frac{\bar{\beta}^3 F(m\bar{a})\sin\alpha}{18m^3\hat{J}}. \tag{5.103}$$

It can be shown that

$$F(ma) \sim \frac{16}{35}(ma)^3 \to 0^+ \tag{5.104}$$

in the regime $ma \ll 1$ for $0 \le \alpha \le \pi$,

$$F(ma) \sim 6\ln(ma) \to \infty \tag{5.105}$$

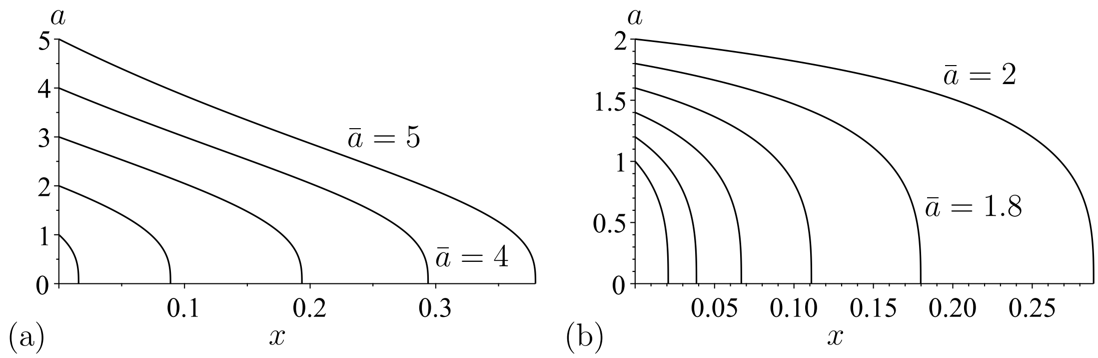

Figure 5.9: Plots of the semi-width a given by (5.102) as a function of x for (a) $\alpha = \pi/4$, $\bar{a} = 1, 2, \ldots, 5$ and (b) $\alpha = 3\pi/4$, $\bar{a} = 1, 1.2, \ldots, 2$ in the case of a rivulet with fixed contact angle and uniform evaporative flux.

in the regime $ma \gg 1$ for $0 \le \alpha < \pi/2$, and

$$F(ma) \sim 15(\pi - ma)^{-3} \to \infty \tag{5.106}$$

as $ma \to \pi^-$ for $\pi/2 < \alpha \le \pi$.

The solution for the semi-width in the case of a vertical rivulet is given explicitly by

$$a = \bar{a}\left(1 - \frac{x}{L}\right)^{\frac{1}{3}}, \tag{5.107}$$

with

$$L = \frac{8\bar{\beta}^3\bar{a}^3}{315\hat{J}} = \frac{2\bar{Q}}{3\hat{J}\bar{a}}. \tag{5.108}$$

Note that the length of a vertical rivulet with fixed contact angle given by (5.108) is 4/3 the length of the vertical rivulet with fixed semi-width given by (5.83).

Figure 5.9 shows the semi-width given implicitly by (5.102) as a function of x for different values of $\bar{a}$ for both a sessile and a pendant rivulet. In particular, Figure 5.9 shows that a decreases from $a = \bar{a}$ at $x = 0$ to $a = 0$ at $x = L$. Furthermore, Figure 5.9 shows that the semi-width a increases as the initial semi-width $\bar{a}$ increases.

5.4.2.1 Rivulet shape

An example of the three-dimensional shape of the rivulet in the case of a vertical rivulet with fixed contact angle is shown in Figure 5.10. In particular, Figure 5.10

illustrates that the rivulet has a rounded nose with shape

$$a \sim \left[\frac{315\hat{J}}{8\bar{\beta}^3 \sin\alpha}(L-x)\right]^{\frac{1}{3}} \to 0^+ \tag{5.109}$$

as $x \to L^-$. Near the nose the slope in the x-direction becomes large according to $\mathrm{d}h_m/\mathrm{d}x = \mathcal{O}((L-x)^{-2/3}) \to -\infty$ as $x \to L^-$. Hence the assumption that the rivulet is slowly varying in x breaks down locally near the nose.

Near $x = 0$ the semi-width behaves like

$$a \sim \bar{a}\left(1 - \frac{18\hat{J}m^3}{\bar{\beta}^3 \sin\alpha f'(m\bar{a})}x\right) \to \bar{a}^-, \tag{5.110}$$

the free surface behaves like

$$h \sim \bar{h} - \frac{18\hat{J}m^3\bar{a}}{\bar{\beta}^3 \sin\alpha f'(m\bar{a})}\frac{\partial h}{\partial a}\bigg|_{a=\bar{a}} x \to \bar{h}^-, \tag{5.111}$$

and the maximum height behaves like

$$h_{\mathrm{m}} \sim \bar{h}_{\mathrm{m}} - \frac{18\hat{J}m^3\bar{a}}{\bar{\beta}^3 \sin\alpha f'(m\bar{a})}\frac{\mathrm{d}h_{\mathrm{m}}}{\mathrm{d}a}\bigg|_{a=\bar{a}} x \to \bar{h}_{\mathrm{m}}^- \tag{5.112}$$

as $x \to 0^+$.

5.4.2.2 The length of a narrow rivulet

In the case of a narrow rivulet (i.e. a rivulet with $0 \le \bar{a} < \pi$) with fixed contact angle, Figure 5.11 shows the length L given by (5.103) as a function of α/π for various values of $\bar{a}$. In particular, Figure 5.11 shows that the rivulet length increases from zero at $\alpha = 0$ to a maximum L_{max} at some value $\alpha = \alpha_{\mathrm{max}}$ and then decreases towards zero at $\alpha = \pi$. In particular, the length of a sessile narrow rivulet behaves like

$$L \sim \frac{\bar{\beta}^3 F(\bar{a})}{18\hat{J}}\alpha \to 0^+ \tag{5.113}$$

in the regime $\alpha \ll 1$. The length of a pendant narrow rivulet behaves like

$$L \sim \frac{\bar{\beta}^3 F(\bar{a})}{18\hat{J}}(\pi - \alpha) \to 0^+ \tag{5.114}$$

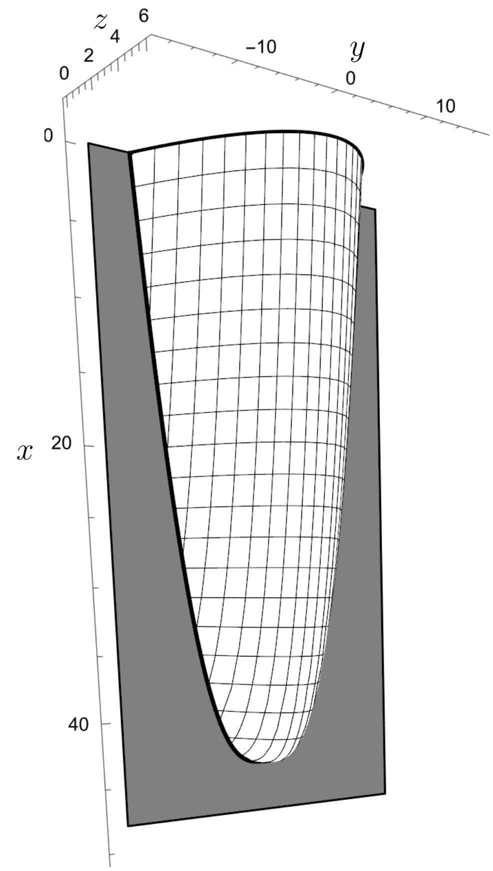

Figure 5.10: Three-dimensional plot of the shape of the rivulet $z = h(x, y)$ given by (5.27), (5.107), and (5.108) in the case of a vertical rivulet with fixed contact angle for $\bar{a} = 12$, $L = 8\bar{a}^3/315 \simeq 43.89$ and $\bar{Q} = 4\bar{a}^4/105 \simeq 789.94$.

as $\alpha \to \pi^-$.

Plots of $L_{\max}$ and $\alpha_{\max}$ are shown in Figure 5.12. In particular, Figure 5.12 shows that the maximum length of a narrow rivulet with fixed contact angle increases monotonically from $L_{\max} \to 0^+$ and $\alpha_{\max} = \pi/2$ as $\bar{a} \to 0^+$ to $L_{\max} \to \infty$ and $\alpha_{\max} \to \pi^-$ as $\bar{a} \to \pi^-$.

5.4.2.3 The length of a wide rivulet

In the case of a wide rivulet (i.e. a rivulet with $\bar{a} \geq \pi$) with fixed contact angle, Figure 5.13 shows the length L given by (5.103) as a function of α/π for various values of $\bar{a}$. In particular, Figure 5.13 shows that the rivulet length increases from $L \to 0^+$ as $\alpha \to 0^+$ to $L \to \infty$ as $\alpha \to \alpha_{\rm crit}^-$, where a rivulet with finite length exists only for $0 \leq \alpha < \alpha_{\rm crit} \leq \pi$. In particular, the length of the rivulet behaves

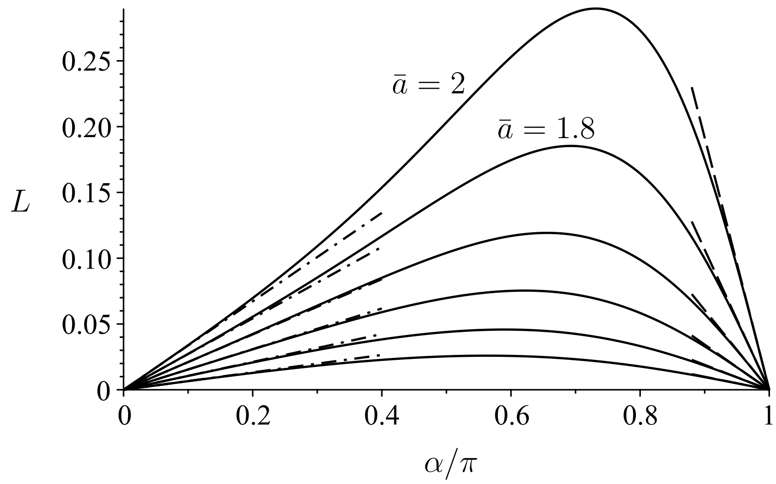

Figure 5.11: Plot of the length L given by (5.103) as a function of α/π and the asymptotic solutions (5.113) and (5.114) in the limits $\alpha \to 0^+$ and $\alpha \to \pi^-$ shown with dash-dotted and dashed lines, respectively, for $\bar{a} = 1, 1.2, 1.4, \ldots, 2$ in the case of a narrow rivulet with fixed contact angle and uniform evaporative flux.

like (5.113) as $\alpha \to 0^+$ and becomes infinitely long according to

$$L \sim \frac{20\bar{\beta}^3\bar{a}}{3\hat{J}(\bar{a}^4 - \pi^4)}(\alpha_{\mathrm{crit}} - \alpha)^{-3} \to \infty \tag{5.115}$$

as $\alpha \to \alpha_{\mathrm{crit}}^-$ for $\bar{a} > \pi$ and

$$L \sim \frac{160\bar{\beta}^3}{3\pi^3\hat{J}}(\pi - \alpha)^{-5} \to \infty \tag{5.116}$$

as $\alpha \to \alpha_{\mathrm{crit}}^- = \pi^-$ for $\bar{a} = \pi$. Note that (5.115) and (5.116) coincide with (5.90) and (5.91), respectively. This shows that in the limit $\alpha \to \alpha_{\mathrm{crit}}^-$, but not otherwise, the length of a rivulet with fixed contact angle is the same as for a rivulet with fixed semi-width.

5.4.2.4 The rivulet length as $\bar{a}$ varies

The variation of L as a function of $\bar{a}$ for a sessile, vertical and pendant rivulet is shown in Figure 5.14 and 5.15.

In the case of a sessile rivulet, Figure 5.14 shows that the length increases from $L \to 0^+$ as $\bar{a} \to 0^+$ to $L \to \infty$ as $\bar{a} \to \infty$. In particular, the length of a sessile

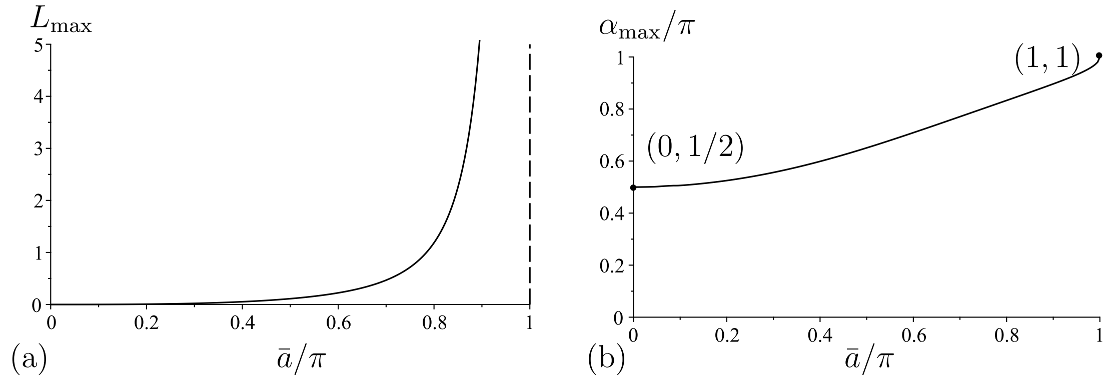

Figure 5.12: Plots of (a) $L_{\max}$ as a function of $\bar{a}/\pi$ and the vertical asymptote at $\bar{a}/\pi = 1$, and (b) $\alpha_{\max}/\pi$ as a function of $\bar{a}/\pi$ in the case of a narrow rivulet with fixed contact angle and uniform evaporative flux.

rivulet with fixed contact angle behaves like

$$L \sim \frac{8\bar{\beta}^3 \sin\alpha}{315\hat{J}}\bar{a}^3 \to 0^+ \tag{5.117}$$

in the regime $\bar{a} \ll 1$ and

$$L \sim \frac{\bar{\beta}^3 \sin\alpha}{3m^3\hat{J}} \ln(m\bar{a}) \to \infty \tag{5.118}$$

in the regime $\bar{a} \gg 1$. Therefore, (5.118) shows that, unlike the length of a rivulet with fixed semi-width which attains an $\mathcal{O}(1)$ value in the limit $\bar{a} \to \infty$ given by (5.93), the length of a rivulet with fixed contact angle becomes infinite in the limit $\bar{a} \to \infty$.

In the case of a vertical rivulet, Figure 5.15 shows that the length increases from $L \to 0^+$ as $\bar{a} \to 0^+$ to $L \to \infty$ as $\bar{a} \to \infty$. In particular, the length of a vertical rivulet with fixed contact angle behaves like (5.117) as $\bar{a} \to 0^+$ and

$$L \sim \frac{8\bar{\beta}^3}{315\hat{J}}\bar{a}^3 \to \infty \tag{5.119}$$

in the regime $\bar{a} \gg 1$.

In the case of a pendant rivulet, Figure 5.15 shows that the length increases from $L \to 0^+$ as $\bar{a} \to 0^+$ to $L \to \infty$ as $\bar{a} \to \bar{a}_{\mathrm{crit}}^-$. In particular, the length of a

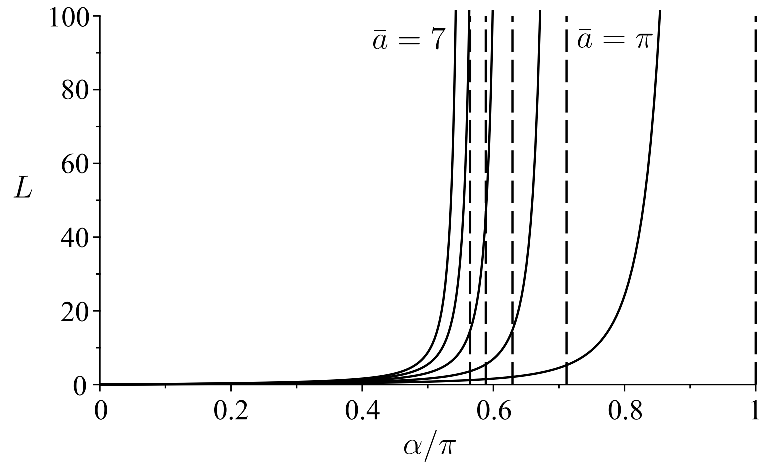

Figure 5.13: Plot of the length L given by (5.103) as a function of α/π and the vertical asymptotes at $\alpha = \alpha_{\text{crit}}$ shown with dashed lines for $\bar{a} = \pi$, 4, 5, 6, 7 in the case of a wide rivulet with fixed contact angle and a uniform evaporative flux.

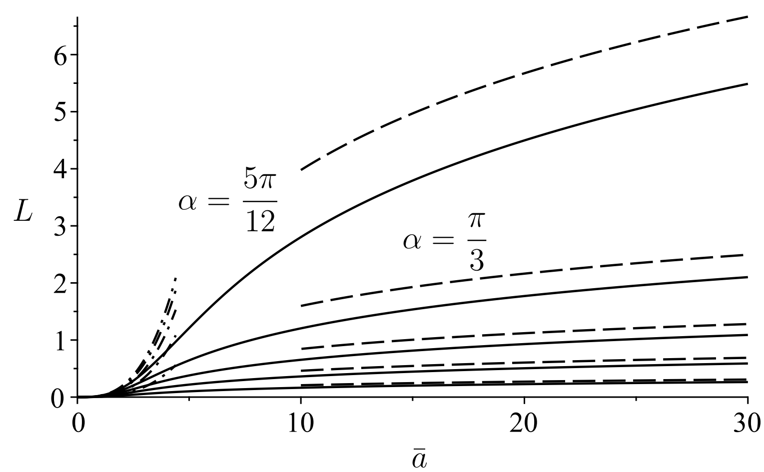

Figure 5.14: Plot of the length L given by (5.103) as a function of $\bar{a}$ and the asymptotic solutions (5.117) and (5.118) in the limits $\bar{a} \to 0^+$ and $\bar{a} \to \infty$ shown with dash-dotted and dashed lines, respectively, for $\alpha = \pi/12$, $\pi/6$, ..., $5\pi/12$ in the case of a sessile rivulet with fixed contact angle and uniform evaporative flux.

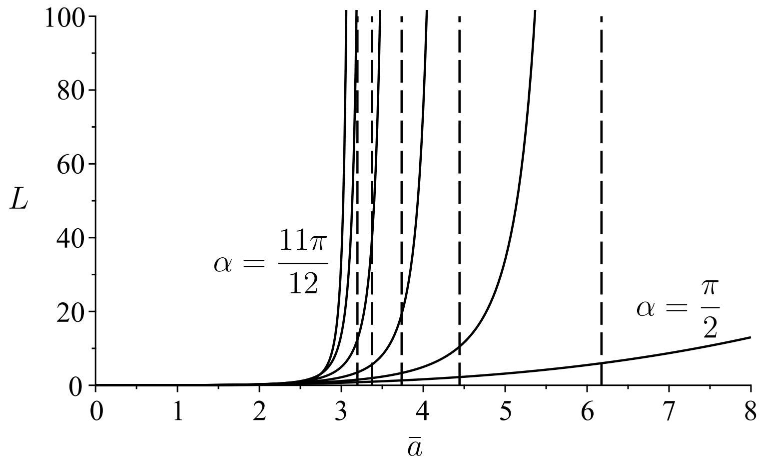

Figure 5.15: Plot of the length L given by (5.103) as a function of $\bar{a}$ and the vertical asymptotes at $\bar{a} = \bar{a}_{\mathrm{crit}} = \pi/m$ shown with dashed lines for $\alpha = 7\pi/12$, $2\pi/3$, …, $11\pi/12$ in the case of a pendant rivulet with fixed contact angle and uniform evaporative flux.

pendant rivulet behaves like (5.117) as $\bar{a} \to 0^+$ and

$$L \sim \frac{5\bar{\beta}^3 \sin\alpha}{6m^6 \hat{J}} (\bar{a}_{\mathrm{crit}} - \bar{a})^{-3} \to \infty \tag{5.120}$$

as $\bar{a} \to \bar{a}_{\mathrm{crit}}^-$.

5.4.2.5 Area and volume

From (5.42) the area of the base of a rivulet with fixed contact angle is given by

$$A = \frac{\bar{\beta}^3 \sin\alpha}{9m^4 \hat{J}} f(m\bar{a}) = \frac{\bar{Q}}{\hat{J}}. \tag{5.121}$$

From (5.42) the volume of a rivulet with fixed contact angle is given by

$$\begin{aligned} V &= \frac{\bar{\beta}^4 \tan\alpha}{9m^3 \hat{J}} \left[\int_0^{m\bar{a}} \frac{g(s) f'(s)}{s} \, \mathrm{d}s - F(m\bar{a}) \right] \\ &= \frac{\bar{\beta} m \bar{Q}}{f(m\bar{a}) \hat{J} \cos\alpha} \left[\int_0^{m\bar{a}} \frac{g(s) f'(s)}{s} \, \mathrm{d}s - F(m\bar{a}) \right]. \end{aligned} \tag{5.122}$$

In the case of a vertical rivulet equations (5.121) and (5.122) reduce to

$$A = \frac{4\bar{\beta}^3\bar{a}^4}{105\hat{J}} = \frac{\bar{Q}}{\hat{J}}, \quad V = \frac{16\bar{\beta}^4\bar{a}^5}{1575\hat{J}} = \frac{4\bar{\beta}\bar{a}\bar{Q}}{15\hat{J}}. \tag{5.123}$$

The base area of a vertical rivulet with fixed contact angle given by (5.123) is identical to the base area of a vertical rivulet with fixed semi-width given by (5.98). The volume of a vertical rivulet with fixed contact angle given by (5.123) is 16/15 the volume of a vertical rivulet with fixed semi-width given by (5.98).

5.5 Evaporating Rivulet: Pseudo diffusion-limited model

In this section we consider the evaporation of the rivulet to be governed by the pseudo diffusion-limited model described in Section 5.3.2. In particular, in this section the evaporative flux therefore takes the form (5.56). Hence (5.18) gives the following differential equation

$$\frac{\mathrm{d}Q}{\mathrm{d}x} = -\hat{\jmath}\left[\sin^{-1}\left(\frac{y}{a}\right)\right]_{-a}^{a} = -\pi\hat{\jmath}, \tag{5.124}$$

and equation (5.19) becomes

$$Q = \bar{Q} - \pi\hat{\jmath}x, \tag{5.125}$$

which since $Q = 0$ at $x = L$ implies immediately that the length of the rivulet L is given by

$$L = \frac{\bar{Q}}{\pi\hat{\jmath}} = \frac{\bar{\beta}^3 \sin\alpha f(m\bar{a})}{9\pi\hat{\jmath}m^4}. \tag{5.126}$$

In the case of a vertical rivulet (5.126) is given by

$$L = \frac{4\bar{\beta}^3\bar{a}^4}{105\pi\hat{\jmath}}. \tag{5.127}$$

Equation (5.126) shows that, unlike for the case of uniform evaporation described in Section 5.4, the length is the same for a rivulet with fixed semi-width or fixed contact angle. Substituting (5.30) into (5.124) we obtain the ordinary differential equation for $\beta(x)$ and/or $a(x)$ given by

$$\frac{\sin\alpha}{9m^4}\frac{\mathrm{d}}{\mathrm{d}x}\left[\beta^3 f(ma)\right] = -\pi\hat{\jmath}. \tag{5.128}$$

5.5.1 Fixed semi-width $a = \bar{a}$

In this subsection we will consider an evaporating rivulet whose semi-width is fixed with constant value $a = \bar{a}$. In particular, we will describe the behaviour of the contact angle and derive expressions for the area of the base and volume of the rivulet.

For a rivulet with fixed semi-width, the ordinary differential equation (5.128) becomes

$$\frac{\mathrm{d}\beta}{\mathrm{d}x} = -\frac{3\pi\hat{\jmath}m^4}{\beta^2\sin\alpha f(m\bar{a})}. \tag{5.129}$$

Solving (5.129) subject to the initial condition $\beta(0) = \bar{\beta}$ gives

$$\beta = \bar{\beta}\left(1 - \frac{105\pi\hat{\jmath}x}{4\bar{\beta}^3\bar{a}^4}\right)^{\frac{1}{3}}. \tag{5.130}$$

Using the end condition $\beta(L) = 0$, (5.130) becomes

$$\beta = \bar{\beta}\left(1 - \frac{x}{L}\right)^{\frac{1}{3}} = \bar{\beta}\left(1 - \frac{\pi\hat{\jmath}x}{\bar{Q}}\right)^{\frac{1}{3}}, \tag{5.131}$$

where the length of the rivulet L is given by (5.126). Figure 5.16 shows the contact angle given by (5.131) as a function of x for different values of $\bar{a}$ for both a sessile and a pendant rivulet. In particular, Figure 5.16 shows that β decreases from $\beta = \bar{\beta}$ at $x = 0$ to $\beta = 0$ at $x = L$. Furthermore, Figure 5.16 shows that the contact angle β increases as the initial semi-width $\bar{a}$ increases.

5.5.1.1 Rivulet shape

The three-dimensional shape of an evaporating rivulet with fixed semi-width and evaporative flux given by (5.56) is qualitatively similar to that shown in Figure 5.3, and so is not plotted here for brevity. In particular, the rivulet has a "square" nose at which its slope in the x-direction becomes large according to $\mathrm{d}h_m/\mathrm{d}x = \mathcal{O}((L-x)^{-2/3}) \to -\infty$ as $x \to L^-$. Hence the assumption that the rivulet is slowly varying in x breaks down locally near the nose. In particular, the contact angle

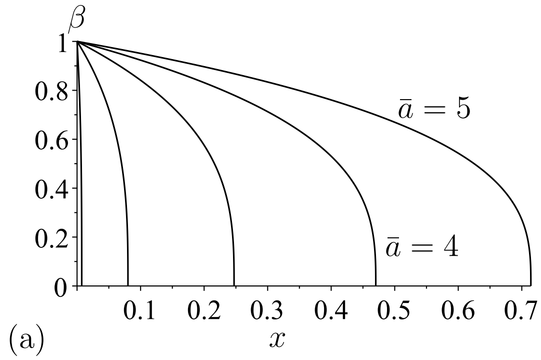

Figure 5.16: Plots of the contact angle β given by (5.131) as a function of x for (a) $\alpha = \pi/4$, $\bar{a} = 1, 2, \ldots, 5$ and (b) $\alpha = 3\pi/4$, $\bar{a} = 1, 1.2, \ldots, 2$ in the case of a rivulet with fixed semi-width and evaporative flux given by (5.56).

near the nose behaves like (5.84) as $x \to L^-$, with L given by (5.126).

Near $x = 0$ the contact angle behaves like (5.85), the free surface behaves like (5.86), and the maximum height behaves like (5.87), as $x \to 0^+$.

5.5.1.2 Area and volume

From (5.42) area of the base of a rivulet with fixed semi-width is given by

$$A = 2\bar{a}L = \frac{2\bar{a}\bar{\beta}^3 \sin\alpha f(m\bar{a})}{9\pi\hat{\jmath}m^4} = \frac{2\bar{a}\bar{Q}}{\pi\hat{\jmath}}. \tag{5.132}$$

From (5.42) the volume of a rivulet with fixed semi-width is given by

$$V = \frac{\bar{\beta}^4 \tan\alpha}{6\pi\hat{\jmath}m^4} f(m\bar{a})(g(m\bar{a}) - 1) = \frac{3\bar{\beta}(g(m\bar{a}) - 1)\bar{Q}}{2\pi\hat{\jmath}\cos\alpha}. \tag{5.133}$$

In the case of a vertical rivulet equations (5.132) and (5.133) reduce to

$$A = 2\bar{a}L = \frac{8\bar{\beta}^3\bar{a}^5}{105\pi\hat{\jmath}} = \frac{2\bar{a}\bar{Q}}{\pi\hat{\jmath}}, \quad V = \frac{\bar{\beta}\bar{a}^2 L}{2} = \frac{2\bar{\beta}^4\bar{a}^6}{105\pi\hat{\jmath}} = \frac{\bar{\beta}\bar{a}^2\bar{Q}}{2\pi\hat{\jmath}}, \tag{5.134}$$

respectively.

5.5.2 Fixed contact angle $\beta = \bar{\beta}$

In this subsection we will consider an evaporating rivulet whose contact angle is fixed with constant value $\beta = \bar{\beta}$. In particular, we will describe the behaviour of

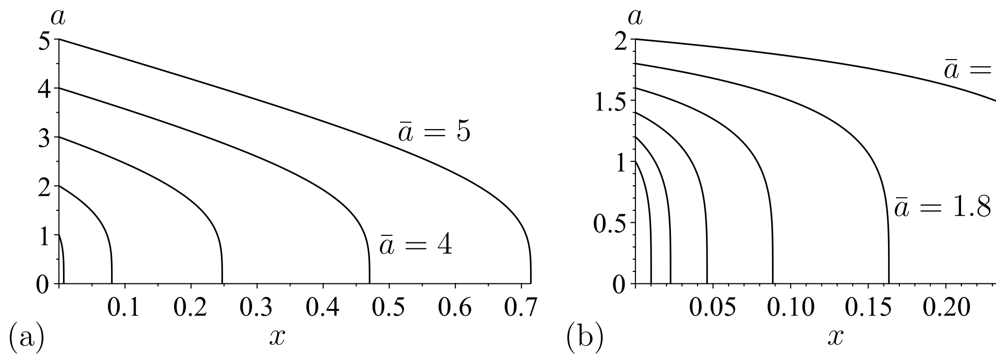

Figure 5.17: Plots of the semi-width a given by (5.136) as a function of x for (a) $\alpha = \pi/4$, $\bar{a} = 1, 2, \ldots, 5$ and (b) $\alpha = 3\pi/4$, $\bar{a} = 1, 1.2, \ldots, 2$ in the case of a rivulet with fixed contact angle and evaporative flux given by (5.56)

the semi-width and derive expressions for the area of the base and volume of the rivulet.

For a rivulet with fixed contact angle, the ordinary differential equation (5.128) becomes

$$\frac{\mathrm{d}(ma)}{\mathrm{d}x} = -\frac{9\pi\hat{\jmath}m^4}{\bar{\beta}^3 \sin\alpha f'(ma)}. \tag{5.135}$$

Solving (5.135) subject to the initial condition $a(0) = \bar{a}$ gives the implicit solution for the semi-width

$$f(ma) = f(m\bar{a})\left(1 - \frac{x}{L}\right) = f(m\bar{a})\left(1 - \frac{\pi\hat{\jmath}x}{\bar{Q}}\right), \tag{5.136}$$

such that L is again given by (5.126).

The solution for the semi-width in the case of a vertical rivulet is given explicitly by

$$a = \bar{a}\left(1 - \frac{x}{L}\right)^{\frac{1}{4}}. \tag{5.137}$$

Figure 5.17 shows the semi-width given implicitly by (5.136) as a function of x for different values of $\bar{a}$ for both a sessile and a pendant rivulet. In particular, Figure 5.17 shows that a decreases from $a = \bar{a}$ at $x = 0$ to $a = 0$ at $x = L$. Furthermore, Figure 5.17 shows that the semi-width a increases as the initial semi-width $\bar{a}$ increases.

5.5.2.1 Rivulet shape

The three-dimensional shape of an evaporating rivulet with fixed contact angle and evaporative flux given by (5.56) is qualitatively similar to that shown in Figure 5.10, and so again is not plotted here for brevity. In particular, the rivulet has a rounded nose with shape

$$a \sim \frac{35 f(m\bar{a})}{12m^4}\left(1-\frac{x}{L}\right)^{\frac{1}{4}} \to 0^+ \tag{5.138}$$

as $x \to L^-$. Near the nose the slope in the x-direction becomes large according to $\mathrm{d}h_m/\mathrm{d}x = \mathcal{O}((L-x)^{-3/4}) \to -\infty$ as $x \to L^-$. Hence the assumption that the rivulet is slowly varying in x breaks down locally near the nose.

Near $x = 0$ the semi-width is given implicitly by

$$a \sim \bar{a} - \frac{f(m\bar{a})}{mLf'(m\bar{a})}x \to \bar{a}^-, \tag{5.139}$$

the free surface behaves like

$$h \sim \bar{h} - \frac{9\pi\hat{\jmath}m^3}{\bar{\beta}^3 \sin\alpha f'(m\bar{a})}\frac{\partial h}{\partial a}\bigg|_{a=\bar{a}} x \to \bar{h}^-, \tag{5.140}$$

and the maximum height behaves like

$$h_{\mathrm{m}} \sim \bar{h}_{\mathrm{m}} - \frac{9\pi\hat{\jmath}m^3}{\bar{\beta}^3 \sin\alpha f'(m\bar{a})}\frac{\mathrm{d}h_{\mathrm{m}}}{\mathrm{d}a}\bigg|_{a=\bar{a}} x \to \bar{h}_{\mathrm{m}}^-, \tag{5.141}$$

as $x \to 0^+$.

5.5.2.2 Area and volume

From (5.42) the base area of a rivulet with fixed contact angle is given by

$$A = \frac{2\bar{\beta}^3 \sin\alpha}{9\pi\hat{\jmath}m^5}\int_0^{m\bar{a}} Mf'(M)\,\mathrm{d}M = \frac{2\bar{Q}}{\pi\hat{\jmath}mf(m\bar{a})}\int_0^{m\bar{a}} Mf'(M)\,\mathrm{d}M. \tag{5.142}$$

From (5.42) the volume of a rivulet with fixed contact angle is given by

$$\begin{aligned} V &= \frac{2\bar{\beta}^4 \tan\alpha}{9\pi\hat{\jmath}m^4} \int_0^{m\bar{a}} [g(M) - 1]f'(M)\, \mathrm{d}M \\ &= \frac{2\bar{\beta}\bar{Q}}{\pi\hat{\jmath}\cos\alpha f(m\bar{a})} \int_0^{m\bar{a}} [g(M) - 1]f'(M)\, \mathrm{d}M. \end{aligned} \tag{5.143}$$

In the case of a vertical rivulet equations (5.142) and (5.143) reduce to

$$A = \frac{32\bar{\beta}^3\bar{a}^5}{525\pi\hat{\jmath}} = \frac{8L\bar{a}}{5} = \frac{8\bar{Q}a}{5\pi\hat{\jmath}}, \quad V = \frac{16\bar{\beta}^4\bar{a}^6}{945\pi\hat{\jmath}} = \frac{4\bar{\beta}\bar{a}^2 L}{9} = \frac{4\bar{\beta}\bar{a}^2\bar{Q}}{9\pi\hat{\jmath}}, \tag{5.144}$$

respectively. The base area of a vertical rivulet with fixed contact angle given by (5.144) is 4/5 the base area of a vertical rivulet with fixed semi-width given by (5.134). The volume of a vertical rivulet with fixed contact angle given by (5.144) is 8/9 the volume of a vertical rivulet with fixed semi-width given by (5.134).

5.5.3 The rivulet length

In this subsection we will discuss the behaviour of the length of the rivulet, which, as we have already described, in the case of the pseudo diffusion-limited model, is the same regardless of whether the rivulet has a fixed semi-width or fixed contact angle. In particular, we will describe the behaviour of the length of narrow, wide, sessile, vertical and pendant rivulets, with respect to the angle of inclination α and initial semi-width $\bar{a}$.

5.5.3.1 The length of a narrow rivulet

In the case of a narrow rivulet with either fixed semi-width or contact angle, Figure 5.18 shows the length L given by (5.126) as a function of α/π for various values of $\bar{a}$. In particular, Figure 5.18 shows that the rivulet length increases from zero at $\alpha = 0$ to a maximum $L = L_{\max}$ at some value $\alpha = \alpha_{\max}$ and then decreases towards zero at $\alpha = \pi$. In particular, the length of a sessile narrow rivulet behaves like

$$L \sim \frac{\bar{\beta}^3 f(\bar{a})}{9\pi\hat{\jmath}}\alpha \to 0^+ \tag{5.145}$$

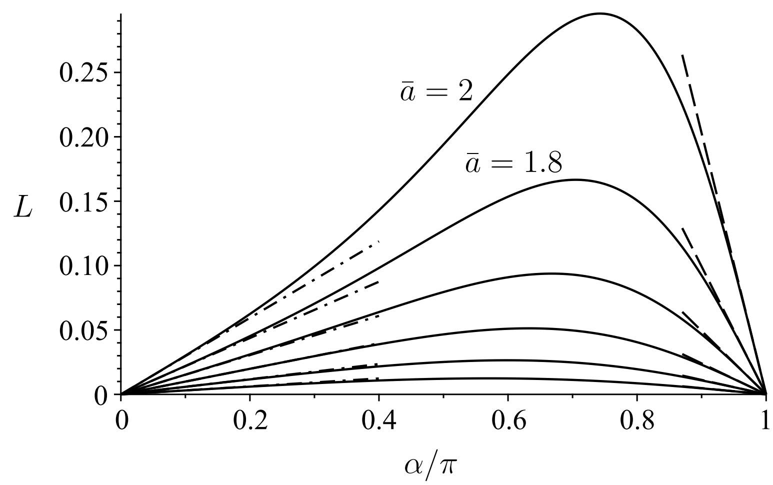

Figure 5.18: Plot of the length L given by (5.126) as a function of α/π and the asymptotic solutions (5.145) and (5.146) in the limits $\alpha \to 0^+$ and $\alpha \to \pi^-$ shown with dash-dotted and dashed lines, respectively, for $\bar{a} = 1, 1.2, 1.4, \ldots, 2$ in the case of a narrow rivulet with either fixed semi-width or contact angle and evaporative flux given by (5.56).

in the regime $\alpha \ll 1$. The length of a pendant narrow rivulet behaves like

$$L \sim \frac{\bar{\beta}^3 f(\bar{a})}{9\pi \hat{\jmath}}(\pi - \alpha) \to 0^+ \tag{5.146}$$

as $\alpha \to \pi^-$.

Plots of $L_{\max}$ and $\alpha_{\max}$ are shown in Figure 5.19. In particular, Figure 5.19 shows that the maximum length of a narrow rivulet with fixed contact angle increases monotonically from $L_{\max} \to 0^+$ and $\alpha_{\max} = \pi/2$ as $\bar{a} \to 0^+$ to $L_{\max} \to \infty$ and $\alpha_{\max} \to \pi^-$ as $\bar{a} \to \pi^-$.

5.5.3.2 The length of a wide rivulet

In the case of a wide rivulet with either fixed semi-width or contact angle, Figure 5.20 shows the length L given by (5.126) as a function of α/π for various values of $\bar{a}$. In particular, Figure 5.20 shows that the rivulet length increases from $L \to 0^+$ as $\alpha \to 0^+$ to $L \to \infty$ as $\alpha \to \alpha_{\text{crit}}^-$, where a rivulet with finite length exists only for $0 \le \alpha < \alpha_{\text{crit}} \le \pi$. In particular, the length of the rivulet behaves like (5.145)

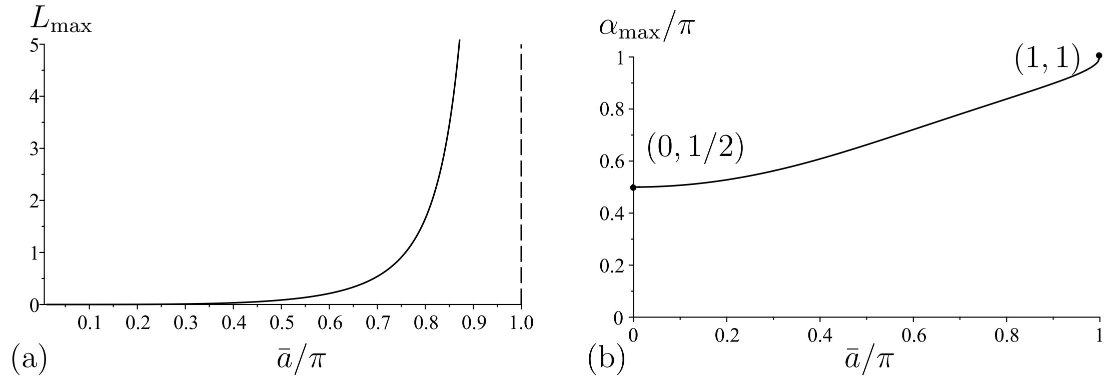

Figure 5.19: Plots of (a) $L_{\max}$ as a function of $\bar{a}/\pi$ and the vertical asymptote at $\bar{a}/\pi = 1$, and (b) $\alpha_{\max}/\pi$ as a function of $\bar{a}/\pi$ in the case of a rivulet with either fixed semi-width or contact angle and evaporative flux given by (5.56).

as $\alpha \to 0^+$ and becomes infinitely long according to

$$L \sim \frac{40\bar{\beta}^3\bar{a}^2}{3\pi\hat{\jmath}(\bar{a}^4 - \pi^4)}(\alpha_{\text{crit}} - \alpha)^{-3} \to \infty \tag{5.147}$$

as $\alpha \to \alpha_{\text{crit}}^-$ for $\bar{a} > \pi$ and

$$L \sim \frac{320\bar{\beta}^3}{3\pi^3\hat{\jmath}}(\pi - \alpha)^{-5} \to \infty \tag{5.148}$$

as $\alpha \to \alpha_{\text{crit}}^- = \pi^-$ for $\bar{a} = \pi$.

5.5.3.3 The rivulet length as $\bar{a}$ varies

The variation of L as a function of $\bar{a}$ for a sessile, vertical and pendant rivulet is shown in Figures 5.21 and 5.22.

In the case of a sessile rivulet, Figure 5.21 shows that the length increases from $L \to 0^+$ as $\bar{a} \to 0^+$ to $L \to \infty$ as $\bar{a} \to \infty$. In particular, the length of a sessile rivulet with either fixed semi-width or fixed contact angle behaves like

$$L \sim \frac{4\bar{\beta}^3 \sin\alpha}{105\pi\hat{\jmath}}\bar{a}^4 \to 0^+ \tag{5.149}$$

in the regime $\bar{a} \ll 1$ and

$$L \sim \frac{2\bar{\beta}^3 \sin\alpha}{3\pi\hat{\jmath}m^3}\bar{a} \to \infty \tag{5.150}$$

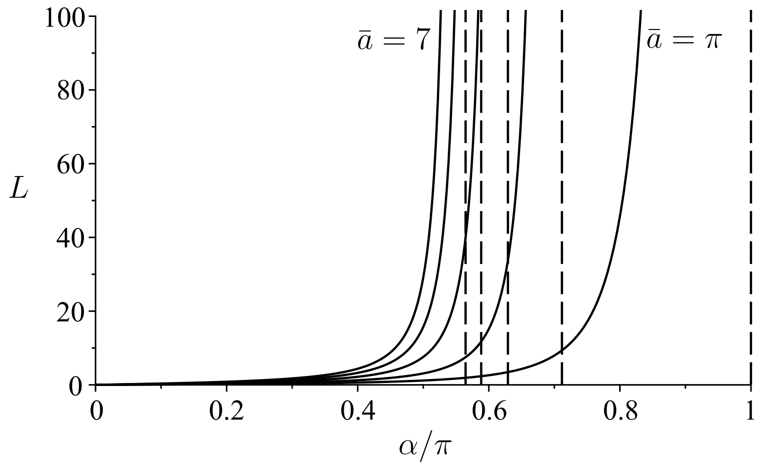

Figure 5.20: Plot of the length L given by (5.126) as a function of α/π and the vertical asymptotes at $\alpha = \alpha_{\text{crit}}$ shown with dashed lines for $\bar{a} = \pi$, 4, 5, 6, 7 in the case of a wide rivulet with either fixed semi-width or contact angle and evaporative flux given by (5.56).

in the regime $\bar{a} \gg 1$. The $\mathcal{O}(1)$ distance between L and the asymptotic solution (5.150), clearly visible in Figure 5.21, is found at next order in the large $\bar{a}$ expansion of (5.126) and is given by $-11\bar{\beta}^3 \sin\alpha/(9\pi\hat{\jmath}m^4)$.

In the case of a vertical rivulet, Figure 5.22 shows that the length increases from $L \to 0^+$ as $\bar{a} \to 0^+$ to $L \to \infty$ as $\bar{a} \to \infty$. In particular, the length of a vertical rivulet with either fixed semi-width or fixed contact angle behaves like (5.149) as $\bar{a} \to 0^+$ and

$$L \sim \frac{4\bar{\beta}^3}{105\pi\hat{\jmath}}\bar{a}^4 \to \infty \tag{5.151}$$

in the regime $\bar{a} \gg 1$.

In the case of a pendant rivulet Figure 5.22 shows that the length increases from $L \to 0^+$ as $\bar{a} \to 0^+$ to $L \to \infty$ as $\bar{a} \to \bar{a}_{\text{crit}}^-$. In particular, the length of a pendant rivulet behaves like (5.149) as $\bar{a} \to 0^+$ and

$$L \sim \frac{5\bar{\beta}^3 \sin\alpha}{3\hat{\jmath}m^7}\left(\bar{a}_{\text{crit}} - \bar{a}\right)^{-3} \to \infty \tag{5.152}$$

as $\bar{a} \to \bar{a}_{\text{crit}}^-$.

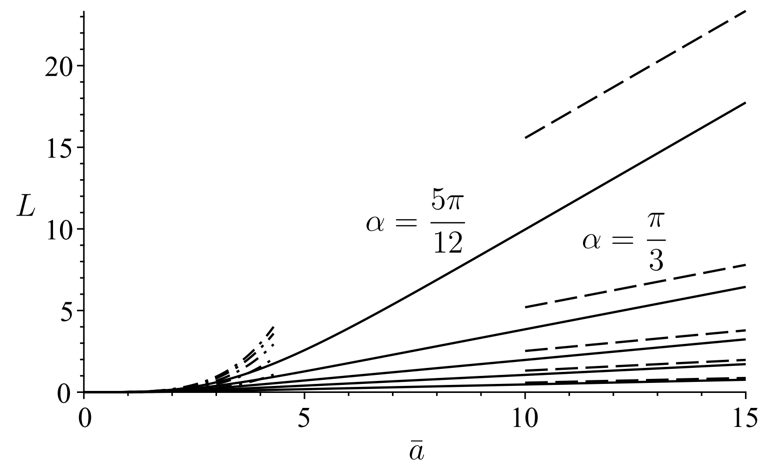

Figure 5.21: Plot of the length L given by (5.126) as a function of $\bar{a}$ and the asymptotic solutions (5.149) and (5.150) in the limits $\bar{a} \to 0^+$ and $\bar{a} \to \infty$ shown with dash-dotted and dashed lines, respectively, for $\alpha = \pi/12, \pi/6, \ldots, 5\pi/12$ in the case of a sessile rivulet with either fixed semi-width or contact angle and evaporative flux given by (5.56).

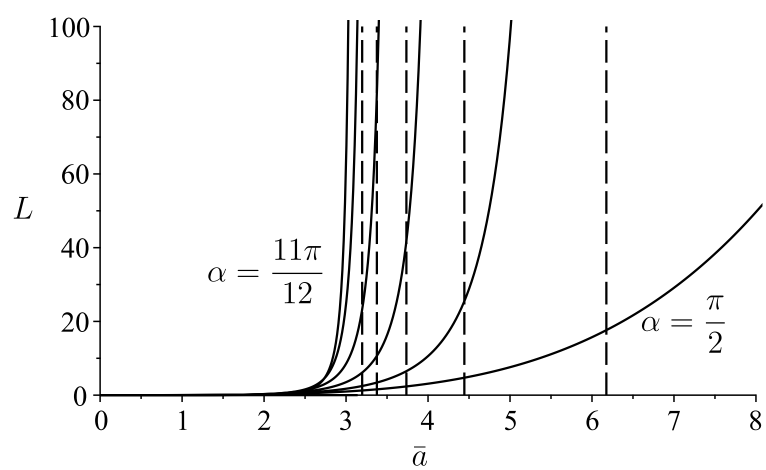

Figure 5.22: Plot of the length of a pendant rivulet with either fixed semi-width or contact angle, L, given by (5.126) as a function of $\bar{a}$ and the vertical asymptotes at $\bar{a} = \bar{a}_{\mathrm{crit}} = \pi/m$ shown with dashed lines for $\alpha = 7\pi/12$, $2\pi/3$, …, $11\pi/12$.

5.6 Evaporating rivulet: One-sided model

In this section we consider the evaporation of the rivulet to be governed by the one-sided model described in Section 5.3.3. In this section the evaporative flux therefore takes the form (5.74).

Hence, (5.18) gives the following differential equation

$$\frac{\mathrm{d}Q}{\mathrm{d}x} = -\frac{4a}{K} R(b, ma), \tag{5.153}$$

where

$$b = \frac{\beta}{Km} \text{ and } \bar{b} = \frac{\bar{\beta}}{Km}, \tag{5.154}$$

and the function $R = R(b, ma)$ is defined by

$$R(b, ma) = \begin{cases} \dfrac{\tanh^{-1}\sqrt{\frac{\tanh\left(\frac{1}{2}ma\right)+b}{\coth\left(\frac{1}{2}ma\right)+b}}}{ma\sqrt{\left(\tanh\left(\frac{1}{2}ma\right)+b\right)\left(\coth\left(\frac{1}{2}ma\right)+b\right)}} & 0 \le \alpha < \dfrac{\pi}{2}, \\ \dfrac{1}{\sqrt{bma(bma+2)}}\tanh^{-1}\sqrt{\dfrac{bma}{bma+2}} & \alpha = \dfrac{\pi}{2}, \\ \dfrac{\tan^{-1}\sqrt{\frac{\tan\left(\frac{1}{2}ma\right)-b}{\cot\left(\frac{1}{2}ma\right)+b}}}{ma\sqrt{\left(\tan\left(\frac{1}{2}ma\right)-b\right)\left(\cot\left(\frac{1}{2}ma\right)+b\right)}} & \dfrac{\pi}{2} < \alpha \le \pi. \end{cases} \tag{5.155}$$

For future reference, we note here that in the case of a sessile rivulet (i.e. with $0 \le \alpha < \pi/2$) and pendant rivulet (i.e. $\pi/2 < \alpha \le \pi$) the function R given by (5.155) behaves like

$$R \to \frac{1-\eta^2}{2\eta}\tanh^{-1}\eta \tag{5.156}$$

as $\alpha \to \pi/2$, where the function $\eta = \eta(a, \beta, K)$ is defined by

$$\eta = \frac{1}{\sqrt{1+\frac{2K}{a\beta}}}, \tag{5.157}$$

which recovers R in the case of a vertical rivulet (i.e. $\alpha = \pi/2$) with b replaced by β/Km as in (5.154). For future reference, we define $\bar{\eta} = \eta(\bar{a}, \bar{\beta}, K)$.

In the limit $b \to \infty$ the function R given by (5.155) behaves like

$$R(b, ma) \sim \frac{\ln(bc(ma))}{2bma}, \tag{5.158}$$

where

$$c(ma) = \begin{cases} 2\sinh(ma) & 0 \le \alpha < \dfrac{\pi}{2}, \\ 2ma & \alpha = \dfrac{\pi}{2}, \\ 2\sin(ma) & \dfrac{\pi}{2} < \alpha \le \pi. \end{cases} \tag{5.159}$$

Note that for sessile, vertical and pendant rivulets, $c(ma) \sim 2ma$ as $ma \to 0^+$ (i.e. with $\alpha \to \pi/2$). In both the limit $b \to 0^+$ and in the limit $ma \to 0^+$, $R(b, ma) \to 1/2$. In the limit $ma \to \infty$ for a sessile rivulet the function R given by (5.155) behaves like

$$R(b, ma) \to \frac{1}{2(1+b)} = \mathcal{O}(1) \tag{5.160}$$

and for a vertical rivulet

$$R(b, ma) \sim \frac{\ln(2bma)}{2bma} \to \infty \tag{5.161}$$

in the regime $ma \gg 1$. In the limit $ma \to ma_{\mathrm{crit}}^-$, the function R given by (5.155) behaves like

$$R \sim \sqrt{\frac{ma_{\mathrm{crit}} - ma}{8b}} \to 0. \tag{5.162}$$

In the limit $\alpha \to \alpha_{\mathrm{crit}}^-$ we have that $b \to b_{\mathrm{crit}}^- = \beta a/(\pi K)$ and the function R given by (5.155) behaves like

$$R \sim \frac{(a^4 - \pi^4)^{\frac{1}{4}}}{4\sqrt{\pi b_{\mathrm{crit}}}} (\alpha_{\mathrm{crit}} - \alpha)^{\frac{1}{2}} \to 0 \tag{5.163}$$

as $\alpha \to \alpha_{\mathrm{crit}}^-$ for $\bar{a} > \pi$ and

$$R \sim \sqrt{\frac{\pi}{8b_{\mathrm{crit}}}}\bigg|_{a=\pi} (\pi - \alpha) \to 0 \tag{5.164}$$

as $\alpha \to \alpha_{\mathrm{crit}}^- = \pi^-$ for $\bar{a} = \pi$.

Substituting (5.30) into (5.153) we obtain the ordinary differential equation for $b(x)$ and/or $a(x)$ given by

$$\frac{\sin\alpha}{9m}\frac{\mathrm{d}}{\mathrm{d}x}\left[b^3 f(ma)\right] = -\frac{4a}{K^4}R(b, ma). \tag{5.165}$$

5.6.1 Fixed semi-width $a = \bar{a}$

In this subsection we will consider an evaporating rivulet whose semi-width is fixed with constant value $a = \bar{a}$. In particular, we will describe the behaviour of the contact angle and the variation of the length of narrow, wide, sessile, vertical and pendant rivulets, with respect to the angle of inclination α, the initial semi-width $\bar{a}$, and K which, as discussed in Section 5.3.3, measures the degree of non-equilibrium at the free surface of the rivulet.

For a rivulet with fixed semi-width, the ordinary differential equation (5.165) becomes

$$\frac{K^4 \sin\alpha f(m\bar{a})}{12m\bar{a}} b^2 \frac{\mathrm{d}b}{\mathrm{d}x} = -R(b, m\bar{a}), \tag{5.166}$$

so that $b = b(x)$ is given implicitly by

$$x = \frac{K^4 \sin\alpha f(m\bar{a})}{12m\bar{a}} \int_b^{\bar{b}} \frac{\tilde{b}^2}{R(\tilde{b}, m\bar{a})}\,\mathrm{d}\tilde{b}. \tag{5.167}$$

Using the end condition $\beta(L) = b(L) = 0$, from (5.167), the length of the rivulet L is given by

$$L = \frac{K^4 f(m\bar{a}) I_{\bar{a}} \sin\alpha}{12m\bar{a}}, \tag{5.168}$$

where

$$I_{\bar{a}}(\bar{b}, m\bar{a}) = \int_0^{\bar{b}} \frac{\tilde{b}^2}{R(\tilde{b}, m\bar{a})}\,\mathrm{d}\tilde{b}. \tag{5.169}$$

In the case of a vertical rivulet by substituting $\tilde{b} = (2/m\bar{a})\sinh^2\xi$ into (5.168), the length (5.168) becomes

$$L = \frac{32K^4}{35}\int_0^{\tanh^{-1}\bar{\eta}} \frac{\sinh^6\xi\cosh^2\xi}{\xi}\,\mathrm{d}\xi = \frac{K^4}{140}\Lambda\left(\tanh^{-1}\bar{\eta}\right), \tag{5.170}$$

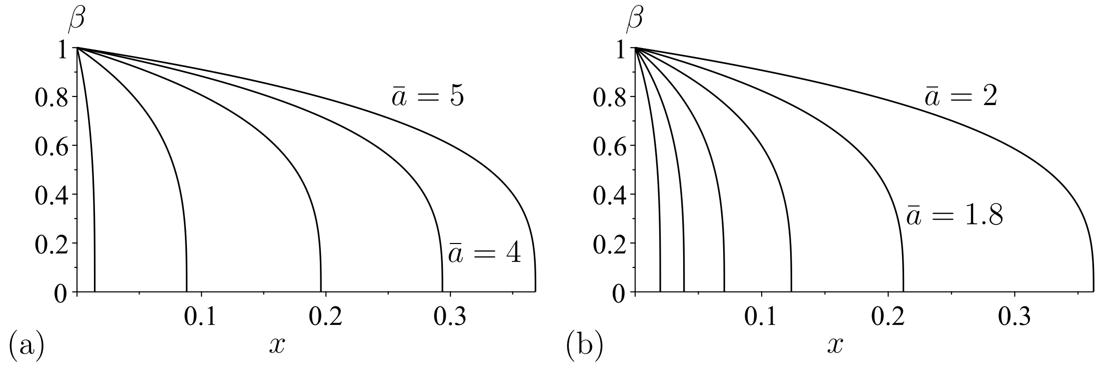

Figure 5.23: Plots of the contact angle β given by (5.167) as a function of x for (a) $\alpha = \pi/4$, $\bar{a} = 1, 2, \ldots, 5$, $K = 1$ and (b) $\alpha = 3\pi/4$, $\bar{a} = 1, 1.2, \ldots, 2$, $K = 1$ in the case of a rivulet with fixed semi-width and evaporative flux given by (5.74).

where the function $\Lambda = \Lambda(\xi)$ is defined by

$$\Lambda(\xi) = \mathrm{Chi}(8\xi) - 4\mathrm{Chi}(6\xi) + 4\mathrm{Chi}(4\xi) + 4\mathrm{Chi}(2\xi) - 5\ln(\xi) - 5\gamma - 11\ln(2) + 4\ln(3), \tag{5.171}$$

in which $\gamma \simeq 0.577$ is Euler's constant and Chi denotes the hyperbolic cosine integral defined by

$$\mathrm{Chi}(\xi) = \gamma + \ln(\xi) + \int_0^\xi \frac{\cosh(s) - 1}{s} \, \mathrm{d}s. \tag{5.172}$$

Figures 5.23 and 5.24 show that the contact angle given implicitly by (5.167) as a function of x for different values of $\bar{a}$ and K, respectively, for both a sessile and a pendant rivulet. In particular, Figures 5.23 and 5.24 show that β decreases from $\beta = \bar{\beta}$ at $x = 0$ to $\beta = 0$ at $x = L$. Furthermore, Figures 5.23 and 5.24 show that the contact angle increases as the initial semi-width $\bar{a}$ and K increases.

5.6.1.1 Rivulet shape

The three-dimensional shape of an evaporating rivulet with fixed semi-width and evaporative flux given by (5.74) is qualitatively similar to that shown in Figure 5.3, and so is not plotted here for brevity. In particular, the rivulet has a "square" nose at which its slope in the x-direction becomes large according to $\mathrm{d}h_{\mathrm{m}}/\mathrm{d}x = \mathcal{O}((L-x)^{-2/3}) \to -\infty$ as $x \to L^-$. Hence the assumption that the rivulet is slowly varying in x breaks down locally near the nose. In particular, the contact angle

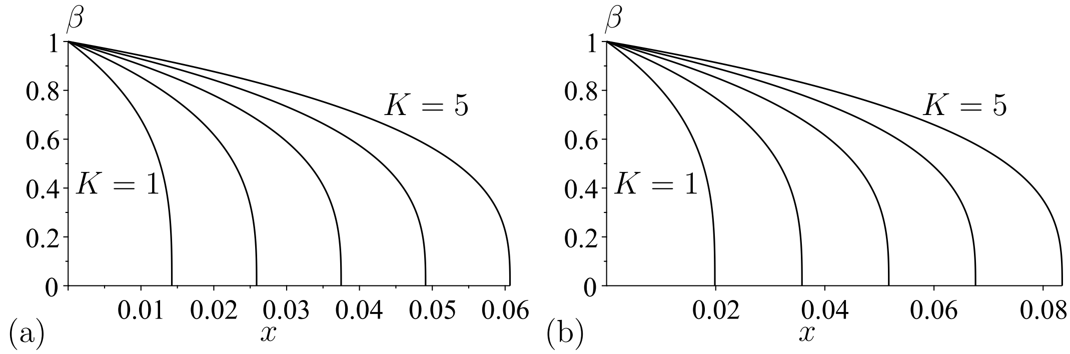

Figure 5.24: Plots of the contact angle β given by (5.167) as a function of x for (a) $\alpha = \pi/4$, $\bar{a} = 1$, $K = 1, 2, \ldots, 5$ and (b) $\alpha = 3\pi/4$, $\bar{a} = 1$, $K = 1, 2, \ldots, 5$ in the case of a rivulet with fixed semi-width and evaporative flux given by (5.74).

near the nose behaves like

$$\beta \sim mK \left[\frac{3I_{\bar{a}}}{2} \left(1 - \frac{x}{L} \right) \right]^{\frac{1}{3}} \to 0^+ \tag{5.173}$$

as $x \to L^+$.

Near $x = 0$ the scaled contact angle b behaves like

$$b \sim \bar{b} \left(1 - \frac{12m\bar{a}R(\bar{b}, m\bar{a})}{\bar{b}K^4 \sin\alpha f(m\bar{a})} x \right) \to \bar{b}^-, \tag{5.174}$$

the free surface behaves like

$$h \sim \bar{h} \left(1 - \frac{12m\bar{a}R(\bar{b}, m\bar{a})}{\bar{b}K^4 \sin\alpha f(m\bar{a})} x \right) \to \bar{h}^-, \tag{5.175}$$

and the maximum height behaves like

$$h_{\mathrm{m}} \sim \bar{h}_{\mathrm{m}} \left(1 - \frac{12m\bar{a}R(\bar{b}, m\bar{a})}{\bar{b}K^4 \sin\alpha f(m\bar{a})} x \right) \to \bar{h}_{\mathrm{m}}^-, \tag{5.176}$$

as $x \to 0^+$.

5.6.1.2 The length of a narrow rivulet

In the case of a narrow rivulet with fixed semi-width, Figures 5.25 and 5.26 show the length L, given by (5.168), as a function of α/π for various values of K and $\bar{a}$, respectively. In particular, Figures 5.25 and 5.26 show that the rivulet length

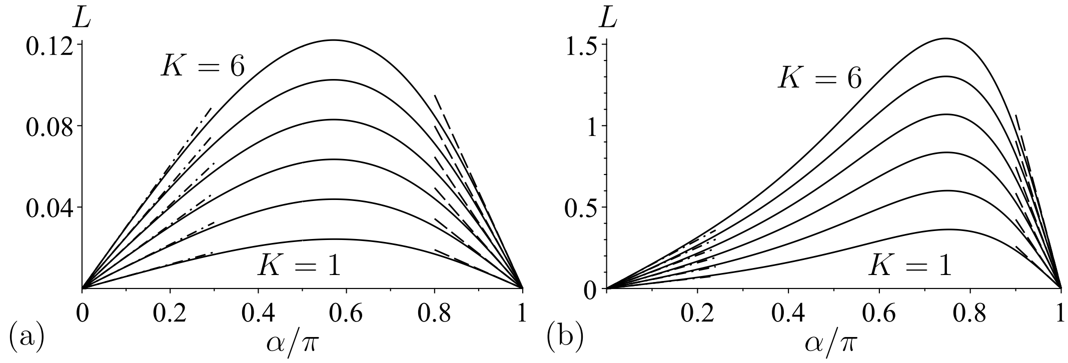

Figure 5.25: Plots of the length L given by (5.168) as a function of α/π and the asymptotic solutions (5.177) and (5.178) in the limits $\alpha \to 0^+$ and $\alpha \to \pi^-$ shown with dash-dotted and dashed lines, respectively, for $K = 1, 2, \ldots, 6$, and (a) $\bar{a} = 1$, (b) $\bar{a} = 2$ in the case of a narrow rivulet with fixed semi-width and evaporative flux given by (5.74).

increases from zero at $\alpha = 0$ to a maximum $L = L_{\max}$ at some value $\alpha = \alpha_{\max}$ and then decreases towards zero at $\alpha = \pi$. In particular, the length of a sessile narrow rivulet behaves like

$$L \sim \frac{K^4 f(\bar{a}) I_{\bar{a}}(\bar{b}_0, \bar{a})}{12\bar{a}} \alpha \to 0 \tag{5.177}$$

in the regime $\alpha \ll 1$. The length of a pendant narrow rivulet behaves like

$$L \sim \frac{K^4 f(\bar{a}) I_{\bar{a}}(\bar{b}_0, \bar{a})}{12\bar{a}} (\pi - \alpha) \to 0 \tag{5.178}$$

as $\alpha \to \pi^-$.

Plots of $L_{\max}$ and $\alpha_{\max}$ are shown in Figure 5.27. In particular, Figure 5.27 shows that the maximum length of a narrow rivulet with fixed semi-width increases monotonically from $L_{\max} \to 0^+$ and $\alpha_{\max} = \pi/2$ as $\bar{a} \to 0^+$ to $L_{\max} \to \infty$ and $\alpha_{\max} \to \pi^-$ as $\bar{a} \to \pi^-$. By comparing Figure 5.25(a) with Figure 5.25(b) it is clear that as $\alpha_{\max}$ increases towards $\alpha_{\max} = \pi$ as $\bar{a}$ increases. This is confirmed by Figure 5.27(b) which shows $\alpha_{\max}/\pi$ as a function of $\bar{a}/\pi$. Figure 5.27(b) also shows that $\alpha_{\max}$ is very weakly dependent on K and decreases only slightly as K increases. This is confirmed by Figure 5.27(c) which shows that $\alpha_{\max}$ increases from $\alpha_{\max}/\pi \simeq 0.570$ to a maximum close to $K = 0$ and thereafter decreases asymptotically towards $\alpha_{\max} \simeq 0.570$ again as $K \to \infty$.

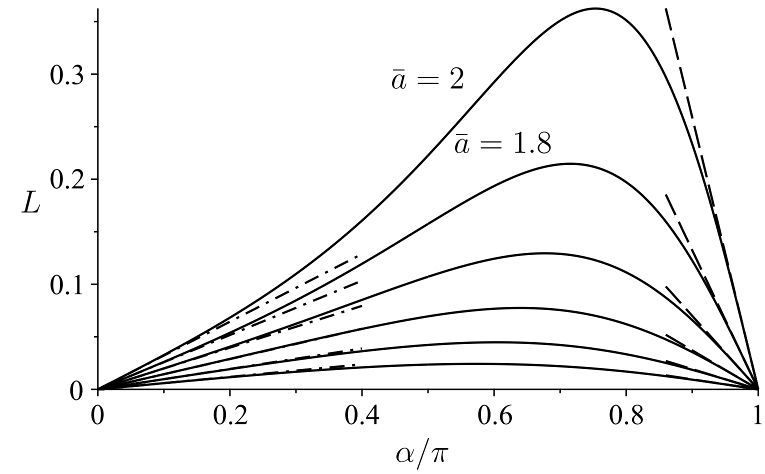

Figure 5.26: Plot of the length L given by (5.168) as a function of α/π and the asymptotic solutions (5.177) and (5.178) in the limits $\alpha \to 0^+$ and $\alpha \to \pi^-$ shown with dash-dotted and dashed lines, respectively, for $K = 1$, $\bar{a} = 1, 1.2, 1.4, \ldots, 2$ in the case of a narrow rivulet with fixed semi-width and evaporative flux given by (5.74).

5.6.1.3 The length of a wide rivulet

In the case of a wide rivulet with fixed semi-width, Figures 5.28 and 5.29 show the length L, given by (5.168), as a function of α/π for various values of K and $\bar{a}$, respectively. In particular, both Figures 5.28 and 5.29 show that the rivulet length increases from $L \to 0^+$ as $\alpha \to 0^+$ to $L \to \infty$ as $\alpha \to \alpha_{\mathrm{crit}}^-$, where a rivulet with finite length exists only for $0 \le \alpha < \alpha_{\mathrm{crit}} \le \pi$, where α_{crit} is given by (1.81). In particular, the length of the rivulet behaves like (5.177) as $\alpha \to 0^+$ and becomes infinitely long according to

$$L \sim \frac{80\sqrt{\bar{a}^3\bar{\beta}^7K}}{7\left(\bar{a}^4 - \pi^4\right)^{\frac{5}{4}}}(\alpha_{\mathrm{crit}} - \alpha)^{-\frac{7}{2}} \to \infty \qquad (5.179)$$

as $\alpha \to \alpha_{\mathrm{crit}}^-$ for $\bar{a} > \pi$ and

$$L \sim \frac{640\sqrt{2\bar{\beta}^7K}}{7\pi^{\frac{7}{2}}}(\pi - \alpha)^{-6} \to \infty \qquad (5.180)$$

as $\alpha \to \alpha_{\mathrm{crit}}^- = \pi^-$ for $\bar{a} = \pi$.

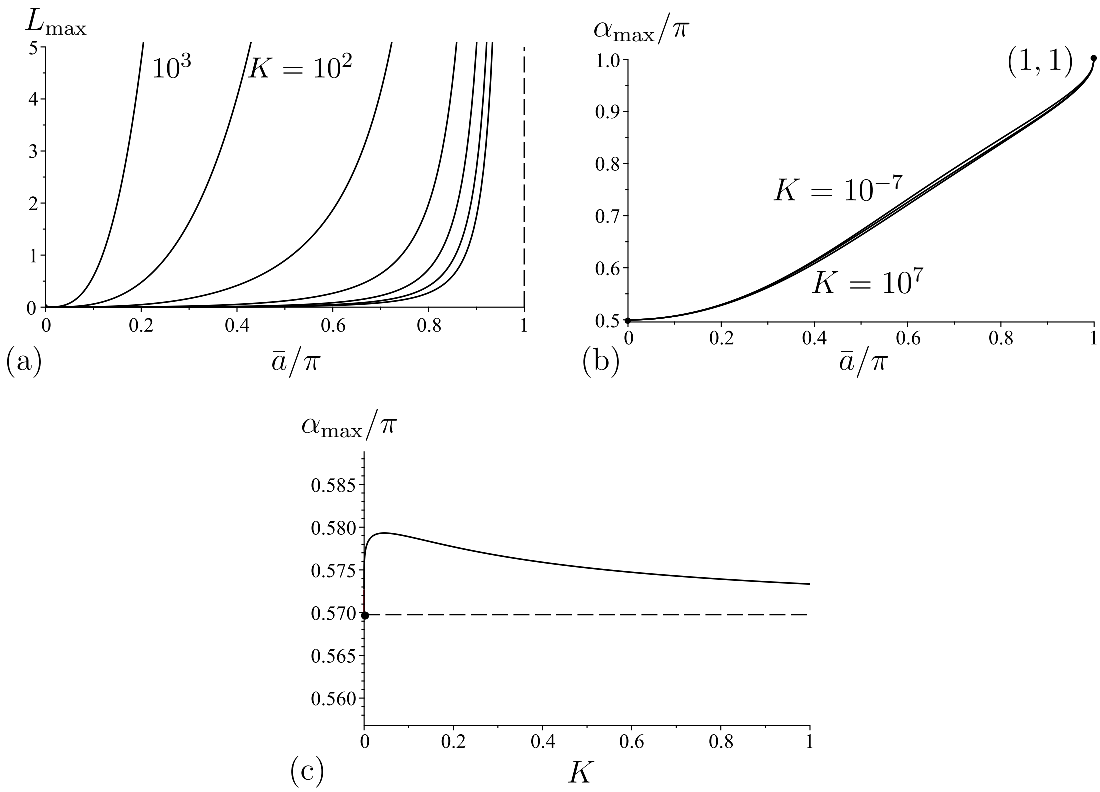

Figure 5.27: Plots of (a) $L_{\max}$ as a function of $\bar{a}/\pi$ for $K = 10^{-3}, 10^{-2}, \ldots, 10^3$ and the vertical asymptote at $\bar{a}/\pi = 1$ shown with a dashed line, (b) $\alpha_{\max}/\pi$ as a function of $\bar{a}/\pi$ for $K = 10^{-7}, 1, 10^7$, and (c) $\alpha_{\max}/\pi$ as a function of K for $\bar{a} = 1$ and the horizontal asymptote at $\alpha_{\max}/\pi \simeq 0.570$ shown with a dashed line in the case of a rivulet with fixed semi-width and evaporative flux given by (5.74).

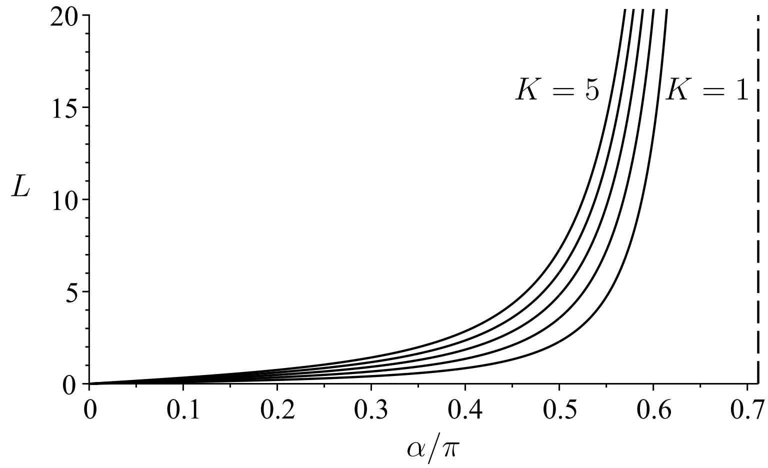

Figure 5.28: Plot of the length L given by (5.168) as a function of α/π for $\bar{a} = 4$ ($> \pi$), $K = 1, 2, \ldots, 5$ and the vertical asymptote at $\alpha/\pi = \alpha_{\rm crit}/\pi \simeq 0.712$ shown with a dashed line in the case of a wide rivulet with fixed semi-width and evaporative flux given by (5.74).

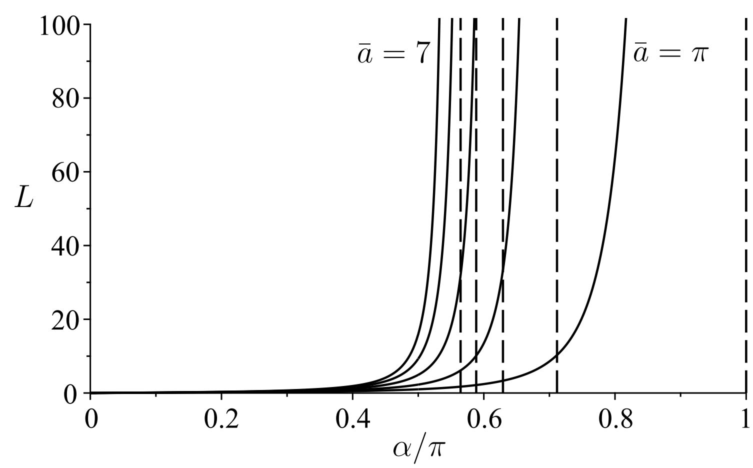

Figure 5.29: Plot of the length L given by (5.168) as a function of α/π and the vertical asymptotes at $\alpha = \alpha_{\rm crit}$ shown with dashed lines for $K = 1$, $\bar{a} = \pi$, 4, 5, 6, 7 in the case of a wide rivulet with fixed semi-width and evaporative flux given by (5.74).

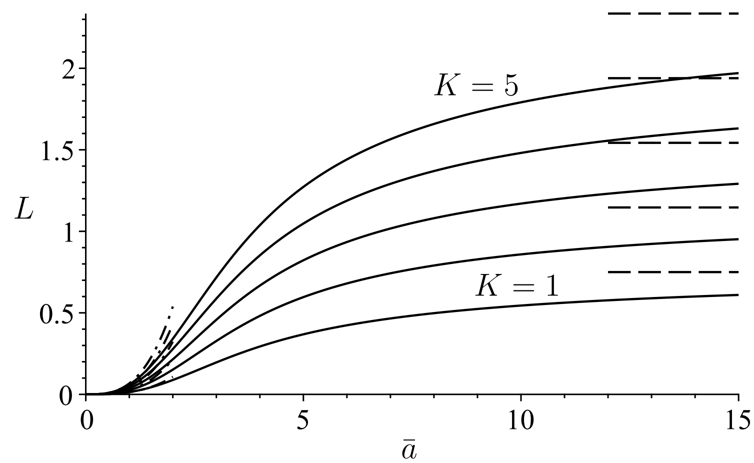

Figure 5.30: Plot of the length L given by (5.168) as a function of $\bar{a}$ and the asymptotic solutions (5.181) and (5.187) in the limits $\bar{a} \to 0^+$ and $\bar{a} \to \infty$ shown with dash-dotted and dashed lines, respectively, for $K = 1, 2, \ldots, 5$, $\alpha = \pi/4$ in the case of a sessile rivulet with fixed semi-width and evaporative flux given by (5.74).

5.6.1.4 The rivulet length as $\bar{a}$ varies

The variation of L as a function of $\bar{a}$ for a sessile, vertical and pendant rivulet with fixed semi-width is shown in Figures 5.30–5.33, respectively.

In the case of a sessile rivulet, Figures 5.30 and 5.32 show that the length increases from $L \to 0^+$ as $\bar{a} \to 0^+$ to a constant value as $\bar{a} \to \infty$. In particular, the length of a sessile rivulet with fixed semi-width behaves like

$$L \sim \frac{2K\bar{\beta}^3 \sin\alpha}{105}\bar{a}^3 \to 0^+ \tag{5.181}$$

in the regime $\bar{a} \ll 1$.

In the limit $\bar{a} \to \infty$, similar to the constant evaporative flux case in Section 5.4, this limit corresponds to the case of a two-dimensional (i.e. an infinitely wide) sessile evaporating sheet. The two-dimensional sheet (away from the thin boundary layers near $y = \pm\bar{a}$) has height

$$h \sim \frac{\beta}{m}. \tag{5.182}$$

Using (5.182), the evaporative flux (5.74) (away from the thin boundary layers near $y = \pm\bar{a}$) is given by

$$J \sim \frac{1}{\beta(x)/m + K}. \tag{5.183}$$

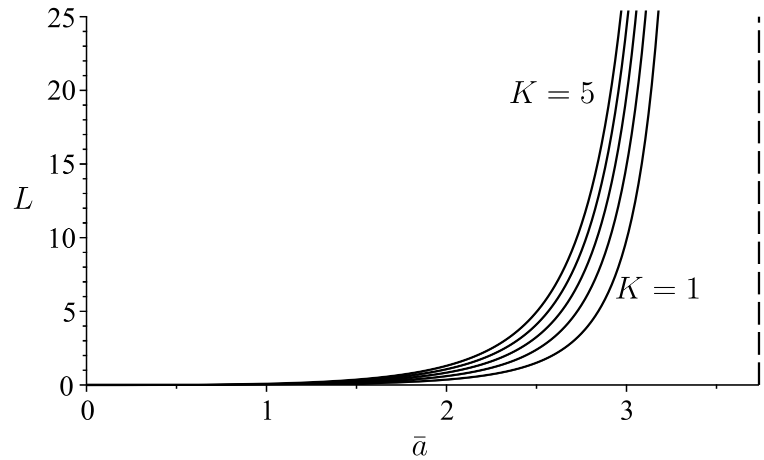

Figure 5.31: Plot of the length L given by (5.168) as a function of $\bar{a}$ for $K = 1, 2, \ldots, 5$, $\alpha = 3\pi/4$ and the vertical asymptote $\bar{a}_{\mathrm{crit}} \simeq 3.736$ shown with a dashed line in the case of a pendant rivulet with fixed semi-width and evaporative flux given by (5.74).

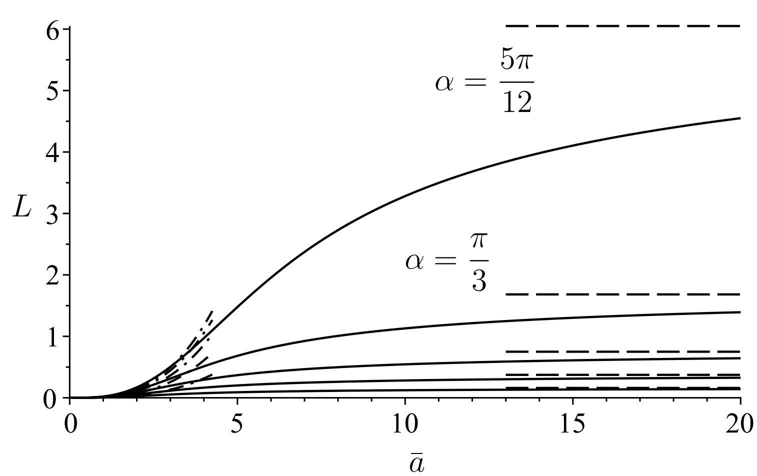

Figure 5.32: Plot of the length L given by (5.168) as a function of $\bar{a}$ and the asymptotic solutions (5.181) and (5.187) in the limits $\bar{a} \to 0^+$ and $\bar{a} \to \infty$ shown with dash-dotted and dashed lines, respectively, for $\alpha = \pi/12, \pi/6, \ldots, 5\pi/12$ in the case of a sessile rivulet with fixed semi-width and evaporative flux given by (5.74).

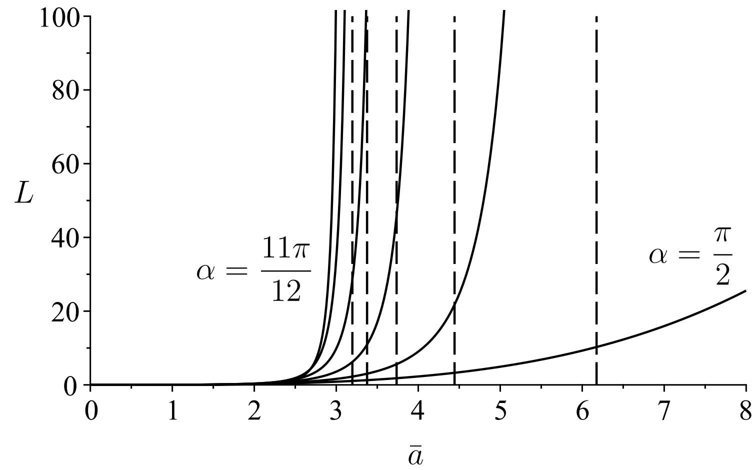

Figure 5.33: Plot of the length L given by (5.168) as a function of $\bar{a}$ and the vertical asymptotes at $\bar{a} = \bar{a}_{\text{crit}} = \pi/m$ shown with dashed lines for $\alpha = \pi/2$, $7\pi/12$, $\ldots$, $11\pi/12$ in the case of a pendant rivulet with fixed semi-width and evaporative flux given by (5.74).

The volume flux in the regime $\bar{a} \gg 1$ is

$$Q \sim \frac{2\beta^3 \sin\alpha}{3m^3}\bar{a} \to \infty. \tag{5.184}$$

The global mass balance (5.18) with Q given by (5.184) and J given by (5.183) then becomes

$$\frac{\mathrm{d}\beta}{\mathrm{d}x} = -\frac{m^4}{\beta^2(\beta + Km)\sin\alpha}. \tag{5.185}$$

Solving (5.185) subject to the initial condition $\beta(0) = \bar{\beta}$, gives the implicit solution for the contact angle in this limit given by

$$3\left(\beta^4 - \bar{\beta}^4\right) + 4Km\left(\beta^3 - \bar{\beta}^3\right) = -\frac{12m^2}{\tan\alpha}x. \tag{5.186}$$

Applying the end condition $\beta(L) = 0$ to (5.186) shows that the length of the rivulet L behaves like

$$L \sim \frac{\bar{\beta}^3 \tan\alpha}{12m^2}\left(3\bar{\beta} + 4Km\right) = \mathcal{O}(1) \tag{5.187}$$

as $\bar{a} \to \infty$. Hence $L = \mathcal{O}(1)$ given by (5.187) again gives the length of a two-dimensional (i.e. an infinitely wide) sessile evaporating sheet.

In the case of a vertical rivulet, Figure 5.33 shows that the length increases from $L \to 0^+$ as $\bar{a} \to 0^+$ to $L \to \infty$ as $\bar{a} \to \infty$. In particular, the length of a vertical rivulet with fixed semi-width behaves like (5.181) in the regime $\bar{a} \ll 1$ and

$$L \sim \frac{(\bar{\beta}\bar{a})^4}{70 \ln\left(\frac{2\bar{a}\bar{\beta}}{K}\right)} \to \infty \tag{5.188}$$

in the regime $\bar{a} \gg 1$.

In the case of a pendant rivulet, Figures 5.31 and 5.33 show that the length increases from $L \to 0^+$ as $\bar{a} \to 0^+$ to $L \to \infty$ as $\bar{a} \to \bar{a}_{\mathrm{crit}}^-$. In particular, the length of a pendant rivulet with fixed semi-width behaves like (5.181) in the regime $\bar{a} \ll 1$ and becomes infinitely long according to

$$L \sim \frac{5\sqrt{2\bar{\beta}^7 K}\sin\alpha}{7m^7}(\bar{a}_{\mathrm{crit}} - \bar{a})^{-\frac{7}{2}} \to \infty \tag{5.189}$$

as $\bar{a} \to \bar{a}_{\mathrm{crit}}^-$.

5.6.1.5 The rivulet length as K varies

The variation of L as a function of K for a sessile, vertical and pendant rivulet is shown in Figures 5.34–5.37. As discussed in Section 5.3.3, the limit $K \to 0^+$ corresponds to the limit in which the evaporative flux becomes large, $J \to \infty$, and so $L \to 0$, i.e. the rivulet evaporates immediately. On the other hand, the limit $K \to \infty$ corresponds to the limit in which the evaporative flux becomes small, $J \to 0^+$, and so $L \to \infty$, i.e. the rivulet does not evaporate and is therefore infinitely long. This is confirmed by Figures 5.34–5.37 which show that the length always increases from $L \to 0^+$ as $K \to 0^+$ to $L \to \infty$ as $K \to \infty$.

In particular, the length of a sessile, vertical and pendant rivulet with fixed semi-width behaves like

$$L \sim \frac{\bar{\beta}^4 \sin\alpha f(m\bar{a})}{24m^4 \ln\left(\frac{\bar{\beta}c(m\bar{a})}{Km}\right)} \to 0^+ \tag{5.190}$$

in the regime $K \ll 1$, where $c(m\bar{a})$ is again given by (5.159). In particular, in the case of a vertical rivulet we have

$$L \sim \frac{(\bar{\beta}\bar{a})^4}{70 \ln\left(\frac{2\bar{\beta}\bar{a}}{K}\right)} \to 0^+ \tag{5.191}$$

in the regime $K \ll 1$.

In the cases of a sessile and a pendant rivulet with fixed semi-width, the rivulet becomes infinitely long according to

$$L \sim \frac{\bar{\beta}^3 \sin\alpha f(m\bar{a})}{18m^4\bar{a}} K \to \infty \tag{5.192}$$

in the regime $K \gg 1$. In this limit, the evaporative flux given by (5.74) behaves like $J \sim 1/K$, i.e. it is uniform as considered in Section 5.4, in which case the length given by (5.192) coincides with (5.82) with $\hat{J} = 1/K$ for **all** cases of α. In particular, in the case of a vertical rivulet

$$L \sim \frac{2\bar{\beta}^3\bar{a}^3}{105} K \to \infty \tag{5.193}$$

in the regime $K \gg 1$. The behaviour of L as a function of K for $0 \le \alpha \le \pi/2$ is shown in Figure 5.36 and for $\pi/2 \le \alpha \le \pi$ is shown in Figure 5.37. As shown in Figure 5.36, the longest rivulet in this range is achieved when $\alpha = \pi/2$, shown with a red line for clarity. As shown in Figure 5.37, the longest rivulet in this range is achieved, rather surprisingly, when $\alpha = 9\pi/16$ and not $\alpha = \pi/2$, the latter of which is shown with a red line for clarity. However, inspection of Figure 5.27 explains this behaviour. In particular, Figure 5.27(b) shows that $\alpha_{\max} > \pi/2$ when $\bar{a} > 0$. This is confirmed by Figure 5.27(c) which shows that $\alpha_{\max} > \pi/2$ for all $K \ge 0$.

5.6.1.6 Area and volume

From (5.42) and (5.43), the area of the base of the rivulet is given by

$$A = 2\bar{a}L = \frac{K^4 f(m\bar{a}) I_{\bar{a}} \sin\alpha}{6m} \tag{5.194}$$

and the volume of the rivulet is given by

$$V = \frac{K^5 f(m\bar{a})(g(m\bar{a}) - 1)\tan\alpha}{6\bar{a}} \int_0^{\bar{b}} \frac{\tilde{b}^3}{R(\tilde{b}, m\bar{a})} \, \mathrm{d}\tilde{b}. \tag{5.195}$$

In the case of a vertical rivulet, by substituting $\tilde{b} = (2/m\bar{a})\sinh^2(\xi)$ into (5.194) and (5.195), the area of the base (5.194) and the volume of the rivulet (5.195)

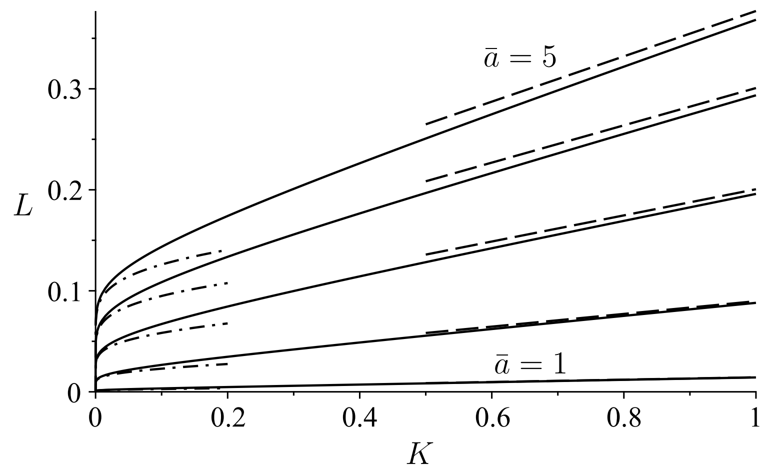

Figure 5.34: Plot of the length L given by (5.168) as a function of K and the asymptotic solutions (5.190) and (5.192) in the limits $K \to 0^+$ and $K \to \infty$ shown with dash-dotted and dashed lines, respectively, for $\bar{a} = 1, 2, \ldots, 5$, $\alpha = \pi/4$ in the case of a sessile rivulet with fixed semi-width and evaporative flux given by (5.74).

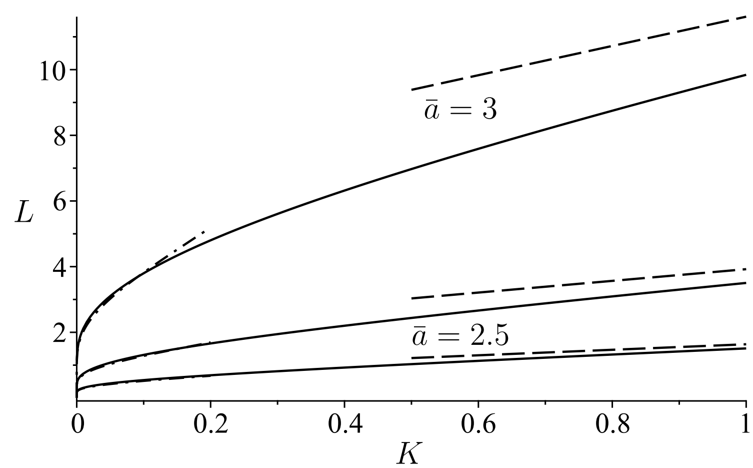

Figure 5.35: Plot of the length L given by (5.168) as a function of K and the asymptotic solutions (5.190) and (5.192) in the limits $K \to 0^+$ and $K \to \infty$ shown with dash-dotted and dashed lines, respectively, for $\bar{a} = 2.5, 2.75, 3$, $\alpha = 3\pi/4$ in the case of a pendant rivulet with fixed semi-width and evaporative flux given by (5.74).

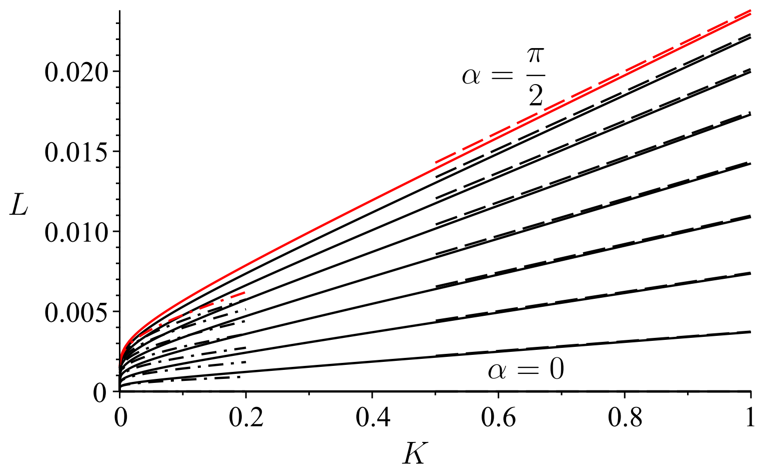

Figure 5.36: Plot of the length L given by (5.168) as a function of K and the asymptotic solutions (5.190) and (5.192) in the limits $K \to 0^+$ and $K \to \infty$ shown with dash-dotted and dashed lines, respectively, for $\alpha = 0$, $\pi/16$, $\pi/8$, $\ldots$, $7\pi/16$, $\pi/2$ (shown with a red line for clarity), $\bar{a} = 1$ in the case of a rivulet with fixed semi-width and evaporative flux given by (5.74).

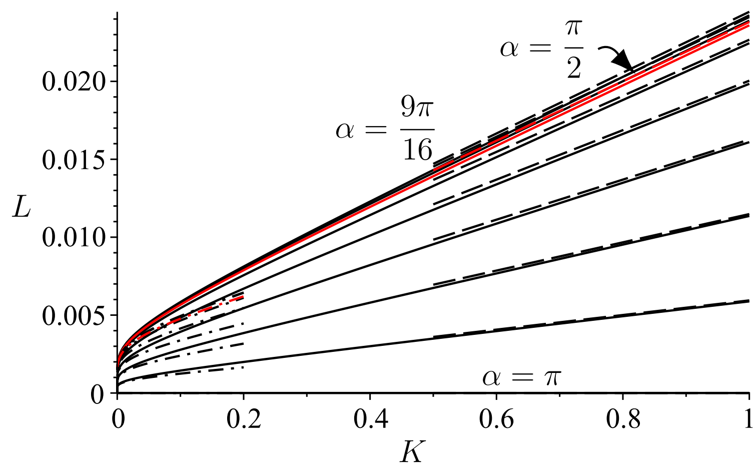

Figure 5.37: Plot of the length L given by (5.168) as a function of K and the asymptotic solutions (5.190) and (5.192) in the limits $K \to 0^+$ and $K \to \infty$ shown with dash-dotted and dashed lines, respectively, for $\alpha = \pi/2$ (shown with a red line for clarity), $9\pi/16$, $5\pi/8$, $11\pi/16$,$\ldots$,$15\pi/16$, π and $\bar{a} = 1$ in the case of a rivulet with fixed semi-width and evaporative flux given by (5.74).

become

$$A = \frac{64\bar{a}K^4}{35}\int_0^{\tanh^{-1}\bar{\eta}} \frac{\sinh^6\xi\cosh^2\xi}{\xi}\,\mathrm{d}\xi \tag{5.196}$$

and

$$V = \frac{128K^5\bar{a}}{105}\int_0^{\tanh^{-1}\bar{\eta}} \frac{\sinh^8\xi\cosh^2\xi}{\xi}\,\mathrm{d}\xi, \tag{5.197}$$

respectively.

5.6.2 Fixed contact angle $\beta = \bar{\beta}$

In this subsection we will consider an evaporating rivulet whose contact angle is fixed with constant value $\beta = \bar{\beta}$. In particular, we will describe the behaviour of the semi-width and the variation of the length of narrow, wide, sessile, vertical and pendant rivulets, with respect to the angle of inclination α, the initial semi-width $\bar{a}$ and K which, as discussed in Section 5.3.3, measures the degree of non-equilibrium at the free surface of the rivulet.

For a rivulet with fixed contact angle, the ordinary differential equation (5.165) becomes

$$\frac{K\bar{\beta}^3\sin\alpha}{36m^4a}\frac{\mathrm{d}f(ma)}{\mathrm{d}x} = -R(\bar{b}, ma), \tag{5.198}$$

so that $a = a(x)$ is given implicitly by

$$x = \frac{K\bar{\beta}^3\sin\alpha}{36m^3}\int_{ma}^{m\bar{a}} \frac{f'(M)}{MR(\bar{b}, M)}\,\mathrm{d}M. \tag{5.199}$$

Using the end condition $a(L) = 0$, (5.199) the length of the rivulet L is given by

$$L = \frac{K\bar{\beta}^3 I_{\bar{\beta}}\sin\alpha}{36m^3}, \tag{5.200}$$

where

$$I_{\bar{\beta}}(\bar{b}, m\bar{a}) = \int_0^{m\bar{a}} \frac{f'(M)}{MR(\bar{b}, M)}\,\mathrm{d}M. \tag{5.201}$$

In the case of a vertical rivulet, by substituting $M = m\tilde{a} = (2/\bar{b})\sinh^2\xi$ into (5.201), the length (5.200) becomes

$$L = \frac{128K^4}{105}\int_0^{\tanh^{-1}\bar{\eta}} \frac{\sinh^6\xi\cosh^2\xi}{\xi}\,\mathrm{d}\xi = \frac{K^4}{105}\Lambda\left(\tanh^{-1}(\bar{\eta})\right). \tag{5.202}$$

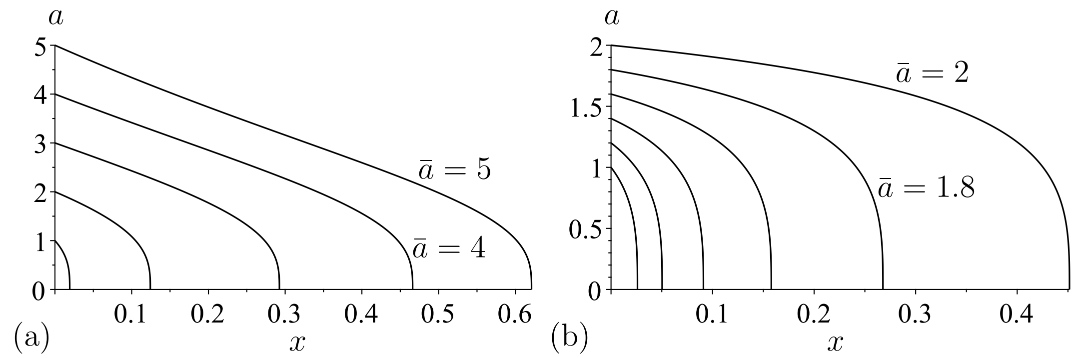

Figure 5.38: Plots of the semi-width a given by (5.199) as a function of x for $K = 1$, (a) $\alpha = \pi/4$, $\bar{a} = 1, 2, \ldots, 5$, and (b) $\alpha = 3\pi/4$, $\bar{a} = 1, 1.2, \ldots, 2$ in the case of a rivulet with fixed contact angle and evaporative flux given by (5.74).

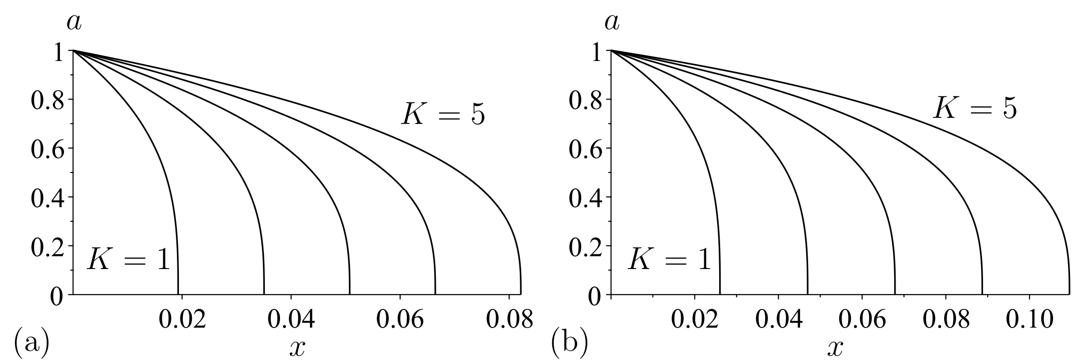

Figure 5.39: Plots of the semi-width a given by (5.199) as a function of x for $\bar{a} = 1$, (a) $\alpha = \pi/4$, $K = 1, 2, \ldots, 5$ and (b) $\alpha = 3\pi/4$, $K = 1, 2, \ldots, 5$ in the case of a rivulet with fixed contact angle and evaporative flux (5.74).

Note that the length of a vertical rivulet with fixed contact angle given by (5.202) is 4/3 the length of a vertical rivulet with fixed semi-width given by (5.170).

Figures 5.38 and 5.39 shows the semi-width given implicitly by (5.199) as a function of x for different values of $\bar{a}$ and K, respectively, for both a sessile and a pendant rivulet. In particular, Figures 5.38 and 5.39 show that β decreases from $\beta = \bar{\beta}$ at $x = 0$ to $\beta = 0$ at $x = L$. Furthermore, Figures 5.38 and 5.39 show that the semi-width increases as the initial semi-width $\bar{a}$ and K increase.

5.6.2.1 Rivulet shape

The three-dimensional shape of an evaporating rivulet with fixed contact angle and evaporative flux given by (5.74) is qualitatively similar to that shown in Figure 5.10, and so again is not plotted here for brevity. In particular, the rivulet has a rounded nose with shape

$$a \sim \frac{1}{m}\left[\frac{35 I_{\bar{\beta}}}{32}\left(1-\frac{x}{L}\right)\right]^{\frac{1}{3}} \to 0^{+} \tag{5.203}$$

as $x \to L^{-}$. Near the nose the slope in the x-direction becomes large according to $\mathrm{d}h_m/\mathrm{d}x = \mathcal{O}((L-x)^{-2/3}) \to -\infty$ as $x \to L^{-}$. Hence the assumption that the rivulet is slowly varying in x breaks down locally near the nose.

Near $x = 0$ the semi-width behaves like

$$a \sim \bar{a} - \frac{36\bar{a}R(\bar{b}, m\bar{a})}{K^4\bar{b}^3 f'(m\bar{a})\sin\alpha} x \to \bar{a}^{-}, \tag{5.204}$$

the free surface behaves like

$$h \sim \bar{h} - \frac{36\bar{a}R(\bar{b}, m\bar{a})}{K^4\bar{b}^3 f'(m\bar{a})\sin\alpha} \left.\frac{\partial h}{\partial a}\right|_{a=\bar{a}} x \to \bar{h}^{-}, \tag{5.205}$$

and the maximum height behaves like

$$h_{\mathrm{m}} \sim \bar{h}_{\mathrm{m}} - \frac{36\bar{a}R(\bar{b}, m\bar{a})}{K^4\bar{b}^3 f'(m\bar{a})\sin\alpha} \left.\frac{\mathrm{d}h_{\mathrm{m}}}{\mathrm{d}a}\right|_{a=\bar{a}} x \to \bar{h}_{\mathrm{m}}^{-} \tag{5.206}$$

as $x \to 0^{+}$.

5.6.2.2 The length of a narrow rivulet

In the case of a narrow rivulet with fixed contact angle, Figures 5.40 and 5.41 show the length L, given by (5.200), as a function of α/π for various values of K and $\bar{a}$, respectively. In particular, Figures 5.40 and 5.41 show that the rivulet length increases from zero at $\alpha = 0$ to a maximum $L = L_{\max}$ at some value $\alpha = \alpha_{\max}$ and then decreases towards zero at $\alpha = \pi$. In particular, the length of a sessile narrow rivulet behaves like

$$L \sim \frac{K\bar{\beta}^3 I_{\bar{\beta}}(\bar{b}_0, \bar{a})}{36}\alpha \to 0^{+} \tag{5.207}$$

in the regime $\alpha \ll 1$. The length of a pendant narrow rivulet behaves like

$$L \sim \frac{K\bar{\beta}^3 I_{\bar{\beta}}(\bar{b}_0, \bar{a})}{36}(\pi - \alpha) \to 0^{+} \tag{5.208}$$

as $\alpha \to \pi^{-}$.

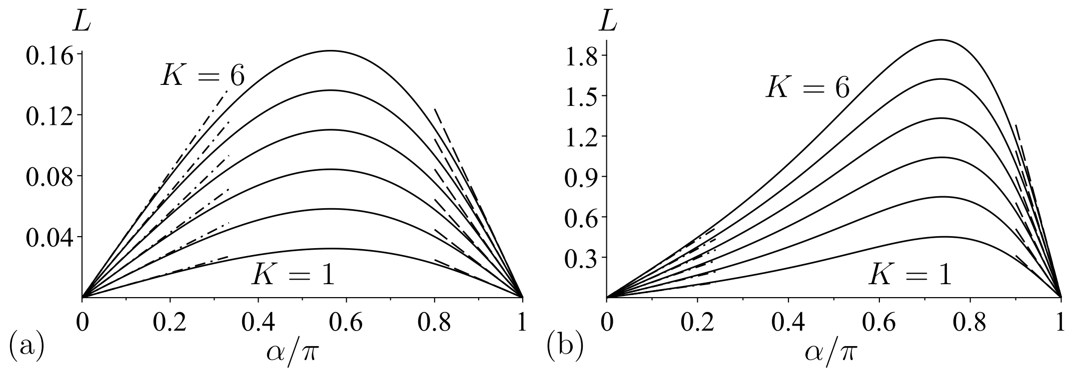

Figure 5.40: Plots of the length L given by (5.200) as a function of α/π and the asymptotic solutions (5.207) and (5.208) in the limits $\alpha \to 0^+$ and $\alpha \to \pi^-$ shown with dash-dotted and dashed lines, respectively, for $K = 1, 2, \ldots, 6$ and (a) $\bar{a} = 1$, (b) $\bar{a} = 2$ in the case of a narrow rivulet with fixed contact angle and evaporative flux given by (5.74).

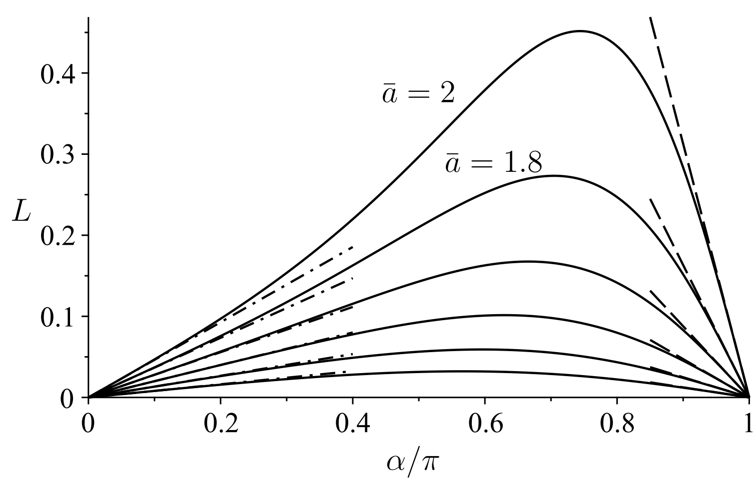

Figure 5.41: Plot of the length L given by (5.200) as a function of α/π and the asymptotic solutions (5.207) and (5.208) in the limits $\alpha \to 0^+$ and $\alpha \to \pi^-$ shown with dash-dotted and dashed lines, respectively, for $K = 1$, $\bar{a} = 1, 1.2, \ldots, 2$ in the case of a narrow rivulet with fixed contact angle and evaporative flux given by (5.74).

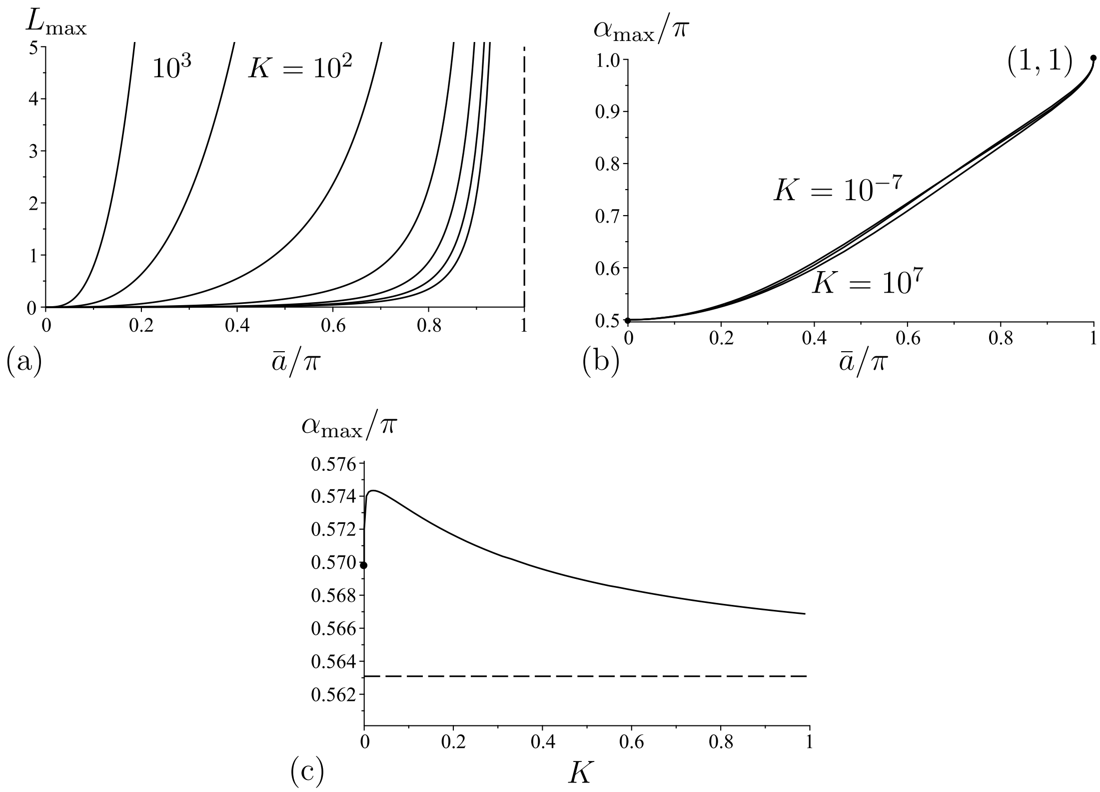

Figure 5.42: Plots of (a) $L_{\max}$ as a function of $\bar{a}/\pi$ for $K = 10^{-3}, 10^{-2}, \ldots, 10^3$ and the vertical asymptote at $\bar{a}/\pi = 1$ shown with a dashed line, (b) $\alpha_{\max}/\pi$ as a function of $\bar{a}/\pi$ for $K = 10^{-7}, 1, 10^7$, and (c) $\alpha_{\max}/\pi$ as a function of K for $\bar{a} = 1$ and the horizontal asymptote at $\alpha_{\max}/\pi \simeq 0.563$ shown with a dashed line in the case of a rivulet with fixed contact angle and evaporative flux given by (5.74).

Plots of $L_{\rm max}$ and $\alpha_{\rm max}$ are shown in Figure 5.42. In particular, Figure 5.42 shows that the maximum length of a narrow rivulet with fixed contact angle increases monotonically from $L_{\rm max} \to 0^+$ and $\alpha_{\rm max} = \pi/2$ as $\bar{a} \to 0^+$ to $L_{\rm max} \to \infty$ and $\alpha_{\rm max} \to \pi^-$ as $\bar{a} \to \pi^-$. By comparing Figure 5.42(a) with Figure 5.42(b) it is clear that as $\alpha_{\rm max}$ increases towards $\alpha_{\rm max} = \pi$ as $\bar{a}$ increases. This is confirmed by Figure 5.42(b) which shows $\alpha_{\rm max}/\pi$ as a function of $\bar{a}/\pi$. Figure 5.42(b) also shows that $\alpha_{\rm max}$ is very weakly dependent on K and decreases only slightly as K increases. This is confirmed by Figure 5.42(c) which shows that $\alpha_{\rm max}$ increases from $\alpha_{\rm max} \simeq 0.578$ to a maximum close to $K = 0$ and thereafter decreases asymptotically towards $\alpha_{\rm max} \simeq 0.563$ as $K \to \infty$.

5.6.2.3 The length of a wide rivulet

In the case of a wide rivulet with fixed contact angle, Figures 5.43 and 5.44 show the length L, given by (5.200), as a function of α/π for various values of K and $\bar{a}$, respectively. In particular, both Figures 5.43 and 5.44 show that the rivulet length increases from $L \to 0^+$ as $\alpha \to 0^+$ to $L \to \infty$ as $\alpha \to \alpha_{\rm crit}^-$, where a rivulet with finite length exists only for $0 \le \alpha < \alpha_{\rm crit} \le \pi$, where $\alpha_{\rm crit}$ is given by (1.81). In particular, the length of the rivulet behaves like (5.207) as $\alpha \to 0^+$ and becomes infinitely long according to

$$L \sim \frac{80\sqrt{\bar{a}^3\bar{\beta}^7K}}{7\left(\bar{a}^4 - \pi^4\right)^{\frac{5}{4}}}(\alpha_{\rm crit} - \alpha)^{-\frac{7}{2}} \to \infty \tag{5.209}$$

as $\alpha \to \alpha_{\rm crit}^-$ for $\bar{a} > \pi$ and

$$L \sim \frac{640\sqrt{2\bar{\beta}^7K}}{7\pi^{\frac{7}{2}}}(\pi - \alpha)^{-6} \to \infty \tag{5.210}$$

as $\alpha \to \alpha_{\rm crit}^- = \pi^-$ for $\bar{a} = \pi$. Note that (5.209) and (5.210) coincide with (5.179) and (5.180), respectively. This shows that in the limit $\alpha \to \alpha_{\rm crit}^-$, but not otherwise, the length of a rivulet with fixed contact angle is the same as for a rivulet with fixed semi-width.

5.6.2.4 The rivulet length as $\bar{a}$ varies

The variation of L as a function of $\bar{a}$ for a sessile, vertical and pendant rivulet with fixed contact angle is shown in Figures 5.45–5.48.

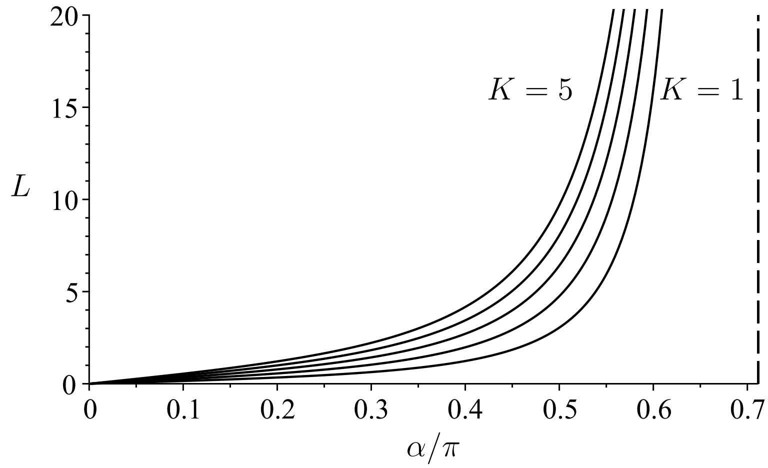

Figure 5.43: Plot of the length L given by (5.200) as a function of α/π for $\bar{a} = 4$ ($> \pi$), $K = 1, 2, \ldots, 5$ and the vertical asymptote at $\alpha/\pi = \alpha_{\mathrm{crit}}/\pi \simeq 0.712$ shown with a dashed line in the case of a wide rivulet with fixed contact angle and evaporative flux given by (5.74).

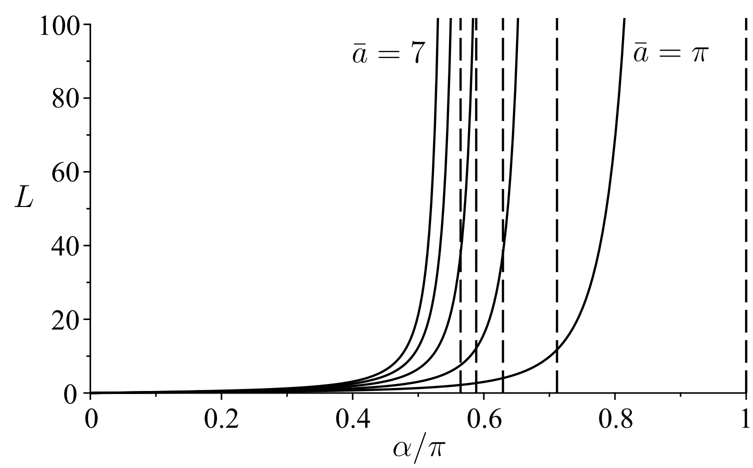

Figure 5.44: Plot of the length L given by (5.200) as a function of α/π and the vertical asymptotes shown with dashed lines at $\alpha = \alpha_{\mathrm{crit}}$ for $K = 1$, $\bar{a} = \pi$, 4, 5, 6, 7 in the case of a wide rivulet with fixed contact angle and evaporative flux given by (5.74).

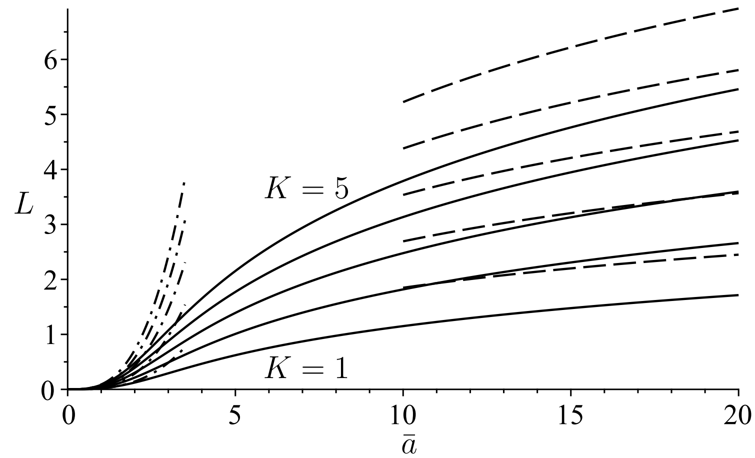

Figure 5.45: Plot of the length L given by (5.200) as a function of $\bar{a}$ and the asymptotic solutions (5.211) and (5.212) in the limits $\bar{a} \to 0^+$ and $\bar{a} \to \infty$ shown with dash-dotted and dashed lines, respectively, for $K = 1, 2, \ldots, 5$, $\alpha = \pi/4$ in the case of a sessile rivulet with fixed contact angle and evaporative flux given by (5.74).

In the case of a sessile rivulet, Figures 5.45 and 5.46 show that the length increases from $L \to 0^+$ as $\bar{a} \to 0^+$ to $L \to \infty$ as $\bar{a} \to \infty$. In particular, the length of a sessile rivulet with fixed contact angle behaves like

$$L \sim \frac{8K\bar{\beta}^3 \sin\alpha}{315}\bar{a}^3 \to 0^+ \tag{5.211}$$

in the regime $\bar{a} \ll 1$ and

$$L \sim \frac{(Km + \bar{\beta})\bar{\beta}^3 \sin\alpha}{3m^4} \ln(m\bar{a}) \to \infty \tag{5.212}$$

in the regime $\bar{a} \gg 1$. Therefore, (5.212) shows that, unlike the length of a rivulet with fixed semi-width which attains an $\mathcal{O}(1)$ value in the limit $\bar{a} \to \infty$ given by (5.187), the length of a rivulet with fixed contact angle becomes infinite in the limit $\bar{a} \to \infty$.

In the case of a vertical rivulet, Figure 5.48 shows that the length increases from $L \to 0^+$ as $\bar{a} \to 0^+$ to $L \to \infty$ as $\bar{a} \to \infty$. In particular, the length of a vertical rivulet with fixed contact angle behaves like (5.211) in the regime $\bar{a} \ll 1$ and

$$L \sim \frac{2(\bar{\beta}\bar{a})^4}{105 \ln\left(\frac{2\bar{a}\bar{\beta}}{K}\right)} \to \infty \tag{5.213}$$

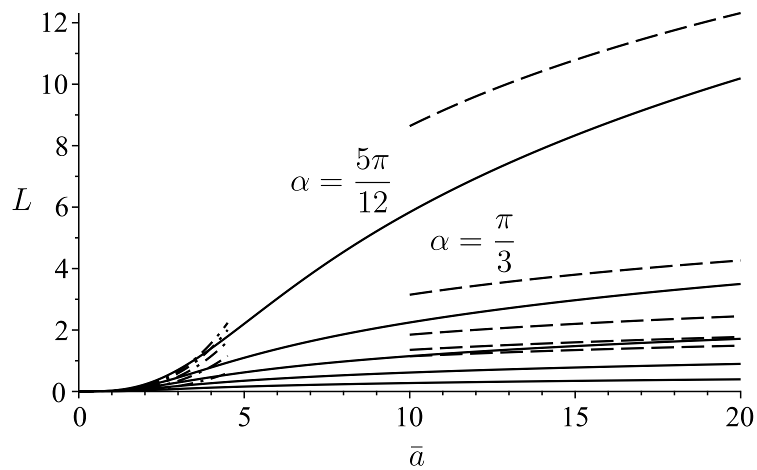

Figure 5.46: Plot of the length L given by (5.200) as a function of $\bar{a}$ and the asymptotic solutions (5.211) and (5.212) in the limits $\bar{a} \to 0^+$ and $\bar{a} \to \infty$ shown with dash-dotted and dashed lines, respectively, for $\alpha = \pi/12$, $\pi/6$, …, $5\pi/12$ in the case of a sessile rivulet with fixed contact angle and evaporative flux given by (5.74).

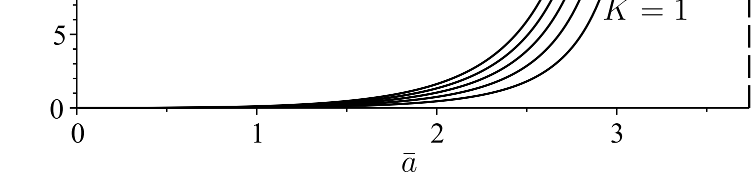

Figure 5.47: Plot of the length L given by (5.200) as a function of $\bar{a}$ for $K = 1$, 2, …, 5, $\alpha = 3\pi/4$ and the vertical asymptote $\bar{a}_{\rm crit} \simeq 3.736$ shown with a dashed line in the case of a pendant rivulet with fixed contact angle and evaporative flux given by (5.74).

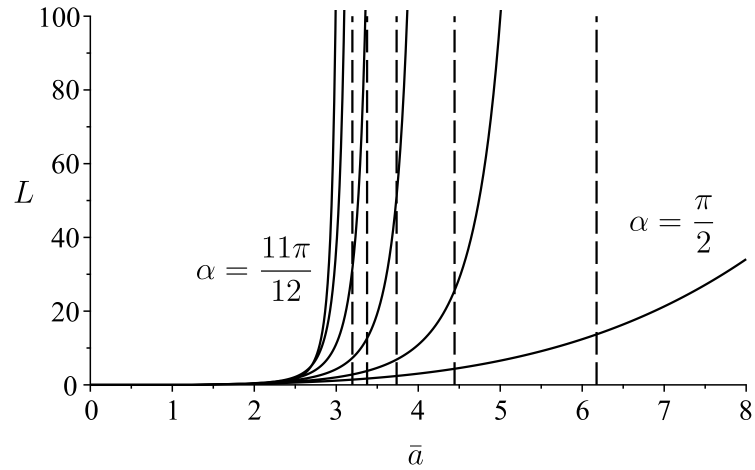

Figure 5.48: Plot of the length L given by (5.200) as a function of $\bar{a}$ and the vertical asymptotes at $\bar{a} = \bar{a}_{\rm crit} = \pi/m$ shown with dashed lines for $\alpha = \pi/2$, $7\pi/12$, $\ldots$, $11\pi/12$ in the case of a pendant rivulet with fixed contact angle and evaporative flux given by (5.74).

in the regime $\bar{a} \gg 1$.

In the case of a pendant rivulet, Figure 5.48 shows that the length increases from $L \to 0^+$ as $\bar{a} \to 0^+$ to $L \to \infty$ as $\bar{a} \to \bar{a}_{\rm crit}^-$. In particular, the length of a pendant rivulet with fixed contact angle behaves like (5.211) as $\bar{a} \to 0^+$ and becomes infinitely long according to

$$L \sim \frac{5\sqrt{2\bar{\beta}^7 K}\sin\alpha}{7m^7}(\bar{a}_{\rm crit} - \bar{a})^{-\frac{7}{2}} \to \infty \qquad (5.214)$$

as $\bar{a} \to \bar{a}_{\rm crit}^-$.

5.6.2.5 The rivulet length as K varies

The variation of L as a function of K for a sessile, vertical and pendant rivulet is shown in Figures 5.49–5.52. As discussed in Section 5.3.3, the limit $K \to 0^+$ corresponds to the limit in which the evaporative flux becomes large, $J \to \infty$, and so $L \to 0^+$, i.e. the rivulet evaporates immediately. On the other hand, the limit $K \to \infty$ corresponds to the limit in which the evaporative flux becomes small, $J \to 0^+$, and so $L \to \infty$, i.e. the rivulet does not evaporate and is therefore infinitely long. This is confirmed by Figures 5.49–5.52 which show that the length always increases from $L \to 0^+$ as $K \to 0^+$ to $L \to \infty$ as $K \to \infty$.

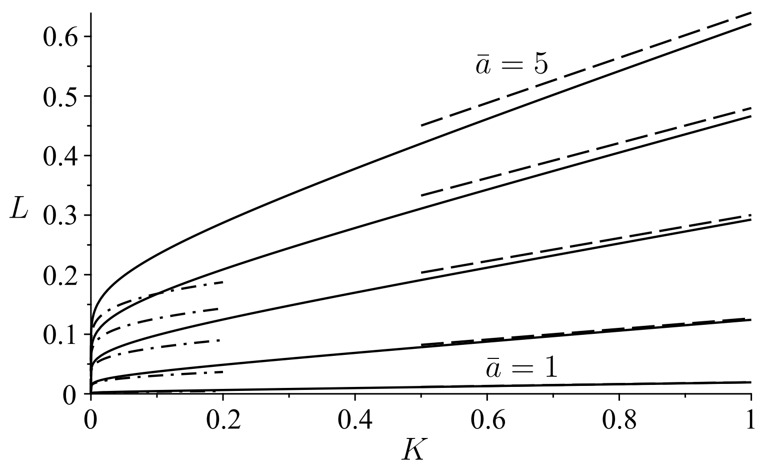

Figure 5.49: Plot of the length L given by (5.200) as a function of K and the asymptotic solutions (5.215) and (5.218) in the limits $K \to 0^+$ and $K \to \infty$ shown with dash-dotted and dashed lines, respectively, for $\bar{a} = 1, 2, \ldots, 5$, $\alpha = \pi/4$ in the case of a sessile rivulet with fixed contact angle and evaporative flux given by (5.74).

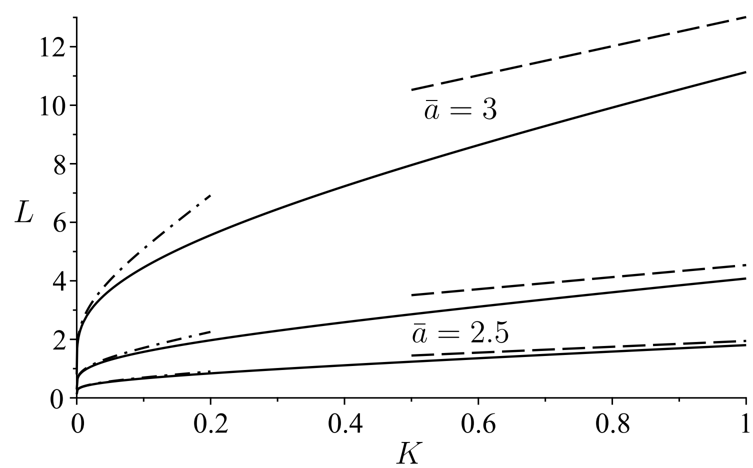

Figure 5.50: Plot of the length L given by (5.200) as a function of K and the asymptotic solutions (5.215) and (5.218) in the limits $K \to 0^+$ and $K \to \infty$ shown with dash-dotted and dashed lines, respectively, for $\bar{a} = 2.5, 2.75, 3$, $\alpha = 3\pi/4$ in the case of a pendant rivulet with fixed contact angle and evaporative flux given by (5.74).

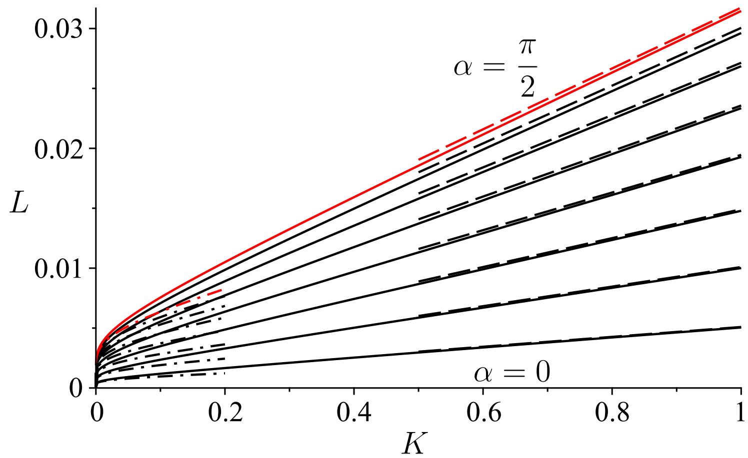

Figure 5.51: Plot of the length L given by (5.200) as a function of K and the asymptotic solutions (5.215) and (5.218) in the limits $K \to 0^+$ and $K \to \infty$ shown with dash-dotted and dashed lines, respectively, for $\alpha = 0$, $\pi/16$, $\pi/8$, ..., $7\pi/16$, $\pi/2$ (with a red line for clarity), and $\bar{a} = 1$ in the case of a rivulet with fixed contact angle and evaporative flux given by (5.74).

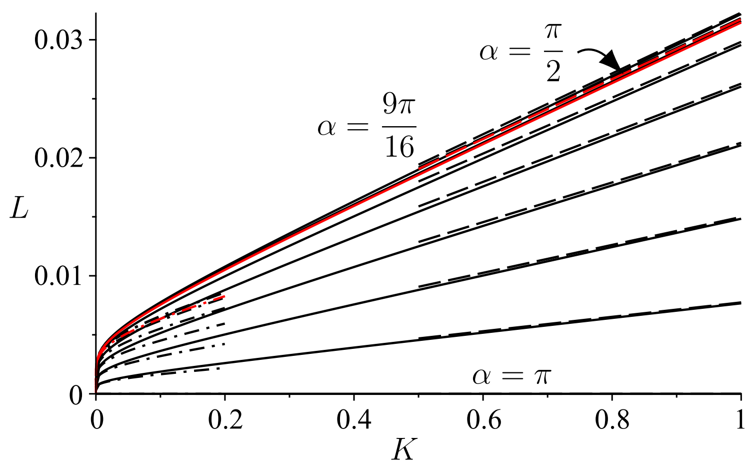

Figure 5.52: Plot of the length L given by (5.200) as a function of K and the asymptotic solutions (5.215) and (5.218) in the limits $K \to 0^+$ and $K \to \infty$ shown with dash-dotted and dashed lines, respectively, for $\alpha = \pi/2$ (with a red line for clarity), $9\pi/16$, $5\pi/8$, $11\pi/16$, ..., $15\pi/16$, π and $\bar{a} = 1$ in the case of a rivulet with fixed contact angle and evaporative flux given by (5.74).

In particular, the length of a sessile, vertical and pendant rivulet with fixed contact angle behaves like

$$L \sim \frac{\bar{\beta}^4 \sin\alpha f(m\bar{a})}{18m^4 \ln\left(\frac{\bar{\beta}c(m\bar{a})}{Km}\right)} \to 0^+ \tag{5.215}$$

in the regime $K \ll 1$, where $c(m\bar{a})$ is given by (5.159). In particular, in the case of a vertical rivulet we have

$$L \sim \frac{2(\bar{\beta}\bar{a})^4}{105 \ln\left(\frac{2\bar{\beta}\bar{a}}{K}\right)} \to 0^+ \tag{5.216}$$

in the regime $K \ll 1$.

In the limit $K \to \infty$ we have $\bar{b} \to 0^+$ and the function R given by (5.155) behaves like $R \to 1/2$. Taking the limit $K \to \infty$ in (5.199) and using the end condition $a(L) = 0$ we have

$$F(ma) \sim \frac{18m^3(L-x)}{K\bar{\beta}^3 \sin\alpha}, \tag{5.217}$$

where $F(m\bar{a})$ is given by (5.101). Hence in the cases of a sessile and a pendant rivulet with fixed contact angle, the rivulet becomes infinitely long according to

$$L \sim \frac{\bar{\beta}^3 \sin\alpha F(m\bar{a})}{18m^3} K \to \infty \tag{5.218}$$

in the regime $K \gg 1$. As mentioned in Section 5.6.1.5, in this limit, the evaporative flux given by (5.74) behaves like $J \sim 1/K$, i.e. it is uniform as considered in Section 5.4, in which case the length given by (5.218) coincides with (5.103) with $\hat{J} = 1/K$ for **all** cases of α. In particular, in the case of a vertical rivulet

$$L \sim \frac{8\bar{a}^3\bar{\beta}^3}{315} K \to \infty \tag{5.219}$$

in the regime $K \gg 1$.

Similarly to the behaviour described in Section 5.6.1.5, the behaviour of L as a function of K for $0 \le \alpha \le \pi/2$ is shown in Figure 5.51 and for $\pi/2 \le \alpha \le \pi$ is shown in Figure 5.52. As shown in Figure 5.51, the longest rivulet in this range is achieved when $\alpha = \pi/2$, shown with a red line for clarity. As shown in Figure 5.52, the longest rivulet in this range is achieved, when $\alpha = 9\pi/16$ and not $\alpha = \pi/2$, the latter of which is shown with a red line for clarity. However, inspection of Figure 5.42 explains this behaviour. In particular, Figure 5.42(b) shows that $\alpha_{\max} > \pi/2$ when $\bar{a} > 0$. This is confirmed by Figure 5.42(c) which shows that $\alpha_{\max} > \pi/2$ for all $K \geq 0$.

5.6.2.6 Area and volume

From (5.42) and (5.43) the area of the base of the rivulet is given by

$$A = \frac{K\bar{\beta}^3 \sin\alpha}{18m^4} \int_0^{m\bar{a}} \frac{f'(M)}{R(\bar{b}, M)}\, \mathrm{d}M \tag{5.220}$$

and the volume of the rivulet is given by

$$V = \frac{K\bar{\beta}^4 \tan\alpha}{18m^3} \int_0^{m\bar{a}} \frac{(g(M) - 1)f'(M)}{MR(\bar{b}, M)}\, \mathrm{d}M. \tag{5.221}$$

In the case of a vertical rivulet, by substituting $M = m\tilde{a} = (2/\bar{b})\sinh^2(\xi)$ into (5.220) and (5.221), the area of the base (5.220) and volume of the rivulet (5.221) become

$$A = \frac{512K^5}{105\bar{\beta}} \int_0^{\tanh^{-1}\bar{\eta}} \frac{\sinh^8\xi \cosh^2\xi}{\xi}\, \mathrm{d}\xi \tag{5.222}$$

and

$$V = \frac{1024K^6}{315\bar{\beta}} \int_0^{\tanh^{-1}\bar{\eta}} \frac{\sinh^{10}\xi \cosh^2\xi}{\xi}\, \mathrm{d}\xi, \tag{5.223}$$

respectively.

5.7 Conclusions

In this chapter we considered the flow of a rivulet on an inclined substrate subject to three different models of evaporation. In Section 5.3 we described these models, namely a uniform evaporation model, the pseudo diffusion-limited model, and the one-sided model, and derived each of their corresponding evaporative fluxes J. Using global conservation of mass we derived governing ordinary differential equations for the semi-width and/or the contact angle of the rivulet. These ordinary differential equations were solved in the cases of fixed semi-width and fixed contact angle and the variation of the length of the rivulet L was analysed as a function of the initial semi-width at the inlet of the rivulet $\bar{a}$, the angle of inclination of the substrate α and, in the case of the one-sided model, the parameter K, which as described in Section 5.3.3, measures the degree of non-equilibrium at the free surface of the rivulet. In particular, in Sections 5.4–5.6 we described the flow of the rivulet with three different evaporative fluxes given by $J = \hat{J}$, equation (5.56) and equation (5.74), respectively, with either a fixed semi-width and decreasing contact angle, or fixed contact angle and decreasing semi-width, and in each case derived explicit solutions for the length of the rivulet.

In the case of a rivulet with fixed semi-width or fixed contact angle, we showed that for all three of the evaporation models considered the behaviour of the length of both narrow and wide rivulets (i.e. rivulets with $\bar{a} < \pi$ and $\bar{a} \geq \pi$, respectively) is qualitatively the same. In particular, the length of a narrow rivulet always increases from zero at $\alpha = 0$ to a maximum $L_{\max}$ at some value $\alpha = \alpha_{\max}$ and then decreases towards zero at $\alpha = \pi$. This behaviour is in accordance with physical intuition as it agrees with the behaviour of the inlet flux $\bar{Q}$ given by (5.32) as described in Section 5.2.5 which shows that $\bar{Q} \to 0^+$ as $\alpha \to 0^+$ and $\bar{Q} \to 0$ as $\alpha \to \pi^-$, i.e. as the inlet flux becomes small, so too does the length of the rivulet. The maximum length $L_{\max}$ and angle $\alpha_{\max}$ always increase monotonically from $L_{\max} \to 0^+$ and $\alpha_{\max} = \pi/2$ as $\bar{a} \to 0^+$ to $L_{\max} \to \infty$ and $\alpha_{\max} \to \pi^-$ as $\bar{a} \to \pi^-$. The length of a wide rivulet always increases from $L \to 0^+$ as $\alpha \to 0^+$ to $L \to \infty$ as $\alpha \to \alpha_{\mathrm{crit}}^-$, where a rivulet with finite length exists only for $0 \leq \alpha < \alpha_{\mathrm{crit}} \leq \pi$ and α_{crit} is given by (1.81). Furthermore, for each evaporation model, the lengths of a wide rivulet with either fixed semi-width or fixed contact angle are the same in the limit $\alpha \to \alpha_{\mathrm{crit}}^-$. This behaviour is in accordance with physical intuition as it agrees with the behaviour of the inlet flux as described in Section 5.2.5 which shows that $\bar{Q} \to \infty$ as $\alpha \to \alpha_{\mathrm{crit}}^-$, i.e. an infinite inlet flux leads to an infinitely large rivulet.

Considering L as a function of $\bar{a}$ we showed that for a sessile rivulet with fixed semi-width the length of the rivulet increases from $L \to 0^+$ as $\bar{a} \to 0^+$ to either a constant $\mathcal{O}(1)$ value for the uniform and one-sided models of evaporation or $L \to \infty$ as $\bar{a} \to \infty$ for the pseudo diffusion-limited model. When the length attains a constant $\mathcal{O}(1)$ value in the limit $\bar{a} \to \infty$ this corresponds to the finite length of an infinitely-wide two-dimensional sheet. For a sessile rivulet with fixed contact angle however, the length always increases from $L \to 0^+$ as $\bar{a} \to 0^+$ to $L \to \infty$ as $\bar{a} \to \infty$ for all of the evaporation models considered. In the case of a vertical rivulet with fixed semi-width or fixed contact angle we showed that the length increases from $L \to 0^+$ as $\bar{a} \to 0^+$ to $L \to \infty$ as $\bar{a} \to \infty$ for all of the evaporation models considered. In the case of a pendant rivulet with fixed semi-width or fixed contact angle we showed that the length increases from $L \to 0^+$ as $\bar{a} \to 0^+$ to $L \to \infty$ as $\bar{a} \to \bar{a}_{\mathrm{crit}}^-$ for all of the evaporation models considered. Again, this behaviour is in accordance with physical intuition as it agrees with the behaviour of the inlet flux as described in Section 5.2.5 which shows that $\bar{Q} \to 0^+$ as $\bar{a} \to 0^+$ and $\bar{Q} \to \infty$ as $\bar{a} \to \infty$ (for sessile or vertical rivulets) or $\bar{a} \to \bar{a}_{\mathrm{crit}}^-$ (for pendant rivulets), i.e. again, as the inlet flux becomes small, so too does the length of the rivulet, and an infinite inlet flux leads to an infinitely large rivulet.

As described in Section 5.6, unlike for the uniform and pseudo diffusion-limited models, for the one-sided model, the substrate is heated with a constant temperature. The evaporative flux was shown to be of the form $J = 1/(h + K)$, where K measures the degree of non-equilibrium at the free surface. In particular, the limit $K \to 0^+$, corresponds to the limit in which the free surface temperature is constant and equal to the saturation temperature, the evaporative flux becomes large, $J \to \infty$, and so the rivulet evaporates immediately. On the other hand, in the limit $K \to \infty$, the evaporative flux becomes small, $J \to 0^+$, and so the rivulet does not evaporate and is therefore infinitely long. This behaviour is confirmed by the analysis in Sections 5.6.1.5 and 5.6.2.5, which shows that in the case of an evaporating rivulet with fixed semi-width and/or fixed contact angle, the length of the rivulet always increases from $L \to 0^+$ as $K \to 0^+$ to $L \to \infty$ as $K \to \infty$.

Finally, for each evaporation model and each case of either a rivulet with fixed semi-width or fixed contact angle, we derived expressions for the area of the base of the rivulet and the volume of the rivulet. For the uniform evaporation model we showed that a vertical rivulet with fixed contact angle is longer, has the same base area, and has a larger volume than a vertical rivulet with fixed semi-width. For the pseudo diffusion-limited model we showed that a vertical rivulet with fixed contact angle has the same length, has a smaller base area, and has a smaller volume than a vertical rivulet with fixed semi-width. For the one-sided model we showed that a vertical rivulet with fixed contact angle is longer than a vertical rivulet with fixed semi-width, however there was no simple relationship between the base area and volume.

In conclusion, in this chapter we considered three different evaporation models and showed that the behaviour of the length of the rivulet is often qualitatively similar for each evaporation model, with only a small number of exceptions, which have been outlined above. The behaviour of the length of the rivulet is therefore, rather surprisingly, largely insensitive to the choice of evaporation model. In particular, for a rivulet with either fixed semi-width or fixed contact angle, for all of the evaporation models considered, the length always becomes small when the inlet flux is small and becomes large when the inlet flux is large. The only exception to this behaviour is in the case of a sessile rivulet with fixed semi-width, in which case the rivulet becomes a two dimensional (i.e. infinitely wide) sheet with finite length when the inlet flux is large, for the uniform and one-sided models only.

Chapter 6

Conclusions and future work

6.1 Conclusions

In this thesis we considered three different thin-film flow problems. For each problem we showed that by applying the thin-film approximation, we were able to simplify the mathematical analysis involved in order to make significant analytical progress in describing the behaviour of the fluid flow.

In Chapter 2 we considered the steady coating flow of a thin film of Newtonian fluid on the outside of a uniformly rotating solid horizontal circular cylinder subject to the effects of gravity and a non-uniform air pressure due to a steady two-dimensional horizontal irrotational airflow with circulation, and showed that the presence of the airflow can result in qualitatively different behaviour of the fluid film from that in classical coating flow in the absence of an airflow.

It was shown that, depending on the speed of the far-field airflow and circulation of the airflow, the film thickness can exhibit two (maximum and minimum), three (maximum, minimum and point of inflexion) or four (two maxima and two minima) stationary points and, in general, has neither top-to-bottom nor right-to-left symmetry (in contrast to two stationary points and top-to-bottom symmetry in classical coating flow). When the maximum possible mass is supported on the cylinder surface we showed that the film thickness can have one or two corners on the top or bottom of the cylinder (in contrast to one corner at the right-hand side of the cylinder in classical coating flow). In addition, when the circulation of the airflow is anticlockwise (i.e. in the same direction as the rotation of the cylinder) the maximum mass of fluid that can be supported on the cylinder is always less than that in classical coating flow, whereas when the circulation is clockwise (i.e. in the opposite direction to the rotation of the cylinder) the maximum mass of fluid that can be supported on the cylinder can be greater than that in classical coating flow. However, whatever the speed of the far-field airflow and the circulation of the airflow the azimuthal velocity of the film is always in the direction of the rotation of the cylinder.

In addition, we carried out a simple linear stability analysis, and showed that, the film thickness is neutrally stable to two-dimensional disturbances, and hence that a more detailed non-linear stability analysis is required.

In Chapter 3 we considered the long-time behaviour of unsteady two-dimensional coating flow of an initially uniform thin film of Newtonian fluid on the outside of a uniformly rotating solid horizontal circular cylinder subject to the effects of gravity, surface tension and a non-uniform air pressure due to a steady two-dimensional horizontal irrotational airflow with circulation, in the case in which the effects of gravity and of capillarity are weak compared with those of viscous shear.

It was shown, in contrast to the conclusion of Newell and Viljoen [118], that regardless of the speed of the far-field airflow or the circulation of the airflow, when the surface tension effects are non-negligible, the film thickness remains finite for all time, and hence we concluded that the film is unconditionally stable. In the case in which surface tension effects are negligible, it was shown that the film is neutrally stable, in agreement with the work in Chapter 2 in the absence of surface tension effects. We showed that as the film evolves the effect of the airflow is to distort the shape of the free surface (so that it is no longer simply circular). Due to this distortion of the free surface, we were unable to identify a uniquely defined lag of the free surface relative to the solid cylinder. This is in contrast to the evolution of the film in the absence of an airflow, previously described by Hinch and Kelmanson [61], who showed that the free surface remains circular for all time and has a uniquely defined offset from the centre of the solid cylinder. It was also shown that increasing surface tension effects suppress the distortion from circular.

In Chapter 4 we considered the open-base configuration of the axisymmetric porous squeeze-film problem in which a thin layer of Newtonian fluid occupying the gap between a flat impermeable bearing moving under a prescribed constant load and a flat porous bed is forced to either flow out of the side of the gap or into the porous bed. Consequently, the fluid in the porous bed is either forced to flow out of the base of the porous bed or remains in the porous bed, when the bearing and porous bed come into contact, which occurs in a finite time.

It was shown that, when the permeability of the porous bed is small, the finite contact time of the bearing and porous bed is large, i.e. $t_{\mathrm{c}} = \mathcal{O}(k^{-2/3}) \gg 1$. Furthermore, when the bearing and porous bed come into contact, most of the fluid particles initially situated in the fluid gap will flow out of the side of the gap. In addition, only fluid particles initially situated very close to the base of the porous bed are able to flow out of the base. On the other hand, when the permeability of the porous bed is large, the finite contact time of the bearing and porous bed is small, i.e. $t_{\mathrm{c}} = \mathcal{O}(k^{-1}) \ll 1$. Furthermore, when the bearing and porous bed come into contact, fluid particles initially situated in the fluid gap will all flow into the porous bed, and none out of the side of the gap. In addition, if the initial volume of the fluid gap is greater than or equal to the volume of fluid in the porous bed, fluid particles initially situated in the porous bed will all flow out of the base. If, however, the initial volume of the fluid gap is less than or equal to the volume of fluid in the porous bed, some of the fluid initially situated in the porous bed will remain in the porous bed.

In Chapter 5 we considered the flow of a thin and slowly-varying rivulet of Newtonian fluid on an inclined substrate subject to the effects of gravity and evaporation. Specifically, we considered three different models of evaporation, namely, evaporation with a uniform evaporative flux at the free surface, a pseudo diffusion-limited model of evaporation and the one-sided model of evaporation.

It was shown that, regardless of the choice of evaporation model, the behaviour of the length of the rivulet is rather surprisingly, largely insensitive to the choice of evaporation model. In particular, for a rivulet with either fixed semi-width or fixed contact angle, for all of the evaporation models considered, the length always becomes small when the inlet flux is small and becomes large when the inlet flux is large. The only exception to this behaviour is in the case of a sessile rivulet with fixed semi-width, in which the rivulet becomes a two-dimensional (i.e. infinitely wide) sheet with finite length when the inlet flux is large, for the uniform and one-sided models only. For the one-sided model, in which the substrate is heated, the behaviour of the length as the temperature-dependent evaporative flux varied was also determined. In particular, in the limit in which the free surface temperature is constant and equal to the saturation temperature, the evaporative flux becomes large, and so the rivulet evaporates immediately. On the other hand, in the limit in which the evaporative flux becomes small, the rivulet does not evaporate and is therefore infinitely long.

6.2 Future work

The work in this thesis has described three thin-film flow problems, and in this section we will briefly discuss possible future work related to each problem.

Firstly, we discuss possible future work for the related problems described in Chapters 2 and 3. In Appendix A we provided the corresponding equations for the fluid pressure, velocity and flux per unit axial length, for the more general situation in which the far-field airflow, rather than being horizontal, is inclined at some prescribed angle α to the horizontal. It would be of interest to investigate how $\alpha \neq 0$ would change the results presented in Chapters 2 and 3. This problem is a possible topic for a future, partly numerical, study. As discussed in Section 1.2, other studies of the effect of an airflow on a thin film of fluid combine a non-uniform air pressure with a non-zero shear stress at the free surface. This would be a natural next step of the analysis in Chapters 2 and 3, which would lead to a more complete description of coating flow subject to an airflow.

Secondly, we consider possible future work for the problem described in Chapter 4. As described in Section 1.4, there are multiple previous works on porous squeeze-film flow that consider a non-flat porous bed and/or bearing shape. In particular, it would be of interest to generalise the shape of the bearing $H^* = H^*(r^*)$ to be, for example, $H^* = (R^*/2n)(r^*/R^*)^{2n}$, where r^* is the radial polar coordinate, R^* is a radial distance associated with bearing and n is an integer (see, for example, [156, 139, 85]), and obtain an expression for the contact time and analyse its behaviour in the limits of small and large permeability.

Finally, we consider possible future work for the problem described in Chapter 5. As discussed in Section 1.5, the work of Ghillani et al. [48] investigated the capillary rise of a rivulet within a groove between a solid substrate and a fibre within a porous bed with uniform evaporation at the free surface, and Alshaikhi et al. [10] investigated the gravity-driven flow, in the absence of evaporation, of a thin, slowly-varying rivulet of fluid over and through a porous substrate. Inspired by this work, a potential extension of the work in Chapter 5 could be to allow the substrate below the evaporating rivulet to be porous. In this case the rivulet would lose mass through the free surface with an evaporative flux $J = J(x, y)$ as well as through the porous substrate with mass flux $Q_{\rm bed} = Q_{\rm bed}(x, y)$, so that the mass balance equation, expressed in notation introduced in Chapter 5, would take the form

$$\frac{\mathrm{d}Q}{\mathrm{d}x} = -\int_{-a(x)}^{+a(x)} J(x, y) + Q_{\rm bed}(x, y)\ \mathrm{d}y. \tag{6.1}$$

It would then be of interest to solve (6.1) to describe the behaviour of the semi-width or contact angle and the finite length of a rivulet with either a fixed contact angle or fixed semi-width, respectively, as the properties of the evaporation and the porous substrate are varied. Additionally, a natural next step in the analysis of the evaporating rivulet problem considered in Chapter 5 would be to consider more complicated models of evaporation and include some (or all) of the physical effects that were neglected to simplify the problem, for example, the effect of vapour recoil, thermocapillary effects and van der Waals forces.

To conclude, in this thesis we have described new aspects of three different thin-film flow problems, however, as discussed in this section, there remain many interesting and unknown aspects of these problems to be investigated in future works.

Appendix A

Airflow inclined at angle α

In this appendix we provide the equations for the more general situation in which the far-field airflow, rather than being horizontal, is inclined at some prescribed angle α (measured anti-clockwise from $\theta = 0$ to the horizontal).

In this case, the air pressure on the free surface of the film, $p_\mathrm{a}^* = p_\mathrm{a}^*(\theta)$, previously given by (1.43), becomes

$$p_\mathrm{a}^* = p_\infty^* + \frac{1}{2}\rho_\mathrm{a}^* \left[U_\infty^{*2} - \left(2U_\infty^* \sin(\theta - \alpha) - \frac{\kappa^*}{2\pi a^*} \right)^2 \right], \tag{A.1}$$

and hence the volume flux, Q^*, previously given by (3.2), becomes

$$Q^* = a^*\Omega^* h^* - \frac{h^{*3}}{3\mu^* a^*} \left[\rho^* g^* a^* \cos\theta - 2\rho_\mathrm{a}^* U_\infty^{*2} \sin 2(\theta - \alpha) + \frac{\rho_\mathrm{a}^* \kappa^* U_\infty^*}{\pi a^*} \cos(\theta - \alpha) \right]. \tag{A.2}$$

Non-dimensionalising and scaling according to (2.3), the pressure $p = p_\mathrm{a}$, previously given by (2.11), is now given by

$$p = p_\mathrm{a} = \frac{1}{2} \left[F^2 - \{ 2F \sin(\theta - \alpha) - K \}^2 \right], \tag{A.3}$$

while the azimuthal velocity, the stream function and the flux are again given by (2.13)–(2.15), respectively, where the function $f = f(\theta)$, previously given by (2.16), is now given by

$$f(\theta) = \cos\theta - 2F^2 \sin 2(\theta - \alpha) + 2FK \cos(\theta - \alpha), \tag{A.4}$$

where F (≥ 0) and K are again defined by (2.12). In particular, the equation for the positions of the stationary points of h, previously given by (2.19), is now given by

$$\sin\theta + 4F^2 \cos 2(\theta - \alpha) + 2FK \sin(\theta - \alpha) = 0. \tag{A.5}$$

Appendix B

Proof that $h^2 f \leq 1$

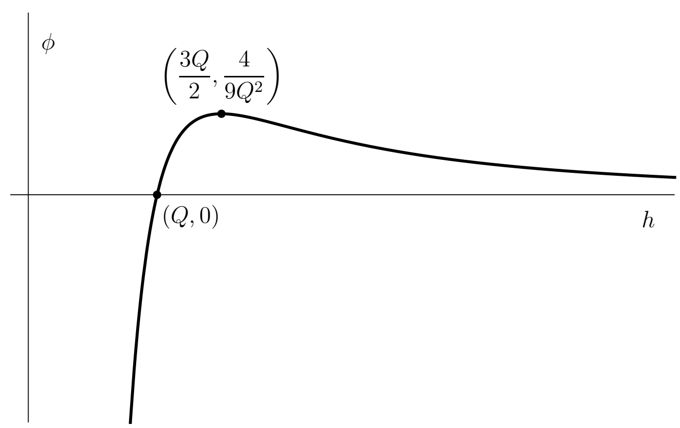

Figure B.1: Sketch of $\phi(h) = 3(h - Q)/h^3$ in the physically relevant case $Q > 0$ as a function of h.

In this appendix we show that for full-film solutions it is necessary that $h^2 f \leq 1$.

Equation (2.15) may be written in the form $f = \phi(h)$, where $\phi(h) = 3(h - Q)/h^3$. Figure B.1 shows a sketch of $\phi(h)$ in the physically relevant case $Q > 0$ as a function of h. For full-film solutions (i.e. for solutions for h that are continuous and strictly positive for all $-\pi < \theta \leq \pi$) it is clear that only the branch of ϕ to the left of its maximum at $h = 3Q/2$, $\phi = 4/(9Q^2)$ is relevant. Thus h must satisfy $h \leq 3Q/2$, and so $3Q - 2h \geq 0$. But (2.15) may also be written in the form $3Q - 2h = h(1 - h^2 f)$, and so we deduce that for full-film solutions it is necessary that $h^2 f \leq 1$.

Appendix C

Proof that $u > 0$

In this appendix we show that the velocity u (and not just the flux Q) is always positive, i.e. the flow of the film is always everywhere in the direction of the rotation of the cylinder.

Equation (2.13) shows that $u \leq 1$ wherever $f > 0$, that $u \equiv 1$ wherever $f = 0$, that $u \geq 1$ wherever $f < 0$, and that u satisfies $u - u_s = (h - y)^2 f/2$, where $u_s = u_s(\theta) = u(\theta, h)$ denotes the velocity at the free surface, given by

$$u_s = 1 - \frac{h^2}{2} f. \tag{C.1}$$

Therefore $u_s \leq u \leq 1$ wherever $f > 0$ and $1 \leq u \leq u_s$ wherever $f < 0$, showing that u_s is the minimum velocity at positions where $f > 0$ and the maximum velocity at positions where $f < 0$. In particular, it is immediately apparent that $u > 0$ wherever $f \leq 0$. We may also prove that $u > 0$ wherever $f > 0$ as follows. From (2.18) and (C.1) we have

$$u_s = \cos\left(\frac{2}{3}\sin^{-1}\frac{3Qf^{1/2}}{2}\right) \quad \text{if} \quad f > 0. \tag{C.2}$$

Writing (2.15) in the form $(h+3Q)(2h-3Q)^2 = (4-9Q^2 f)h^3$ shows that f satisfies $f \leq 4/(9Q^2)$ for all θ, and so if $f > 0$ then $0 < 3Qf^{1/2}/2 \leq 1$. Thus (C.2) gives $1/2 \leq u_s < 1$, which, together with the above result that $u_s \leq u \leq 1$ wherever $f > 0$, gives $1/2 \leq u_s \leq u \leq 1$, and so, in particular, $u > 0$ wherever $f > 0$.

Appendix D

Saddle points of Q

In this appendix we show that the flux Q, regarded as a function of θ and h, has no minimum or maximum stationary points, and, depending on the values of F and K, has either one or two saddle points.

The flux Q is given by equation (2.15), where the function $f = f(\theta)$ is given by (2.16) and can be conveniently expressed in terms of the parameter β introduced in (2.38) as

$$f(\theta) = 4F^2\,(\beta - \sin\theta)\cos\theta. \tag{D.1}$$

Stationary points of Q are determined by the criticality conditions (2.22) which require, in particular, that $f > 0$. The derivative $\partial^2 Q/\partial h^2$ and the Hessian determinant $\mathcal{H}$, given by

$$\mathcal{H} = \frac{\partial^2 Q}{\partial h^2}\frac{\partial^2 Q}{\partial \theta^2} - \left(\frac{\partial^2 Q}{\partial h\,\partial \theta}\right)^2 = \frac{h^4}{3}\left(2ff'' - 3f'^2\right), \tag{D.2}$$

take the values $\partial^2 Q/\partial h^2 = -2/h\,(< 0)$ and $\mathcal{H} = 2h^2 f''/3$ at a stationary point, showing that if $f'' > 0$ then the stationary point is a maximum and if $f'' < 0$ then it is a saddle. In particular, we conclude that Q has no minimum stationary point. Moreover, from (D.1) the condition $f' = 0$ gives

$$\beta\sin\theta = -\cos 2\theta, \tag{D.3}$$

using which one may show readily that the conditions $f > 0$ and $f'' > 0$ for a maximum stationary point cannot be satisfied simultaneously. Hence we deduce that Q has no maximum stationary point, and therefore any stationary point of

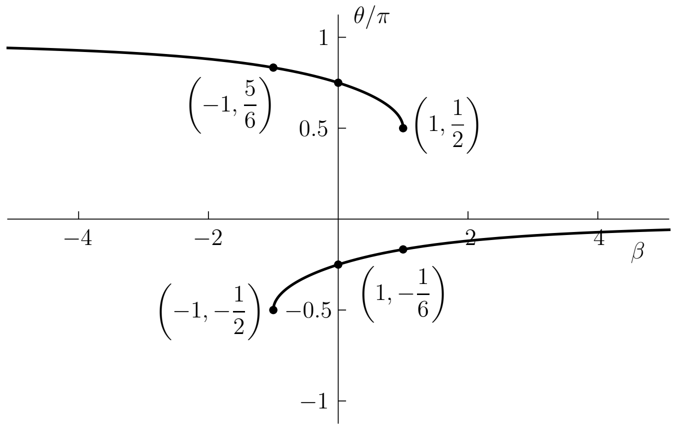

Figure D.1: Plot of θ/π given by (D.3) as a function of β for $-\pi/2 \leq \theta < 0$ and $\pi/2 \leq \theta < 1$.

Q can only be a saddle.

The conditions for a saddle, namely $f > 0$, $f' = 0$ and $f'' < 0$, require that $\sin 2\theta \leq 0$, in addition to (D.3). Figure D.1 shows the solutions for θ as a function of β. In particular, Figure D.1 shows that for $\beta < -1$ the function Q has one saddle point, in $5\pi/6 < \theta < \pi$, for $-1 \leq \beta \leq 1$ it has two saddle points, one in $-\pi/2 \leq \theta \leq -\pi/6$ and the other in $\pi/2 \leq \theta \leq 5\pi/6$, and for $\beta > 1$ it has one saddle point, in $-\pi/6 < \theta < 0$.

Appendix E

Two-dimensional porous squeeze-film problem

The analysis in this appendix follows from the axisymmetric porous squeeze-film problem described in Chapter 4. The two-dimensional problem is also of interest and the analysis is very similar throughout. In this appendix we summarise some of the key results for the finite contact times of the two-dimensional porous squeeze-film problem which can then be compared with the corresponding axisymmetric results in Chapter 4.

Consider with respect to the two-dimensional Cartesian coordinates (x^*, z^*), the two-dimensional porous squeeze-film flow of a layer of fluid in a thin gap between a flat impermeable layer with semi-width $\mathcal{L}^*$ moving subject to the dimensional load $L^*(t^*)$ per unit width. The problem is non-dimensionalised in the same manner as in the axisymmetric problem with R^* replaced with $\mathcal{L}^*$ and $V^* = L_0^* H_\mathrm{p}^*/(\mu^* \mathcal{L}^{*2})$ in replace of $V^* = L_0^* H_\mathrm{p}^*/(\mu^* R^{*3})$. The two-dimensional version of the closed-base configuration has been described by Knox et al. [86], and hence here we shall describe only the equations for the two-dimensional version of the open-base configuration.

Following a similar analysis to that described in Chapter 4, we find the horizontal and vertical velocities in the fluid layer to be

$$u = \frac{(z-h)(z(k^{\frac{1}{2}} + \bar{\alpha}h) + k^{\frac{1}{2}}h)}{2(k^{\frac{1}{2}} + \bar{\alpha}h)} \frac{\partial p}{\partial x} \tag{E.1}$$

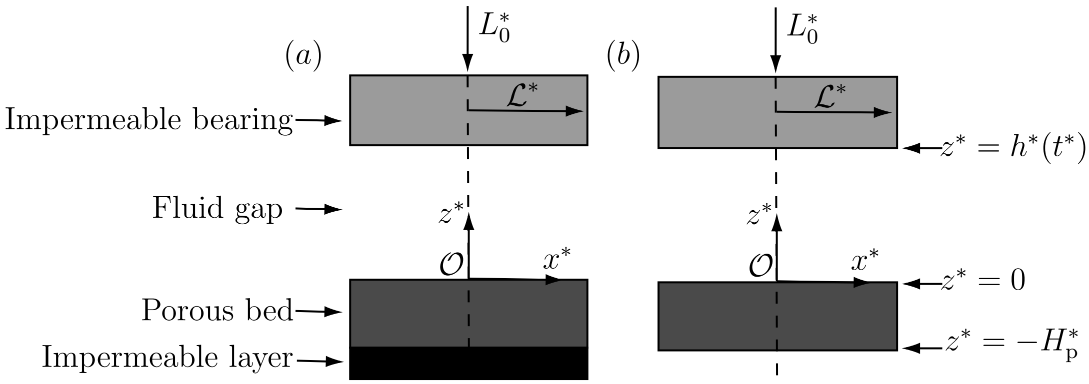

Figure E.1: The set up of the two-dimensional porous squeeze-film problem where either (a) there is an impermeable layer below the porous bed or (b) the base of the porous bed is open to the atmosphere.

and

$$w = -\frac{z(2k^{\frac{1}{2}}(z^2 - 3h^2) + \bar{\alpha}hz(2z - 3h))}{12(k^{\frac{1}{2}} + \bar{\alpha}h)}\frac{\partial^2 p}{\partial x^2} - kp. \tag{E.2}$$

The horizontal and vertical velocities in the porous bed are given by

$$U = 0, \quad \text{and} \quad W = -kp. \tag{E.3}$$

The unsteady Reynolds equation is given by

$$\frac{\mathrm{d}h}{\mathrm{d}t} = \frac{h^3(4k^{\frac{1}{2}} + \bar{\alpha}h)}{12(k^{\frac{1}{2}} + \bar{\alpha}h)}\frac{\partial^2 p}{\partial x^2} - kp. \tag{E.4}$$

Solving for $p(x,t)$ using the two-dimensional equivalents of (4.31) and (4.32), along with the load condition now given by

$$L = 2\int_0^1 p \; \mathrm{d}x, \tag{E.5}$$

we find that, in the case $L = L_0$, the fluid pressure is given by

$$p(x,t) = \frac{L_0}{2}\left[\frac{\eta\left(\cosh(\eta x) - \cosh(\eta)\right)}{\sinh(\eta) - \eta\cosh(\eta)}\right], \tag{E.6}$$

where η is given by (4.70).

Again following the same analysis as in Chapter 4, we can find an implicit solution for the bearing height $h(t)$, and hence, when $h = 0$ we can find an implicit solution for the contact time, which is given by

$$t_{\mathrm{c}} = \frac{2}{kL_0} \int_0^d 1 - \frac{\sinh(\eta(s))}{\eta \cosh(\eta(s))} \, \mathrm{d}s. \tag{E.7}$$

Performing a similar asymptotic analysis in the limits of small and large k as in Chapter 4 we find that the leading-order contact time in the limit of small permeability is given by

$$t_{\mathrm{c}} \sim \frac{3.59338}{L_0 k^{\frac{2}{3}}} \gg 1 \tag{E.8}$$

as $k \to 0$ and in the limit of large permeability the leading-order contact time is given by

$$t_{\mathrm{c}} \sim \frac{2d}{L_0 k} \ll 1 \tag{E.9}$$

as $k \to \infty$. Considering the case $\bar{\alpha} \to 0$, we can again derive a different asymptotic solution for the contact time in the limit $k \to 0$ which is more accurate when $\bar{l}_{\mathrm{s}} \to \infty$ (i.e. in the limit $\bar{\alpha} \to 0$). In this case, the leading-order contact time is given by

$$t_{\mathrm{c}} \sim \frac{2.26369}{L_0 k^{\frac{2}{3}}} \gg 1 \tag{E.10}$$

as $k \to 0$.

For completeness, the two-dimensional asymptotic solutions for the contact time in the limit of small and large $\hat{k}$ for the closed-base configuration can be obtained by rescaling t with $3\pi/16$, except in the case $\hat{k} \to \infty$ when $l_{\mathrm{s}} \to 0$ (i.e. in the limit $\alpha \to \infty$). This particular case was not reported in Knox et al. [84] and, by following similar steps as were used to derive (4.56), we find it to be

$$t_{\mathrm{c}} \sim \frac{1}{9\hat{k}L_0} \ln\left(\frac{d+2}{2}\right) \ll 1 \tag{E.11}$$

as $\hat{k} \to \infty$.

Bibliography

[1] E. Achenbach. Distribution of local pressure and skin friction around a circular cylinder in cross-flow up to Re $= 5\times10^6$. *Journal of Fluid Mechanics*, 34(4):625–639, 1968.

[2] D. J. Acheson. *Elementary Fluid Dynamics*. Oxford University Press, 1990.

[3] V. S. Ajaev. Viscous flow of a volatile liquid on an inclined heated surface. *Journal of Colloid and Interface Science*, 280(1):165–173, 2004.

[4] V. S. Ajaev. *Interfacial Fluid Mechanics*. Springer, 2012.

[5] V. S. Ajaev, T. Gambaryan-Roisman, and P. Stephan. Static and dynamic contact angles of evaporating liquids on heated surfaces. *Journal of Colloid and Interface Science*, 342(2):550–558, 2010.

[6] V. S. Ajaev and O. A. Kabov. Heat and mass transfer near contact lines on heated surfaces. *International Journal of Heat and Mass Transfer*, 108:918–932, 2017.

[7] D. E. Aljure, I. Rodríguez, O. Lehmkuhl, C. D. Pérez-Segarra, and A. Oliva. Influence of rotation on the flow over a cylinder at Re = 5000. *International Journal of Heat and Fluid Flow*, 55:76–90, 2015.

[8] R. F. Allen and C. M. Biggin. Longitudinal flow of a lenticular liquid filament down an inclined plane. *Physics of Fluids*, 17(2):287–291, 1974.

[9] A. S. Alshaikhi, S. K. Wilson, and B. R. Duffy. Rivulet flow down a slippery substrate. *Physics of Fluids*, 32(7):072011, 2020.

[10] A. S. Alshaikhi, S. K. Wilson, and B. R. Duffy. Rivulet flow over and through a permeable membrane. *Physical Review Fluids*, 6(10):104003, 2021.

[11] J. Ashmore, A. E. Hosoi, and H. A. Stone. The effect of surface tension on rimming flows in a partially filled rotating cylinder. *Journal of Fluid Mechanics*, 479:65–98, 2003.

[12] D. R. Baral, K. Hutter, and R. Greve. Asymptotic theories of large-scale motion, temperature, and moisture distribution in land-based polythermal ice sheets: A critical review and new developments. *Applied Mechanics Reviews*, 54(3):215–256, 2001.

[13] D. Barreiro-Villaverde, A. Gosset, and M. A. Mendez. On the dynamics of jet wiping: Numerical simulations and modal analysis. *Physics of Fluids*, 33(6):062114, 2021.

[14] J. Barrett and C. Clement. Kinetic evaporation and condensation rates and their coefficients. *Journal of Colloid and Interface Science*, 150(2):352–364, 1992.

[15] G. K. Batchelor. *Introduction to Fluid Dynamics*. Cambridge University Press, 1967.

[16] J. Bear. *Dynamics of Fluids in Porous Media*. Dover Publications, 1972.

[17] G. S. Beavers and D. D. Joseph. Boundary conditions at a naturally permeable wall. *Journal of Fluid Mechanics*, 30(1):197–207, 1967.

[18] E. S. Benilov and S. B. G. O'Brien. Inertial instability of a liquid film inside a rotating horizontal cylinder. *Physics of Fluids*, 17(5):052106, 2005.

[19] G. J. B. Black. Theoretical Studies of Thin-Film Flows. M. Phil. Thesis (University of Strathclyde, Glasgow), 2002.

[20] R. J. Braun, R. Usha, G. B. McFadden, T. A. Driscoll, L. P. Cook, and P. E. King-Smith. Thin film dynamics on a prolate spheroid with application to the cornea. *Journal of Engineering Mathematics*, 73:121–138, 2012.

[21] H. C. Brinkman. A calculation of the viscous force exerted by a flowing fluid on a dense swarm of particles. *Flow, Turbulence and Combustion*, 1(1):27–34, 1949.

[22] J. P. Burelbach, S. G. Bankoff, and S. H. Davis. Nonlinear stability of evaporating/condensing liquid films. *Journal of Fluid Mechanics*, 195:463–494, 1988.

[23] M. Cachile, M. A. Aguirre, M. Lenschen, and A. Calvo. Flow of a thin liquid film coating a horizontal stationary cylinder. *Physical Review E*, 88(6):063005, 2013.

[24] A.-M. Cazabat and G. Guena. Evaporation of macroscopic sessile droplets. *Soft Matter*, 6(12):2591–2612, 2010.

[25] V. Charitatos and S. Kumar. Droplet evaporation on soft solid substrates. *Soft Matter*, 17(41):9339–9352, 2021.

[26] V. Charitatos, T. Pham, and S. Kumar. Droplet evaporation on inclined substrates. *Physical Review Fluids*, 6(8):084001, 2021.

[27] B.-P. E. Clapeyron. Mémoir sur la puissance motrice de la chaleur. *Journal de L'École Royale Polytechnique*, 1:153–190, 1834.

[28] R. Clausius. Ueber die bewegende kraft der wärme und die gesetze, welche sich daraus für die wärmelehre selbst ableiten lassen. *Annalen der Physik*, 155(3):368–397, 1850.

[29] W. Cornwall. To replace controversial plastic additive BPA, a chemical company teams up with unlikely allies. https://www.science.org/content/article/replace-controversial-plastic-additive-bpa-chemical-company-teams-unlikely-allies. Accessed: 14.12.2022.

[30] R. V. Craster and O. K. Matar. Dynamics and stability of thin liquid films. *Reviews of Modern Physics*, 81(3):1131, 2009.

[31] H.-M. D'Ambrosio, T. Colosimo, B. R. Duffy, S. K. Wilson, L. Yang, C. D. Bain, and D. E. Walker. Evaporation of a thin droplet in a shallow well: theory and experiment. *Journal of Fluid Mechanics*, 927:A43, 2021.

[32] H. Darcy. *Les fontaines publiques de la ville de Dijon*. V. Dalmont, 1856.

[33] R. D. Deegan. Pattern formation in drying drops. *Physical Review E*, 61(1):475, 2000.

[34] R. D. Deegan, O. Bakajin, T. F. Dupont, G. Huber, S. R. Nagel, and T. A. Witten. Capillary flow as the cause of ring stains from dried liquid drops. *Nature*, 389(6653):827–829, 1997.

[35] R. D. Deegan, O. Bakajin, T. F. Dupont, G. Huber, S. R. Nagel, and T. A. Witten. Contact line deposits in an evaporating drop. *Physical Review E*, 62(1):756, 2000.

[36] A. K. Dodeja, S. C. Sarma, and H. Abichandani. Heat transfer during evaporation of milk to high solids in thin film scraped surface heat exchanger. *Journal of Food Process Engineering*, 12(3):211–225, 1990.

[37] B. R. Duffy and H. K. Moffatt. Flow of a viscous trickle on a slowly varying incline. *The Chemical Engineering Journal and the Biochemical Engineering Journal*, 60(1-3):141–145, 1995.

[38] B. R. Duffy and S. K. Wilson. Thin-film and curtain flows on the outside of a rotating horizontal cylinder. *Journal of Fluid Mechanics*, 394:29–49, 1999.

[39] G. J. Dunn, S. K. Wilson, B. R. Duffy, S. David, and K. Sefiane. A mathematical model for the evaporation of a thin sessile liquid droplet: Comparison between experiment and theory. *Colloids and Surfaces A: Physicochemical and Engineering Aspects*, 323(1-3):50–55, 2008.

[40] G. J. Dunn, S. K. Wilson, B. R. Duffy, S. David, and K. Sefiane. The strong influence of substrate conductivity on droplet evaporation. *Journal of Fluid Mechanics*, 623:329–351, 2009.

[41] C. H. Ellen and C. V. Tu. An analysis of jet stripping of liquid coatings. *Journal of Fluids Engineering*, 106(4):399–404, 1984.

[42] P. L. Evans, L. W. Schwartz, and R. V. Roy. Steady and unsteady solutions for coating flow on a rotating horizontal cylinder: Two-dimensional theoretical and numerical modeling. *Physics of Fluids*, 16(8):2742–2756, 2004.

[43] P. L. Evans, L. W. Schwartz, and R. V. Roy. Three-dimensional solutions for coating flow on a rotating horizontal cylinder: Theory and experiment. *Physics of Fluids*, 17(7):072102, 2005.

[44] M. Fogliati, D. Fontana, M. Garbero, M. Vanni, G. Baldi, and R. Donde. CFD simulation of paint deposition in an air spray process. *JCT Research*, 3:117–125, 2006.

[45] T. Gambaryan-Roisman. Liquids on porous layers: wetting, imbibition and transport processes. *Current Opinion in Colloid and Interface Science*, 19(4):320–335, 2014.

[46] T. Gambaryan-Roisman and P. Stephan. Flow and stability of rivulets on heated surfaces with topography. *Journal of Heat Transfer*, 131(3):033101, 2009.

[47] S. Gehrmann and H. Bunjes. Preparation of lipid nanoemulsions by premix membrane emulsification with disposable materials. *International Journal of Pharmaceutics*, 511(2):741–744, 2016.

[48] N. Ghillani, M. Heinz, and T. Gambaryan-Roisman. Capillary rise and evaporation of a liquid in a corner between a plane and a cylinder: A model of imbibition into a nanofiber mat coating. *The European Physical Journal Special Topics*, 229:1799–1818, 2020.

[49] M. B. Glauert. The flow past a rapidly rotating circular cylinder. *Proceedings of the Royal Society of London. Series A. Mathematical and Physical Sciences*, 242(1228):108–115, 1957.

[50] S. L. Goren. The hydrodynamic force resisting the approach of a sphere to a plane permeable wall. *Journal of Colloid and Interface Science*, 69(1):78–85, 1979.

[51] A Gosset and J. M. Buchlin. Jet wiping in hot-dip galvanization. *Journal of Fluids Engineering*, 129(4):466–475, 2007.

[52] R. W. Griffiths. The dynamics of lava flows. *Annual Review of Fluid Mechanics*, 32:477–518, 2000.

[53] C. M. Groh and M. A. Kelmanson. Multiple-timescale asymptotic analysis of transient coating flows. *Physics of Fluids*, 21(9):091702, 2009.

[54] C. M. Groh and M. A. Kelmanson. Computer-algebra multiple-timescale method for spatially periodic thin-film viscous-flow problems. *International Journal for Numerical Methods in Fluids*, 68(11):1457–1470, 2012.

[55] C. M. Groh and M. A. Kelmanson. Inertially induced cyclic solutions in thin-film free-surface flows. *Journal of Fluid Mechanics*, 755:628–653, 2014.

[56] J. B. Grotberg. Pulmonary flow and transport phenomena. *Annual Review of Fluid Mechanics*, 26:529–571, 1994.

[57] T. Grypachevska. Brown and black mountain under white clouds. https://unsplash.com/photos/80x3QULJDN4. Accessed: 21.09.2023.

[58] E. B. Hansen and M. A. Kelmanson. Steady, viscous, free-surface flow on a rotating cylinder. *Journal of Fluid Mechanics*, 272:91–108, 1994.

[59] M. Haynes and M. Pradas. On the lifetimes of two-dimensional droplets on smooth wetting patterns. *Journal of Engineering Mathematics*, 135(1):2, 2022.

[60] Y. Hikami and N. Shiraishi. Rain-wind induced vibrations of cables stayed bridges. *Journal of Wind Engineering and Industrial Aerodynamics*, 29(1-3):409–418, 1988.

[61] E. J. Hinch and M. A. Kelmanson. On the decay and drift of free-surface perturbations in viscous thin-film flow exterior to a rotating cylinder. *Proceedings of the Royal Society of London. Series A: Mathematical, Physical and Engineering Sciences*, 459(2033):1193–1213, 2003.

[62] E. J. Hinch, M. A. Kelmanson, and P. D. Metcalfe. Shock-like free-surface perturbations in low-surface-tension, viscous, thin-film flow exterior to a rotating cylinder. *Proceedings of the Royal Society of London. Series A: Mathematical, Physical and Engineering Sciences*, 460(2050):2975–2991, 2004.

[63] M. Hlaváček. The role of synovial fluid filtration by cartilage in lubrication of synovial joints – I. Mixture model of synovial fluid. *Journal of Biomechanics*, 26(10):1145–1150, 1993.

[64] M. Hlaváček. The role of synovial fluid filtration by cartilage in lubrication of synovial joints – II. Squeeze-film lubrication: Homogeneous filtration. *Journal of Biomechanics*, 26(10):1151–1160, 1993.

[65] M. Hlaváček and J. Novak. The role of synovial fluid filtration by cartilage in lubrication of synovial joints – III. Squeeze-film lubrication: Axial symmetry under low-loading conditions. *Journal of Biomechanics*, 28(10):1193–1198, 1995.

[66] D. Holland, B. R. Duffy, and S. K. Wilson. Thermocapillary effects on a thin viscous rivulet draining steadily down a uniformly heated or cooled slowly varying substrate. *Journal of Fluid Mechanics*, 441:195–221, 2001.

[67] P. D. Howell, H. Kim, M. G. Popova, and H. A. Stone. Rivulet flow over a flexible beam. *Journal of Fluid Mechanics*, 796:285–305, 2016.

[68] P. D. Howell, J. Robinson, and H. A. Stone. Gravity-driven thin-film flow on a flexible substrate. *Journal of Fluid Mechanics*, 732:190–213, 2013.

[69] H. Hu and R. G. Larson. Analysis of the microfluid flow in an evaporating sessile droplet. *Langmuir*, 21(9):3963–3971, 2005.

[70] R. E. Johnson. Steady-state coating flows inside a rotating horizontal cylinder. *Journal of Fluid Mechanics*, 190:321–342, 1988.

[71] A. D. Johnstone, B. Kosasih, Q. P. Le, A. Dixon, and W. Renshaw. Coating film profiles generated by fluctuating location of the wiping pressure and shear stress. *ISIJ International*, 59(2):319–325, 2019.

[72] S. Kandlikar, S. Garimella, D. Li, S. Colin, and M. R. King. *Heat Transfer and Fluid Flow in Minichannels and Microchannels*. Elsevier, 2005.

[73] J. Kang, X. Fu, W. Liu, and P. Dario. Investigation on microheat pipe array with arteries. *Journal of Thermophysics and Heat Transfer*, 24(4):803–810, 2010.

[74] S. Kang, H. Choi, and S. Lee. Laminar flow past a rotating circular cylinder. *Physics of Fluids*, 11(11):3312–3321, 1999.

[75] T. Karmakar and G. P. Raja Sekhar. Squeeze-film flow between a flat impermeable bearing and an anisotropic porous bed. *Physics of Fluids*, 30(4):043604, 2018.

[76] E. D. Kay, S. Hibberd, and H. Power. Inertial effects at moderate Reynolds number in thin-film rimming flows driven by surface shear. *Physics of Fluids*, 25(10):102108, 2013.

[77] E. D. Kay, S. Hibberd, and H. Power. A depth-averaged model for non-isothermal thin-film rimming flow. *International Journal of Heat and Mass Transfer*, 70:1003–1015, 2014.

[78] E. D. Kay, S. Hibberd, and H. Power. Non-isothermal rimming flow with the effects of surface shear and droplet impact. *Physics of Fluids*, 27(12):122105, 2015.

[79] M. A. Kelmanson. On inertial effects in the Moffatt–Pukhnachov coating-flow problem. *Journal of Fluid Mechanics*, 633:327–353, 2009.

[80] S. Khabthani, A. Sellier, and F. Feuillebois. Lubricating motion of a sphere towards a thin porous slab with Saffman slip condition. *Journal of Fluid Mechanics*, 867:949–968, 2019.

[81] A. C. King and E. O. Tuck. Thin liquid layers supported by steady air-flow surface traction. *Journal of Fluid Mechanics*, 251:709–718, 1993.

[82] A. C. King, E. O. Tuck, and J. M. Vanden-Broeck. Air-blown waves on thin viscous sheets. *Physics of Fluids A: Fluid Dynamics*, 5(4):973–978, 1993.

[83] M. Knoche and M. J. Bukovac. Surfactants influence foliar absorption of gibberellic acid by sour cherry leaves. *Journal of the American Society for Horticultural Science*, 117(1):80–84, 1992.

[84] D. J. Knox. *Squeeze-film Flows, with Application to the Human Knee Joint.* Ph.D. Thesis, University of Strathclyde, 2014.

[85] D. J. Knox, B. R. Duffy, S. McKee, and S. K Wilson. Squeeze-film flow between a curved impermeable bearing and a flat porous bed. *Physics of Fluids*, 29(2):023101, 2017.

[86] D. J. Knox, S. K. Wilson, B. R. Duffy, and S. McKee. Porous squeeze-film flow. *IMA Journal of Applied Mathematics*, 80(2):376–409, 2015.

[87] D. Y. Kochkin, F. V. Ronshin, and V. V. Cheverda. Experimental study of heat transfer in FC-72 fluid rivulet over heated vertical plate. *Journal of Engineering Thermophysics*, 31(4):603–608, 2022.

[88] F. A. Kulacki, S. Acharya, Y. Chudnovsky, R. M. Cotta, R. Devireddy, V. K. Dhir, M. P. Mengüç, J. Mostaghimi, and K. Vafai. *Handbook of Thermal Science and Engineering*. Springer, 2018.

[89] R. G. Larson. Transport and deposition patterns in drying sessile droplets. *AIChE Journal*, 60(5):1538–1571, 2014.

[90] C. Lemaitre, P. Hémon, and E. de Langre. Thin water film around a cable subject to wind. *Journal of Wind Engineering and Industrial Aerodynamics*, 95(9-11):1259–1271, 2007.

[91] G. A. Leslie, S. K. Wilson, and B. R. Duffy. Thermoviscous coating and rimming flow. *The Quarterly Journal of Mechanics and Applied Mathematics*, 65(4):483–511, 2012.

[92] G. A. Leslie, S. K Wilson, and B. R. Duffy. Three-dimensional coating and rimming flow: a ring of fluid on a rotating horizontal cylinder. *Journal of Fluid Mechanics*, 716:51–82, 2013.

[93] Q. Liu, Y. Yan, L. Meng, Z. Zhang, and P. Zhou. Influence of airflow disturbance on the uniformity of spin coating film thickness on large area rectangular substrates. *Coatings*, 12(9):1253, 2022.

[94] A. v. B. Lopes, U. Thiele, and A. L. Hazel. On the multiple solutions of coating and rimming flows on rotating cylinders. *Journal of Fluid Mechanics*, 835:540–574, 2018.

[95] Maplesoft (a division of Waterloo Maple Inc., Waterloo, Ontario, Canada). Maple version 2022.2. https://www.maplesoft.com/, 2022.

[96] H. Masoud and J. D. Felske. Analytical solution for inviscid flow inside an evaporating sessile drop. *Physical Review E*, 79(1):016301, 2009.

[97] A. J. T. M. Mathijssen, M. Lisicki, V. N. Prakash, and E. J. L. Mossige. Culinary fluid mechanics and other currents in food science. *Reviews of Modern Physics*, 95(2):025004, 2023.

[98] G. McHale, S. Aqil, N. J. Shirtcliffe, M. I. Newton, and H. Y. Erbil. Analysis of droplet evaporation on a superhydrophobic surface. *Langmuir*, 21(24):11053–11060, 2005.

[99] G. McHale, S. M. Rowan, M. I. Newton, and M. K. Banerjee. Evaporation and the wetting of a low-energy solid surface. *The Journal of Physical Chemistry B*, 102(11):1964–1967, 1998.

[100] R. A. McKinlay, A. W. Wray, and S. K. Wilson. Late-time draining of a thin liquid film on the outer surface of a circular cylinder. *Physical Review Fluids*, 8(8):084001, 2023.

[101] F. Melo. Localized states in a film-dragging experiment. *Physical Review E*, 48(4):2704, 1993.

[102] M. A. Mendez, A. Gosset, B. Scheid, M. Balabane, and J. M. Buchlin. Dynamics of the jet wiping process via integral models. *Journal of Fluid Mechanics*, 911:A47, 2021.

[103] S. Middleman. The effect of induced air-flow on the spin coating of viscous liquids. *Journal of Applied Physics*, 62(6):2530–2532, 1987.

[104] A. Mikelić and W. Jäger. On the interface boundary condition of Beavers, Joseph, and Saffman. *SIAM Journal on Applied Mathematics*, 60(4):1111–1127, 2000.

[105] A. J. Mitchell, B. R. Duffy, and S. K. Wilson. Coating flow on a rotating cylinder in the presence of an irrotational airflow with circulation. *Journal of Fluid Mechanics*, 932:A33, 2022.

[106] A. J. Mitchell, B. R. Duffy, and S. K. Wilson. Unsteady coating flow on a rotating cylinder in the presence of an irrotational airflow with circulation. *Physics of Fluids*, 34(4):043105, 2022.

[107] S. Mittal and B. Kumar. Flow past a rotating cylinder. *Journal of Fluid Mechanics*, 476:303–334, 2003.

[108] H. K. Moffatt. Behaviour of a viscous film on the outer surface of a rotating cylinder. *Journal de Mécanique*, 16(5):651–673, 1977.

[109] D. W. Moore. The flow past a rapidly rotating circular cylinder in a uniform stream. *Journal of Fluid Mechanics*, 2(6):541–550, 1957.

[110] N. Murisic and L. Kondic. On evaporation of sessile drops with moving contact lines. *Journal of Fluid Mechanics*, 679:219–246, 2011.

[111] P. R. K. Murti. Squeeze-film behaviour in porous circular disks. *Journal of Lubrication Technology*, 96(2):206–209, 1974.

[112] P. R. K. Murti. Effect of velocity slip in an externally pressurised porous thrust bearing working with an incompressible fluid. *Journal of Applied Mechanics*, 43(3):404–408, 1976.

[113] T. G. Myers, J. P. F. Charpin, and S. J. Chapman. The flow and solidification of a thin fluid film on an arbitrary three-dimensional surface. *Physics of Fluids*, 14(8):2788–2803, 2002.

[114] T. G. Myers, J. P. F. Charpin, and C. P. Thompson. Slowly accreting ice due to supercooled water impacting on a cold surface. *Physics of Fluids*, 14(1):240–256, 2002.

[115] T. G. Myers, H. X. Liang, and B. Wetton. The stability and flow of a rivulet driven by interfacial shear and gravity. *International Journal of Non-Linear Mechanics*, 39(8):1239–1249, 2004.

[116] K. Myrillas, A. Gosset, P. Rambaud, and J. M. Buchlin. CFD simulation of gas-jet wiping process. *The European Physical Journal Special Topics*, 166(1):93–97, 2009.

[117] P. Naphade, A. Mukhopadhyay, and S. Chakrabarti. Mathematical modelling of jet finishing process for hot-dip zinc coatings on steel strip. *ISIJ International*, 45(2):209–213, 2005.

[118] H. Newell and H. Viljoen. Stability analysis of a thin film on a rotating cylinder with low airflow. *Physics of Fluids*, 31(3):034106, 2019.

[119] D. A. Nield. The Beavers–Joseph boundary condition and related matters: A historical and critical note. *Transport in Porous Media*, 78:537–540, 2009.

[120] W. Nusselt. Die oberflachenkondensation des wasserdamphes. *Vereines deutscher Ingenieure*, 60:541–546, 1916.

[121] W. Nusselt. Die oberflachenkondensation des wasserdamphes. *Vereines deutscher Ingenieure*, 60:569–575, 1916.

[122] S. B. G. O'Brien. Linear stability of rimming flow. *Quarterly of Applied Mathematics*, 60(2):201–211, 2002.

[123] A. Offner and G. Z. Ramon. The interaction of a particle and a polymer brush coating a permeable surface. *Journal of Fluid Mechanics*, 913:R3, 2021.

[124] A. Oron, S. H. Davis, and S. G. Bankoff. Long-scale evolution of thin liquid films. *Reviews of Modern Physics*, 69(3):931–980, 1997.

[125] A. Öztekin, D. E. Bornside, R. A. Brown, and P. K. Seidel. The connection between hydrodynamic stability of gas flow in spin coating and coated film uniformity. *Journal of Applied Physics*, 77(6):2297–2308, 1995.

[126] S. B. G. O'Brien. A model for the coating of cylindrical light bulbs. In L. Arkeryd, J. Bergh, P. Brenner, and R. Pettersson, editors, *In Progress in Industrial Mathematics*, pages 46–55. Teubner, B. G., Oxford, 1998.

[127] S. B. G. O'Brien. A mechanism for linear instability in two-dimensional rimming flow. *Quarterly of Applied Mathematics*, 60(2):283–299, 2002.

[128] H. J. Palmer. The hydrodynamic stability of rapidly evaporating liquids at reduced pressure. *Journal of Fluid Mechanics*, 75(3):487–511, 1976.

[129] C. Paterson, S. K. Wilson, and B. R. Duffy. Pinning, de-pinning and re-pinning of a slowly varying rivulet. *European Journal of Mechanics B/Fluids*, 41:94–108, 2013.

[130] C. Paterson, S. K. Wilson, and B. R. Duffy. Strongly coupled interaction between a ridge of fluid and an inviscid airflow. *Physics of Fluids*, 27(7):072104, 2015.

[131] C. H. Pearson and D. J. Rath. A hydraulic press for extracting fluids from plant tissue samples. *Industrial Crops and Products*, 29(2-3):634–637, 2009.

[132] C. A. Perazzo and J. Gratton. Navier–Stokes solutions for parallel flow in rivulets on an inclined plane. *Journal of Fluid Mechanics*, 507:367–379, 2004.

[133] R. C. Peterson, P. K. Jimack, and M. A. Kelmanson. On the stability of viscous free–surface flow supported by a rotating cylinder. *Proceedings of the Royal Society of London. Series A: Mathematical, Physical and Engineering Sciences*, 457(2010):1427–1445, 2001.

[134] V. H. Pham, T. V. Cuong, S. H. Hur, E. W. Shin, J. S. Kim, J. S. Chung, and Kim. E. J. Fast and simple fabrication of a large transparent chemically-converted graphene film by spray-coating. *Carbon*, 48(7):1945–1951, 2010.

[135] R. G. Picknett and R. Bexon. The evaporation of sessile or pendant drops in still air. *Journal of Colloid and Interface Science*, 61(2):336–350, 1977.

[136] Y. O. Popov. Evaporative deposition patterns: Spatial dimensions of the deposit. *Physical Review E*, 71(3):036313, 2005.

[137] V. V. Pukhnachev. Motion of a liquid film on the surface of a rotating cylinder in a gravitational field. *Journal of Applied Mechanics and Technical Physics*, 18(3):344–351, 1977.

[138] G. Z. Ramon and E. M. V. Hoek. On the enhanced drag force induced by permeation through a filtration membrane. *Journal of Membrane Science*, 392–393:1–8, 2012.

[139] G. Z. Ramon, H. E. Huppert, J. R. Lister, and H. A. Stone. On the hydrodynamic interaction between a particle and a permeable surface. *Physics of Fluids*, 25(7):073103, 2013.

[140] R. B. Reboucas and M. Loewenberg. Collision rates of permeable particles in creeping flows. *Physics of Fluids*, 33(8):083322, 2021.

[141] R. B. Reboucas and M. Loewenberg. Near-contact approach of two permeable spheres. *Journal of Fluid Mechanics*, 925:A1, 2021.

[142] R. B. Reboucas and M. Loewenberg. Resistance and mobility functions for the near-contact motion of permeable particles. *Journal of Fluid Mechanics*, 938:A27, 2022.

[143] B. Reisfeld and S. G. Bankoff. Non-isothermal flow of a liquid film on a horizontal cylinder. *Journal of Fluid Mechanics*, 236:167–196, 1992.

[144] A. C. Robertson, I. J. Taylor, S. K. Wilson, B. R. Duffy, and J. M. Sullivan. Numerical simulation of rivulet evolution on a horizontal cable subject to an external aerodynamic field. *Journal of Fluids and Structures*, 26(1):50–73, 2010.

[145] P. G. Saffman. On the boundary condition at the surface of a porous medium. *Studies in Applied Mathematics*, 50(2):93–101, 1971.

[146] M. Salafi, N. Asasian-Kolur, S. Sharifian, and A. Ghadimi. A flat-plate spiral-channeled membrane heat exchanger for methane dehumidification: Comparison of kraft paper and thin-film composite membrane. *International Journal of Thermal Sciences*, 167:107046, 2021.

[147] F. G. H. Schofield, D. Pritchard, S. K. Wilson, and K. Sefiane. The lifetimes of evaporating sessile droplets of water can be strongly influenced by thermal effects. *Fluids*, 6(4):141, 2021.

[148] F. G. H. Schofield, S. K. Wilson, D. Pritchard, and K. Sefiane. The lifetimes of evaporating sessile droplets are significantly extended by strong thermal effects. *Journal of Fluid Mechanics*, 851:231–244, 2018.

[149] F. G. H. Schofield, A. W. Wray, D. Pritchard, and S. K. Wilson. The shielding effect extends the lifetimes of two-dimensional sessile droplets. *Journal of Engineering Mathematics*, 120(1):89–110, 2020.

[150] R. W. Schrage. *A Theoretical Study of Interphase Mass Transfer*. Columbia University Press, 1953.

[151] M. Schremb, I. V. Roisman, and C. Tropea. Normal impact of supercooled water drops onto a smooth ice surface: experiments and modelling. *Journal of Fluid Mechanics*, 835:1087–1107, 2018.

[152] R. K. Singh, J. E. Galvin, G. A. Whyatt, and X. Sun. Breakup of a liquid rivulet falling over an inclined plate: Identification of a critical Weber number. *Physics of Fluids*, 29(5):052101, 2017.

[153] M. Sparks. Physicists finally figured out why food sticks to a frying pan. https://www.newscientist.com/article/2266479-physicists-finally-figured-out-why-food-sticks-to-a-frying-pan. Accessed: 14.12.2022.

[154] T. Sparks and G. Chase. *Filters and Filtration Handbook*. Elsevier, 2015.

[155] D. Stojković, M. Breuer, and F. Durst. Effect of high rotation rates on the laminar flow around a circular cylinder. *Physics of Fluids*, 14(9):3160–3178, 2002.

[156] H. A. Stone. On lubrication flows in geometries with zero local curvature. *Chemical Engineering Science*, 60(17):4838–4845, 2005.

[157] J. M. Sullivan, S. K. Wilson, and B. R. Duffy. A thin rivulet of perfectly wetting fluid subject to a longitudinal surface shear stress. *Quarterly Journal of Mechanics and Applied Mathematics*, 61(1):25–61, 2008.

[158] E. Sultan, A. Boudaoud, and M. B. Amar. Diffusion-limited evaporation of thin polar liquid films. *Journal of Engineering Mathematics*, 50:209–222, 2004.

[159] A. Z. Szeri. *Fluid Film Lubrication*. Cambridge University Press, 1998.

[160] D. Takagi and H. E. Huppert. Flow and instability of thin films on a cylinder and sphere. *Journal of Fluid Mechanics*, 647:221–238, 2010.

[161] A. J. Tanasijczuk, C. A. Perazzo, and J. Gratton. Navier–Stokes solutions for steady parallel-sided pendent rivulets. *European Journal of Mechanics-B/Fluids*, 29(6):465–471, 2010.

[162] I. J. Taylor and A. C. Robertson. Numerical simulation of the airflow-rivulet interaction associated with the rain-wind induced vibration phenomenon. *Journal of Wind Engineering and Industrial Aerodynamics*, 99(9):931–944, 2011.

[163] I. J. Taylor and A. C. Robertson. Numerical investigation of the coupled interaction between an unsteady aerodynamic flow field and a water film coating on a circular cylinder. *Journal of Fluids and Structures*, 54:312–331, 2015.

[164] M. Tembely, R. Attarzadeh, and A. Dolatabadi. On the numerical modeling of supercooled micro-droplet impact and freezing on superhydrophobic surfaces. *International Journal of Heat and Mass Transfer*, 127:193–202, 2018.

[165] M. Toberman, M. Inall, T. Boyd, E. Dumount, and C. Griffiths. Nonlinear internal waves and plumes generated in response to sea-loch outflow, AUV, and time-lapse photography observations. *Journal of Geophysical Research: Oceans*, 122(7):5522–5544, 2017.

[166] G. D. Towell and L. B. Rothfeld. Hydrodynamics of rivulet flow. *AIChE Journal*, 12(5):972–980, 1966.

[167] E. O. Tuck and J. M. Vanden-Broeck. Influence of surface tension on jet-stripped continuous coating of sheet materials. *AIChE Journal*, 30(5):808–811, 1984.

[168] M. Van Dyke. *Perturbation Methods in Fluid Mechanics.* Parabolic, 1975.

[169] D. C. Venerus. Squeeze flows in liquid films bound by porous disks. *Journal of Fluid Mechanics*, 855:860–811, 2018.

[170] R. L. Verma. Effect of velocity slip in an externally pressurised porous circular thrust bearing. *Wear*, 63(2):239–244, 1980.

[171] M. Villegas-Díaz, H. Power, and D. S. Riley. On the stability of rimming flows to two-dimensional disturbances. *Fluid Dynamics Research*, 33(1-2):141–172, 2003.

[172] M. Villegas-Díaz, H. Power, and D. S. Riley. Analytical and numerical studies of the stability of thin-film rimming flow subject to surface shear. *Journal of Fluid Mechanics*, 541:317–344, 2005.

[173] M. R. E. Warner, R. V. Craster, and O. K. Matar. Surface patterning via evaporation of ultrathin films containing nanoparticles. *Journal of Colloid and Interface Science*, 267(1):92–110, 2003.

[174] C. W. Watts. The accretion of ice on the wing of an aeroplane. https://www.flickr.com/photos/63366024@N00/3168468245/in/dateposted/. Accessed: 14.12.2022.

[175] S. Whitaker. Flow in porous media I: A theoretical derivation of Darcy's law. *Transport in Porous Media*, 1:3–25, 1986.

[176] S. D. R. Wilson and J. Williams. The flow of a liquid film on the inside of a rotating cylinder, and some related problems. *Physics of Fluids*, 9(8):2184–2190, 1997.

[177] S. K. Wilson and H.-M. D'Ambrosio. Evaporation of sessile droplets. *Annual Review of Fluid Mechanics*, 55:481–509, 2023.

[178] S. K. Wilson and B. R. Duffy. A rivulet of perfectly wetting fluid draining steadily down a slowly varying substrate. *IMA Journal of Applied Mathematics*, 70(2):293–322, 2005.

[179] S. K. Wilson and B. R. Duffy. Unidirectional flow of a thin rivulet on a vertical substrate subject to a prescribed uniform shear stress at its free surface. *Physics of Fluids*, 17(10):108105, 2005.

[180] S. K. Wilson, R. Hunt, and B. R. Duffy. On the critical solutions in coating and rimming flow on a uniformly rotating horizontal cylinder. *The Quarterly Journal of Mechanics and Applied Mathematics*, 55(3):357–383, 2002.

[181] S. K. Wilson, J. M. Sullivan, and B. R. Duffy. The energetics of the breakup of a sheet and of a rivulet on a vertical substrate in the presence of a uniform surface shear stress. *Journal of Fluid Mechanics*, 674:281–306, 2011.

[182] Wolfram Research Inc. (Champaign, IL, USA). Mathematica version 12. https://www.wolfram.com/, 2022.

[183] A. W. Wray and R. Cimpeanu. Reduced-order modelling of thick inertial flows around rotating cylinders. *Journal of Fluid Mechanics*, 898:A1, 2020.

[184] A. W. Wray, D. T. Papageorgiou, and O. K. Matar. Reduced models for thick liquid layers with inertia on highly curved substrates. *SIAM Journal on Applied Mathematics*, 77(3):881–904, 2017.

[185] A. W. Wray, P. S. Wray, B. R. Duffy, and S. K. Wilson. Contact-line deposits from multiple evaporating droplets. *Physical Review Fluids*, 6(7):073604, 2021.

[186] H. Wu. Squeeze-film behavior for porous annular disks. *Journal of Lubrication Technology*, 92(4):593–596, 1970.

[187] L. Wu. Spin coating of thin liquid films on an axisymmetrically heated disk. *Physics of Fluids*, 18(6):063602, 2006.

[188] A. L. Yarin, J. B. Szczech, C. M. Megaridis, J. Zhang, and D. R. Gamota. Lines of dense nanoparticle colloidal suspensions evaporating on a flat surface: Formation of non-uniform dried deposits. *Journal of Colloid and Interface Science*, 294(2):343–354, 2006.

[189] E. Yariv. Lifetime of evaporating two-dimensional sessile droplets. *Physical Review E*, 107(6):L063101, 2023.

[190] C. S. Yih. Instability of a rotating liquid film with a free surface. *Proceedings of the Royal Society of London. Series A. Mathematical and Physical Sciences*, 258(1292):63–89, 1960.

[191] R. Zenit. Some fluid mechanical aspects of artistic painting. *Physical Review Fluids*, 4(11):110507, 2019.

[192] L. Zhang, Y. R. Li, L. Q. Zhou, and C. M. Wu. Comparison study on the calculation formula of evaporation mass flux through the plane vapour-liquid interface. *Journal of Physics: Conference Series*, 925(1):012019, 2017.

[193] Y. Zhang, Q-P. Cui, F. Q. Shao, J. S. Wang, and H. Y. Zhao. Influence of air-knife wiping on coating thickness in hot-dip galvanizing. *Journal of Iron and Steel Research International*, 19(6):70–78, 2012.